Neutron scattering studies of molten salts

by

Malcolm Andrew Howe

St Catherine's College

Oxford

A thesis submitted for

the degree of

Doctor of Philosophy

Michaelmas Term

mcmlxxxvij

Contents

	List of figures	3
	List of tables	7
	List of symbols	8
	Acknowledgements	12
	Abstract	14
Chapter 1.	Introduction	16
Chapter 2.	The scattering of neutrons by condensed matter	23
Chapter 3.	Structure factors and other correlation functions	36
Chapter 4.	Neutron transport theory	68
Chapter 5.	Instruments and equipment used in neutron scattering experiments	79
Chapter 6.	The corrections applied to neutron scattering data	87
Chapter 7.	Multiple scattering of neutrons	93
Chapter 8.	Inelasticity corrections - deviations from the static approximation	101
Chapter 9.	The structure of lithium chloride and its admixture with potassium chloride	116
Chapter 10.	The temperature dependence of the structure of molten caesium chloride by time-of-flight diffractometry	130
Chapter 11.	The dynamics of molten caesium chloride	142
Chapter 12.	The structure and dynamics of molten and fast ion conducting silver iodide	150
Appendix A.	Neutron scattering parameters and properties of molten salts	167
Appendix B.	Properties of Heisenberg operators	169
Appendix C.	Delta functions and Fourier transforms	173
Appendix D.	The conditioning of sets of linear equations	177
	References	181

List of figures

5.1 The region of $(Q-\omega)$ space accessible using IN6 with 5.1Å neutrons and IN4 with 1.05Å neutrons 84

7.1 The single, double, and multiple scattering for caesium chloride on D4B. 98

7.2 The single and multiple scattering for caesium chloride on IN4. 100

7.3 The single and multiple scattering for silver iodide on IN6. 100

8.1 Integration paths for D4B with incident wavelengths of 0.7Å and 0.5Å 115

8.2 Integration paths for the LAD detectors. 115

9.1 Partial radial distribution functions for NaCl, RbCl, and CsCl. 117

9.2 Scattering intensities for $^{7}Li^{35}Cl$, $^{7}Li^{N}CL$ and $^{7}Li^{37}Cl$, container and furnace. 119

9.3 Total structure factors for $^{7}Li^{N}Cl$, $^{7}Li^{35}CL$ and $^{7}Li^{37}Cl$. 119

9.4 The partial structure factors $A_{++}(Q)$, $A_{+-}(Q)$, and $A_{--}(Q)$ for LiCL obtained from the three total structure factors 120

9.5 The partial pair distribution functions for lithium chloride obtained from the three partial structure factors. 120

9.6 The partial structure factors $A_{\mathrm{like}}(Q)$ and $A_{\mathrm{unlike}}(Q)$ obtained from the total structure factors of $^{7}Li^{35}Cl$ and $^{7}Li^{37}Cl$. 121

9.7 The scattering from $^{7}Li^{N}Cl$ compared with that expected from combination of the two partial structure factors $A_{\mathrm{like}}(Q)$ and $A_{\mathrm{unlike}}(Q)$. 121

9.8 The partial structure factors $A_{NN}(Q)$, $A_{Nq}(Q)$, and $A_{qq}(Q)$, for LiCl obtained from the three total structure factors. 122

9.9 The partial structure factors $A_{NN}(Q)$ and $A_{qq}(Q)$, obtained from two samples (assuming $A_{Nq}(Q)=0$). 122

9.10 The partial pair distribution function $g_{\mathrm{like}}(r)$ compared with $g_{++}(r)$ and $g_{--}(r)$ from simulation. 124

9.11 The partial pair distribution function $g_{\text{unlike}}(r)$ compared with $g_{+-}(r)$ from simulation. 124

9.12 The total pair distribution functions for the three samples of LiCl compared with simulation. 124

9.13 The scattering from ($^{(0)}$Li/K)Cl as a function of time. 127

9.14 Scattering for (^{7}Li/K)Cl, KCl, ($^{(0)}$Li/K)Cl, container and furnace. 127

9.15 Corrected cross-sections for KCl, ($^{(0)}$Li/K)Cl, and (^{7}Li/K)Cl. 128

9.16 $g_T(r)$ for KCl compared with simulation. 128

9.17 The combination of lithium partial structure factors obtained from the two total structure factors for (Li/K)Cl. 128

9.18 $g_T(r)$ for the two samples of (Li/K)Cl. 128

10.1 Scattering intensities for CsCl, a container, furnace, and vanadium calibration at an angle of 90° on LAD. 130

10.2 Scattering intensities for CsCl, a container, furnace, and vanadium calibration at an angle of 5° on LAD. 130

10.3 The cross-section for CsCl at 670°C measured at six angles. 131

10.4 The cross-section for CsCl at 970°C measured at six angles. 131

10.5 Structure factors for caesium chloride at 670°C obtained by the maximum entropy method and by cubic spline smoothing compared with the experimental points. 139

10.6 Structure factors for caesium chloride at 970°C obtained by the maximum entropy method and by cubic spline smoothing compared with the experimental points. 139

10.7 Structure factor for caesium chloride at 670°C compared with the data from the different detectors. 139

10.8 Structure factor for caesium chloride at 970°C compared with the data from the different detectors. 139

10.9 $g_T(r)$ for caesium chloride at 670°C obtained in different ways. 139

10.10 $g_T(r)$ for caesium chloride at 970°C obtained in different ways. 139

10.11 Structure factor of caesium chloride as determined by LAD and D4B. 140

10.12 Structure factor of caesium chloride at 670°C and 970°C. 140

10.13 $g_T(r)$ of caesium chloride at 670°C and 970°C compared with a Monte Carlo simulation and the D4B results at 695°C. 140

10.14 $g_T(r)$ of caesium chloride at 670°C and 970°C compared with a molecular dynamics simulation. 140

11.1 Quasi-dispersion curves for molten caesium chloride. 146

11.2 Scattering cross-sections for caesium chloride measured on IN4. 147

11.3 $S(Q,\omega)$ for caesium chloride as determined by six detectors of IN4. 147

11.4 $S(Q,\omega)$ for caesium chloride. 147

11.5 Width of the quasi-elastic peak of $S(Q,\omega)$ for caesium chloride. 147

11.6 $S_T(Q)$ for caesium chloride compared with the result from LAD. 147

11.7 $C_T(Q,\omega)$ for caesium chloride determined by the six lowest angle detectors of IN4. 147

12.1 Elastic scattering from α-^{109}AgI, α-^{N}AgI, container and furnace at 300°C as measured on D4B. 154

12.2 Diffuse total structure factors for α-^{N}AgI and α-^{109}AgI. 154

12.3 Diffuse partial structure factors for α-AgI. 154

12.4 Partial pair distribution functions for α-AgI. 154

12.5 Elastic scattering from molten ^{107}AgI, ^{N}AgI, ^{109}AgI, silica cell and furnace measured on D4B. 156

12.6 Cross-section for ^{107}AgI at 300°C and 600°C. 156

12.7 Cross-sections for molten ^{107}AgI, ^{N}AgI, and ^{109}AgI at 600°C. 156

12.8 Radial distribution functions for ^{107}AgI at 300°C and 600°C. 156

12.9 Partial structure factors for molten AgI. 158

12.10 Partial pair distribution functions for molten AgI from an HNC calculation. 160

12.11 $g_T(r)$ for the AgI samples compared with the HNC calculation. 160

12.12 Scattering intensities for α-^{N}AgI, molten ^{N}AgI, α-^{109}AgI, molten ^{109}AgI, a silica container and the furnace at a scattering angle of 11.9° on IN6. 163

12.13 Scattering intensities for α-^{N}AgI, molten ^{N}AgI, α-^{109}AgI, molten ^{109}AgI, a silica container and the furnace at a scattering angle of 111.6° on IN6. 163

12.14 Corrected spectra for α-^{N}AgI, molten ^{N}AgI, α-^{109}AgI, and molten ^{109}AgI at a scattering angle of 97.3°. 163

12.15 Scattering intensities for molten ^{N}AgI. 163

12.16 Quasi-dispersion curve for molten ^{N}AgI. 163

12.17 Surface plot of scattering from molten ^{N}AgI (energy vs. angle). 163

12.18 Surface plot of scattering from molten ^{N}AgI (energy vs. momentum transfer). 163

12.19 $C(Q,\omega)$ for molten ^{N}AgI. 163

12.20 Scattering intensities for molten ^{109}AgI. 163

12.21 Scattering intensities for α-^{N}AgI. 163

12.22 The height and width of the quasi-elastic peak of $S(Q,\omega)$ for molten ^{N}AgI. 166

12.23 $S_T(Q)$ for molten ^{N}AgI calculated by integration of $S_T(Q,\omega)$ compared with the diffraction result. 166

List of tables

1. Determinations of the structures of molten salts 22

2. Determinations of the dynamics of molten salts 22

3. Double scattering from cylinders as a function of μr and μh 94

4. Double scattering from cylinders as a function of μr and r/h 94

5. Features of the structures of alkali halides 117

6. Conditioning numbers for molten salt structure determinations 180

List of symbols

The main symbols used in this thesis are listed here under the chapter in which they first occur.

Chapter two

E	neutron energy
E_ξ, E_η	energy of nuclear states ξ, η
E_0	energy of nuclear state
H	Hamiltonian operator
I	nuclear spin
N	number of atom
Q	momentum transfer
$\boldsymbol{R}$	position of nucleus
$S(Q)$	static structure factor
$S_{\alpha\beta}(Q)$	partial static structure factor
$S_\alpha(Q)$	self part of static structure factor
$S(Q,\omega)$	dynamic structure factor
$S^d(Q,\omega)$	distinct part of dynamic structure factor
$S^s(Q,\omega)$	self part of dynamic structure factor
$S_{\alpha\beta}(Q,\omega)$	partial dynamic structure factor
$S_\alpha(Q,\omega)$	partial single particle dynamic structure factor
$S_T(Q,\omega)$	total (neutron weighted) dynamic structure factor
$V(r)$	potential
b	neutron scattering length
c_i	fractional concentration of isotope i
$\hbar$	Planck's constant divided by 2π
i	$\sqrt{-1}$
i	index representing isotopes
j, j'	index representing atoms
$\boldsymbol{k}$	incident neutron wavevector
$\boldsymbol{k}'$	scattered neutron wavevector
m	neutron mass
p_ξ	statistical weight of state ξ
$\boldsymbol{r}$	position
$\boldsymbol{r_j}(t)$	position of atom j
t	time
Γ	width of nuclear resonance
Ω	solid angle
α, β	indices representing chemical species
δ	Dirac delta function
ξ, η	nuclear states
$\rho_j(\boldsymbol{Q},t)$	density function $= e^{i\boldsymbol{Q}.\boldsymbol{r_j}(t)}$
$\rho_j(\boldsymbol{Q})$	$\rho_j(\boldsymbol{Q},0)$
σ	cross-section
σ_s	scattering cross-section
σ_a	absorption cross-section

ω	angular frequency
$\langle \ \vert$and$\vert \ \rangle$	state vectors
$\langle \ \rangle$	thermal average

Chapter three

$A_{\alpha\beta}(Q)$	partial structure factors
$A_T(Q)$	total structure factor
$C_{XY}^{T}(Q,t)$	transverse current correlation function
$C_{XY}^{L}(Q,t)$	longitudinal current correlation function
$C_{XY}^{L}(Q,\omega)$	power spectrum of $C_{XY}^{L}(Q,t)$
C_P	isobaric heat capacity
C_V	isovolumetric heat capacity
D	diffusion constant
D_T	thermal diffusivity
E_r	recoil energy
$F(Q)$	coherent scattering function
$G(r,t)$	van Hove pair correlation function
$G^d(r,t)$	distinct part of $G(r,t)$
$G^s(r,t)$	self part of $G(r,t)$
$I(Q,t)$	intermediate correlation function
$I^s(Q,t)$	self part of $I(Q,t)$
K_T	isothermal compressibility
M	particle mass
P	transition probability
$S^{\mathrm{sym}}(Q,\omega)$	symmetrised dynamic structure factor
$S_0(Q)$, $S_1(Q)$	moments of $S(Q,\omega)$
$S_T(Q)$	total structure factor
$S_{XY}(Q)$	partial structure factor based on properties X and Y
$S_{++}(Q)$, $S_{\pm-}(Q)$, $S_{--}(Q)$	structure factors based on particle type
$S_{MM}(Q)$, $S_{Mq}(Q)$, $S_{qq}(Q)$	structure factors based on mass and charge
$S_{NN}(Q)$, $S_{Nq}(Q)$, $S_{qq}(Q)$	structure factors based on number and charge
T	temperature
V	volume
V_0	a small volume of fluid
X, Y	general properties

a_N, a_M, a_q	coefficients of partial structure factors in cross-section
$c(r)$	direct correlation function
c_α	fractional concentration of species α
c_S	adiabatic sound velocity
c_T	isothermal sound velocity
$g(r)$	pair distribution function
$g_T(r)$	total pair distribution function
$g_{\alpha\beta}(r)$	partial pair distribution function
j_α	particle currents
j_X	property currents
k_B	Boltzmann constant
n	number of atoms in a small volume
$\boldsymbol{p}$	momentum
$\boldsymbol{v}$	particle velocity

$\delta_{\alpha\beta}$	Kronecker delta
κ	thermal conductivity
ρ	number density

$\rho_j(\boldsymbol{r},t)$	density operator $= \delta(\boldsymbol{r}-\boldsymbol{r_j}(t))$
$\rho(\boldsymbol{r},t)$	localised density operator
$\rho(\boldsymbol{r})$	$\rho(\boldsymbol{r},0)$
†	Hermitian conjugate
*	complex conjugate

Chapter four

$A(\boldsymbol{k}_0)$	cross-sectional area of sample perpendicular to the beam
G_0, G_1, G_2	integrals
H_0, H_1, H_2	attenuation functions
$L(\boldsymbol{r},\boldsymbol{k})$	distance from $\boldsymbol{r}$ to surface in direction $-\boldsymbol{k}$
S	surface of sample
$S(\boldsymbol{k})$	part of surface visible from direction of $\boldsymbol{k}$
a	radius of sample
$\hat{\boldsymbol{e}}$	unit vector normal to the surface of the sample
$f(r,k,t)$	neutron density
h	height of sample
j	number of times scattered
$\boldsymbol{k}_j$	wavevector of neutron scattered j times
$\hat{\boldsymbol{k}}$	unit vector in direction of $\boldsymbol{k}$
$k_x,\ k_y,\ k_z$	components of $\boldsymbol{k}$
$p_s(\boldsymbol{k}_{j-1},\boldsymbol{k}_j)$	transition probability
z	cylindrical polar coordinate
Γ	transference function
Φ	beam intensity
δ	ratio of secondary scattering to primary scattering
$\xi,\ \eta$	dummy variables of integration
θ	cylindrical polar coordinate
μ	total cross-section density
μ_a	absorption cross-section density
μ_s	scattering cross-section density
φ	angle of $\boldsymbol{k}$ from x-axis
ω	angular frequency of neutron scattered j times

Chapter six

$A_{C,CH}$ etc	attenuation coefficients
$F(\theta)$	geometrical factor
$I_C,\ I_S,$ etc	notional scattering intensities
I_S^E etc	experimental scattering intensities
$N_S,\ N_V$	number of sample, vanadium atoms in beam
$P_\alpha(\theta)$	Placzek correction
W_V	Debye-Waller factor for vanadium
$\Delta_S,\ \Delta_V$	multiple scattering fraction for sample and vanadium
$\varepsilon(\theta)$	energy dependence of detector efficiency
θ	scattering angle
τ	time of flight (reciprocal velocity)

Chapter eight

A	a term in the integration
C	count rate
P	inelasticity correction
$P_1,\ P_2$	first and second terms in inelasticity correction
Q_e	momentum transfer for perfectly elastic scattering
d_1	length of primary flight path
d_2	length of secondary flight path
f	fractiona path length $= d_1/(d_1 + d_2)$
k_e	wavevector of elastically scattered neutrons
x	dimensionless energy transfer $= m\omega/\hbar k_e^2$
$\varepsilon(k')$	detector efficiency
$\varepsilon_1,\ \varepsilon_2$	functions of the derivatives of ε
λ	incident neutron wavelength
λ'	scattered neutron wavelength
λ_e	wavelength of elastically scattered neutrons
$\phi(\lambda)$	incident neutron flux
$\phi_1,\ \phi_2$	functions of the derivatives of ϕ

Chapter nine

Z_α	atomic number of species α
$r_+,\ r_-$	cationic and anionic radii
r_{+-}	sum of anionic and cationic radii

Chapter ten

$E(Q),\ E_j$	experimental approximation to $S(Q)$
$F(Q)$	$S(Q)$ convoluted with resolution function
H	information entropy
N	number of data points
$R(Q,Q'),\ R(Q,t)$	resolution functions
λ	Lagrangian multiplier
σ	standard deviation of data

Acknowledgements

I should like to thank the following people:

Dr Robert McGreevy who has been a good supervisor to me, providing advice and encouragement on numerous occasions.

Professor E W J Mitchell who, before he became chairman of the Science and Engineering Research Council (SERC), was jointly my supervisor with Dr McGreevy, for a number of useful discussions and a continued interest in my work.

The staff of the ILL and of ISIS, particularly Drs Pierre Chieux and Adrian Barnes at ILL and Dr Spencer Howells at ISIS.

Mrs Pam Butler and her staff of the University Liaison Secretariat at the Rutherford Appleton Laboratory who have always been most helpful in making arrangements for visits to Grenoble.

The technical staff of the Clarendon Laboratory, especially Mr George Matthews in the research workshop.

The staff of Oxford University Computing Service who have always been willing to help with any problems.

Mr Phil Gullidge of the University of Bristol for sample purification.

Professor Imre Ruff, Andras Baranyai and Laszlo Pusztai of the Loránd Eötvös University, Budapest for useful discussions and their hospitality during my visit to Hungary.

SERC for financial support.

Michael Fairbanks, Sally Day, and David Keen (as well as Robert McGreevy) who have been good company on trips to Grenoble as well as at home.

Finally, I wish to thank Alexis Kiff for the invaluable help and advice she has given me during the production of this thesis and for the hours she has spent correcting my solecisms.

Abstract

A number of neutron scattering experiments have been performed in order to obtain structural and dynamical information about some molten salts. Inelastic scattering has produced information about the dispersion of the optic mode in molten caesium chloride in the equivalent of the first Brillouin zone. A diffraction experiment, using isotopic substitution, on lithium chloride leads to the conclusion that the cation-anion coordination is approximately tetrahedral, a result that meets the predictions of simulations; it also demonstrates the difficulties produced by small systematic errors in experiments of this type. Due to equipment failure an experiment on a mixture of lithium chloride and potassium chloride was inconclusive but it is clear that it is feasible and should be repeated.

Diffraction and inelastic neutron scattering experiments on silver iodide in its molten and fast ion conducting α-phase show that the disordered structure of the two is very similar and not unlike that of molten cuprous chloride in having very little structure in the cation-cation correlation. In contrast the dynamics differ considerably - in addition to an acoustic mode the melt shows strong modes that have dispersion curves approximately at constant Q; these modes, which are related to the peaks in the static structure factor, are not seen in the α-phase.

The temperature dependence of molten caesium chloride has been investigated using the time of flight diffractometer LAD. The analysis of this data required new correction procedures including consideration

of inelasticity corrections and resolution effects. These are discussed and the latter is treated using a maximum entropy method. The structure is found to vary little over the temperature range used, less than is predicted by simulation. The results are not consistent with the hypothesis that the discrepancy between simulation and experiment for this salt is due to incorrect scaling of the simulation potential.

Chapter one

Introduction

The idea that all in nature consists of fundamental indivisible particles and of void is over two thousand years old, originating, it is said, with Leucippus, the founder of the Atomic School of Greek philosophy. The atomic system was fully worked out by Democritus and developed by Epicurus and the Roman Lucretius whose poem *De Rerum Natura* [1/1] was well known to the educated of the nineteenth century when atomic theory in its modern form became well established.

Despite the long currency of the idea it is only in the last seventy-five years that we have been able to gain any detailed information concerning the arrangement of these atoms in matter. That the atoms in a crystal would be arranged in a regular fashion was a reasonable assumption and it enabled Friedrich *et al* [1/2] to predict and then demonstrate, in 1912, the diffraction of x-rays by crystals. Since then the technique of diffraction, not only of x-rays but of neutrons and electrons too, has been used to determine the structure of many thousands of crystalline materials, many of them being very complicated, and has helped us to reach a detailed understanding of this class of matter.

The study of liquid structure is almost as old, the first diffraction patterns from liquids being obtained in 1916 [1/3] though it took ten or fifteen years before the relation of this diffraction pattern to the

distribution of particles in the fluid was realised and the first radial distribution function determined [1/4,1/5]. In the following years radial distribution functions were obtained for many elemental liquids [1/6]. The extension to systems containing more than one type of atom is not as simple as it is for crystals for which the structure is determined by fitting a model structure, taking into account the scattering properties of the different atoms, to the diffraction pattern. This is not possible for liquids, or non-crystalline solids, as one cannot form suitable model structures.

It was not until neutron scattering experiments became a practical possibility that this could be remedied. For a liquid containing two types of atoms there are three pair correlation functions each of which contribute to the diffraction pattern in a proportion determined by the scattering lengths of the correlated atoms. For some elements the scattering length varies considerably between different isotopes. This means that by using these different isotopes it is possible to obtain three different diffraction patterns, each being a different combination of the three correlation functions (partial structure factors). Solution of this set of simultaneous equations yields the individual functions. This technique of isotopic variation, or substitution, was first used by Enderby *et al* [1/7] on the alloy Cu_6Sn_5; since then it has been used on many different liquids and glasses.

Compared with our understanding of crystals our understanding of liquids and disordered solids is not yet at a very advanced stage. This is partly due to the relative difficulty of theoretical work in this area, and partly due to the limitations of the experimental techniques.

It is in an attempt to improve this situation that this work has been done.

Neutron scattering studies have been done on one-component liquid systems such as inert gases (e.g. argon [1/8]) and molten metals (e.g. [1/9]), on binary systems such as molten alloys and molten salts, and on molecular systems such as organic liquids, water (e.g. [1/10]), and aqueous solutions (e.g. [1/11]). This work concerns molten salts which are of interest because:

i) Their binary nature means there are interactions between unlike particles but not so many as to be untractable; it also causes an extra dynamic mode (analogous to the optic mode in a crystal) compared to one component systems.

ii) In purely ionic salts there are no vibrational or rotational excitations due to molecular groupings which would make the structure more complicated.

iii) The principal interaction is Coulombic which suggests that these systems would show a large degree of charge ordering, in contrast to inert gas mixtures and molten alloys (except that in some molten alloys there is a large degree of charge transfer, e.g. Au/Cs [1/12]).

iv) The interaction potential is expected to be fairly simple which allows the possibility of reasonably realistic computer simulations; comparison of these with experiment provides information about the form of these potentials.

1.1 Structural studies

The structural studies of molten salts, to date, are summarised in table 1. These are nearly all chlorides because the scattering lengths of the two chlorine isotopes, ^{35}Cl and ^{37}Cl, differ by a factor of approximately five which makes them suitable for isotopic substitution. The other halogens have no suitable isotopes, nor do most of the alkali or alkaline earth metals. The nickel halide structures have been determined using nickel isotopes.

The results of Derrien and Dupuy for KCl, CsCl, and AgCl are not reliable; they show small scale structure because of the method of data analysis [1/17]. The results for CsCl, RbCl, and NaCl show the features which are typical of alkali halides: these are discussed in chapter nine in relation to the structure of LiCl which has been studied as the final member of this set of alkali chlorides, and the one with the smallest cation size. Indeed the Li^+ ion is very much smaller than the Cl^- ion, having approximately one third the radius, and is significantly smaller than the other alkali metal ions. This means that the effects of ion size are investigated by this experiment.

Silver iodide was selected for study partly because it is one of the few iodides that could be studied, as relatively few cations with isotopes suitable for substitution are available; and partly because it exhibits a solid phase (α-AgI) which is fast ion conducting. That is, it shows very high electrical conductivity which is due to the transport of Ag^+ ions; these Ag^+ ions are highly disordered and are often said to have a liquid like structure: we are here able to see how similar it is to the structure of molten silver iodide.

Nothing is known of the structure of mixtures of molten salts and how solution of one in another disturbs the structure of the pure salt. For this reason the mixture of 10% LiCl, 90% KCl has been studied. This composition was chosen because it has been found that the Li^+ ion has an unusually low mobility [1/27], lower than it does in pure lithium chloride or if dissolved in potassium chloride in different concentrations. This would suggest that a structural distortion might be observed at this composition.

The commissioning of the spallation neutron source (ISIS) at the Rutherford-Appleton Laboratory in 1986 meant that there were new instruments available for workers in neutron scattering. One of these was the LAD diffractometer which was designed for research into the structure of liquids and amorphous solids. Being at a pulsed source it works in a different way to conventional diffractometers and so the data treatment methods are different. For one of the first experiments using this instrument it was decided to study how the structure of caesium chloride varies with temperature. Caesium chloride was chosen because its structure near the melting point is already well known so a comparison could be made between LAD and D4B which had been used for the previous determination. Little is known of the temperature dependence of the structure of molten salts - all the determinations listed in table 1 have been done within 30° to 50° of the melting point - and it was felt that this was a good opportunity to improve our knowledge a little.

1.2 Dynamical studies

Relatively little work has been done on the dynamics (that is, the equivalent to phonons in a crystal) of liquids. The inelastic cross-section is the combination of five correlation functions (two single particle functions as well as the three pair functions); partly because the inelastic scattering cross-sections are low, it has not been possible to determine them all by isotopic substitution. Despite this it is possible to obtain useful information; the work summarised in table 2 includes some in which isotopes have been used to determine the nature of excitable modes.

This thesis includes a study of the dynamics of silver iodide both molten and in its fast-ion conducting phase. Work on $SrCl_2$, another fast ion conductor, has shown a mode present in the melt and in the fast ion conducting phase that is not observed in other alkaline earth chlorides. It was postulated that this was, therefore, connected with the fast ion conductivity. It was of interest to see whether something similar occurred in AgI.

Results for caesium chloride are also presented. Work involving isotopes had already been done on this salt leading to dispersion curves for acoustic and optic type modes. The point of this experiment was to use the IN4 instrument to look for the optic mode at a lower momentum transfer than had been possible in the previous experiment which used IN6.

1.3 This work

The first four chapters of this thesis form an introduction in which are presented the theoretical results required later. The next four chapters concern data collection and correction; established correction methods are described briefly and new calculations concerning multiple scattering and inelasticity corrections are introduced. The results of the experimental work together with work on data analysis and discussion are presented in the remaining chapters.

Table 1. Determinations of the structures of molten salts

Alkali halides		
LiCl	This study	
NaCl	Edwards, Enderby, Howe R A, and Page	[1/13]
	Biggin and Enderby	[1/14]
KCl	Derrien and Dupuy	[1/15]
RbCl	Mitchell, Poncet, and Stewart	[1/16]
CaCl	Derrien and Dupuy	[1/15]
	Locke, Messoloras, Stewart, McGreevy, and Mitchell	[1/17]
Alkaline earth halides		
$MgCl_2$	Biggin, Gay, and Enderby	[1/18]
$CaCl_2$	Biggin and Enderby	[1/19]
$SrCl_2$	McGreevy and Mitchell	[1/20]
$BaCl_2$	Edwards, Howe R A, Enderby, and Page	[1/21]
Halides of transition metals		
CuCl	Page and Mika	[1/22]
	Eisenberg, Jal, Dupuy, Chieux, and Knoll	[1/23]
AgCl	Derrien and Dupuy	[1/24]
AgI	This study	
$ZnCl_2$	Biggin and Enderby	[1/25]
$NiCl_2$	Newport, Howe R A, and Wood	[1/26]
$MnCl_2$	Biggin, Gay, and Enderby	[1/18]

Table 2. Determinations of the dynamics of molten salts

Alkali halides

NaI	McGreevy, Mitchell and Margaça	[1/28]
KBr	Copley and Dolling	[1/29]
RbCl	McGreevy, Mitchell and Margaça	[1/28]
	McGreevy and Mitchell	[1/30]
RbBr	Price and Copley	[1/31]
CsCl	McGreevy, Mitchell and Margaça	[1/28]
	McGreevy, Mitchell, Margaça and Howe	[1/32]
	this study	

Alkaline earth halides

$MgCl_2$	McGreevy and Mitchell	[1/33]
$MgBr_2$	Fairbanks, Howe and McGreevy	[1/34]
$CaCl_2$	McGreevy and Mitchell	[1/33]
$CaBr_2$	Fairbanks, Howe and McGreevy	[1/34]
$SrCl_2$	Margaça, McGreevy and Mitchell	[1/35]
$SrBr_2$	Fairbanks, Howe and McGreevy	[1/34]

Halides of transition metals

AgI	This study	
$ZnCl_2$	Fairbanks, Howe and McGreevy	[1/34]

Chapter two

The scattering of neutrons by condensed matter

2.1 Scattering of neutrons by a nucleus

A proper treatment of neutron scattering employs the complexities of scattering theory; although such detail is not required here it is worth giving the matter a little consideration as it is sometimes the cause of confusion. What follows, then, should be thought of, not as being rigorous, but as a relatively simple justification of the results obtained. A more complicated analysis can be found elsewhere (for example [2/1]).

We shall limit our discussion to bound atoms: atoms that are effectively of infinite mass. The justification of this is that a neutron that scatters from an atom in a crystal transfers momentum to the lattice as a whole rather than to the individual atom; there is no recoil of the struck atom. This is, of course, not entirely true but it is generally considered to be a good enough approximation even for a liquid.

The interaction is almost entirely between the neutron and the nucleus of the scatterer. Scattering from the electrons, which occurs because of the neutron's magnetic moment, is important only from magnetic materials which are not to be considered here; otherwise it

accounts for roughly one part in ten thousand of the scattering and so can safely be ignored. Another consequence of the magnetic moment and spin of the neutron is that the scattering depends on the relative orientations of neutron and nuclear spins unless, of course, the nucleus is spinless. We shall initially consider this simpler case.

The neutron-nuclear interaction is very strong but only for very small separations. It is the short range of the force compared with nuclear dimensions that makes neutron scattering a fairly weak probe of condensed matter. Because this range is short compared with the wavelengths of low energy neutrons used in neutron scattering experiments, as is the nuclear radius, the scattering must contain only s-wave components which means it is isotropic. (This is not true for nuclei that are not bound as the interaction is then not observed in the centre of mass reference frame.)

If we use Fermi's Golden Rule to write the differential scattering cross-section for the transition between scatterer states ξ and η

$$\frac{d^2\sigma_{\eta\xi}}{d\Omega dE} = \left(\frac{m}{2\pi\hbar^2}\right)^2 \frac{k'}{k} \left|\langle \eta \boldsymbol{k}' | V | \xi \boldsymbol{k} \rangle\right|^2 \delta\left(\hbar\omega + E_\xi - E_\eta\right)$$

(2/1)

then we must use a delta function form for the potential as this is the only way to obtain isotropic scattering using the first Born approximation (as (2/1) is known). This is called the Fermi pseudopotential and is defined as

$$V(r) = \frac{2\pi\hbar^2}{m}\, b\, \delta(\boldsymbol{r} - \boldsymbol{R})$$

(2/2)

where $\boldsymbol{R}$ is the position of the nucleus; the parameter b, having the dimensions of length, is known as the scattering length. It should not be thought that (2/2) represents the true potential. The use of the Golden Rule, which is derived from perturbation theory, is not applicable to neutron scattering for which the interaction is very strong. The Fermi pseudopotential is simply a formal device to produce, using the first Born approximation, the result that we know to be correct, namely isotropic scattering.

Inserting (2/2) in (2/1) and putting $R = 0$ gives

$$\frac{d^2\sigma_{\eta\xi}}{d\Omega dE} = b^2 \frac{k'}{k} |\langle \eta \boldsymbol{k}' | \delta(\boldsymbol{r}) | \xi \boldsymbol{k} \rangle|^2 \, \delta\left(\hbar\omega + E_\xi - E_\eta\right)$$

(2/3)

For a single bound nucleus the initial and final scatterer states are the same provided that the incident neutrons are of insufficient energy to bring about transitions to excited nuclear states; this is generally the case. The neutron states $|\boldsymbol{k}\rangle$ have wave-functions $e^{i\boldsymbol{k}.\boldsymbol{r}}$ so we find that

$$\frac{d^2\sigma}{d\Omega dE} = b^2 \, \delta(\hbar\omega)$$

(2/4)

And so

$$\frac{d\sigma}{d\Omega} = b^2$$

(2/5)

$$\sigma = 4\pi b^2$$

(2/6)

2.2 Scattering from collections of atoms

For a collection of N nuclei the total differential cross-section is the sum of those for all the different transitions:

$$\frac{d^2\sigma}{d\Omega dE} = \sum_{\xi} p_{\xi} \sum_{\eta} \frac{d^2\sigma_{\xi\eta}}{d\Omega dE}$$

(2/7)

where p_{ξ} is the statistical weight of the initial state ξ. The interaction potential is now

$$V(r) = \frac{2\pi\hbar^2}{m} \sum_{j=1}^{N} b_j \delta(\boldsymbol{r} - \boldsymbol{r}_j)$$

(2/8)

where $\boldsymbol{r}_j$ is the position of the j^{th} nucleus and b_j is its scattering length. This gives a cross-section

$$\frac{d^2\sigma}{d\Omega dE} = \sum_{\xi} p_{\xi} \sum_{\eta} \frac{k'}{k} |\langle \eta \boldsymbol{k}' | \sum_{j} b_j \, \delta(\boldsymbol{r} - \boldsymbol{r}_j) | \xi \boldsymbol{k} \rangle|^2 \, \delta\big(\hbar\omega + E_{\xi} - E_{\eta}\big)$$

(2/9)

Putting in the neutron wave-functions this becomes

$$\frac{d^2\sigma}{d\Omega dE} = \sum_{\xi} p_{\xi} \sum_{\eta} \frac{k'}{k} |\langle \eta | \int e^{-i\boldsymbol{k}'.\boldsymbol{r}} \sum_{j} b_j \, \delta(\boldsymbol{r} - \boldsymbol{r}_j) e^{i\boldsymbol{k}.\boldsymbol{r}} d\boldsymbol{r} \, | \xi \rangle|^2 \, \delta\big(\hbar\omega + E_{\xi} - E_{\eta}\big)$$

(2/10)

$$= \sum_{\xi} p_{\xi} \sum_{\eta} \frac{k'}{k} |\langle \eta | \sum_{j} b_j \, e^{i\boldsymbol{Q}.\boldsymbol{r}_j} | \xi \rangle|^2 \; \delta\big(\hbar\omega + E_{\xi} - E_{\eta}\big)$$

(2/11)

where $\boldsymbol{Q} = \boldsymbol{k} - \boldsymbol{k}'$ is the momentum transferred to the scatterer. The delta function can be written as an integral:

$$\delta\left(\hbar\omega + E_\xi - E_\eta\right) = \frac{1}{2\pi\hbar}\int_{-\infty}^{\infty} e^{-it(\hbar\omega+E_\xi-E_\eta)/\hbar}dt$$

(2/12)

which enables us to write

$$\frac{d^2\sigma}{d\Omega dE} = \frac{1}{2\pi\hbar}\sum_\xi p_\xi \sum_\eta \frac{k'}{k}\,|\langle\eta|\sum_j b_j\, e^{i\boldsymbol{Q}.\boldsymbol{r}_j}|\xi\rangle|^2 \int_{-\infty}^{\infty} e^{-it(\hbar\omega+E_\xi-E_\eta)/\hbar}dt$$

(2/13)

$$= \frac{1}{2\pi\hbar}\,\frac{k'}{k}\int_{-\infty}^{\infty} dt\; e^{-i\omega t}\sum_\xi p_\xi \sum_\eta \langle\xi|\sum_j b_j\, e^{-i\boldsymbol{Q}.\boldsymbol{r}_j}|\eta\rangle \quad \langle\eta|e^{itE_\eta/\hbar} \sum_{j'} b_{j'}\, e^{i\boldsymbol{Q}.\boldsymbol{r}_{j'}} e^{-itE_\xi/\hbar}|\xi\rangle$$

(2/14)

$$= \frac{1}{2\pi\hbar}\frac{k'}{k}\int_{-\infty}^{\infty} dt\; e^{-i\omega t}\sum_\xi p_\xi \sum_\eta \langle\xi|\sum_j b_j\, e^{-i\boldsymbol{Q}.\boldsymbol{r}_j}|\eta\rangle \quad \langle\eta|e^{itH/\hbar} \sum_{j'} b_{j'}\, e^{i\boldsymbol{Q}.\boldsymbol{r}_{j'}} e^{-itH/\hbar}|\xi\rangle$$

(2/15)

The last step is obtained because the states ξ and η are eigenstates of the system of which H is the Hamiltonian. We can introduce a Heisenberg operator (see appendix B) $\boldsymbol{r_j}(t)$ (where $\boldsymbol{r_j}$ will mean $\boldsymbol{r_j}(0)$) and write

$$\frac{d^2\sigma}{d\Omega dE} = \frac{1}{2\pi\hbar}\,\frac{k'}{k}\int_{-\infty}^{\infty} dt\; e^{-i\omega t}\sum_\xi p_\xi \sum_\eta \langle\xi|\sum_j b_j\, e^{-i\boldsymbol{Q}.\boldsymbol{r}_j}|\eta\rangle\,\langle\eta|\sum_{j'} b_{j'}\, e^{i\boldsymbol{Q}.\boldsymbol{r}_{j'}(\boldsymbol{t})}|\xi\rangle$$

(2/16)

$$= \frac{1}{2\pi\hbar}\,\frac{k'}{k}\int_{-\infty}^{\infty} \langle\sum_j\sum_{j'} b_j b_{j'}\,\rho_j(-\boldsymbol{Q},0)\rho_{j'}(\boldsymbol{Q},t)\rangle\;\; e^{-i\omega t}\,dt$$

(2/17)

where $\langle \ldots \rangle$ indicates a thermal average and we have introduced the single particle function $\rho_j(\boldsymbol{Q},t)$, the definition of which is obvious. For the case of identical nuclei the b_j are all equal and we see that

$$\frac{1}{N}\frac{d^2\sigma}{d\Omega dE} = b^2\,\frac{k'}{k}\,S(\boldsymbol{Q},\omega)$$

(2/18)

where we have introduced the dynamic structure factor $S(\boldsymbol{Q},\omega)$. The significance of this will be discussed in the next chapter but for the moment it will be sufficient to give its definition:

$$S(\boldsymbol{Q},\omega) = \frac{1}{2\pi\hbar}\,\frac{k'}{k}\int_{-\infty}^{\infty}\langle\sum_j\sum_{j'}\rho_j(-\boldsymbol{Q},0)\rho_{j'}(\boldsymbol{Q},t)\rangle\; e^{-i\omega t}\,dt$$

(2/19)

If we have a mixture of isotopes the scattering lengths must be included in the averaging. It is convenient to consider separately the part of the sum in which $j = j'$:

$$\frac{1}{N}\frac{d^2\sigma}{d\Omega dE} = \frac{1}{2\pi\hbar N}\,\frac{k'}{k}\int_{-\infty}^{\infty}\langle\sum_j\sum_{j'\neq j} b_j b_{j'}\rho_j(-\boldsymbol{Q},0)\rho_{j'}(\boldsymbol{Q},t)\rangle\; e^{-i\omega t}\,dt$$

$$+\,\frac{1}{2\pi\hbar N}\,\frac{k'}{k}\int_{-\infty}^{\infty}\langle\sum_j b_j^2\rho_j(-\boldsymbol{Q},0)\rho_j(\boldsymbol{Q},t)\rangle\; e^{-i\omega t}\,dt$$

(2/20)

Each b_j can be considered as the sum of the mean value of the scattering length of the nuclei and the deviation from that mean. Similarly b_j^2 can be treated as the mean of the square of the scattering length plus a deviation. Because these deviations are randomly distributed the mean value of the sums which contain them is zero and

$$\frac{1}{N}\frac{d^2\sigma}{d\Omega dE} = \frac{1}{2\pi\hbar N}\frac{k'}{k}\bar{b}^2\int_{-\infty}^{\infty}\langle\sum_j\sum_{j'\neq j}\rho_j(-\boldsymbol{Q},0)\rho_{j'}(\boldsymbol{Q},t)\rangle\, e^{-i\omega t}\,dt$$
$$+\frac{1}{2\pi\hbar N}\frac{k'}{k}\overline{b^2}\int_{-\infty}^{\infty}\langle\sum_j\rho_j(-\boldsymbol{Q},0)\rho_j(\boldsymbol{Q},t)\rangle\, e^{-i\omega t}\,dt$$

(2/21)

which can be written in terms of the self and distinct parts of the structure factor, the definitions of which are apparent, as

$$\frac{1}{N}\frac{d^2\sigma}{d\Omega dE} = \bar{b}^2\frac{k'}{k}S^d(\boldsymbol{Q},\omega) + \overline{b^2}\frac{k'}{k}S^s(\boldsymbol{Q},\omega)$$

(2/22)

By including the $j = j'$ term in the first sum we can also write this as

$$\frac{1}{N}\frac{d^2\sigma}{d\Omega dE} = \bar{b}^2\frac{k'}{k}S(\boldsymbol{Q},\omega) + (\overline{b^2} - \bar{b}^2)\frac{k'}{k}S^s(\boldsymbol{Q},\omega)$$

(2/23)

The first term is called the coherent part of the scattering and is due to the distribution of the mean part of the scattering length with whatever order is present in the scatterer, while the second, incoherent, term is due to the random arrangement of the deviation from this mean.

In the case of a single isotope, but this time including spin dependence, the variation in scattering length is over scattering events rather than over scatterers but we still obtain the results in (2/22) although this time the interpretation of the mean scattering lengths is slightly different. If the scattering nucleus has spin I then the scattering interaction can take place in a spin state of $I + ½$ or of $I - ½$ (as the neutron has spin ½) which it does with probabilities $(I+1)/(2I+1)$ and $I/(2I+1)$ respectively. Thus, if the scattering lengths for the two cases are $b^{(+)}$ and $b^{(-)}$,

$$\bar{b} = \frac{I+1}{2I+1}\, b^{(+)} + \frac{I}{2I+1} b^{(-)}$$

$$\overline{b^2} = \frac{I+1}{2I+1}\, b^{(+)2} + \frac{I}{2I+1} b^{(-)2}$$

(2/24)

It is these scattering lengths that are used to describe the neutron scattering properties of nuclei; from time to time tables of the most reliable values are compiled. One compiled by Koester and Yelon (included in [2/1]) has been used for this work.

The extension of (2/22) to a mixture of isotopes with spin is straight forward; by summing over the isotopes we get

$$\bar{b} = \sum_i c_i \bar{b}_i$$

$$\overline{b^2} = \sum_i c_i \overline{b_i^2}$$

(2/25)

where the scattering lengths for each isotope are given by (2/25).

2.3 Scattering from chemical mixtures

For a chemical mixture we write (2/17) as

$$\frac{1}{N}\frac{d^2\sigma}{d\Omega dE} = \frac{1}{2\pi\hbar N}\,\frac{k'}{k}\int_{-\infty}^{\infty} \sum_\alpha \sum_\beta \langle \sum_j^\alpha \sum_{j'}^\beta b_j b_{j'}\, \rho_j(-\boldsymbol{Q}, 0)\rho_{j'}(\boldsymbol{Q}, t)\rangle \;\; e^{-i\omega t}\, dt$$

(2/26)

where α and β label chemical species and their presence on the sums over j and j' mean that the sum should be taken over atoms of that species only. This then gives us

$$\frac{1}{N}\frac{d^2\sigma}{d\Omega dE} = \frac{k'}{k}\sum_\alpha\sum_\beta \bar{b}_\alpha\bar{b}_\beta S^d_{\alpha\beta}(\boldsymbol{Q},\omega) + \frac{k'}{k}\sum_\alpha \overline{b^2}_\alpha S_\alpha(\boldsymbol{Q},\omega)$$
$$= \frac{k'}{k}\sum_\alpha\sum_\beta \bar{b}_\alpha\bar{b}_\beta S_{\alpha\beta}(\boldsymbol{Q},\omega) + \frac{k'}{k}\sum_\alpha (\overline{b^2}_\alpha - \bar{b}^2_\alpha) S_\alpha(\boldsymbol{Q},\omega)$$

(2/27)

where, again, we have the division into coherent and incoherent parts. We have introduced partial structure factors $S_{\alpha\beta}(\boldsymbol{Q},\omega)$ which are defined in the same manner as the structure factor was previously except that the sums are over atoms of the relevant species only. Notice that the incoherent scattering for the mixture of isotopes

$$\frac{1}{N}\frac{d^2\sigma_{\text{inc}}}{d\Omega dE} = \frac{k'}{k}\left(\sum_i c_i\overline{b_i^2} - \left(\sum_i c_i\overline{b_i}\right)^2\right) S^S(\boldsymbol{Q},\omega)$$

(2/28)

using (2/24)) is not of the same form as that for a chemical mixture

$$\frac{1}{N}\frac{d^2\sigma_{\text{inc}}}{d\Omega dE} = \frac{k'}{k}\sum_\alpha \left(\overline{b_\alpha^2} - \overline{b_\alpha}^2\right) S_\alpha(\boldsymbol{Q},\omega)$$

(2/29)

despite the fact that it clearly can make no difference to the scattering whether the variation in scattering length is due to a mixture of isotopes or a mixture of chemical species. This demonstrates that the distinction between coherent and incoherent scattering is to some extent arbitrary. (It is sometimes stated that incoherent scattering is that in which the spin of the neutron is reversed. Although, in the absence of exchange forces in the scatterer, such scattering must be incoherent as it is, in principle, possible to determine which atom did the scattering which means no interference is possible, this is not generally true of all the incoherent scattering).

We shall consider coherent scattering to be that due to the scattering potential averaged over isotopes and spin states of each chemical species but not over the species.

The structure factor (2/19), which is the sum of all the partial structure factors, has a physical significance in mixtures as well as in monatomic liquids although it is not directly related to the neutron scattering cross-section. It would not be unreasonable to call this the total structure factor but we shall not do so (we shall see in the next chapter that it can be considered to be the number-number partial structure factor). This term will, instead, be used to describe the combination of partial structure factors defining the cross-section (which depends on the isotopes used). So that this has the same dimensions as the partial structure factors we include as a denominator

$$\overline{b^2} = \sum_{\alpha} c_\alpha \overline{b^2}_\alpha$$

(2/30)

which represents the total scattering cross-section. Using this the total (neutron weighted) dynamic structure factor is defined as

$$S_T(\boldsymbol{Q},\omega) = \left(\sum_{\alpha}\sum_{\beta} \bar{b}_\alpha \bar{b}_\beta S_{\alpha\beta}(\boldsymbol{Q},\omega) + \sum_{\alpha} (\overline{b^2}_\alpha - \bar{b}_\alpha^2) S_\alpha(\boldsymbol{Q},\omega) \right) / \overline{b^2}$$

(2/31)

2.4 The static approximation

The response of the target sample to the incident neutrons is often derived from states the energy of which is bounded and very much less than the energy of the neutrons. It then essentially entails all those states. This means that, in the absence of fine energy resolution, the

energy conserving delta function in the cross-section is unimportant, the conservation of energy can be neglected, and to a good approximation the scattering appears to be elastic. This makes the cross-section in (2/11) become

$$\frac{d^2\sigma}{d\Omega dE} = \sum_{\xi} p_{\xi} \sum_{\eta} \langle \eta | \sum_{j} b_j \, e^{i\boldsymbol{Q}.\boldsymbol{r}_j} | \xi \rangle^2 \, \delta(\hbar\omega)$$

(2/32)

This is known as the static approximation. Integrating over energy we find that

$$\frac{d\sigma}{d\Omega} = < \sum_{j} \sum_{j'} b_j b_{j'} \, \rho_j(-\boldsymbol{Q}) \rho_{j'}(\boldsymbol{Q}, t) >$$

(2/33)

Following exactly the same procedure as we have done above we find that for a chemical mixture, in the static approximation

$$\frac{1}{N}\frac{d\sigma}{d\Omega} = \frac{1}{N} \sum_{\alpha} \sum_{\beta} \langle \sum_{j}^{\alpha} \sum_{j'}^{\beta} b_j b_{j'} \, \rho_j(-\boldsymbol{Q}) \rho_{j'}(\boldsymbol{Q}, t) \rangle$$

(2/34)

which can be written in terms of partial structure factors, in the same way as was (2/26), as

$$\begin{aligned} \frac{1}{N}\frac{d\sigma}{d\Omega} &= \sum_{\alpha} \sum_{\beta} \bar{b}_{\alpha} \bar{b}_{\beta} S^{d}_{\alpha\beta}(\boldsymbol{Q}) + \sum_{\alpha} \overline{b^2}_{\alpha} S_{\alpha}(\boldsymbol{Q}) + \\ &= \sum_{\alpha} \sum_{\beta} \bar{b}_{\alpha} \bar{b}_{\beta} S_{\alpha\beta}(\boldsymbol{Q}) + \sum_{\alpha} (\overline{b^2}_{\alpha} - \bar{b}^2_{\alpha}) S_{\alpha}(\boldsymbol{Q}) \end{aligned}$$

(2/35)

where, in (2/35) we again have a division into coherent and incoherent parts. It can be seen that the incoherent part is a constant (that is, it is not a function of $\boldsymbol{Q}$).

The static approximation is not really good enough for the systems studied in this thesis. The inelasticity corrections described in chapter eight are an attempt to calculate the deviations from it.

2.5 Nuclear resonances and neutron absorption

So far we have considered scattering for which the neutrons have far less energy than any nuclear states and so we have been able to neglect the effect of nuclear structure. This is not always the case and generally we have to consider the possibility of a transition to an excited nuclear state. It is necessary to say no more here than that the Breit-Wigner resonance formulae are appropriate to this situation and give cross-sections for neutron scattering and for neutron absorption as

$$\sigma_s = 4\pi b^2 + \frac{\pi\Gamma_n^2 + 4\pi k b \Gamma_n (E - E_0)}{k^2\left((E - E_0)^2 + \frac{1}{4}\Gamma^2\right)}$$

(2/36)

$$\sigma_a = \frac{\pi\Gamma_n\Gamma_\gamma}{k^2\left((E - E_0)^2 + \frac{1}{4}\Gamma^2\right)}$$

(2/37)

where $\Gamma_n \propto k$ the width for scattering of the neutron, Γ_γ is the width for radiative capture, $\Gamma = \Gamma_n + \Gamma_\gamma$, E_0 is the energy of the nuclear state and E is the energy of the neutron. Because these are so complicated we can only hope to obtain useful results if the incident neutron energy is well below that of any nuclear resonance. In this case, because $\Gamma_n \propto k$, (2/36) and (2/37) become

$$\sigma_s = 4\pi b^2$$

(2/38)

$$\sigma_a \propto \frac{1}{k}$$

(2/39)

the first of which is familiar and the second of which tells us that well below a resonance the absorption cross-section of a nucleus is proportional to the wavelength of the incident neutron. Measured values of the cross-section are usually quoted for an incident neutron velocity of 2200 ms^{-1} (λ=1.798Å); (2/39) can be used to calculate the value at the required wavelength.

Chapter three.

Structure factors and other correlation functions

Because liquids are highly disordered systems they cannot be described in the same terms as are crystals for which the crystal symmetry is exploited. Instead we describe the microscopic properties in terms of correlation functions - correlations between pairs, or sets, of particles averaged over the entire system. In statistical mechanical terms these are ensemble averages and it is clear that they should be related to the thermodynamic properties of the system; thus they provide a link between the microscopic and the bulk properties of liquids.

3.1 Pair correlation functions

Although the systems we are considering can be described well by classical mechanics it is necessary to use quantum mechanics to properly calculate the correlation functions. The position of the j^{th} particle is therefore represented by the Heisenberg operator $\boldsymbol{r}_j(t)$. It is convenient to define the single particle density operator (also a Heisenberg operator)

$$\rho_j(\boldsymbol{r},t) = \delta(\boldsymbol{r} - \boldsymbol{r}_j(t)) \qquad (3/1)$$

By summing over all the particles we obtain the localised particle density

$$\rho(\boldsymbol{r},t) = \sum_j \rho_j(\boldsymbol{r},t) = \sum_j \delta(\boldsymbol{r} - \boldsymbol{r}_j(t))$$

(3/2)

Using the first of these a time dependent pair correlation function [3/1] can be defined

$$G(\boldsymbol{r},t) = \frac{1}{N}\int \sum_j \sum_{j'} \langle \rho_j(\boldsymbol{r}' - \boldsymbol{r},0)\rho_{j'}(\boldsymbol{r}',t)\rangle \; d\boldsymbol{r}'$$

(3/3)

which is the probability of finding a particle at $\boldsymbol{r}$ at time t given that there is one at the origin at time $t = 0$. The thermal, or ensemble, averaging, indicated by $\langle \ldots \rangle$, produces this probabilistic interpretation; N, the number of particles, provides the correct normalisation. $G(\boldsymbol{r},t)$ can be written as the sum of the self part and the distinct part where the former describes the correlation of a particle with itself

$$G^s(\boldsymbol{r},t) = \frac{1}{N}\int \sum_j \langle \rho_j(\boldsymbol{r}' - \boldsymbol{r},0)\rho_j(\boldsymbol{r}',t)\rangle \; d\boldsymbol{r}'$$

(3/4)

and the latter describes correlations between different particles

$$G^d(\boldsymbol{r},t) = \frac{1}{N}\int \sum_j \sum_{j' \neq j} \langle \rho_j(\boldsymbol{r}' - \boldsymbol{r},0)\rho_{j'}(\boldsymbol{r}',t)\rangle \; d\boldsymbol{r}'$$

(3/5)

The instantaneous structure of the liquid is described by this function at $t = 0$. The self term is simply a delta function, $\delta(\boldsymbol{r})$, and so we define the pair distribution function $g(\boldsymbol{r})$ to be

$$g(\boldsymbol{r}) = G^d(\boldsymbol{r},0)/\rho$$

$$= \frac{1}{\rho N}\int \sum_j \sum_{j' \neq j} \langle \rho_j(\boldsymbol{r}' - \boldsymbol{r})\rho_{j'}(\boldsymbol{r}')\rangle \; d\boldsymbol{r}'$$

(3/6)

where by $\rho_j(\boldsymbol{r})$ we mean $\rho_j(\boldsymbol{r},0)$ and the factor $1/\rho$ is conventionally introduced.

By performing the integrations in (3/4) to (3/6) we can write

$$G^s(\boldsymbol{r},t) = \frac{1}{N}\sum_j \langle \delta\big(\boldsymbol{r}_j(t) - \boldsymbol{r_j}(0) - \boldsymbol{r}\big)\rangle \tag{3/7}$$

$$G^d(\boldsymbol{r},t) = \frac{1}{N}\sum_j \sum_{j'\neq j} \langle \delta\big(\boldsymbol{r}_{j'}(t) - \boldsymbol{r_j}(0) - \boldsymbol{r}\big)\rangle \tag{3/8}$$

$$g(\boldsymbol{r}) = \frac{1}{\rho N}\sum_j \sum_{j'\neq j} \langle \delta\big(\boldsymbol{r}_{j'} - \boldsymbol{r_j} - \boldsymbol{r}\big)\rangle \tag{3/9}$$

from which it is clear that

$$\int G^s(\boldsymbol{r},t)\, d\boldsymbol{r} = 1 \tag{3/10}$$

$$\int G^d(\boldsymbol{r},t)\, d\boldsymbol{r} = N \tag{3/11}$$

$$\int g(\boldsymbol{r})\, d\boldsymbol{r} = V \tag{3/12}$$

At large distances in a liquid there are no correlations between particle positions so that

$$\lim_{r\to\infty} g(\boldsymbol{r}) = 1 \tag{3/13}$$

It is so that this limit is unity that the factor $1/\rho$ was introduced in (2/6). At short distances, because the atoms cannot penetrate each other,

$$\lim_{r\to 0} g(\boldsymbol{r}) = 0$$

(3/14)

3.2 Structure factors

We define the intermediate correlation function $I(\boldsymbol{Q},t)$ as the inverse Fourier transform of $G(\boldsymbol{r},t)$:

$$I(\boldsymbol{Q},t) = \int G(\boldsymbol{r},t)\, e^{i\boldsymbol{Q}.\boldsymbol{r}}\, d\boldsymbol{r}$$

(3/15)

$$= \frac{1}{N}\sum_{j}\sum_{j'} \langle e^{i\boldsymbol{Q}.\boldsymbol{r}_{j'}(t)} e^{-i\boldsymbol{Q}.\boldsymbol{r}_{j}}\rangle$$

(3/16)

$$= \frac{1}{N}\sum_{j}\sum_{j'} \langle \rho_{j'}(\boldsymbol{Q},t)\rho_{j}(-\boldsymbol{Q},0)\rangle$$

(3/17)

where we have defined

$$\rho_j(\boldsymbol{Q},t) = \int \rho_j(\boldsymbol{r},t) e^{i\boldsymbol{Q}.\boldsymbol{r}} d\boldsymbol{r}$$

$$= e^{i\boldsymbol{Q}.\boldsymbol{r}_j(t)}$$

(3/18)

The self, or single particle, intermediate correlation function is defined similarly in terms of the self part of the pair distribution function $G_s(\boldsymbol{r},t)$ so that

$$I_s(\boldsymbol{Q},t) = \frac{1}{N}\sum_{j} \langle \rho_j(\boldsymbol{Q},t)\rho_j(-\boldsymbol{Q},0)\rangle$$

(3/19)

The time Fourier transforms of these are

$$S(\boldsymbol{Q},\omega) = \frac{1}{2\pi\hbar}\int I(\boldsymbol{Q},t)\, e^{-i\omega t}\, dt$$

$$= \frac{1}{2\pi\hbar N} \int \sum_{j} \sum_{j'} \langle \rho_{j'}(\boldsymbol{Q}, t) \rho_j(-\boldsymbol{Q}, 0) \rangle \; e^{-i\omega t} \; dt$$

(3/20)

and

$$S_s(\boldsymbol{Q}, \omega) \; = \frac{1}{2\pi\hbar N} \int \sum_{j} \langle \rho_j(\boldsymbol{Q}, t) \rho_j(-\boldsymbol{Q}, 0) \rangle \; e^{-i\omega t} \; dt$$

(3/21)

The former is known as the dynamic structure factor or, because it is directly related to the neutron scattering cross-section, the scattering law; the latter is the self part of this. These functions are those introduced in the previous chapter to describe neutron scattering and are directly related to the scattering cross-section, as was seen there. We see that $G(\boldsymbol{r}, t)$ and $S(\boldsymbol{Q}, \omega)$ are related by

$$G(\boldsymbol{r}, t) \; = \frac{\hbar}{8\pi^3} \int \int S(\boldsymbol{Q}, \omega) \, e^{-i(\boldsymbol{Q}.\boldsymbol{r} - \omega t)} \; d\boldsymbol{Q} \, d\omega$$

(3/22)

$$S(\boldsymbol{Q}, \omega) \; = \frac{1}{2\pi\hbar} \int \int G(\boldsymbol{r}, t) \, e^{i(\boldsymbol{Q}.\boldsymbol{r} - \omega t)} \; d\boldsymbol{r} \, dt$$

(3/23)

We can define the static structure factor to be the integral over energy of this

$$S(\boldsymbol{Q}) \; = \hbar \int S(\boldsymbol{Q}, \omega) \, d\omega$$

(3/24)

$$= \frac{1}{2\pi N} \int \int \sum_{j} \sum_{j'} \langle \rho_{j'}(\boldsymbol{Q}, t) \rho_j(-\boldsymbol{Q}, 0) \rangle \; e^{-i\omega t} \; dt \; d\omega$$

(3/25)

$$= \frac{1}{N} \int \sum_{j} \sum_{j'} \langle \rho_{j'}(\boldsymbol{Q}, t) \rho_j(-\boldsymbol{Q}, 0) \rangle \ \delta(t) \ dt$$

(3/26)

$$= \frac{1}{N} \sum_{j} \sum_{j'} \langle \rho_{j'}(\boldsymbol{Q}) \rho_j(-\boldsymbol{Q}) \rangle$$

(3/27)

and, for the self part,

$$S_s(\boldsymbol{Q}) = 1$$

(3/28)

By using (3/20) we can also write $S(\boldsymbol{Q})$ as

$$S(\boldsymbol{Q}) = \frac{1}{2\pi} \int \int \int G(\boldsymbol{r}, t) \, e^{i(\boldsymbol{Q}.\boldsymbol{r} - \omega t)} \ d\boldsymbol{r} \ dt \ d\omega$$

(3/29)

$$= \int \int G(\boldsymbol{r}, t) \, e^{i\boldsymbol{Q}.\boldsymbol{r}} \, \delta(t) \ d\boldsymbol{r} \, dt$$

(3/30)

$$= \int G(\boldsymbol{r}, 0) \, e^{i\boldsymbol{Q}.\boldsymbol{r}} \ d\boldsymbol{r}$$

(3/31)

$$= \int \delta(\boldsymbol{r}) \, e^{i\boldsymbol{Q}.\boldsymbol{r}} \ d\boldsymbol{r} + \rho \int g(\boldsymbol{r}) \, e^{i\boldsymbol{Q}.\boldsymbol{r}} \ d\boldsymbol{r}$$

(3/32)

$$= 1 + \rho \int g(\boldsymbol{r}) \, e^{i\boldsymbol{Q}.\boldsymbol{r}} \ d\boldsymbol{r}$$

(3/33)

And inversely

$$g(\boldsymbol{r}) = \frac{1}{8\pi^3 \rho} \int (S(Q) - 1) \, e^{-i\boldsymbol{Q}.\boldsymbol{r}} \ d\boldsymbol{Q}$$

(3/34)

3.3 Analytic properties of the scattering functions

Since $r_j(t)$ is an Hermitian operator we see that

$$\rho_j^\dagger(\boldsymbol{r},t) = \rho_j(\boldsymbol{r},t)$$

(3/35)

$$\rho_j^\dagger(\boldsymbol{Q},t) = \rho_j(\boldsymbol{Q},t)$$

(3/36)

Using these and the result (see appendix B)

$$\langle\rho_j(\boldsymbol{Q},0)\rho_{j'}(-\boldsymbol{Q},t)\rangle = \langle\rho_{j'}(-\boldsymbol{Q},t)\rho_j(\boldsymbol{Q},i\hbar/k_BT)\rangle$$

(3/37)

it is easy to prove the following results:

$$\begin{aligned}
&I(\boldsymbol{Q},t) = I^*(\boldsymbol{Q},-t)\\
&G(\boldsymbol{r},t) = I^*(-\boldsymbol{r},-t)\\
&S(\boldsymbol{Q},\omega) = S^*(\boldsymbol{Q},\omega)\\
&S(\boldsymbol{Q}) = S^*(\boldsymbol{Q})\\
&g(\boldsymbol{r}) = g^*(\boldsymbol{r})\\
&I(\boldsymbol{Q},t) = I(-\boldsymbol{Q},-t+i\hbar/k_BT)\\
&G(\boldsymbol{r},t) = G(-\boldsymbol{r},-t+i\hbar/k_BT)\\
&S(\boldsymbol{Q},\omega) = e^{\hbar\omega/k_BT}S(-\boldsymbol{Q},-\omega)
\end{aligned}$$

(3/38)

The structure factors $S(\boldsymbol{Q})$ and $S(\boldsymbol{Q},\omega)$ are real, as they must be as they represent the observable scattering; so too is the static pair distribution function $g(\boldsymbol{r})$ but the time dependent pair distribution function $G(\boldsymbol{r},t)$ is, in general, complex. In the classical limit this too is real; the imaginary part of $G(\boldsymbol{r},t)$ is therefore a result of quantum effects.

For all the systems we shall be considering

$$G(\boldsymbol{r},t) = G(-\boldsymbol{r},t)$$

(3/39)

from which it follows that

$$S(\boldsymbol{Q},\omega) = S(-\boldsymbol{Q},\omega) \tag{3/40}$$

$$S(\boldsymbol{Q},\omega) = e^{\hbar\omega/k_BT}\, S(\boldsymbol{Q},-\omega) \tag{3/41}$$

This is known as the condition of detailed balance. It is sometimes convenient to define a symmetrised dynamic structure factor

$$S^{sym}(\boldsymbol{Q},\omega) = e^{\hbar\omega/2k_BT} S(\boldsymbol{Q},\omega) \tag{3/42}$$

so that

$$S^{sym}(\boldsymbol{Q},\omega) = S^{sym}(\boldsymbol{Q},-\omega) \tag{3/43}$$

3.4 Moments of the dynamic structure factor

We define the energy moments of the dynamic structure factor by

$$S_n(\boldsymbol{Q}) = \int_{-\infty}^{\infty} S(\boldsymbol{Q},\omega)(\hbar\omega)^n\, d(\hbar\omega) \tag{3/44}$$

We have already obtained the zeroth moment of both coherent and incoherent parts of $S(\boldsymbol{Q},\omega)$ from (3/30)

$$S_0(\boldsymbol{Q}) = 1 + \rho \int g(\boldsymbol{r})\, e^{i\boldsymbol{Q}.\boldsymbol{r}}\ \ d\boldsymbol{r} \tag{3/45}$$

$$S_{s0}(\boldsymbol{Q}) = 1 \tag{3/46}$$

Some higher order moments have been found by Placzek [3/2] and, more simply, by Rahman *et al* [3/3] who show that

$$\int \left(\hbar\omega - \frac{\hbar^2 Q^2}{2M}\right) S_s(\boldsymbol{Q},\omega)d\omega \; = \hbar\boldsymbol{Q}\langle v_{\boldsymbol{Q}}\rangle = 0$$

(3/47)

and

$$\int \left(\hbar\omega - \frac{\hbar^2 Q^2}{2M}\right)^2 S_s(\boldsymbol{Q},\omega)d\omega \; = \hbar^2\boldsymbol{Q}^2\langle v_{\boldsymbol{Q}}^2\rangle$$

(3/48)

where $v_{\boldsymbol{Q}}$ is the component of the particle velocity in the direction of $\boldsymbol{Q}$. The term $\hbar^2Q^2/2M$ has a simple interpretation: if a neutron scatters from a nucleus with a change of wavevector $\boldsymbol{Q}$ then by conservation of momentum we have

$$\hbar\boldsymbol{Q} = \boldsymbol{p}' - \boldsymbol{p}$$

(3/49)

where $\boldsymbol{p}$ and $\boldsymbol{p}'$ and the momenta of the nucleus before and after the scattering; the gain in kinetic energy of the nucleus is

$$\frac{1}{2M}\left(p'^2 - p^2\right) = \frac{1}{2M}(\hbar^2Q^2 + 2\,\hbar\boldsymbol{p}.\boldsymbol{Q})$$

(3/50)

which, as the mean value of $\boldsymbol{p}.\boldsymbol{Q}$ is zero, has a mean value, the mean recoil energy, of

$$E_r = \frac{\hbar^2Q^2}{2M}$$

(3/51)

(3/47) gives the result

$$S_{1s}(\boldsymbol{Q}) = E_r = \frac{\hbar^2Q^2}{2M}$$

(3/52)

Substitution of this into (3/48) yields

$$S_{2s}(\boldsymbol{Q}) = E_r^2 + \hbar^2 Q^2 \langle v_{\boldsymbol{Q}}^2 \rangle$$

(3/53)

where, as is shown by classical mechanics,

$$\langle v_{\boldsymbol{Q}}^2 \rangle = \frac{k_B T}{2M}$$

(3/54)

There are quantum mechanical corrections to this, involving the potential energy of the system, but for most liquids, and particularly for molten salts, these are negligible. Without them

$$S_{2s}(\boldsymbol{Q}) = \frac{\hbar^2 Q^2 k_B T}{M} + \frac{\hbar^4 Q^4}{4M^2}$$

(3/55)

The first moment of the coherent structure factor is the same as that of the incoherent

$$S_1(\boldsymbol{Q}) = \frac{\hbar^2 Q^2}{M}$$

(3/56)

The expression for the second moment is rather more complicated than that of its incoherent counterpart due to terms arising from correlations between the momenta of different particles but its leading terms are the same and we shall again neglect all others.

$$S_2(\boldsymbol{Q}) = \frac{\hbar^2 Q^2 k_B T}{M} + \frac{\hbar^4 Q^4}{4M^2}$$

(3/57)

These expressions for the moments of the dynamic structure factor are sometimes known as sum rules.

3.5 Bragg scattering, $I(\boldsymbol{Q},\infty)$ and $G(\boldsymbol{r},\infty)$

The function $I(\boldsymbol{Q},t)$ tends to some limit as t tends to infinity. Writing it as

$$I(Q,t) = I(\boldsymbol{Q},\infty) + I'(\boldsymbol{Q},t) \tag{3/58}$$

where $I(\boldsymbol{Q},\infty)$ is the limiting value of $I(\boldsymbol{Q},t)$ and $I'(\boldsymbol{Q},t)$ tends to zero at large t we get

$$S(\boldsymbol{Q},\omega) = \frac{1}{2\pi\hbar}\int_{-\infty}^{\infty}(I(\boldsymbol{Q},\infty) + I'(\boldsymbol{Q},t))\, e^{-i\omega t}\, dt \tag{3/59}$$

$$= \frac{1}{\hbar}\delta(\omega)I(\boldsymbol{Q},\infty) + \frac{1}{2\pi\hbar}\int_{-\infty}^{\infty} I'(\boldsymbol{Q},t)\, e^{-i\omega t}\, dt \tag{3/60}$$

The first term, containing the delta function, represents the Bragg scattering while the second term is inelastic scattering. This is not zero at zero energy transfer although it is negligible compared to the Bragg scattering. We see that the Bragg scattering is proportional to the function

$$I(\boldsymbol{Q},\infty) = \frac{1}{N}\sum_{j}\sum_{j'}\langle e^{-i\boldsymbol{Q}.\boldsymbol{r}_{j'}}\, e^{i\boldsymbol{Q}.\boldsymbol{r}_{j}(\infty)}\rangle \tag{3/61}$$

$$= \frac{1}{N}\sum_{j}\sum_{j'}\langle e^{-i\boldsymbol{Q}.\boldsymbol{r}_{j'}}\rangle\langle e^{i\boldsymbol{Q}.\boldsymbol{r}_{j}(\infty)}\rangle \tag{3/62}$$

$$= \frac{1}{N}\sum_{j}\sum_{j'}\langle e^{-i\boldsymbol{Q}.\boldsymbol{r}_{j'}}\rangle\langle e^{i\boldsymbol{Q}.\boldsymbol{r}_{j}}\rangle \tag{3/63}$$

where we have made use of the facts that as t tends to infinity there is no correlation between $\boldsymbol{r}_{j'}(0)$ and $\boldsymbol{r}_j(t)$ and that the expectation value of the second term in (3/62) must be independent of time. We are left with a familiar result for Bragg scattering from a lattice.

We can use the same reasoning to obtain from (3/3), putting $t = \infty$, the result

$$G(\boldsymbol{r}, \infty) = \frac{1}{N} \int \langle \rho(\boldsymbol{r}') \rangle \langle \rho(\boldsymbol{r}') \rho(\boldsymbol{r}' + \boldsymbol{r}) \rangle \, d\boldsymbol{r}' \tag{3/64}$$

where $\rho(\boldsymbol{r})$ is the particle density operator defined in (3/2). This is sometimes known as the Patterson function.

3.6 Scattering from liquids

For a liquid the time averaged density is uniform; that is

$$\rho(\boldsymbol{r}) = \rho = \frac{N}{V} \tag{3/65}$$

Therefore

$$G(\boldsymbol{r}, \infty) = \rho \tag{3/66}$$

Putting $G(\boldsymbol{r}, \infty)$ is constant in (3/15) gives

$$I(\boldsymbol{Q}, \infty) \propto \delta(\boldsymbol{Q}) \tag{3/67}$$

so there is Bragg scattering only at $\boldsymbol{Q} = 0$. But this is not scattering at all; it is merely the unscattered neutron beam. We conclude that there is no Bragg scattering from a liquid. Because $G(\boldsymbol{r}, t)$ tends to a non-zero limit at large t and also at large $\boldsymbol{r}$, $S(\boldsymbol{Q}, \omega)$ has a delta function

behaviour at $\omega = 0,\ \boldsymbol{Q} = 0$. This does not correspond to actual scattering and it is convenient to remove it by subtracting from $G(\boldsymbol{r},t)$ its limiting value in the Fourier transform defining $S(\boldsymbol{Q},\omega)$ to give

$$S(\boldsymbol{Q},\omega) = \frac{1}{2\pi\hbar}\int\int (G(\boldsymbol{r},t)-\rho)e^{i(\boldsymbol{Q}.\boldsymbol{r}-\omega t)}\ d\boldsymbol{r}\ dt \qquad (3/68)$$

The static structure factor, being the zeroth moment of this, is modified accordingly and becomes

$$S(\boldsymbol{Q}) = 1 + \rho\int (g(\boldsymbol{r}) - 1)\, e^{i\boldsymbol{Q}.\boldsymbol{r}}\ d\boldsymbol{r} \qquad (3/69)$$

As $g(\boldsymbol{r})$ depends only on $|\boldsymbol{r}|$ in a liquid we can put

$$S(Q) = 1 + \rho\int_0^\infty r^2\, dr\, (g(r) - 1)\int_{-1}^{1} e^{iQr\cos\theta}\, d(\cos\theta) \qquad (3/70)$$

$$= 1 + \frac{4\pi\rho}{Q}\int_0^\infty r\ (g(r) - 1)\ \sin Qr\ dr \qquad (3/71)$$

And conversely

$$g(r) = 1 + \frac{1}{2\pi^2\rho r}\int_0^\infty Q\ (S(Q) - 1)\ \sin Qr\ dQ \qquad (3/72)$$

3.7 The compressibility limit of $S(Q)$

At $\boldsymbol{Q} = 0$ we have

$$S(0) = 1 + \rho\int_0^\infty (g(r) - 1)\ dr \qquad (3/73)$$

which is related to density fluctuation in the liquid. The number of atoms, n, in a fixed volume V_0 fluctuates about its mean value $\langle n \rangle = \rho V_0$. The quantity $\langle n^2 \rangle$ is given by

$$\langle n^2 \rangle = \rho \int_{V_0} d\boldsymbol{r}_1 \int_{V_0} d\boldsymbol{r}_2 \, G(\boldsymbol{r}_2 - \boldsymbol{r}_1, 0)$$

(3/74)

$$= \rho \int_{V_0} d\boldsymbol{r}_1 \int_{V_0} d\boldsymbol{r}_2 \, (\delta(\boldsymbol{r}_2 - \boldsymbol{r}_1) + \rho g(\boldsymbol{r}_2 - \boldsymbol{r}_1))$$

(3/75)

$$= \rho V_0 + \rho^2 \int_{V_0} d\boldsymbol{r}_1 \int_{V_0} d\boldsymbol{r}_2 \, g(\boldsymbol{r}_2 - \boldsymbol{r}_1)$$

(3/76)

$$= \langle n \rangle + \langle n \rangle \rho \int_{V_0} g(\boldsymbol{r}) \, d\boldsymbol{r}$$

(3/77)

$$= \langle n \rangle \left(1 + \rho \int_{V_0} (g(\boldsymbol{r}) - 1) \, d\boldsymbol{r} \right) + \langle n \rangle^2$$

(3/78)

So that

$$S(0) = \frac{\langle n^2 \rangle - \langle n \rangle^2}{\langle n \rangle}$$

(3/79)

$$= \frac{\langle \Delta n \rangle^2}{\langle n \rangle}$$

(3/80)

where $\Delta n = n - \langle n \rangle$. Thermodynamic arguments can be used to relate this to the isothermal compressibility K_T (see, for example, [3/4]).

$$S(0) = \rho k_B T K_T$$

(3/81)

3.8 Multicomponent liquids and partial correlation functions

In the same way that the cross-section for neutron scattering from a monatomic fluid can be written in terms of the dynamic structure factor, that for multicomponent systems may be written, as was shown in the previous chapter, in terms of the partial structure factors defined by

$$S_{\alpha\beta}(Q,\omega) = \frac{1}{2\pi\hbar N}\int \sum_{j}^{\alpha}\sum_{j'}^{\beta}\langle \rho_{j'}(\boldsymbol{Q},t)\rho_j(-\boldsymbol{Q},0)\rangle\ e^{-i\omega t}\,dt$$

(3/82)

where the indices α and β are labels describing the species and may take the values of any of the component species. For two component molten salts it is convenient to write these as + and - for cation and anion respectively so that the partial structure factors are $S_{++}(\boldsymbol{Q},\omega)$, $S_{+-}(\boldsymbol{Q},\omega)$ and $S_{--}(\boldsymbol{Q},\omega)$) (it is easily shown that $S_{-+}(\boldsymbol{Q},\omega)$ is identical to $S_{+-}(\boldsymbol{Q},\omega)$ and that the same is true for all partial correlation functions). There are $\frac{1}{2}n(n+1)$ of these partial structure factors in an n component liquid together with n incoherent structure factors

$$S_{\alpha}(Q,\omega) = \frac{1}{2\pi\hbar N}\int \sum_{j}^{\alpha}\langle \rho_j(\boldsymbol{Q},t)\rho_j(-\boldsymbol{Q},0)\rangle\ e^{-i\omega t}\,dt$$

(3/83)

Because the sum is over particles of one species only but N, the total number of particles, still appears in this expression the zeroth moment of this is clearly

$$S_{0\alpha}(\boldsymbol{Q}) = c_{\alpha}$$

(3/84)

where c_{α} is the fractional concentration of species α. Similarly the next two moments are

$$S_{1\alpha}(\boldsymbol{Q}) = c_\alpha \frac{\hbar^2 Q^2}{2M_\alpha}$$

(3/85)

$$S_{2\alpha}(\boldsymbol{Q}) = c_\alpha \frac{\hbar^2 Q^2 k_B T}{M_\alpha} + c_\alpha \frac{\hbar^4 Q^4}{4M_\alpha^2}$$

(3/86)

The first and second moments of the coherent structure factors can be shown to be

$$S_{1\alpha\beta}(\boldsymbol{Q}) = c_\alpha \delta_{\alpha\beta} \frac{\hbar^2 Q^2}{2M_\alpha}$$

(3/87)

$$S_{2\alpha\beta}(\boldsymbol{Q}) = c_\alpha \delta_{\alpha\beta} \frac{\hbar^2 Q^2 k_B T}{M_\alpha} + c_\alpha \delta_{\alpha\beta} \frac{\hbar^4 Q^4}{4M_\alpha^2}$$

(3/88)

The zeroth moment of the coherent structure factor defines the partial static structure factors, $S_{\alpha\beta}(\boldsymbol{Q})$

$$S_{0\alpha\beta}(\boldsymbol{Q}) = S_{\alpha\beta}(\boldsymbol{Q}) = \frac{1}{N} \sum_{j}^{\alpha} \sum_{j'}^{\beta} \langle \rho_{j'}(\boldsymbol{Q}) \rho_j(-\boldsymbol{Q}) \rangle$$

(3/89)

This is not the only possible definition; it differs from that of Ashcroft and Langreth [3/5] who include a factor $\sqrt{c_\alpha c_\beta}$ on the right hand side of this expression. As $\boldsymbol{Q}$ approaches zero these partial structure factors also approach a compressibility limit:

$$S_{\alpha\beta}(0) = c_\alpha c_\beta \rho k_B T K_T$$

(3/90)

while at large Q the value approaches the limit

$$S_{\alpha\beta}(\infty) = c_\alpha \delta_{\alpha\beta}$$

(3/91)

Partial time dependent pair distribution functions can also be defined:

$$G_{\alpha\beta}(\boldsymbol{r}, t) = \frac{\hbar}{8\pi^3} \int\int S_{\alpha\beta}(\boldsymbol{Q}, \omega)\, e^{-i(\boldsymbol{Q}.\boldsymbol{r} - \boldsymbol{\omega t})}\ d\boldsymbol{Q}\ d\omega$$

(3/92)

$$= \frac{1}{N} \sum_{j}^{\alpha} \sum_{j'}^{\beta} \langle \delta(\boldsymbol{r}_{j'}(t) - \boldsymbol{r}_j - \boldsymbol{r}) \rangle$$

(3/93)

The single particle functions are defined in an analogous way. The limiting values of these functions are

$$G_\alpha(\boldsymbol{r}, 0) = c_\alpha \delta(\boldsymbol{r})$$

(3/94)

$$G_{\alpha\beta}(\boldsymbol{r}, 0) = c_\alpha \delta_{\alpha\beta} \delta(\boldsymbol{r}) + \rho c_\alpha c_\beta g_{\alpha\beta}(\boldsymbol{r})$$

(3/95)

$$G_{\alpha\beta}(\boldsymbol{r}, \infty) = c_\alpha c_\beta \rho$$

(3/96)

where the Kronecker delta term arises because only when $\alpha = \beta$ does the function $G_{\alpha\beta}(\boldsymbol{r}, t)$ contain the self part $G_\alpha(\boldsymbol{r}, t)$. The partial pair distribution function $g_{\alpha\beta}(\boldsymbol{r})$ is defined in the obvious way:

$$g_{\alpha\beta}(\boldsymbol{r}) = \frac{1}{\rho N} \sum_{j}^{\alpha} \sum_{j'}^{\beta} \langle \delta(\boldsymbol{r}_{j'} - \boldsymbol{r}_j - \boldsymbol{r}) \rangle$$

(3/97)

The equivalent of (3/31) is

$$S_{\alpha\beta}(\boldsymbol{Q}) = \int G_{\alpha\beta}(\boldsymbol{r}, 0)\, e^{i\boldsymbol{Q}.\boldsymbol{r}}\ d\boldsymbol{r}$$

(3/98)

Using (3/95) this becomes

$$S_{\alpha\beta}(\boldsymbol{Q}) = c_\alpha\delta_{\alpha\beta} + \rho c_\alpha c_\beta \int g_{\alpha\beta}(\boldsymbol{r})\, e^{i\boldsymbol{Q}.\boldsymbol{r}}\ d\boldsymbol{r}$$

(3/99)

If, as before, we redefine the structure factors to be the Fourier transforms of $G_{\alpha\beta}(\boldsymbol{r},t) - G_{\alpha\beta}(\boldsymbol{r},\infty)$, to remove the delta function at the origin, we get

$$S_{\alpha\beta}(\boldsymbol{Q}) = c_\alpha\delta_{\alpha\beta} + \rho c_\alpha c_\beta \int \left(g_{\alpha\beta}(\boldsymbol{r}) - 1\right) e^{i\boldsymbol{Q}.\boldsymbol{r}}\ d\boldsymbol{r}$$

(3/100)

For a liquid at large $\boldsymbol{Q}$

$$S_{\alpha\beta}(\infty) = c_\alpha\delta_{\alpha\beta}$$

(3/101)

Inverting the Fourier transform gives

$$g_{\alpha\beta}(\boldsymbol{r}) - 1 = \frac{1}{8\pi^3\rho}\int \frac{S_{\alpha\beta}(\boldsymbol{Q}) - c_\alpha\delta_{\alpha\beta}}{c_\alpha c_\beta}\ e^{-i\boldsymbol{Q}.\boldsymbol{r}}\ d\boldsymbol{Q}$$

(3/102)

This looks more like the monatomic case if we define a different set of partial structure factors (sometimes known as the Faber-Ziman partials [3/6]) by

$$S_{\alpha\beta}(\boldsymbol{Q}) - c_\alpha\delta_{\alpha\beta} = c_\alpha c_\beta (A_{\alpha\beta}(\boldsymbol{Q}) - 1)$$

(3/103)

so that

$$g_{\alpha\beta}(\boldsymbol{r}) - 1 = \frac{1}{8\pi^3\rho}\int \left(A_{\alpha\beta}(\boldsymbol{Q}) - 1\right) e^{-i\boldsymbol{Q}.\boldsymbol{r}}\ d\boldsymbol{Q}$$

(3/104)

and conversely

$$A_{\alpha\beta}(\boldsymbol{Q}) - 1 = \rho \int \left(g_{\alpha\beta}(\boldsymbol{r}) - 1\right) e^{i\boldsymbol{Q}.\boldsymbol{r}} \; d\boldsymbol{Q}$$

(3/105)

Integrating over all angles these become

$$g_{\alpha\beta}(r) - 1 = \frac{1}{2\pi^2 \rho r} \int_0^\infty Q\left(A_{\alpha\beta}(Q) - 1\right) \; sin\, Qr \;\; dQ$$

(3/106)

and

$$A_{\alpha\beta}(Q) - 1 = \frac{4\pi\rho}{Q} \int_0^\infty r\left(g_{\alpha\beta}(r) - 1\right) \; sin\, Qr \;\; dr$$

(3/107)

The limiting values of the Faber-Ziman partials are

$$A_{\alpha\beta}(0) = 1 + \rho k_B T K_T - \frac{\delta_{\alpha\beta}}{c_\alpha}$$

(3/108)

and

$$A_{\alpha\beta}(\infty) = 1$$

(3/109)

Using (2/36) and (3/103) the coherent scattering cross-section can be written in terms of these partials as

$$\frac{d\sigma_{coh}}{d\Omega} = \sum_\alpha \sum_\beta c_\alpha c_\beta \bar{b}_\alpha \bar{b}_\beta \left(A_{\alpha\beta}(Q) - 1\right) + \sum_\alpha c_\alpha \overline{b_\alpha}^2$$

(3/110)

and the total cross-section is

$$\frac{d\sigma}{d\Omega} = \sum_\alpha \sum_\beta c_\alpha c_\beta \bar{b}_\alpha \bar{b}_\beta \left(A_{\alpha\beta}(Q) - 1\right) + \sum_\alpha c_\alpha \overline{b_\alpha^2}$$

(3/111)

The equivalent to (2/31) for the elastic case gives the total static structure factor

$$S_T(Q) = \left(\sum_\alpha \sum_\beta \bar{b}_\alpha \bar{b}_\beta S_{\alpha\beta}(Q) + \sum_\alpha c_\alpha \left(\overline{b_\alpha^2} - \overline{b_\alpha}^2 \right) \right) / \overline{b^2}$$

(3/112)

from which may be subtracted the second term to give a coherent structure factor. It is also convenient to define another total structure factor by

$$A_T(Q) = \sum_\alpha \sum_\beta c_\alpha c_\beta \bar{b}_\alpha \bar{b}_\beta \left(A_{\alpha\beta}(Q) - 1 \right) / \bar{b}^2 + 1$$

(3/113)

Where

$$\bar{b} = \sum_\alpha c_\alpha \bar{b}_\alpha$$

(3/114)

so that we may define the total radial distribution function to be its transform

$$g_T(r) - 1 = \frac{1}{2\pi^2 \rho r} \int_0^\infty Q(A_T(Q) - 1) \ sin\, Qr \ \ dQ$$

(3/115)

$$= \frac{1}{2\pi^2 \rho r} \sum_\alpha \sum_\beta c_\alpha c_\beta \bar{b}_\alpha \bar{b}_\beta \int_0^\infty Q \left(A_{\alpha\beta}(Q) - 1 \right) / \overline{b^2} \, sin\, Qr \ \ dQ$$

(3/116)

$$= \sum_\alpha \sum_\beta c_\alpha c_\beta \bar{b}_\alpha \bar{b}_\beta \, g_{\alpha\beta}(r) / \overline{b^2}$$

(3/117)

This has limits $g_T(0) = 0$ and $g_T(\infty) = 1$. Finally, it is useful to define the coherent scattering function

$$F(Q) = \sum_{\alpha}\sum_{\beta} c_\alpha c_\beta \bar{b}_\alpha \bar{b}_\beta \left(A_{\alpha\beta}(Q) - 1\right)$$

(3/118)

which is that part of the scattering that is related to the partial structure factors $A_{\alpha\beta}(Q)$.

3.9 More structure factors - charge, number and mass correlations

We may define a property density ρ_X in terms of the particle densities

$$\rho_X(\boldsymbol{Q}, t) = \frac{\sum_\alpha X_\alpha \rho_\alpha(\boldsymbol{Q}, t)}{\sum_\alpha |X_\alpha|}$$

(3/119)

where X_α is the value of the property X for particles of type α. The denominator removes the dimensionality of the property. By analogy with (3/17) we can form partial intermediate scattering functions for the properties

$$I_{XY}(\boldsymbol{Q}, t) = \frac{1}{N}\langle \rho_X(\boldsymbol{Q}, t)\rho_Y(-\boldsymbol{Q}, 0)\rangle$$

(3/120)

$$= \frac{\sum_\alpha \sum_\beta X_\alpha Y_\beta I_{\alpha\beta}(\boldsymbol{Q}, t)}{\sum_\alpha \sum_\beta |X_\alpha|\ |Y_\beta|}$$

(3/121)

and in a similar manner, other partial property correlation functions, in particular static structure factors

$$S_{XY}(\boldsymbol{Q}) = \frac{\sum_\alpha \sum_\beta X_\alpha Y_\beta S_{\alpha\beta}(\boldsymbol{Q})}{\sum_\alpha \sum_\beta |X_\alpha|\ |Y_\beta|}$$

(3/122)

which have the limiting values

$$S_{XY}(0) = \frac{\sum_\alpha \sum_\beta X_\alpha Y_\beta}{\sum_\alpha \sum_\beta |X_\alpha| \, |Y_\beta|} \rho k_B T K_T$$

(3/123)

and

$$S_{XY}(\infty) = \frac{\sum_\alpha c_\alpha X_\alpha Y_\alpha}{\sum_\alpha \sum_\beta |X_\alpha| \, |Y_\beta|}$$

(3/124)

The matrix defining the $S_{XY}(Q)$ in terms of the $S_{\alpha\beta}(Q)$ can be inverted to give, for binary systems

$$S_{\alpha\beta}(Q) = \sum_X \sum_Y \frac{(|X_+| + |X_-|)(|Y_+| + |Y_-|) X_{\alpha*} Y_{\beta*}}{(X_+ Y_- - X_- Y_+)^2} S_{XY}(Q)$$

(3/125)

where the label $\alpha*$ means the opposite to α, that is for $S_{++}(Q)$ $X_{\alpha*}$ is X_-. It can now be shown that the coherent scattering cross-section can be written, in terms of these partial structure factors, as

$$\frac{d\sigma_{coh}}{d\Omega} = a_X^2 S_{XX}(Q) + 2 a_X a_Y S_{XY}(Q) + a_Y^2 S_{YY}(Q)$$

(3/126)

where the coefficients a_X and a_Y are defined by

$$a_X = \frac{(|X_+| + |X_-|)\left(Y_+ \bar{b}_- - Y_- \bar{b}_+\right)}{(X_+ Y_- - X_- Y_+)}$$

(3/127)

and similarly for a_Y. Properties frequently considered are particle mass, charge, and number (which is equal to unity for each species). For a binary system these give partial structure factors

$$S_{qq} = c_-^2 S_{++} + c_+^2 S_{--} - 2c_+c_-S_{+-}$$

$$S_{Mq} = (M_+c_- S_{++} - M_-c_+ S_{--} + (M_-c_- - M_+c_+)S_{+-})/(M_+ + M_-)$$

$$S_{MM} = (M_+^2 S_{++} + M_-^2 S_{--} - 2M_+M_-S_{+-})/(M_+ + M_-)^2$$

$$S_{Nq} = \tfrac{1}{2}c_- S_{++} - \tfrac{1}{2}c_+ S_{--} + \tfrac{1}{2}(c_- - c_+)S_{+-}$$

$$S_{NN} = \tfrac{1}{4}(S_{++} + S_{--} + 2S_{+-})$$

(3/128)

Apart from the factor of $\frac{1}{4}$ the number-number partial structure factor is the same sum over all particles as is the structure factor of a monatomic liquid. The number and charge partial structure factors are essentially the same (apart from some constants) as the number and concentration partials defined by Bhatia and Thornton [3/7]. The coefficients describing the scattering cross-section are

$$a_M = \left(c_+\bar{b}_+ + c_-\bar{b}_-\right)(M_+ + M_-)/(c_+M_+ + c_-M_-)$$

$$a_q = \left(M_+\bar{b}_- + M_-\bar{b}_+\right)/(c_+M_+ + c_-M_-)$$

(3/129)

for mass and charge and

$$a_N = 2\left(c_+\bar{b}_+ + c_-\bar{b}_-\right)$$

$$a_q = \bar{b}_+ + \bar{b}_-$$

(3/130)

for number and charge. The charge neutrality of the mixture has been used to write particle charges in terms of concentrations.

3.10 Current correlations

As we have defined particle and property densities, so too may we define particle currents

$$\boldsymbol{j}_\alpha(\boldsymbol{Q},t)=\sum_k^\alpha \boldsymbol{j}_k(\boldsymbol{Q},t)=\sum_k^\alpha \boldsymbol{v}_k e^{i\boldsymbol{Q}.\boldsymbol{r}_k(t)}$$

(3/131)

and property currents

$$\boldsymbol{j}_X(\boldsymbol{Q},t)=\frac{\sum_\alpha X_\alpha \boldsymbol{j}_\alpha(\boldsymbol{Q},t)}{\sum_\alpha |X_\alpha|}$$

(3/132)

where $\boldsymbol{v}_k$ is the velocity of the k^{th} particle. Because of the vector nature of these currents there are both longitudinal and transverse current-current correlation functions:

$$C_{XY}^L(\boldsymbol{Q},t)=\frac{1}{N}\langle \boldsymbol{Q}.\boldsymbol{j}_X(-\boldsymbol{Q},0)\ \boldsymbol{Q}.\boldsymbol{j}_Y(\boldsymbol{Q},t)\rangle$$

(3/133)

$$C_{XY}^T(\boldsymbol{Q},t)=\frac{1}{N}\langle \boldsymbol{Q}\times\boldsymbol{j}_X(-\boldsymbol{Q},0).\boldsymbol{Q}\times\boldsymbol{j}_Y(\boldsymbol{Q},t)\rangle$$

(3/134)

Instead of describing a fluid in terms of correlations of n types of particles we could equally well do so in terms of correlations of n properties. Which is the most useful description depends on the fluid and on the aspects of its behaviour that are under consideration. The acoustic and optic modes in a binary ionic crystal are analogous to the mass-mass and charge-charge correlations in an ionic fluid [3/8] and so it is useful to consider dynamic properties in terms of the functions

$$C_{MM}^L(\boldsymbol{Q},t)=\frac{1}{N}\langle \boldsymbol{Q}.\boldsymbol{j}_M(-\boldsymbol{Q},0)\ \boldsymbol{Q}.\boldsymbol{j}_M(\boldsymbol{Q},t)\rangle$$

(3/135)

$$C_{qq}^L(\boldsymbol{Q},t)=\frac{1}{N}\langle \boldsymbol{Q}.\boldsymbol{j}_q(-\boldsymbol{Q},0)\ \boldsymbol{Q}.\boldsymbol{j}_q(\boldsymbol{Q},t)\rangle$$

(3/136)

Where

$$j_M(\boldsymbol{Q},t) = \frac{M_+\boldsymbol{j}_+(\boldsymbol{Q},t) + M_-\boldsymbol{j}_-(\boldsymbol{Q},t)}{M_+ + M_-}$$

(3/137)

$$j_q(\boldsymbol{Q},t) = c_-\boldsymbol{j}_+(\boldsymbol{Q},t) - c_+\boldsymbol{j}_-(\boldsymbol{Q},t)$$

(3/138)

These modes are strictly independent only at $\boldsymbol{Q} = 0$. At other values of $\boldsymbol{Q}$ the cross-correlation function

$$C^L_{Mq}(\boldsymbol{Q},t) = \frac{1}{N}\langle \boldsymbol{Q}.\boldsymbol{j}_M(-\boldsymbol{Q},0)\, \boldsymbol{Q}.\boldsymbol{j}_q(\boldsymbol{Q},t)\rangle$$

(3/139)

is generally not equal to zero. A proper description of the dynamic modes would be in terms of current-current correlations for which the cross-correlation vanishes for all $\boldsymbol{Q}$, as is the case for acoustic and optic modes along symmetry directions in a crystal; as it has not been possible to find such functions it is useful to pursue the analogy of the mass-mass and charge-charge correlations as acoustic and optic modes.

The power spectrum of the current correlations is given by the time Fourier transform

$$C^L_{XY}(\boldsymbol{Q},\omega) = \frac{1}{2\pi}\int C^L_{XY}(\boldsymbol{Q},t)\, e^{-i\omega t}\, dt$$

(3/140)

Using the continuity equation (which represents particle or property conservation)

$$\frac{\partial}{\partial t}\rho_X(\boldsymbol{Q},t) + i\boldsymbol{Q}.\boldsymbol{j}_X(\boldsymbol{Q},t) = 0$$

(3/141)

we can write

$$C_{XY}^{L}(Q,t) = -\frac{1}{N}\langle\frac{\partial}{\partial t}\rho_X(-\boldsymbol{Q},0)\frac{\partial}{\partial t}\rho_Y(\boldsymbol{Q},t)\rangle$$

(3/142)

$$= -\frac{1}{N}\langle\rho_X(-\boldsymbol{Q},0)\frac{\partial^2}{\partial t^2}\rho_Y(\boldsymbol{Q},t)\rangle$$

(3/143)

$$= -\frac{\partial^2}{\partial t^2}S_{XY}(\boldsymbol{Q},t)$$

(3/144)

So that

$$C_{XY}^{L}(Q,\omega) = \omega^2 S_{XY}(\boldsymbol{Q},\omega)$$

(3/145)

For a justification of this, particular the step (3/142) to (3/143) see, for example, [3/9]. There is no such simple relation for the transverse currents.

3.11 Single particle correlations and diffusive motions

The position of a free particle is given by

$$\boldsymbol{r}(t) = \boldsymbol{r}(0) + \boldsymbol{p}t/M$$

(3/146)

where $\boldsymbol{p}$ is its momentum. This means that the self intermediate scattering function for a free particle is, from (3/19)

$$I_s(\boldsymbol{Q},t) = \langle e^{i\boldsymbol{Q}.\boldsymbol{p}t/M} \rangle$$

(3/147)

$$= \frac{\int d\boldsymbol{p}\, e^{-p^2/2Mk_BT}\, e^{i\boldsymbol{Q}.\boldsymbol{p}t/M}}{\int d\boldsymbol{p}\, e^{-p^2/2Mk_BT}}$$

(3/148)

$$= e^{-Q^2t^2k_BT/2M}$$

(3/149)

from which we get

$$S(Q,\omega) = \frac{1}{2\pi\hbar}\int_{-\infty}^{\infty} e^{-Q^2t^2k_BT/2M}\, e^{-i\omega t}\, dt$$

(3/150)

$$= \sqrt{\frac{M}{2\pi\hbar^2 k_B T Q^2}}\; e^{-M\omega^2/2Q^2k_BT}$$

(3/151)

Because no correlations exist between free particles (as in a dilute gas) we see immediately that $S(Q,\omega) = S^s(Q,\omega)$. This is a Gaussian function with a half width determined by Q^2k_BT/M where k_BT/M is the mean square thermal velocity in the direction of $\boldsymbol{Q}$.

In a fluid particles interact but we can argue that the self correlation function $G^s(\boldsymbol{r},t)$ must, on some time scales, be related to the diffusion of the particles in the system. The diffusion equation should be obeyed by this function for times long compared with the collision time and distances long compared with the mean free path:

$$D\,\nabla^2\, G^s(\boldsymbol{r},t) = \frac{\partial}{\partial t}\, G^s(\boldsymbol{r},t)$$

(3/152)

where D is the diffusion constant. The solution of this is

$$G^s(\boldsymbol{r},t) = (4\pi D|t|)^{-3/2}\, e^{-r^2/4D|t|}$$

(3/153)

which gives

$$S^s(\boldsymbol{Q},\omega) = \frac{1}{\hbar}\,\frac{2DQ^2}{\omega^2 + (DQ^2)^2}$$

(3/154)

This is a Lorentzian form with a half width determined by D. This is only true for long times, or small ω, and at small $\boldsymbol{Q}$. (In general we expect such macroscopic arguments to apply only at small $\boldsymbol{Q}$, long wavelengths.) At larger momentum transfer $S^s(\boldsymbol{Q},\omega)$ should change from this Lorentzian form to the free particle Gaussian form.

The contributions of $S^s(\boldsymbol{Q},\omega)$ to the total scattering are small in the systems we are studying, the coherent scattering being more important. One way of considering this is by using the Vineyard approximation [3/10]. The distinct function $G^d(\boldsymbol{r},t)$ can be written as

$$G^d(\boldsymbol{r},t) = \int g(\boldsymbol{r}')\, P(\boldsymbol{r}-\boldsymbol{r}',t)\, d\boldsymbol{r}'$$

(3/155)

where $P(\boldsymbol{r}-\boldsymbol{r}',t)$ is the probability of a particle being at $\boldsymbol{r}$ at time t given that there was one at $\boldsymbol{r}'$ at $t = 0$. The Vineyard approximation consists of putting $P \equiv G^s$ so that $G^d(\boldsymbol{r},t)$ is the convolution of $g(\boldsymbol{r})$ and $G^s(\boldsymbol{r},t)$:

$$G^d(\boldsymbol{r},t) = \int g(\boldsymbol{r}')\, G^s(\boldsymbol{r}-\boldsymbol{r}',t)\, d\boldsymbol{r}'$$

(3/156)

which means that

$$S^d(\boldsymbol{Q},\omega) = S(\boldsymbol{Q})S^s(\boldsymbol{Q},\omega)$$

(3/157)

so the width of the quasi-elastic scattering is given by the width of $S^s(\boldsymbol{Q},\omega)$ as described above. For a binary system the equivalent to this is

$$S^d_{++}(\boldsymbol{Q},\omega) = S_{++}(\boldsymbol{Q})S_+(\boldsymbol{Q},\omega)$$
$$S^d_{--}(\boldsymbol{Q},\omega) = S_{--}(\boldsymbol{Q})S_-(\boldsymbol{Q},\omega)$$
$$S^d_{+-}(\boldsymbol{Q},\omega) = \tfrac{1}{2}S_{+-}(\boldsymbol{Q})\big(S_+(\boldsymbol{Q},\omega)+S_-(\boldsymbol{Q},\omega)\big)$$

(3/158)

It can be seen, though, that the moments of $S(\boldsymbol{Q},\omega)$ given using this approximation are not correct.

At small $\boldsymbol{Q}$ hydrodynamic arguments can be used to show [3/11] that $S(\boldsymbol{Q},\omega)$ consists of a Brillouin doublet peaking at frequencies of $\pm c_S Q$ (where c_S is the adiabatic sound velocity) and a central Rayleigh peak given by

$$S(Q,\omega) = \frac{2k_BT}{\hbar M c_T^2}\left(1-\frac{C_V}{C_P}\right)\frac{Q^2D_T}{\omega^2+(D_TQ^2)^2} + \text{Brillouin terms}$$

(3/159)

where c_T is the isothermal sound velocity, C_V and C_P heat capacities and D_T is the thermal diffusivity:

$$D_T = \frac{\kappa}{\rho C_P}$$

(3/160)

where κ is the thermal conductivity. Thus at very low $\boldsymbol{Q}$ the width of the coherent quasi-elastic scattering is determined by the thermal diffusivity whereas the width of the incoherent quasi-elastic scattering is determined by the diffusion constant.

3.12 Calculation of $g(r)$ from the interaction potential

The fundamental problem of liquid state theory is to determine $g(r)$ given a knowledge of the pair potential $V(r)$. As $g(r)$ appears in nearly all of the thermodynamic expressions describing the liquid state this would mean that the thermodynamic properties of a system, as well as the structure, could be deduced just from the potential.

The total correlation between two particles may be considered to consist of two parts: the direct correlation between the two and also an indirect correlation imposed via a third particle. We can write it, therefore, as a sum of the direct part and the average of the indirect part over all possible positions of the third particle. This is the basis of the Ornstein-Zernike integral equation [3/12]

$$g(\boldsymbol{r}) = 1 + c(\boldsymbol{r}) + \rho \int c(|\boldsymbol{r} - \boldsymbol{r}'|)(g(\boldsymbol{r}') - 1)\, d\boldsymbol{r}' \qquad (3/161)$$

which defines the direct correlation function $c(\boldsymbol{r})$. By Fourier transforming this and relating the Fourier transform of $g(r) - 1$ to $S(Q)$ it can be shown that

$$\frac{4\pi}{Q} \int r\, c(r) \sin Qr \; dr = \frac{S(Q) - 1}{\rho S(Q)} \qquad (3/162)$$

The sine Fourier transform of this expression relates the direct correlation function to the structure factor; thus $c(r)$ is experimentally accessible.

At low densities we expect the asymptotic form

$$c(r) \approx g(r) - 1$$

(3/163)

and

$$g(r) \approx e^{-V(r)/k_B T}$$

(3/164)

from the Boltzmann factor. At the higher densities found in liquids this is not the case. The basis of several theoretical methods is to write down an approximation for $c(r)$ in terms of $V(r)$ and then solve the integral equation (3/161). Some such approximations are:

i) The mean spherical approximation (MSA) [3/13] in which

$$g(r) = 0 \qquad (r < \sigma)$$

$$c(r) = -\frac{V(r)}{k_B T} \qquad (r > \sigma)$$

(3/165)

where σ is the effective atomic radius.

ii) The hypernetted chain (HNC) approximation (e.g. [3/14])

$$c(r) = g(r) - 1 - ln\, g(r) - \frac{V(r)}{k_B T}$$

(3/166)

iii) The Percus-Yevick (PY) approximation [3/15]

$$c(r) = g(r)\left(1 - e^{V(r)/k_B T}\right)$$

(3/167)

It is generally considered that the HNC approximation is best for molten salts because it treats the long range interactions better than the others. The results of such theoretical calculations depend not only on the potential chosen but also on the approximation used. For this

reason a lot of work is done on computer simulation and indeed theoretical approximations are often tested by comparing their results with those of simulation.

There are two methods of computer simulation: the Monte Carlo method developed by Metropolis *et al* [3/16]; and the molecular dynamics method. In the former lots of configurations are generated randomly and saved according to their probability (given by the Boltzmann factor). All the saved configurations can then be used to calculate $g(r)$ and other structural information. This method is limited to equilibrium conditions and static properties of the liquid. Molecular dynamics, in which all the interatomic forces are calculated and Newton's laws of motion solved so that the trajectories of the particles can be followed, can be used to study non-equilibrium conditions and dynamic behaviour. It is not quite true to say that the results of simulations depend only on the potential used. The calculation must be done using a fairly small number of particles (perhaps a few hundred) which are confined within a box. Some boundary conditions must be applied so that the edges of the box are not surfaces (in which case the simulation would be of a small droplet and not of the bulk fluid) and the choice of these might affect the results obtained. Further, it can hardly be expected that correlations on a length scale larger than the box size would be observed in a simulation. Nonetheless this technique is very useful for understanding liquids and interpreting the results of experiments.

Chapter four

Neutron transport theory

Our consideration of neutron scattering has so far considered only single scattering events and related the cross-section for these to correlation functions describing the structure and dynamics of the scatterer. In a real experiment the situation is more complicated than this as scattered neutrons may be absorbed and they may be scattered again. Both absorption and scattering can occur in the sample or in its surroundings such as its container. Neutrons will also be detected that have been scattered not by the sample but solely by the container or other obstructions in the beam. We must consider the effects of all these interactions if we are to properly determine the cross-section for a single scattering event.

Neutron transport theory, which is outlined below following the treatment of Sears [4/1], enables us to calculate the effects of multiple scattering and also attenuation due to absorption, although it is unnecessarily complicated for the latter. We shall consider a single sample, without container, for this; this provides a reasonable estimate of the multiple scattering observed experimentally. The effect of attenuation is easily obtained by extension to more complicated situations.

4.1 A neutron transport equation

Let us denote by μ_s and μ_a the scattering and absorption cross-sections per unit volume and by μ their sum. We now define the function $f_j(\boldsymbol{r},\boldsymbol{k},t)$ to be the density of neutrons of momentum $\hbar\boldsymbol{k}$ at point $\boldsymbol{r}$ in the sample at time t that have already been scattered j times. As we choose to use samples that are fairly small compared to the mean free path of the neutrons we expect rapid convergence of

$$f(\boldsymbol{r},\boldsymbol{k},t)=\sum_{j=0}^{\infty} f_j(\boldsymbol{r},\boldsymbol{k},t) \tag{4/1}$$

The current density of neutrons that have been scattered j times is

$$\frac{\hbar\boldsymbol{k}}{m} f_j(\boldsymbol{r},\boldsymbol{k},t) \tag{4/2}$$

Using this we can write a continuity equation. If V is an arbitrary volume bounded by a surface S then the rate of increase of neutrons of momentum $\hbar\boldsymbol{k}_j$, that have been scattered j times, inside V is equal to the rate at which such neutrons enter V through S less the rate at which they are scattered or absorbed in V plus the rate at which neutrons that have been scattered $j-1$ times are scattered from momentum $\hbar\boldsymbol{k}_{j-1}$ to $\hbar\boldsymbol{k}_j$:

$$\frac{\partial}{\partial t}\int_V d\boldsymbol{r}\, f_j(\boldsymbol{r},\boldsymbol{k}_j,t)=\int_S dS\,(-\hat{\boldsymbol{e}}).\frac{\hbar\boldsymbol{k}_j}{m} f_j(\boldsymbol{r},\boldsymbol{k}_j,t)-\int d\boldsymbol{r}\, f_j(\boldsymbol{r},\boldsymbol{k}_j,t)\mu(\boldsymbol{k}_j)V$$
$$+\int_V\int d\boldsymbol{r}\, d\boldsymbol{k}_{j-1}\, f_{j-1}(\boldsymbol{r},\boldsymbol{k}_{j-1},t)p_s(\boldsymbol{k}_{j-1},\boldsymbol{k}_j) \tag{4/3}$$

where $\hat{\boldsymbol{e}}$ is a unit vector in the direction of the outward normal at a point $\boldsymbol{r}$ on S and $p_s(\boldsymbol{k}_{j-1},\boldsymbol{k}_j)$ is the transition probability for scattering

neutrons between momenta $\hbar\boldsymbol{k}_{j-1}$ and $\hbar\boldsymbol{k}_j$. The surface integral can be rewritten using Gauss's theorem:

$$\frac{\partial}{\partial t}\int_V d\boldsymbol{r}\, f_j(\boldsymbol{r},\boldsymbol{k}_j,t) = -\int_V d\boldsymbol{r}\,\nabla.\frac{\hbar\boldsymbol{k}_j}{m} f_j(\boldsymbol{r},\boldsymbol{k}_j,t) - \int d\boldsymbol{r}\, f_j(\boldsymbol{r},\boldsymbol{k}_j,t)\mu(\boldsymbol{k}_j)\frac{\hbar\boldsymbol{k}_j}{m} + \int_V\int d\boldsymbol{r}\, d\boldsymbol{k}_{j-1}\, f_{j-1}(\boldsymbol{r},\boldsymbol{k}_{j-1},t)p_s(\boldsymbol{k}_{j-1},\boldsymbol{k}_j)$$

(4/4)

or

$$\int_V d\boldsymbol{r}\left(\frac{\partial}{\partial t}+\frac{\hbar}{m}\boldsymbol{k}_j.\nabla+\frac{\hbar k_j}{m}\mu(\boldsymbol{k}_j)\right) f_j(\boldsymbol{r},\boldsymbol{k}_j,t) = \int_V\int d\boldsymbol{r}\, d\boldsymbol{k}_{j-1}\, f_{j-1}(\boldsymbol{r},\boldsymbol{k}_{j-1},t)p_s(\boldsymbol{k}_{j-1},\boldsymbol{k}_j)$$

(4/5)

But this is true for an arbitrary volume so it must be the case that

$$\left(\frac{m}{\hbar k_j}\frac{\partial}{\partial t}+\widehat{\boldsymbol{k}}_j.\nabla+\mu(\boldsymbol{k}_j)\right) f_j(\boldsymbol{r},\boldsymbol{k}_j,t) = \int d\boldsymbol{k}_{j-1}\, f_{j-1}(\boldsymbol{r},\boldsymbol{k}_{j-1},t)\Gamma(\boldsymbol{k}_{j-1},\boldsymbol{k}_j)$$

(4/6)

where $\widehat{\boldsymbol{k}}_j$ is a unit vector in the direction of $\boldsymbol{k}$ and $\Gamma(\boldsymbol{k}_{j-1},\boldsymbol{k}_j)$ is the transference function defined by

$$\Gamma(\boldsymbol{k}_{j-1},\boldsymbol{k}_j) = \frac{\hbar\rho\sigma_s}{4\pi m k_j} S(\boldsymbol{k}_{j-1}-\boldsymbol{k}_j,\omega_{j-1}-\omega_j)$$

(4/7)

(4/6) is our neutron transport equation.

4.2 Steady state solution

Removing the time dependence from the neutron transport equation leaves us with

$$\left(\hat{\boldsymbol{k}}_j.\nabla + \mu(\boldsymbol{k}_j)\right) f_j(\boldsymbol{r},\boldsymbol{k}_j) = \int d\boldsymbol{k}_{j-1}\, f_{j-1}(\boldsymbol{r},\boldsymbol{k}_{j-1}) \Gamma(\boldsymbol{k}_{j-1},\boldsymbol{k}_j)$$

(4/8)

The samples we are interested are convex at all points so we need not consider neutrons re-entering the sample. If we define the function $L(\boldsymbol{r},\hat{\boldsymbol{k}})$ to be the distance from a point $\boldsymbol{r}$ in the sample to the surface in the direction of $-\hat{\boldsymbol{k}}$, that is the distance a neutron of wavevector $\boldsymbol{k}$ must travel to reach $\boldsymbol{r}$, we can write the boundary condition that only $j = 0$ neutrons enter the sample as

$$f_j\left(\boldsymbol{r} - L(\boldsymbol{r},\hat{\boldsymbol{k}})\hat{\boldsymbol{k}},\boldsymbol{k}\right) = 0 \text{ for } j > 1; \quad \boldsymbol{k} \text{ directed into the sample}$$

(4/9)

Further, if the sample is completely bathed in a uniform, collimated, monoenergetic beam of neutrons of momentum $\hbar\boldsymbol{k}_0$ we also require that

$$f_0\left(\boldsymbol{r} - L(\boldsymbol{r},\hat{\boldsymbol{k}})\hat{\boldsymbol{k}},\boldsymbol{k}\right) = \Phi\, \delta(\boldsymbol{k} - \boldsymbol{k}_0)$$

(4/10)

where Φ is a constant representing beam intensity.

It can be shown that a set of solutions to the transport equation with these boundary conditions is

$$f_0(\boldsymbol{r},\boldsymbol{k}) = \Phi\, \delta(\boldsymbol{k} - \boldsymbol{k}_0)\, e^{-\mu(\boldsymbol{k})L(\boldsymbol{r},\hat{\boldsymbol{k}})}$$

$$f_j(\boldsymbol{r},\boldsymbol{k}) = \int d\boldsymbol{k}'\, \Gamma(\boldsymbol{k}',\boldsymbol{k}) \int_0^{L(\boldsymbol{r},\hat{\boldsymbol{k}})} d\xi\, e^{\mu(\boldsymbol{k})\xi}\, f_{j-1}\left(\boldsymbol{r} - \xi\hat{\boldsymbol{k}},\boldsymbol{k}'\right)$$

(4/11)

4.3 Scattering cross-section

If $d^2\sigma$ is the number of neutrons per unit flux per unit time to emerge from the sample with momentum $\hbar\boldsymbol{k}$ we see that

$$d^2\sigma = \frac{m}{\Phi \hbar k_0} \int_{S(\hat{\boldsymbol{k}})} dS\, \hat{\boldsymbol{e}}.\boldsymbol{k}\, \frac{\hbar}{m}\, f(\boldsymbol{r},\boldsymbol{k}) d\boldsymbol{k}$$

(4/12)

where $S(\hat{\boldsymbol{k}})$ is that part of the surface which is visible from the direction of $\boldsymbol{k}$ (so $\hat{\boldsymbol{e}}.\hat{\boldsymbol{k}} > 0$). Now,

$$d\boldsymbol{k} = k^2\, dk\, d\Omega = mk\, d\Omega\, d\omega$$

(4/13)

where $d\Omega$ is an element of solid angle and $\hbar\omega$ is the neutron energy. This gives us

$$\frac{d^2\sigma}{d\Omega d\omega} = \frac{mk^2}{\Phi k_0} \int_{S(\hat{\boldsymbol{k}})} dS\, \hat{\boldsymbol{e}}.\hat{\boldsymbol{k}}\; f(\boldsymbol{r},\boldsymbol{k})$$

(4/14)

Using the general solution obtained in (4/11) this becomes

$$\frac{d^2\sigma}{d\Omega d\omega} = \frac{mk^2}{\Phi k_0} \int_{S(\hat{\boldsymbol{k}})} dS\, \hat{\boldsymbol{e}}.\hat{\boldsymbol{k}}\, (\Phi\, \delta(\boldsymbol{k}-\boldsymbol{k}_0)\, e^{-\mu(\boldsymbol{k})L(\boldsymbol{r},\hat{\boldsymbol{k}})} + \sum_{j=1}^{\infty} \int d\boldsymbol{k}'\, \Gamma(\boldsymbol{k}',\boldsymbol{k}) \int_0^{L(\boldsymbol{r},\hat{\boldsymbol{k}})} d\xi\, e^{\mu(\boldsymbol{k})\xi}\; f_{j-1}(\boldsymbol{r}-\xi\hat{\boldsymbol{k}},\boldsymbol{k}'))$$

(4/15)

4.4 The transmitted beam

The first term in (4/15) describes unscattered neutrons

$$\frac{d^2\sigma_0}{d\Omega d\omega} = \frac{mk^2}{k_0} \int_{S(\hat{\boldsymbol{k}})} dS\, \hat{\boldsymbol{e}}.\hat{\boldsymbol{k}}\; \delta(\boldsymbol{k}-\boldsymbol{k}_0)\, e^{-\mu(\boldsymbol{k})L(\boldsymbol{r},\hat{\boldsymbol{k}})}$$

(4/16)

$$= mk_0\, \delta(\boldsymbol{k}-\boldsymbol{k}_0) \int_{S(\hat{\boldsymbol{k}})} dS\, \hat{\boldsymbol{e}}.\hat{\boldsymbol{k}}\;\; e^{-\mu(\boldsymbol{k})L(\boldsymbol{r},\hat{\boldsymbol{k}})}$$

(4/17)

Putting

$$A(\boldsymbol{k}_0) = \int_{S(\hat{\boldsymbol{k}}_0)} dS\, \hat{\boldsymbol{e}}.\hat{\boldsymbol{k}}_0$$

(4/18)

which is the cross-sectional area of the sample perpendicular to the incident neutron beam, we can write

$$\frac{d^2\sigma_0}{d\Omega d\omega} = mk_0\, \delta(\boldsymbol{k} - \boldsymbol{k}_0)\, A(\boldsymbol{k}_0)\, H_0(\boldsymbol{k}_0)$$

(4/19)

where $H_0(\boldsymbol{k}_0)$ is the fraction of neutrons transmitted; that is, an attenuation factor, and is given by

$$H_0(\boldsymbol{k}_0) = \frac{1}{A(\boldsymbol{k}_0)} \int_{S(\hat{\boldsymbol{k}})} dS\, \hat{\boldsymbol{e}}.\hat{\boldsymbol{k}}\ \ e^{-\mu(\boldsymbol{k})L(\boldsymbol{r},\hat{\boldsymbol{k}})}$$

(4/20)

$$= \frac{1}{A(\boldsymbol{k}_0)} \int_{S(\hat{\boldsymbol{k}})} dS\, \hat{\boldsymbol{e}}.\hat{\boldsymbol{k}}\ \ G_0(\boldsymbol{r}, \boldsymbol{k}_0)$$

(4/21)

where, for convenience, we have defined

$$G_0(\boldsymbol{r}, \boldsymbol{k}_0) = e^{-\mu(\boldsymbol{k})L(\boldsymbol{r},\hat{\boldsymbol{k}})}$$

(4/22)

4.5 Singly scattered neutrons

Single scattering is given by the $j = 1$ term in (4/15). Substituting for $\Gamma(\boldsymbol{k}', \boldsymbol{k})$ and $f_0(\boldsymbol{r}, \boldsymbol{k})$ from (4/7) and (4/11) and using the function G_0 we get

$$\frac{d^2\sigma_1}{d\Omega d\omega} = \frac{\hbar k \rho \sigma_s}{4\pi k_0} S(\boldsymbol{Q}, \omega) \int_{S(\hat{\boldsymbol{k}})} dS\, \hat{\boldsymbol{e}}.\hat{\boldsymbol{k}}\ \ \int_0^{L(\boldsymbol{r},\hat{\boldsymbol{k}})} d\xi\, e^{\mu(\boldsymbol{k})\xi}\ G_0\left(\boldsymbol{r} - \xi\hat{\boldsymbol{k}}, \boldsymbol{k}_0\right)$$

(4/23)

$$= \frac{\hbar k \rho \sigma_s}{4\pi k_0} S(\boldsymbol{Q}, \omega) \int_{S(\hat{\boldsymbol{k}})} dS\, \hat{\boldsymbol{e}}.\hat{\boldsymbol{k}}\, G_1(\boldsymbol{r}, \boldsymbol{k}_0, \boldsymbol{k})$$

(4/24)

$$= \hbar \frac{k}{k_0} \frac{\sigma_s}{4\pi} \rho V\, H_1(\boldsymbol{k}_0, \boldsymbol{k}) S(\boldsymbol{Q}, \omega)$$

(4/25)

where we have defined

$$G_1(\boldsymbol{r}, \boldsymbol{k}_0, \boldsymbol{k}) = \int_0^{L(\boldsymbol{r}, \hat{\boldsymbol{k}})} d\xi\, e^{\mu(\boldsymbol{k})\xi}\, G_0\left(\boldsymbol{r} - \xi\hat{\boldsymbol{k}}, \boldsymbol{k}_0\right)$$

(4/26)

and the function

$$H_1(\boldsymbol{k}_0, \boldsymbol{k}) = \frac{1}{V} \int_{S(\hat{\boldsymbol{k}})} dS\, \hat{\boldsymbol{e}}.\hat{\boldsymbol{k}}\, G_1(\boldsymbol{r}, \boldsymbol{k}_0, \boldsymbol{k})$$

(4/27)

describes the attenuation of scattered neutrons due to absorption and secondary scattering (so $H_1 \leq 1$).

4.6 Secondary scattering

In a similar way it can be shown that the cross-section for doubly scattered neutrons is

$$\frac{d^2\sigma_2}{d\Omega d\omega} = \hbar \frac{k}{k_0} \frac{\sigma_s}{4\pi} \rho V\, \frac{\rho \sigma_s}{4\pi} \int d\Omega_1 \int \hbar\, d\omega_1\, S(\boldsymbol{k}_1 - \boldsymbol{k}, \omega_1 - \omega) S(\boldsymbol{k_0} - \boldsymbol{k_1}, \omega_0 - \omega_1)\, H_2(\boldsymbol{k}_0, \boldsymbol{k}_1, \boldsymbol{k})$$

(4/28)

where $d\Omega_1$ is an element of solid angle in the direction of $\boldsymbol{k}_1$ (the wavevector of the neutron after it has been scattered once) and

$$G_2(\boldsymbol{r}, \boldsymbol{k}_0, \boldsymbol{k}_1, \boldsymbol{k}) = \int_0^{L(\boldsymbol{r},\hat{\boldsymbol{k}})} d\xi \; e^{\mu(\boldsymbol{k})\xi} \; G_1\left(\boldsymbol{r} - \xi\hat{\boldsymbol{k}}, \boldsymbol{k}_0, \boldsymbol{k}_1\right)$$

(4/29)

$$H_2(\boldsymbol{k}_0, \boldsymbol{k}_1, \boldsymbol{k}) = \frac{1}{V}\int_{S(\hat{\boldsymbol{k}})} dS \; \hat{\boldsymbol{e}}.\hat{\boldsymbol{k}} \; G_2(\boldsymbol{r}, \boldsymbol{k}_0, \boldsymbol{k}_1, \boldsymbol{k})$$

(4/30)

so that the ratio of secondary to primary scattering is

$$\delta(\boldsymbol{k}_0, \boldsymbol{k}) = \frac{\rho\sigma_s/4\pi}{H_1(\boldsymbol{k}_0, \boldsymbol{k})S(\boldsymbol{Q}, \omega)} \int d\Omega_1 \int \hbar \, d\omega_1 \; S(\boldsymbol{k}_1 - \boldsymbol{k}, \omega_1 - \omega) S(\boldsymbol{k}_0 - \boldsymbol{k}_1, \omega_0 - \omega_1) \; H_2(\boldsymbol{k}_0, \boldsymbol{k}_1, \boldsymbol{k})$$

(4/31)

4.7 Reduction to a cylindrical geometry

The geometry of the experiments presented in this thesis is that of a cylindrical sample with its axis perpendicular to the direction of the incident neutron beam and to the direction of the detected scattered neutrons.

Let us define a Cartesian coordinate system with its origin at the centre of the base of the cylinder, its z-axis parallel to the cylinder, and its x-axis lying along the path of the incident neutrons. If ϕ is the angle which the scattered momentum, $\hbar\boldsymbol{k}$, of the neutrons makes with the x-axis then

$$\hat{\boldsymbol{k}} = (\hat{k}_x, \hat{k}_y, 0) = (\cos\phi, \sin\phi, 0)$$

(4/32)

All the surface integrals to be evaluated are of the form

$$\int_{S(\hat{\boldsymbol{k}})} dS \; \hat{\boldsymbol{e}}.\hat{\boldsymbol{k}} \; F(\boldsymbol{r})$$

(4/33)

where $F(\boldsymbol{r})$ is some function of position. The surface $S(\boldsymbol{k})$ is that half of the curved surface within $\pm\pi/2$ of the direction of $\boldsymbol{k}$. This means that, for a cylinder of radius a and height h, the integral becomes

$$\int_{S(\hat{\boldsymbol{k}})} dS\, \hat{\boldsymbol{e}}.\hat{\boldsymbol{k}}\, F(\boldsymbol{r}) = a\int_0^h dz \int_{\phi-\pi/2}^{\phi+\pi/2} d\theta(\cos\phi\cos\theta + \sin\phi\sin\theta)\, F(\boldsymbol{r})$$

(4/34)

where $r = (a\cos\theta, a\sin\theta, z)$.

We also require the function $L(r,\hat{\boldsymbol{k}})$. In the most general case $r=(x,y,z)$ is anywhere inside the sample and $\hat{\boldsymbol{k}} = (\hat{k}_x, \hat{k}_y, \hat{k}_z)$ is in any direction. From the definition of $L(\boldsymbol{r},\hat{\boldsymbol{k}})$ we know that the point

$$(x - L\hat{k}_x, y - L\hat{k}_y, z - L\hat{k}_z)$$

(4/35)

lies on the surface of the cylinder. For this to be the case either

$$\left(x - L\hat{k}_x\right)^2 + (y - L\hat{k}_y)^2 = a^2 \text{ and } 0 \le z - L\hat{k}_z \le h$$

(4/36)

or

$$z - L\hat{k}_z = 0$$

(4/37)

or

$$z - L\hat{k}_z = h$$

(4/38)

Solving these gives the result

$$L(\boldsymbol{r},\hat{\boldsymbol{k}}) = \frac{x\hat{k}_x + y\hat{k}_y + \sqrt{a^2(\hat{k}_x^2+\hat{k}_y^2) - (x\hat{k}_y - y\hat{k}_x)^2}}{\hat{k}_x^2+\hat{k}_y^2}$$

provided this satisfies $0 \le z - L(\boldsymbol{r},\hat{\boldsymbol{k}})\hat{k}_z \le h$ otherwise

$$= \frac{z}{\hat{k}_z} \qquad \text{if } \hat{k}_z > 0$$

$$= \frac{z-h}{\hat{k}_z} \qquad \text{if } \hat{k}_z < 0$$

(4/39)

4.8 Attenuation of single scattering for a cylindrical sample

Using the results of the last section and substituting for G_1 in (4/27) gives

$$H_1(\boldsymbol{k}_0,\boldsymbol{k}) = \frac{1}{\pi a h}\int_0^h dz \int_{\phi-\pi/2}^{\phi+\pi/2} d\theta(\cos\phi\cos\theta + \sin\phi\sin\theta) \int_0^{L(\boldsymbol{r},\hat{\boldsymbol{k}})} d\xi\, e^{\mu(\boldsymbol{k})\xi}\, e^{-\mu(\boldsymbol{k}_0)L(\boldsymbol{r}-\xi\hat{\boldsymbol{k}},\hat{\boldsymbol{k}}_0)}$$

(4/40)

but as $\boldsymbol{k}$ and $\boldsymbol{k}_0$ lie in the x-y plane neither the integrand nor the limits of integration depend on z so we can integrate with respect to z to get

$$H_1(\boldsymbol{k}_0,\boldsymbol{k}) = \frac{1}{\pi a}\int_{\phi-\pi/2}^{\phi+\pi/2} d\theta\cos(\theta-\phi) \int_0^{L(\boldsymbol{r},\hat{\boldsymbol{k}})} d\xi\, e^{\mu(\boldsymbol{k})\xi}\, e^{-\mu(\boldsymbol{k}_0)L(\boldsymbol{r}-\xi\hat{\boldsymbol{k}},\hat{\boldsymbol{k}}_0)}$$

(4/41)

where $r = (a\cos\theta, a\sin\theta, 0)$. With a little elementary geometry it can be shown that $a\,d\theta\cos(\theta-\phi)\,d\xi$ is an element of area. This means the integral may also be written as an integral over the cross-sectional surface as

$$H_1(\boldsymbol{k}_0,\boldsymbol{k}) = \frac{1}{\pi a^2}\int_0^{2\pi} d\theta \int_0^a r\,dr\; e^{-\mu(\boldsymbol{k}_0)L(\boldsymbol{r},\hat{\boldsymbol{k}}_0)}\, e^{-\mu(\boldsymbol{k})L(\boldsymbol{r},-\hat{\boldsymbol{k}})}$$

(4/42)

4.9 Multiple scattering in the elastic approximation

If we are interested only in elastic scattering we may approximate $S(\boldsymbol{Q},\omega)$ by $S(\boldsymbol{Q})\delta(\omega)$. The ratio of secondary scattering to the average primary scattering is then

$$\delta(\boldsymbol{k}_0,\boldsymbol{k}) = \frac{\hbar\rho\sigma_s}{4\pi H_1(\boldsymbol{k}_0,\boldsymbol{k})}\int d\Omega_1\; S(\boldsymbol{k}_1-\boldsymbol{k})S(\boldsymbol{k}_0-\boldsymbol{k}_1)\,H_2(\boldsymbol{k}_0,\boldsymbol{k}_1,\boldsymbol{k})$$

(4/43)

where $\boldsymbol{k}_0^2=\boldsymbol{k}_1^2=\boldsymbol{k}^2$. It is easily shown that for a cylinder

$$H_2(\boldsymbol{k}_0,\boldsymbol{k}_1,\boldsymbol{k}) = \frac{1}{\pi a h}\int_0^h dz\int_{\theta_1}^{\theta_2}d\theta\int_{\phi-\frac{\pi}{2}}^{\phi+\frac{\pi}{2}}\int_0^{L(\boldsymbol{r},\hat{\boldsymbol{k}})}d\xi\int_0^{L(\boldsymbol{r}-\xi\boldsymbol{k},\hat{\boldsymbol{k}}_1)}d\eta\;(\hat{k}_x\cos\theta+\hat{k}_y\sin\theta)\;e^{-\mu(\xi+\eta+L(\boldsymbol{r}-\xi\hat{\boldsymbol{k}}-\eta\hat{\boldsymbol{k}}_1,\hat{\boldsymbol{k}}_0)}$$

(4/44)

where $r = (a\cos\theta, a\sin\theta, 0)$ and θ_1 and θ_2 are given by the two values of $\tan^{-1}k_y/k_x$.

Chapter five

Instruments and equipment used in neutron scattering experiments

In order to perform a neutron scattering experiment it is first necessary to have a source of neutrons. Neutron sources can be divided into two types: reactors such as DIDO at AERE Harwell (although this is no longer generally available to university experimenters) and the High Flux Reactor (HFR) at the Institut Laue-Langevin (ILL) in Grenoble, France; and pulsed sources such as ISIS at the Rutherford Appleton Laboratory (RAL). These different types of source require quite different instruments.

5.1 The Institut Max von Laue - Paul Langevin

The ILL was founded in 1967 by France and West Germany with the aim of constructing and running a high flux neutron beam reactor together with a large number of instruments. The reactor reached its nominal operating power of 57MW in December 1971. In January 1973 the United Kingdom became an equal partner, contributing its share of the past investment. The ILL has been run by these three countries as an international institute ever since, with Spain joining as a junior member in 1986.

The thermal neutron flux, in equilibrium with the moderator at a temperature of 300K, has a Maxwellian distribution peaking at 1.2Å; it is directed towards the instruments down beam lines and guide tubes. The

wavelength spectrum is modified for some of the beam and guide tubes by the inclusion of a hot source (graphite at 2000K) and a cold source (liquid deuterium at 25K) which enhance the neutron intensity in the wavelength ranges 0.4Å $< \lambda <$ 0.8Å and $\lambda <$ 4Å respectively. The flux varies from one beam line to another but is typically of the order of 10^{10} neutrons $cm^{-2}s^{-1}$ [5/1].

5.2 ISIS

ISIS started life as the Spallation Neutron Source (SNS) which was built, partly out of bits of the old Nimrod and Nina linear accelerators, in existing buildings owned by the Rutherford Appleton Laboratory. The first neutrons appeared in December 1985; the following year user experiments began. With the official opening, the source was named after Isis, the principal and most powerful goddess of ancient Egypt, wife and sister of Osiris and daughter of Heaven and Earth, who had the power to bring the dead back to life. International collaboration is now being actively sought.

H^- ions are created and injected into a 70 MeV linear accelerator. They are then stripped of their electrons and the resulting protons are accelerated in a synchrotron. Pulses of protons are taken from the synchrotron ring and send down a beam line to collide with a depleted uranium (i.e. depleted in fissile uranium-235) target and so produce a large number of neutrons. ISIS is designed to give, at full performance, which it has not yet reached, a 200μA (time averaged) 800MeV proton beam operating at 50Hz. The main differences from a reactor source are that the neutrons are produced in pulses and that, because of the high energy

of the colliding protons, a not insignificant number of high energy neutrons are produced. The spectral and pulse shape characteristics of the neutrons are varied by the different moderators provided - two of liquid water at 316K, one of liquid methane at 95K (to give relatively sharp pulse widths), and one of liquid hydrogen at 25K (to enhance the production of low energy neutrons) [5/2,5/3].

5.3 The liquids diffractometer D4B

D4B is located on beam tube H8 (hot neutrons) at ILL. Designed for liquids or amorphous solids, it has medium resolution and allows the structure factor to be determined between approximately 0.25Å^{-1} and 20Å^{-1}. It works in the way conventional for diffraction experiments - a monochromatic beam of neutrons is incident on the sample and the scattered intensity is measured as a function of scattering angle. Because it is designed for amorphous samples, for which orientation is unimportant, scattering is measured in one (horizontal) plane only.

The incident neutron beam is monochromated by Bragg reflection from a copper crystal and is continuously variable according to the angle of the crystal. As $\lambda/2$ filters (to cut out neutrons of half the required wavelength which are also Bragg scattered) are available for wavelengths of 0.5Å and 0.7Å one of these two values is usually used.

There are two detector arms which move around the sample as the experiment proceeds so scanning the whole angular range of interest, although for some of the experiments presented in this thesis only one of the arms was in operation. Together they can cover scattering angles between 1.5° and 130°. Each arm is equipped with a 64 cell ^{3}He

multidetector with a gas pressure of 15 bars allowing a reasonable detection efficiency even at low wavelengths.

The sample is enclosed in a fixed vacuum vessel inside which can be placed a vanadium heater making it possible to reach temperatures of up to 1300K.

The data is collected by a PDP-11 computer, where it may also be manipulated to a limited extent, before being transferred to the central computer of the ILL (a DEC 1091-S, now being replaced by a VAX 8650). There it is written onto magnetic tape to be brought to Oxford. The main analysis of the data from this and the other instruments has been done on the main computer of the Oxford University Computing Service (for most of this work an ICL 2988).

5.4 The liquids and amorphous materials diffractometer LAD

LAD, at ISIS, is designed for essentially the same tasks as D4B, but being at a pulsed source it has to achieve them in a different way. All the neutrons, coming from the methane moderator, are allowed to strike the sample and the scattered neutrons are counted at a number of fixed detectors (at scattering angles of 5°, 10°, 20°, 35°, 58°, 90°, and 150°) as a function of time. As the neutrons all start from the moderator at the same time, the time they take to reach the detector is a measure of their energy (assuming elastic scattering). Thus, at one angle, the elastic scattering is determined for a whole range of incident neutron energies and so momentum transfers. The ranges of momentum transfer measured by the different detectors overlap, covering

a range from approximately 0.3Å^{-1} to 100Å^{-1} which extends far higher than is necessary for molten salts.

The data is collected on a dedicated VAX 11/730 computer and is then transferred to a central VAX 8600. On both of these it may be manipulated quite extensively. It can then be transferred directly to Oxford via the Joint Academic Network (JANET).

5.5 The time of flight spectrometers IN4 and IN6

These spectrometers, both at the ILL, are designed to look at inelastic scattering over a large range of energy and momentum transfers. A monochromatic beam is pulsed onto the sample and the scattered neutron intensity measured at a number of detectors as a function of time; the time of flight determines the energy and momentum transfer of the scattering process.

For IN4, sited on a thermal neutron beam line, the incident wavelength may be anything in the range 0.84Å $< \lambda <$ 4.0Å, obtained by Bragg reflection from two crystals of copper or graphite, one of which is rotating (the other may also rotate, but did not do so for the experiment described later) so as to produce a pulsed beam. IN6 is located on a cold neutron guide and is restricted to wavelengths of 4.1Å, 4.6Å, 5.1Å, or 5.9Å which are produced by a graphite monochromator. The beam is then pulsed by a rotating chopper. IN4 has detectors at 2¼° spacing from a scattering angle of 2¼° to one of 76½° as well as two at the negative angles -2¼° and -4½° making a total of 36. IN6 has 19 detectors at angles of 11.9°, 16.9°, 20.7°, 25.9°, 30.8°,

35.5°, 40.5°, 45.8°, 50.6°, 55.7°, 61.2°, 66.8°, 71.8°, 77.8°, 84.6°, 90.6°, 97.3°, 105°, and 111.6°.

The region of (Q,ω) space that may be looked at is determined by the incident neutron wavelength and by the instrument geometry and so varies both for and between IN4 and IN6. Examples are shown in figure 5.1. IN4 covers a much larger range than does IN6 but the energy resolution obtained is poorer.

As for D4B, data from both these instruments is collected by a dedicated PDP-11 computer and later transferred via a direct link to the central computer.

5.6 IRIS and HET

IRIS (for high resolution quasi-elastic and inelastic scattering) and HET (high energy transfer) are two inelastic scattering spectrometers at ISIS. They have not been used in this work and are only mentioned briefly for comparison with the reactor case. HET works in the same manner as IN4 and IN6 - pulses of monochromatic neutrons (produced by a rotating chopper) are incident on the sample; the scattered neutrons are counted as a function of time of flight. IRIS also works on a time of flight principle but here the whole neutron pulse, with the exception of some neutrons at the extremes of the wavelength range which are excluded, is incident on the sample and it is the scattered neutrons that are selected at a particular wavelength and counted as a function of time of flight.

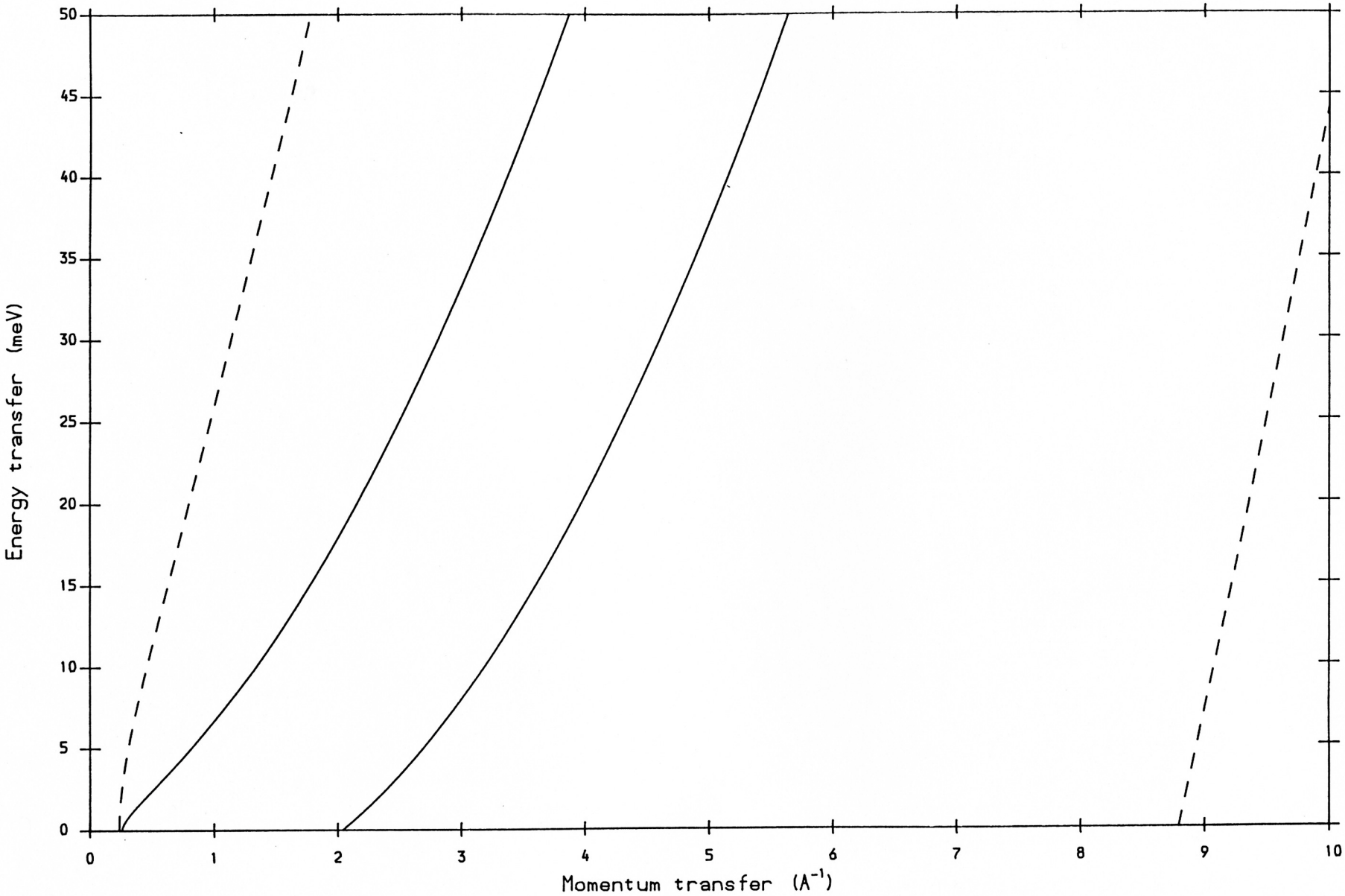


Figure 5.1 The regions of (Q-ω) space accessible using IN6 with 5.1A neutrons (between solid lines) and IN4 with 1.05A neutrons (between broken lines).

5.7 Furnaces

All the instruments described above are provided with furnaces that allow temperatures of up to 1000°C to be attained. The D4B furnace consists of a 0.125 mm vanadium foil heating element in the form of a cylinder of 23 mm internal diameter which is placed coaxially around the sample and through which is passed a high current (200 A or so). Two thermocouples are placed close to the sample, one of which is used by a temperature controller to maintain the temperature within 5°C, or closer, of its required value; the other is used as a check. So that the hot vanadium is not oxidised the sample area must be under vacuum (more so than is necessary to reduce air scattering to negligible proportions).

All the other furnaces used work on the same principle although, of course, the design details vary.

5.8 Sample containers

Two types of containers have been used in these experiments: vanadium, and silica. Vanadium is an almost totally incoherent scatterer which is an advantage for elastic scattering as it avoids problems with Bragg peaks. Being a metal it is easily fashioned into containers of known dimensions which are consistent from one container to the next. The incoherence of vanadium scattering is not such an advantage for inelastic scattering but it is convenient to use the same containers for elastic and inelastic scattering experiments; the same samples can then be used for both without unsealing the containers.

The vanadium containers used are made in the Clarendon workshop from solid vanadium rod and are the same as those described by McGreevy [5/4]. They have an internal diameter of 0.35" (8.89 mm) and an external diameter of 0.38" (9.652 mm) and may be filled to a height of approximately 1½" (35 mm) before being sealed under vacuum by electron beam welding. The containers used for CsCl were manufactured at Reading University and are of a slightly different size, having internal and external diameters of 9.0 mm and 9.8 mm respectively, but otherwise they are similar.

Vanadium is not suitable for all samples as it reacts with salts containing metal ions that are less electropositive than it such as zinc or silver. For this reason a different material had to be used for the experiments involving molten silver iodide. Silica was chosen: this has an amorphous structure so no Bragg peaks are observed and it can be heated to high temperatures. The containers were made out of tubing, chosen for its consistent thickness, sealed off at both ends in a hot flame. For the IN6 experiment vitreous silica tubing of internal and external diameters of 5 mm and 7 mm was used to make containers that could be filled to a height of approximately 10cm; these cracked on cooling and so new containers of quartz of the same dimensions were used for the experiment on D4B.

Chapter six

The corrections applied to neutron scattering data

The scattering measured in an experiment comes not only from the sample; there are also contributions from the sample container and its surroundings, both of which also attenuate the scattered neutron beam. It is necessary to determine these contributions and then make a few other corrections so that the scattering cross-section of the sample may be obtained. These processes are similar for the different instruments used so they will be first described in detail for IN6 data (and IN4 data which is essentially the same) and then the different corrections used for D4B and LAD will be discussed.

6.1 Corrections for IN6 and IN4 data

We measure spectra for the sample in its container, the empty container, and the background (mainly from the furnace). We may write these intensities as:

$$I_S^E = A_{S,SC} I_S + A_{C,SC} I_C + I_H$$

$$I_C^E = A_{C,C} I_C + I_H$$

$$I_H^E = I_H$$

(6/1)

where the I^E represent the experimentally observed intensities, the I denote the 'true' intensities, and the $A_{S,SC}$ etc. are attenuation coefficients ($A_{S,SC}$ being the attenuation of sample scattering by the

sample and container, for example). In doing so we assume that sample, container, and background scattering are completely separate; that is, for example, that no neutrons are scattered in the sample and then later in the container. This is clearly an approximation but one that is generally considered valid. From this set of equations we get

$$I_S = \frac{1}{A_{S,SC}}\left(I_S^E - \frac{A_{C,SC}}{A_{C,C}} I_C^E - \left(1 - \frac{A_{C,SC}}{A_{C,C}}\right) I_H^E\right)$$

(6/2)

The attenuation coefficients, which are functions of angle and energy, are calculated by a method due to Poncet [6/1] in which equation (4/42) is extended to an integration over the cross-sectional area of the sample or container of the exponential terms describing the attenuation before and after scattering. The method of Gaussian quadrature is used to evaluate these integrals. In doing this we are effectively assuming that the attenuation of multiply scattered neutrons is the same as that of singly scattered neutrons (or that multiple scattering is negligible).

Multiple scattering of neutrons is considered in chapter seven where it is demonstrated that it is not important for the samples we have used. Ignoring it, the corrected intensity we have obtained, as a function of scattering angle, θ, and time of flight, τ, is

$$I_S(\theta,\tau) = \frac{d^2\sigma}{d\Omega d\tau} \Delta\tau \, F(\theta) \, \varepsilon(\tau)$$

(6/3)

where $\Delta\tau$ is the time channel width and $F(\theta)$ is a function that depends on the detector arrangement and efficiency. $\varepsilon(\tau)$ is the energy dependent

part of the detector efficiency: for IN6 this is approximated by the expression

$$\varepsilon(\tau) = e^{A\tau}(1 - e^{-B\tau})$$

With $A = 2.4923 \times 10^{-5}$

$B = 1.43604 \times 10^{-3}$

(6/4)

for τ in units of μsm^{-1}. The factor $F(\theta)$ is removed by measuring the scattering from vanadium. As this is an almost totally incoherent scatterer the intensity integrated over the elastic peak (after correction for variation with energy of detector efficiency) can be written as

$$I_V(\theta) = N_V \overline{b^2}_V e^{-2W_V(\theta)} F(\theta)$$

(6/5)

where N_V is the total number of vanadium atoms in the beam and W_V is the Debye-Waller factor which has a value of W_V =0.007. This means the cross-section can be obtained:

$$\frac{1}{N_S}\frac{d^2\sigma}{d\Omega d\tau} = \overline{b^2}_V e^{-2W_V(\theta)} \frac{N_V I_S(\theta,\tau)}{N_S \Delta\tau}$$

(6/6)

As

$$\frac{d^2\sigma}{d\Omega d\omega} = \frac{m}{\hbar\tau^3}\frac{d^2\sigma}{d\Omega d\tau}$$

(6/7)

we can get the double differential cross-section

$$\frac{1}{N_S}\frac{d^2\sigma}{d\Omega d\omega} = \frac{m}{\hbar\tau^3}\overline{b^2}_V e^{-2W_V(\theta)} \frac{N_V I_S(\theta,\tau)}{N_S \Delta\tau}$$

(6/8)

This is related to the dynamic structure factor by the factor k'/k (see equation (2/27)) so that the observed cross-section

$$\frac{d^2\sigma}{d\Omega d\omega} \propto (\omega' - \omega)^2 \, S(\theta, \tau)$$

(6/9)

and is proportional to $S(\theta,\tau)$ at low energy transfers while at high energy transfers it is proportional to $C^L(\theta,\tau)$. One can obtain information about dynamics directly from this or from the functions $S(\theta,\tau)$ and $C^L(\theta,\tau)$ which may be calculated.

6.2 D4B corrections

In this case we include attenuation by the heater so the set of expressions (6/1) becomes

$$I_S^E = A_{S,SCH} I_S + A_{C,SCH} I_C + A_{H,SCH} I_H$$
$$I_C^E = A_{C,CH} I_C + A_{H,CH} I_H$$
$$I_H^E = A_{H,H} I_H$$

(6/10)

so that

$$I_S = \frac{1}{A_{S,SCH}} \left(I_S^E - \frac{A_{C.SCH}}{A_{C,CH}} I_C^E - \frac{1}{A_{H,H}} \left(A_{H.SCH} - \frac{A_{C,SCH}}{A_{C,CH}} \right) I_H^E \right)$$

(6/11)

The coefficients, which depend on angle only as scattering is elastic, are evaluated in a similar way to those used for IN6 experiments [6/2].

There is an added complication at low angles - there is an increased count rate due to the incident beam diverging and hitting the detectors.

If we consider this to be a constant contribution then at low angles we can write

$$I_S^E = A_{S,SCH} I_S + A_{C,SCH} I_C + A_{H,SCH} I_H + I_B$$

$$I_C^E = A_{C,CH} I_C + A_{H,CH} I_H + I_B$$

$$I_H^E = A_{H,H} I_H + I_B$$

(6/12)

I_B is obtained by assuming that the vanadium spectrum is a straight line so that it may be extrapolated from its value at high angles to low angles; the difference between this and the observed scattering gives $I_B(\theta)$. This vanadium spectrum may be a single spectrum or the sum of all the vanadium spectra (e.g. container spectrum added to furnace spectrum if the container is made of vanadium). It would be possible to write this low angle part as a sample independent part and a part that is attenuated by the sample; these parts could be determined by using two vanadium spectra, for example the vanadium container and furnace: this has been found to make no significant difference.

The intensity now obtained is given by

$$I_S(\theta) = \left(\frac{d\sigma}{d\Omega} + N_S \overline{b^2}_S \Delta_S - N_S \sum_\alpha c_\alpha \overline{b^2}_\alpha P_\alpha(\theta) \right) F(\theta)$$

(6/13)

where Δ_S is the multiple scattering fraction and $P_\alpha(\theta)$ is the Placzek or inelasticity correction which accounts for the deviation from the static approximation; both of these will be discussed in more detail in later chapters. $F(\theta)$ depends on the detector geometry. As vanadium scattering is almost totally incoherent we can write it as

$$I_V(\theta) = N_V \overline{b^2}_V (1 - P_V(\theta) + \Delta_V)\, F(\theta)$$

(6/14)

so the sample cross-section is given by

$$\frac{1}{N_S}\frac{d\sigma}{d\Omega} = \frac{N_V}{N_S}\overline{b^2}_V (1 - P_V(\theta) + \Delta_V)\frac{I_S(\theta)}{I_V(\theta)} + \sum_\alpha c_\alpha \overline{b^2}_\alpha P_\alpha(\theta) - \Delta_S \overline{b^2}_S$$

(6/15)

$I_V(\theta)$ is fitted with a straight line or curve (ignoring the small Bragg peaks) as it is structureless. The multiple scattering is obtained from a table (see chapter seven), the inelasticity corrections from the formula derived in chapter eight.

6.3 LAD corrections

The same procedure as for IN6 experiments is used to correct for container and background scattering. Obtaining the cross-section from the scattering intensity one follows essentially the same path as one does for D4B. The multiple scattering in this case is a function of wavelength, and so momentum transfer, whereas it is constant for D4B. The inelasticity corrections are also different (see chapter eight) and require calculation of the wavelength derivatives of the incident flux which are obtained by fitting a smooth curve to the incident spectrum as measured by a monitor. Finally one obtains a set of cross-sections over different Q ranges, one for each detector. These must be combined to give $S(Q)$ over the entire experimental range; this problem is discussed in chapter eleven.

Chapter seven

Multiple scattering of neutrons

There are two ways of calculating the effects of multiple scattering of neutrons. One is by evaluation of the integrals resulting from the solution of the neutron transport equation in chapter four. The other uses the Monte Carlo method to effectively simulate a neutron scattering experiment.

7.1 Elastic scattering

The amount of secondary scattering, relative to primary scattering, can be calculated using (4/42) and (4/43). It is found, and this is confirmed by experiment and by the Monte Carlo work, that this is, to a very good approximation, isotropic and independent of the form of $S(Q)$. This means that these expressions can be simplified to give

$$\delta(\boldsymbol{k}_0,\boldsymbol{k}) = \frac{\mu_s}{\mu}\,\frac{\hbar\mu}{4\pi^2 ahH_1(\boldsymbol{k}_0,\boldsymbol{k})}$$

$$\int d\Omega_1 \int_0^h dz \int_{\theta_1}^{\theta_2} d\theta \int_0^{L(\boldsymbol{r},\hat{\boldsymbol{k}})} d\xi \int_0^{L(\boldsymbol{r}-\xi\boldsymbol{k},\hat{\boldsymbol{k}}_1)} d\eta\,(\hat{k}_x\cos\theta + \hat{k}_y\sin\theta)\; e^{-\mu(\xi+\eta+L(\boldsymbol{r}-\xi\hat{\boldsymbol{k}}-\eta\hat{\boldsymbol{k}}_1,\hat{\boldsymbol{k}}_0)} \tag{7/1}$$

$$= \frac{\mu_S}{\mu}\,\delta_0(\boldsymbol{k}_0,\boldsymbol{k}) \tag{7/2}$$

with an arbitrary choice of the direction of $\boldsymbol{k}$. It can be seen that the δ_0 depends only on the values of μa and μh. This integral may be

calculated numerically, for example by Gaussian quadrature, as has been done by Sears [7/1] for a number of values of μa and μh. Blech and Averbach [7/2] also did such a calculation but introduced a simplification in their treatment which resulted in values somewhat lower than those of Sears. I have done this calculation too, partly to check these results, and partly because δ was required for values of μa and μh outside the ranges for which results had previously been calculated. These results are given in tables 3 and 4; they are in good agreement with those of Sears. It is not easy to calculate the many dimensioned integrals that describe higher orders of scattering; instead it is assumed that the ratio of n^{th} to $n-1^{\text{th}}$ order scattering is also δ so that the multiple scattering is

$$\Delta = \delta + \delta^2 + \delta^3 + \cdots$$

$$= \frac{\delta}{1-\delta} \qquad (7/3)$$

Provided that the multiple scattering is small, this must be at least approximately correct.

7.2 Monte Carlo calculation

The principle of the Monte Carlo method is to follow a succession of neutrons through the sample generating scattering events with the appropriate probability and counting them as they arrive at the detectors according to whether they have been singly or multiply scattered. For a general discussion of this sort of problem see [7/3].

Table 3. Double scattering from a cylinder

		mu x r									
		0.01	0.02	0.03	0.04	0.05	0.06	0.07	0.08	0.09	0.10
	0.01	.006487	.009337	.011273	.012918	.014430	.015859	.017241	.018581	.019895	.021186
	0.02	.008345	.012907	.016082	.018514	.020524	.022292	.023926	.025457	.026922	.028331
	0.03	.009329	.015082	.019257	.022544	.025254	.027545	.029559	.031376	.033058	.034654
	0.04	.009943	.016577	.021559	.025549	.028879	.031740	.034224	.036422	.038413	.040252
	0.05	.010373	.017678	.023324	.027910	.031777	.035119	.038059	.040671	.043019	.045144
	0.06	.010691	.018518	.024711	.029822	.034166	.037941	.041278	.044260	.046962	.049408
	0.07	.010934	.019177	.025847	.031417	.036171	.040345	.044043	.047361	.050365	.053123
	0.08	.011116	.019722	.026792	.032746	.037899	.042418	.046448	.050076	.053369	.056390
	0.09	.011255	.020179	.027582	.033893	.039391	.044228	.048567	.052477	.056039	.059313
	0.10	.011368	.020564	.028253	.034889	.040679	.045835	.050437	.054624	.058429	.061942
	0.20	.011892	.022505	.031990	.040463	.048189	.055289	.061854	.067909	.073546	.078822
	0.30	.012074	.023185	.033435	.042913	.051616	.059708	.067286	.074384	.081113	.087489
	0.40	.012159	.023527	.034185	.044156	.053530	.062303	.070528	.078301	.085700	.092738
	0.50	.012212	.023736	.034623	.044935	.054666	.063908	.072661	.080924	.088794	.096321
mu x h	0.60	.012251	.023882	.034928	.045446	.055454	.064975	.074072	.082753	.091019	.098917
	0.70	.012281	.023981	.035145	.045809	.056017	.065765	.075087	.084027	.092632	.100856
	0.80	.012302	.024048	.035314	.046093	.056430	.066362	.075874	.084999	.093807	.102304
	0.90	.012317	.024102	.035447	.046312	.056759	.066814	.076491	.085777	.094741	.103409
	1.00	.012327	.024151	.035551	.046490	.057028	.067175	.076975	.086405	.095510	.104310
	1.10	.012335	.024192	.035629	.046641	.057247	.067481	.077367	.086914	.096144	.105069
	1.50	.012360	.024308	.035841	.047024	.057851	.068308	.078448	.088266	.097807	.107090
	2.00	.012377	.024374	.036011	.047279	.058237	.068894	.079219	.089230	.098986	.108488
	2.50	.012389	.024412	.036113	.047454	.058477	.069206	.079670	.089829	.099717	.109351
	3.00	.012397	.024440	.036167	.047576	.058653	.069435	.079944	.090196	.100203	.109947
	3.50	.012403	.024459	.036206	.047653	.058785	.069611	.080165	.090449	.100516	.110352
	4.00	.012406	.024473	.036239	.047703	.058882	.069749	.080341	.090662	.100755	.110632
	4.50	.012407	.024485	.036264	.047742	.058946	.069858	.080481	.090836	.100961	.110860
	5.00	.012408	.024496	.036284	.047776	.058993	.069937	.080596	.090979	.101134	.111060
	5.50	.012408	.024504	.036300	.047805	.059033	.069995	.080688	.091098	.101276	.111230
	6.00	.012408	.024511	.036313	.047829	.059067	.070039	.080757	.091197	.101398	.111372

Table 3 (continued). Double scattering from a cylinder

		mu x r									
		0.01	0.02	0.03	0.04	0.05	0.06	0.07	0.08	0.09	0.10
	0.01	.033095	.043586	.052916	.061206	.068579	.075115	.080892	.085960	.090375	.094183
	0.02	.040759	.051434	.060845	.069175	.076576	.083136	.088933	.094018	.098447	.102267
	0.03	.047940	.058893	.068451	.076873	.084324	.090909	.096719	.101816	.106256	.110087
	0.04	.054675	.065997	.075742	.084278	.091809	.098452	.104297	.109411	.113857	.117689
	0.05	.060954	.072772	.082746	.091420	.099042	.105748	.111643	.116795	.121266	.125111
	0.06	.066823	.079238	.089480	.098312	.106037	.112818	.118765	.123956	.128460	.132329
	0.07	.072317	.085375	.095949	.104964	.112809	.119670	.125676	.130911	.135446	.139341
	0.08	.077459	.091206	.102179	.111391	.119365	.126320	.132390	.137672	.142242	.146163
	0.09	.082239	.096769	.108144	.117602	.125724	.132770	.138916	.144248	.148854	.152805
	0.10	.086693	.102066	.113864	.123611	.131879	.139040	.145255	.150646	.155293	.159269
	0.20	.117933	.142873	.160358	.173532	.184040	.192754	.200072	.206258	.211468	.215822
	0.30	.136256	.168609	.191895	.209443	.222988	.233758	.242520	.249721	.255697	.260650
	0.40	.148418	.186553	.214497	.235766	.252421	.265540	.276055	.284528	.291431	.297018
	0.50	.157093	.199841	.231583	.256009	.275210	.290529	.302839	.312728	.320654	.326996
mu x h	0.60	.163537	.209974	.244958	.272066	.293539	.310721	.324570	.335831	.344802	.352021
	0.70	.168471	.218031	.255744	.285089	.308544	.327402	.342656	.355011	.365012	.373027
	0.80	.172455	.224527	.264490	.295932	.321048	.341365	.357906	.371311	.382163	.390858
	0.90	.175705	.229846	.271819	.305022	.331650	.353281	.370910	.385297	.396940	.406304
	1.00	.178384	.234262	.277981	.312670	.340749	.363497	.382173	.397374	.409779	.419758
	1.10	.180656	.238019	.283237	.319304	.348588	.372448	.391949	.407965	.420982	.431554
	1.50	.186937	.248734	.298149	.338389	.371366	.398528	.421002	.439505	.454643	.466945
	2.00	.191190	.256604	.309310	.352657	.388582	.418537	.443435	.464097	.481102	.495099
	2.50	.193856	.261302	.316311	.361656	.399553	.431189	.457758	.479907	.498258	.513366
	3.00	.195621	.264440	.321005	.367831	.407015	.439981	.467610	.490779	.510092	.526007
	3.50	.196881	.266759	.324252	.372269	.412458	.446293	.474840	.498748	.518674	.535210
	4.00	.197855	.268509	.326753	.375534	.416567	.451104	.480250	.504794	.525284	.542202
	4.50	.198618	.269856	.328748	.378040	.419733	.454868	.484514	.509479	.530410	.547760
	5.00	.199243	.270933	.330355	.380100	.422187	.457854	.487945	.513274	.534500	.552165
	5.50	.199762	.271836	.331666	.381821	.424230	.460265	.490735	.516389	.537887	.555763
	6.00	.200190	.272595	.332758	.383263	.425964	.462225	.493044	.518980	.540714	.558794

Table 4. Double scattering from a cylinder

		r/h									
		0.05	0.10	0.15	0.20	0.25	0.30	0.35	0.40	0.45	0.50
	0.05	0.0570	0.0547	0.0524	0.0501	0.0482	0.0464	0.0448	0.0433	0.0419	0.0407
	0.10	0.1084	0.1042	0.1002	0.0962	0.0927	0.0895	0.0865	0.0837	0.0812	0.0788
	0.15	0.1550	0.1495	0.1441	0.1388	0.1339	0.1295	0.1253	0.1215	0.1179	0.1146
	0.20	0.1974	0.1908	0.1844	0.1780	0.1721	0.1666	0.1615	0.1568	0.1523	0.1482
	0.25	0.2360	0.2285	0.2214	0.2142	0.2075	0.2012	0.1953	0.1897	0.1845	0.1796
	0.30	0.2713	0.2632	0.2554	0.2476	0.2402	0.2333	0.2267	0.2205	0.2147	0.2092
	0.35	0.3036	0.2950	0.2868	0.2785	0.2706	0.2631	0.2560	0.2492	0.2429	0.2368
	0.40	0.3331	0.3242	0.3156	0.3070	0.2987	0.2908	0.2832	0.2760	0.2692	0.2627
	0.45	0.3602	0.3510	0.3422	0.3333	0.3247	0.3164	0.3085	0.3009	0.2938	0.2869
	0.50	0.3851	0.3757	0.3667	0.3576	0.3489	0.3403	0.3321	0.3242	0.3168	0.3096
	0.55	0.4080	0.3985	0.3894	0.3801	0.3712	0.3624	0.3540	0.3459	0.3382	0.3308
	0.60	0.4290	0.4194	0.4102	0.4009	0.3919	0.3830	0.3744	0.3662	0.3583	0.3506
	0.65	0.4483	0.4387	0.4294	0.4201	0.4110	0.4021	0.3934	0.3850	0.3769	0.3691
	0.70	0.4660	0.4564	0.4472	0.4379	0.4287	0.4197	0.4110	0.4025	0.3943	0.3864
	0.75	0.4822	0.4726	0.4635	0.4542	0.4451	0.4361	0.4273	0.4188	0.4105	0.4026
	0.80	0.4971	0.4876	0.4784	0.4693	0.4602	0.4512	0.4424	0.4338	0.4256	0.4176
	0.85	0.5107	0.5013	0.4922	0.4831	0.4741	0.4651	0.4564	0.4478	0.4396	0.4315
mu x r	0.90	0.5232	0.5138	0.5048	0.4958	0.4869	0.4780	0.4693	0.4608	0.4526	0.4445
	0.95	0.5346	0.5253	0.5164	0.5075	0.4987	0.4899	0.4812	0.4728	0.4646	0.4566
	1.00	0.5449	0.5357	0.5270	0.5182	0.5095	0.5008	0.4923	0.4839	0.4758	0.4678
	1.50	0.6075	0.5997	0.5922	0.5850	0.5777	0.5704	0.5631	0.5560	0.5490	0.5420
	2.00	0.6268	0.6204	0.6142	0.6084	0.6025	0.5965	0.5906	0.5849	0.5792	0.5734
	2.50	0.6296	0.6243	0.6192	0.6144	0.6096	0.6047	0.5999	0.5952	0.5906	0.5859
	3.00	0.6274	0.6230	0.6187	0.6147	0.6106	0.6066	0.6026	0.5987	0.5949	0.5909
	3.50	0.6247	0.6209	0.6171	0.6137	0.6102	0.6068	0.6034	0.6001	0.5968	0.5934
	4.00	0.6224	0.6192	0.6159	0.6129	0.6098	0.6068	0.6039	0.6010	0.5981	0.5952
	4.50	0.6210	0.6182	0.6153	0.6126	0.6098	0.6072	0.6046	0.6020	0.5995	0.5969
	5.00	0.6203	0.6178	0.6152	0.6128	0.6103	0.6079	0.6056	0.6033	0.6010	0.5987
	5.50	0.6202	0.6180	0.6157	0.6135	0.6112	0.6090	0.6069	0.6048	0.6027	0.6006
	6.00	0.6205	0.6187	0.6166	0.6145	0.6125	0.6104	0.6085	0.6065	0.6046	0.6027
	6.50	0.6212	0.6196	0.6177	0.6158	0.6139	0.6121	0.6103	0.6085	0.6067	0.6049
	7.00	0.6222	0.6208	0.6192	0.6174	0.6156	0.6139	0.6122	0.6106	0.6089	0.6072
	7.50	0.6234	0.6222	0.6208	0.6192	0.6175	0.6159	0.6144	0.6128	0.6112	0.6096
	8.00	0.6247	0.6238	0.6225	0.6211	0.6195	0.6180	0.6166	0.6151	0.6136	0.6121
	8.50	0.6262	0.6255	0.6244	0.6231	0.6217	0.6203	0.6189	0.6175	0.6161	0.6147
	9.00	0.6277	0.6273	0.6264	0.6252	0.6239	0.6226	0.6213	0.6200	0.6187	0.6173

Table 4 (continued). Double scattering from a cylinder

		r/h									
		0.05	0.10	0.15	0.20	0.25	0.30	0.35	0.40	0.45	0.50
	0.05	0.0395	0.0384	0.0374	0.0364	0.0355	0.0347	0.0339	0.0331	0.0324	0.0318
	0.10	0.0766	0.0745	0.0726	0.0708	0.0691	0.0675	0.0660	0.0645	0.0632	0.0619
	0.15	0.1115	0.1086	0.1058	0.1032	0.1008	0.0985	0.0964	0.0943	0.0924	0.0905
	0.20	0.1443	0.1406	0.1371	0.1339	0.1308	0.1279	0.1252	0.1225	0.1201	0.1177
	0.25	0.1751	0.1708	0.1666	0.1628	0.1591	0.1557	0.1524	0.1493	0.1463	0.1435
	0.30	0.2040	0.1991	0.1944	0.1900	0.1858	0.1819	0.1782	0.1746	0.1712	0.1680
	0.35	0.2311	0.2257	0.2206	0.2157	0.2111	0.2067	0.2026	0.1986	0.1948	0.1912
	0.40	0.2566	0.2508	0.2452	0.2399	0.2349	0.2301	0.2256	0.2213	0.2171	0.2132
	0.45	0.2805	0.2743	0.2683	0.2627	0.2573	0.2522	0.2474	0.2427	0.2383	0.2341
	0.50	0.3028	0.2963	0.2900	0.2841	0.2784	0.2731	0.2679	0.2630	0.2583	0.2538
	0.55	0.3237	0.3169	0.3104	0.3042	0.2983	0.2927	0.2873	0.2821	0.2771	0.2724
	0.60	0.3433	0.3363	0.3296	0.3231	0.3170	0.3111	0.3055	0.3002	0.2950	0.2901
	0.65	0.3617	0.3545	0.3475	0.3409	0.3346	0.3285	0.3228	0.3172	0.3118	0.3067
	0.70	0.3788	0.3715	0.3644	0.3576	0.3511	0.3449	0.3390	0.3332	0.3277	0.3225
	0.75	0.3949	0.3874	0.3802	0.3733	0.3667	0.3603	0.3543	0.3484	0.3427	0.3373
	0.80	0.4098	0.4023	0.3949	0.3879	0.3812	0.3748	0.3686	0.3626	0.3569	0.3514
	0.85	0.4237	0.4161	0.4087	0.4017	0.3949	0.3884	0.3821	0.3760	0.3702	0.3646
mu x r	0.90	0.4367	0.4291	0.4216	0.4145	0.4077	0.4011	0.3948	0.3886	0.3827	0.3770
	0.95	0.4487	0.4411	0.4337	0.4265	0.4197	0.4131	0.4067	0.4005	0.3945	0.3887
	1.00	0.4599	0.4523	0.4449	0.4377	0.4309	0.4242	0.4178	0.4116	0.4055	0.3997
	1.50	0.5350	0.5281	0.5213	0.5147	0.5083	0.5021	0.4960	0.4900	0.4841	0.4785
	2.00	0.5676	0.5618	0.5561	0.5505	0.5451	0.5397	0.5344	0.5292	0.5240	0.5190
	2.50	0.5811	0.5763	0.5716	0.5669	0.5624	0.5579	0.5534	0.5489	0.5445	0.5402
	3.00	0.5869	0.5830	0.5790	0.5751	0.5713	0.5675	0.5637	0.5599	0.5561	0.5524
	3.50	0.5900	0.5867	0.5833	0.5800	0.5767	0.5734	0.5702	0.5669	0.5637	0.5604
	4.00	0.5923	0.5893	0.5864	0.5835	0.5807	0.5778	0.5750	0.5721	0.5693	0.5665
	4.50	0.5943	0.5917	0.5891	0.5866	0.5840	0.5815	0.5790	0.5765	0.5740	0.5715
	5.00	0.5963	0.5940	0.5917	0.5894	0.5872	0.5849	0.5827	0.5804	0.5781	0.5759
	5.50	0.5985	0.5964	0.5943	0.5922	0.5902	0.5882	0.5861	0.5840	0.5820	0.5799
	6.00	0.6007	0.5988	0.5969	0.5950	0.5932	0.5913	0.5894	0.5875	0.5857	0.5838
	6.50	0.6031	0.6013	0.5996	0.5978	0.5961	0.5944	0.5927	0.5909	0.5892	0.5875
	7.00	0.6055	0.6039	0.6022	0.6006	0.5990	0.5975	0.5959	0.5943	0.5926	0.5910
	7.50	0.6081	0.6065	0.6050	0.6035	0.6020	0.6005	0.5990	0.5975	0.5960	0.5945
	8.00	0.6107	0.6092	0.6078	0.6064	0.6050	0.6036	0.6022	0.6008	0.5993	0.5979
	8.50	0.6133	0.6120	0.6106	0.6093	0.6079	0.6066	0.6053	0.6040	0.6026	0.6013
	9.00	0.6160	0.6147	0.6134	0.6122	0.6109	0.6097	0.6084	0.6072	0.6059	0.6047

In order to do this we must be able to generate an event according to a probability distribution $P(y)$ (that is, $P(y)\,dy$ is the probability that y is in the interval dy about y). Computers are generally provided with software to generate pseudorandom numbers ξ, with uniform probability in the range 0 to 1; that is with a distribution $Q(\xi)$ where

$$Q(\xi) = \begin{cases} 1, & 0 \le \xi \le 1 \\ 0, & \xi < 0, 1 < \xi \end{cases}$$

(7/4)

It is necessary to make a transformation to obtain our required distribution. If we write

$$\xi = \xi(y)$$

(7/5)

Then

$$dy = \frac{d\xi}{dy}\,dy$$

(7/6)

and we require

$$P(y)\,dy = Q(\xi)\frac{d\xi}{dy}\,dy$$

(7/7)

Or

$$\xi = \int_{-\infty}^{y} \frac{P(y')}{Q(\xi)}\,dy'$$

(7/8)

$$= \int_{-\infty}^{y} P(y')\,dy', \qquad 0 \le \xi \le 1$$

(7/9)

Using this we can obtain a value y with the appropriate probability by generating a ξ with uniform probability and putting it in the equation.

The neutron may start at any position across the beam profile. We choose this at random (assuming a uniform profile). Next we must generate a scattering position. The distribution of mean free paths is given by

$$P(y)\,dy = e^{-\mu y}\mu\,dy \tag{7/10}$$

Putting this in (7/9) we get

$$\xi = 1 - e^{-\mu y} \tag{7/11}$$

or, as we are at liberty to put $\xi - 1$ for ξ,

$$y = -\frac{\ln \xi}{\mu} \tag{7/12}$$

enabling us to generate a path length. If this exceeds the distance through which the neutron might travel through the sample then it is unscattered; otherwise we have found a position at which it is scattered. In practice it is inefficient to allow neutrons to be unscattered (as usually the vast majority are). Instead, the weight with which we will finally count it is reduced according to the probability that it did not escape from the sample:

$$e^{-\mu d} \tag{7/13}$$

where d is the distance through the sample it must travel in order to escape. We force it to be scattered simply by choosing a path length y

such that $0 \leq y \leq d$ which we can generate using (7/11) provided we choose ξ so that $\xi \leq e^{-\mu d}$; this can be done by putting

$$\xi = e^{-\mu d} + \xi'(1 - e^{-\mu d})$$

(7/14)

where ξ' is uniformly distributed between 0 and 1. This gives

$$y = -\frac{1}{\mu} ln\left(e^{-\mu d} + \xi'(1 - e^{-\mu d})\right)$$

(7/15)

Having chosen a position at which the neutron is scattered we must choose a direction of motion for the scattered neutron. This is determined by two angles - the scattering angle and an azimuthal angle. The scattering angle must be chosen from the probability distribution

$$\frac{S(\theta)}{\int_0^\pi S(\theta')d\theta'} d\theta$$

(7/16)

So we can put

$$\xi(\theta) = \frac{\int_0^\theta S(\theta')d\theta'}{\int_0^\pi S(\theta')d\theta'}$$

(7/17)

We choose some function $S(\theta)$ for our calculation which is, in general, non-analytic. Thus we can obtain a set of values θ, $\xi(\theta)$ from the above expression. As $\xi(\theta)$ is a monotonic function this tabulation can just as easily be thought of as defining $\theta(\xi)$. This means that we can choose a random ξ, and obtain a scattering angle. The azimuthal angle is then chosen to be between 0 and 2π with uniform probability. Rather than see if this new direction causes the neutron, if it is not scattered again, to hit a detector it is more efficient to calculate, for each detector,

the probability of the neutron striking that detector and counting it with its weight multiplied by this probability. (It is also more efficient - in that it reduces the variance of our final estimate – to count together for positive and negative angles, that is ,for example, to calculate the probability for +10° and -10° and take the mean.)

We can now continue this whole process - choosing a position for the neutron to be scattered again, reducing its weight to allow for the probability of it escaping the sample, counting it at all the detectors with the appropriate weight, and choosing a new direction of motion. Eventually, when the weight is sufficiently small, we stop following it and start again with a new neutron.

Figure 7.1 shows the results obtained using an experimental result for CsCl as the $S(\theta)$.

The aim was to simulate a D4B experiment in our standard sample containers so a wavelength of λ=0.7Å, with μa=0.091, μh=0.61 were used. We see that the double, and total multiple, scattering are isotropic. The double scattering value of 0.0925 (with standard deviation 0.0010) compares with the value 0.0920 calculated numerically (interpolation from table 3).

7.3 Correction of D4B and LAD data for multiple scattering

To correct D4B data for multiple scattering the quantity δ_0 is obtained from interpolation from a table of values and thus δ and Δ calculated using (7/2) and (7/3). This is done for the vanadium and for the sample and the results are used in (6/15). If the vanadium is a cylinder the multiple scattering is estimated by considering it to be a

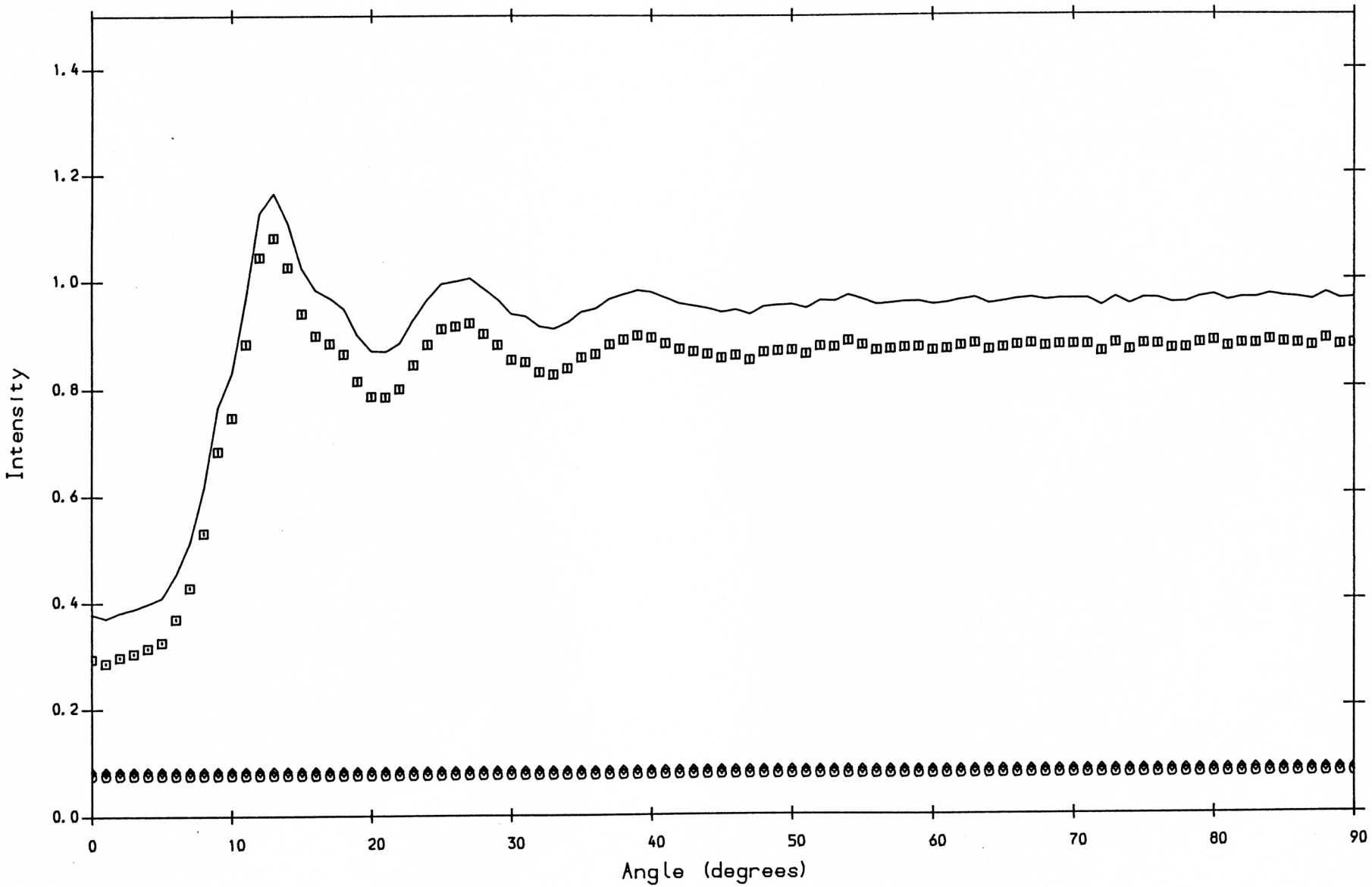


Figure 7.1 The single scattering (⊡), double scattering (⊙) and multiple scattering (◈) contributing to the total scattering (line) for caesium chloride on D4B. The standard deviation is shown by the error bars.

rod of the same diameter containing the same number of atoms. For D4B data it is not really important if the value for multiple scattering is not very accurate as any error is a flat level which will be subtracted from the spectrum in due course anyway.

The same procedure is followed for LAD data, but for this, because the absorption cross-section varies with neutron wavelength, δ (though not δ_0) and Δ are not constant; they are calculated at a few wavelength values and interpolated to the others. In this case any error in the calculation of the multiple scattering will cause a slowly varying systematic error in the determined cross-section. This would be most serious at short wavelengths where the absorption is lowest and so would show up as a slope in the structure factor at high Q.

7.4 Inelastic multiple scattering

The calculation of this numerically involves another integration compared to the elastic case and it must be done as a function of scattered neutron energy whereas the elastic result is obtained at one Q point only due to the isotropy of elastic multiple scattering. This makes the calculation rather time consuming.

Because of this only a Monte Carlo investigation was undertaken. This is similar to that done for elastic scattering, the difference being that a scattering event must produce a change in energy as well as a change in direction of the neutron. This is slightly more complicated than the elastic case as one must choose a Q and an ω) (the other degree of freedom is the azimuthal angle which may, again, be chosen from a uniform probability distribution) from a probability distribution

determined by $S(Q,\omega)$ - that is, they are not chosen from separate distributions. However the principle is the same and it has been described in detail by other authors [7/4,7/5] so it will not be repeated here.

To run the programme one must insert an $S(Q,\omega)$. If this is obtained from experiment it will not be the true function as it will already contain the multiple scattering. This means that any attempt to correct for multiple scattering should, in principle, use some sort of iteration. Further it requires that $S(Q,\omega)$ be known for all possible scattering processes, not just those measured by the experiment. Such a correction has not been attempted, rather the results here are used to demonstrate that multiple scattering does not have a significant effect for the experiments described in this thesis.

Figures 7.2 and 7.3 use as input the $S(Q,\omega)$ obtained from the IN4 experiment on CsCl and the IN6 experiment on AgI with the appropriate dimensions and scattering properties for these experiments. The results show that the multiple scattering is a relatively small contribution over most of the energy range and that it does not show any structure on the scale that is considered significant in the total scattering (that is, it is generally smaller than the statistical errors in the total cross-section). We conclude that we are justified in ignoring the effect of multiple scattering in our consideration of these two experiments.

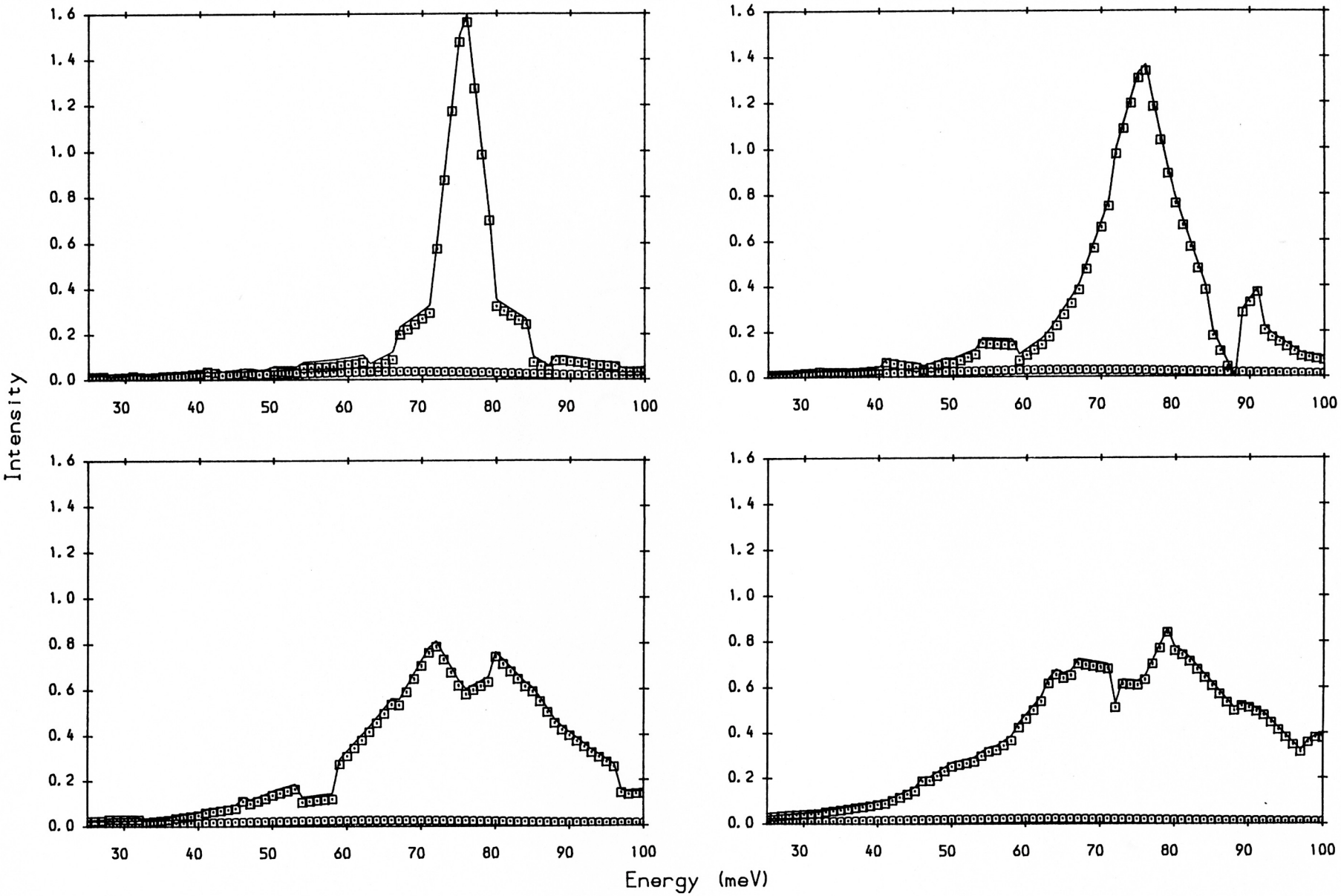


Figure 7.2 The single scattering (□) and multiple scattering (◇) contributing to the total scattering (line) for caesium chloride as measured at scattering angles of 10°, 30°, 50°, and 70° by IN4.

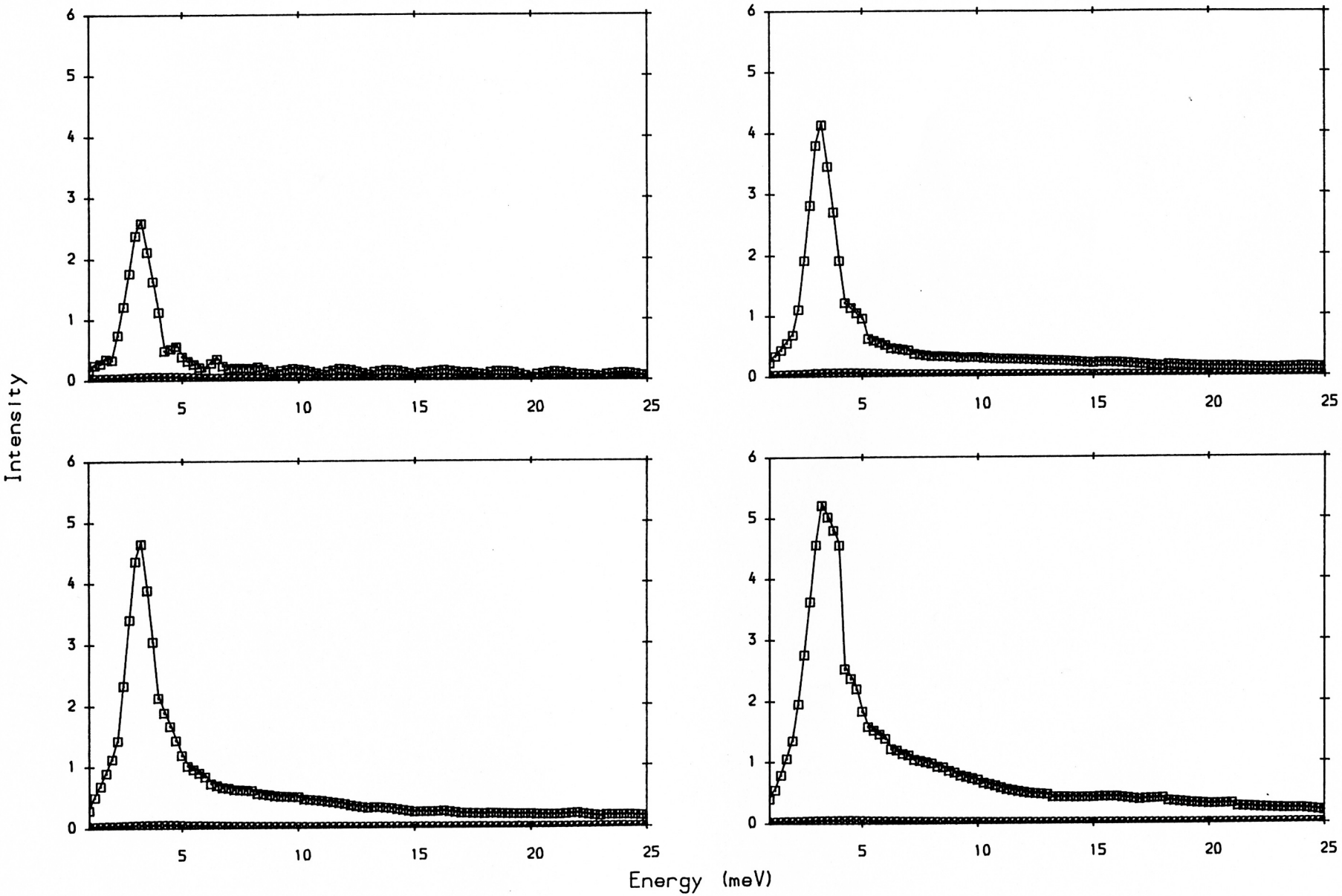


Figure 7.3 The single scattering (⊡) and multiple scattering (◈) contributing to the total scattering (line) for silver iodide as measured at scattering angles of 10°, 30°, 50°, and 70° on IN6.

Chapter eight

Inelasticity corrections - deviations from the static approximation

In a diffraction experiment we count all the neutrons that are scattered into a given solid angle, regardless of their energy, effectively integrating the inelastic differential scattering cross-section with respect to energy. In general this integration is not at constant Q but along a different path in $Q-\omega$ space determined by the experimental arrangement. Because of this the scattered intensity is not directly related to the static structure factor, $S_T(Q)$, as it is in the static approximation. By expanding the function describing the scattering as a power series it is possible to calculate the deviation from the static approximation. This is known as the Placzek correction [8/1] or the inelasticity correction (it would be zero for a system in which the scattering was perfectly elastic).

8.1 Time of flight diffractometry

We first consider the case of time of flight diffractometry as the steady state monochromatic beam case can then be derived from this. The treatment is similar to that of Powles [8/2] but includes higher order terms.

The number of neutrons detected in a frequency range $\Delta\omega$ is proportional to

$$\frac{k'}{k}\overline{b^2}\,S_T(Q,\omega)\Delta\omega$$

(8/1)

where, as in (2/31)

$$S_T(Q,\omega) = \left(\sum_\alpha\sum_\beta \bar{b}_\alpha\bar{b}_\beta S_{\alpha\beta}(Q,\omega) + \sum_\alpha(\overline{b_\alpha^2}-\bar{b}_\alpha^2)S_\alpha(Q,\omega)\right)/\overline{b^2}$$

(8/2)

so the number detected in a time channel of width Δt at time t is proportional to

$$\overline{b^2}\,S_T(Q,\omega)\frac{\partial\omega}{\partial t}\Big|_\lambda \Delta t$$

(8/3)

and the count rate per unit solid angle at time t at fixed angle θ is

$$C(\theta,t) = \overline{b^2}\int d\lambda\,\phi(\lambda)\varepsilon(k')\,\frac{k'}{k}S_T(Q,\omega)\frac{\partial\omega}{\partial t}\Big|_\lambda$$

(8/4)

where we have integrated, at constant time of flight, over the incident spectrum $\phi(\lambda)$ ($\phi(\lambda)\,\delta\lambda$ being the number of neutrons in a range $\delta\lambda$ about λ incident on the sample). $\varepsilon(k')$ is the detector efficiency; k', Q, and ω are appropriate to the neutron arriving at the detector at time t.

It is convenient to write this integral in terms of Q_e, the momentum transfer for perfectly elastic scattering at time t (of neutrons with wavelength λ_e). As a function of Q_e the count rate is

$$C(\theta,Q_e) = \overline{b^2}\int d\lambda\,\phi(\lambda)\varepsilon(k')\,\frac{k'}{k}S_T(Q,\omega)\frac{\partial\omega}{\partial t}\Big|_\lambda\frac{dt}{dQ_e}$$

(8/5)

If the incident and scattered path lengths are d_1 and d_2 the time of flight is

$$t = \frac{m}{\hbar}\left(\frac{d_1}{k} + \frac{d_2}{k'}\right) = \frac{m}{2\pi\hbar}(\lambda d_1 + \lambda' d_2)$$

(8/6)

k and k' are related via ω:

$$\hbar\omega = \frac{\hbar^2}{2m}(k^2 - k'^2)$$

(8/7)

$$k' = k\sqrt{1 - \frac{2m\omega}{\hbar k^2}}$$

(8/8)

which means that λ and ω are related to each other only via various constants so we may change the integration to one over ω:

$$C(\theta, Q_e) = \overline{b^2}\int d\omega\ \phi(\lambda)\varepsilon(k')\ \frac{k'}{k} S_T(Q,\omega)\frac{\partial\omega}{\partial t}\Big|_\lambda \frac{\partial\lambda}{\partial\omega}\Big|_t \frac{dt}{dQ_e}$$

(8/9)

$$= -\overline{b^2}\int d\omega\ \phi(\lambda)\varepsilon(k')\ \frac{k'}{k} S_T(Q,\omega)\frac{\partial\lambda}{\partial t}\Big|_\omega \frac{dt}{dQ_e}$$

(8/10)

Q is related to k, k', and k_e via the scattering angle θ:

$$Q^2 = k^2 + k'^2 - 2kk'\cos\theta$$

(8/11)

$$Q_e^2 = 2k_e^2\,(1 - \cos\theta)$$

(8/12)

$$Q_e = 2k_e\ \sin\theta/2$$

(8/13)

Using (8/6) for elastically scattered neutrons we also have

$$t = \frac{m(d_1 + d_2)}{\hbar k_e} = \frac{m\lambda_e(d_1 + d_2)}{2\pi\hbar}$$

(8/14)

(8/6) to (8/8) and (8/11) to (8/14) define the path over which integration of (8/9) is performed.

We wish to relate this integral to integrals at constant Q of $S_T(Q,\omega)$. To do this we expand $S_T(Q,\omega)$ as a Taylor series in Q^2 (as this is slightly easier than expanding as a function of Q):

$$S_T(Q,\omega) = S_T(Q_e,\omega) + \left.\frac{\partial S_T}{\partial(Q^2)}\right|_{Q=Q_e}(Q^2 - Q_e^2) + \left.\frac{\partial^2 S_T}{\partial(Q^2)^2}\right|_{Q=Q_e}\frac{(Q^2 - Q_e^2)^2}{2} + \cdots$$

(8/15)

If we now expand all the other terms in the integrand as power series in ω we can express the integral in terms of moments of $S_T(Q,\omega)$

Eliminating k' from (8/13) and (8/14) gives

$$Q_e t = \frac{2m}{\hbar}(d_1 + d_2)\sin\theta/2$$

(8/16)

From which it follows that

$$\frac{dt}{dQ_e} = -\frac{t}{Q_e}$$

(8/17)

Substituting (8/8) into (8/6) we get

$$t = \frac{m}{\hbar k}\left(d_1 + d_2\left(1 - \frac{2m\omega}{\hbar k^2}\right)^{-\frac{1}{2}}\right)$$

(8/18)

$$= \frac{m\lambda}{2\pi\hbar}\left(d_1 + d_2\left(1 - \frac{m\omega\lambda^2}{2\pi^2\hbar}\right)^{-\frac{1}{2}}\right)$$

(8/19)

So that

$$\left.\frac{\partial t}{\partial \lambda}\right|_{\omega} = \frac{m}{\hbar}\left(\frac{d_1}{2\pi} + \frac{4\pi^2 d_2}{(4\pi^2 - 2\lambda^2 m\omega/\hbar)^{3/2}}\right)$$

(8/20)

And

$$\left.\frac{\partial \lambda}{\partial t}\right|_{\omega} = \left(\left.\frac{\partial t}{\partial \lambda}\right|_{\omega}\right)^{-1}$$

(8/21)

$$= \frac{2\pi\hbar/m}{d_1 + 8\pi^3 d_2(4\pi^2 - m\omega\lambda^2/\hbar)^{-3/2}}$$

(8/22)

Multiplying (8/19) and (8/22) gives

$$\left.\frac{\partial \lambda}{\partial t}\right|_{\omega} t = \frac{\lambda(1 - \lambda^2 m\omega/2\pi^2\hbar)(d_1(1 - \lambda^2 m\omega/2\pi^2\hbar)^{1/2} + d_2)}{(1 - \lambda^2 m\omega/2\pi^2\hbar)^{3/2} d_1 + d_2}$$

(8/23)

$$= \lambda A$$

(8/24)

where we have introduced A ($A = 1$ when $\omega = 0$) for convenience. Using (8/24) and (8/17) in (8/10) gives

$$C(\theta, Q_e) = \overline{b^2}\int d\omega\ \phi(\lambda)\varepsilon(k')\frac{k'}{k}S_T(Q,\omega)\frac{\lambda A}{Q_e}$$

(8/25)

$$= \frac{\phi(\lambda_e)\varepsilon(k_e)\lambda_e}{Q_e}\overline{b^2}\int d\omega\ \frac{\phi(\lambda)}{\phi(\lambda_e)}\frac{\varepsilon(k')}{\varepsilon(k_e)}\frac{k'}{k}S_T(Q,\omega)\frac{\lambda}{\lambda_e}A$$

(8/26)

The form of the integral in (8/26) is useful as it is clear that the leading term in an expansion about $\omega = 0$ using the Taylor expansion of $S_T(Q,\omega)$ will be $\int S_T(Q_e,\omega)d\omega$ which contains the structural information we wish to find. We shall now drop the term outside the integral which is a constant for a given detector and time channel (and so will be accounted for by the vanadium calibration). The next step is to obtain series expansions of all the terms in the integrand. To do this we introduce the dimensionless quantity

$$x = \frac{m\omega}{\hbar k_e^2}$$

(8/27)

We shall expand to second order in x dropping all higher order terms.

From (8/8) we get

$$\frac{k'}{k} = \frac{\lambda}{\lambda'} = \left(1 - 2\frac{k_e^2}{k^2}x\right)^{1/2}$$

(8/28)

$$= 1 - \left(\frac{\lambda}{\lambda_e}\right)^2 x - \frac{1}{2}\left(\frac{\lambda}{\lambda_e}\right)^4 x^2 - \ldots$$

(8/29)

Similarly

$$\frac{k}{k'} = \frac{\lambda'}{\lambda} = 1 + \left(\frac{\lambda}{\lambda_e}\right)^2 x + \frac{3}{2}\left(\frac{\lambda}{\lambda_e}\right)^4 x^2 - \ldots$$

(8/30)

Eliminating t between (8/6) and (8/14) gives

$$\lambda d_1 + \lambda' d_2 = \lambda_e(d_1 + d_2)$$

(8/31)

So that

$$\frac{\lambda_e}{\lambda'} = \frac{k'}{k_e} = \frac{d_1\lambda/\lambda' + d_2}{d_1 + d_2}$$

(8/32)

$$= f\frac{\lambda}{\lambda'} + (1-f)$$

(8/33)

where we have introduced the fractional path length

$$f = \frac{d_1}{d_1 + d_2}$$

(8/34)

Substituting (8/29) in (8/33) gives

$$\frac{\lambda_e}{\lambda'} = \frac{k'}{k_e} = 1 - f\left(\left(\frac{\lambda}{\lambda_e}\right)^2 x + \frac{1}{2}\left(\frac{\lambda}{\lambda_e}\right)^4 x^2 + \cdots\right)$$

(8/35)

Similarly

$$\frac{\lambda}{\lambda_e} = \frac{k_e}{k} = \frac{1}{f}\left(1 - (1-f)\frac{\lambda'}{\lambda_e}\right)$$

(8/36)

$$= \frac{1}{f}\left(1 - (1-f)\left((1-f) + f\frac{\lambda}{\lambda'}\right)^{-1}\right)$$

(8/37)

$$= \frac{1}{f}\left(1 - \left(1 + \frac{f}{1-f}\frac{\lambda}{\lambda'}\right)^{-1}\right)$$

(8/38)

where we have used (8/33). (8/8) allows us to write this as

$$\frac{\lambda}{\lambda_e} = \frac{k_e}{k} = \frac{1}{f}\left(1 - \left(1 + \frac{f}{1-f}\left(1 - 2\left(\frac{\lambda}{\lambda_e}\right)^2 x\right)^{1/2}\right)^{-1}\right)$$

(8/39)

and so obtain a power series for λ/λ_e by expanding the right hand side as a Taylor series about $x = 0$ and then substituting it into itself until there are no terms in λ/λ_e up to second order in x:

$$\frac{\lambda}{\lambda_e} = 1 + (f-1)\left(\frac{\lambda}{\lambda_e}\right)^2 x + \tfrac{1}{2}(f-1)(2f+1)\left(\frac{\lambda}{\lambda_e}\right)^4 x^2 + \ldots$$

(8/40)

$$= 1 + (f-1)x + 3(f-1)\left(f - \tfrac{1}{2}\right)x^2 + \ldots$$

(8/41)

after sufficient substitution. This can now be used in (8/29), (8/30) and (8/35) to give

$$\frac{k'}{k} = \frac{\lambda}{\lambda'} = 1 - x + \tfrac{1}{2}(3-4f)x^2 + \cdots$$

(8/42)

$$\frac{k}{k'} = \frac{\lambda'}{\lambda} = 1 + x + \tfrac{1}{2}(4f-1)x^2 + \cdots$$

(8/43)

$$\frac{k'}{k_e} = \frac{\lambda_e}{\lambda'} = 1 - fx - \tfrac{1}{2}(4f^2 - 3f)x^2 + \cdots$$

(8/44)

The constant A defined by (8/23) and (8/24) can be expanded to give

$$A = 1 + 2(\lambda/\lambda_e)^2(1-f)x - 6(\lambda/\lambda_e)^4 f(1-f)x^2 + \cdots$$

(8/45)

$$= 1 - 2(1-f)x + 2(5f-2)(f-1)x^2 + \cdots$$

(8/46)

$\phi(\lambda)$ is expanded as a Taylor series about λ_e to give

$$\frac{\phi(\lambda)}{\phi(\lambda_e)} = 1 + \frac{\phi'(\lambda_e)}{\phi(\lambda_e)}\left(\frac{\lambda}{\lambda_e} - 1\right)\lambda_e + \frac{1}{2}\frac{\phi''(\lambda_e)}{\phi(\lambda_e)}\left(\frac{\lambda}{\lambda_e} - 1\right)^2 \lambda_e^2$$

(8/47)

$$= 1 + \lambda_e(f-1)\frac{\phi'(\lambda_e)}{\phi(\lambda_e)}x + \frac{\lambda_e(f-1)}{\phi(\lambda_e)}\left(3\left(f - \tfrac{1}{2}\right)\phi'(\lambda_e) + \tfrac{1}{2}\lambda_e(f-1)\phi''(\lambda_e)\right)x^2 + \cdots$$

(8/48)

$$= 1 + (f-1)\phi_1 x + \left(3(f-1)\left(f - \tfrac{1}{2}\right)\phi_1 + \tfrac{1}{2}(f-1)^2\phi_2\right)x^2 + \cdots$$

(8/49)

where

$$\phi_1 = \lambda_e \frac{\phi'(\lambda_e)}{\phi(\lambda_e)}$$

(8/50)

$$\phi_2 = \lambda_e^2 \frac{\phi''(\lambda_e)}{\phi(\lambda_e)}$$

(8/51)

and the primes indicate differentiation. Similarly we get

$$\frac{\varepsilon(k')}{\varepsilon(k_e)} = 1 - \varepsilon_1 f x + \frac{1}{2}(f^2\varepsilon_2 - f\varepsilon_1)x^2 + \cdots$$

(8/52)

where

$$\varepsilon_1 = k_e \frac{\varepsilon'(k_e)}{\varepsilon(k_e)}$$

(8/53)

$$\varepsilon_2 = k_e^2 \frac{\varepsilon''(k_e)}{\varepsilon(k_e)}$$

(8/54)

Finally, we require an expansion of $Q^2 - Q_e^2$. This is obtained by elimination of $\cos\theta$ between (8/11) and (8/12) giving

$$Q^2 = k^2 + k'^2 - 2kk'\left(1 - \frac{Q_e^2}{2k_e^2}\right)$$

(8/55)

$$= k_e^2\left(\frac{k^2}{k_e^2} + \frac{k'^2}{k_e^2} - 2\frac{k}{k_e}\frac{k'}{k_e}\right) + \frac{k}{k_e}\frac{k'}{k_e}Q_e^2$$

(8/56)

So

$$Q^2 - Q_e^2 = k_e^2\left(\frac{k}{k_e} - \frac{k'}{k_e}\right)^2 + \left(\frac{k}{k_e}\frac{k'}{k_e} - 1\right)Q_e^2$$

(8/57)

$$= k_e^2\left(\frac{k}{k'} - 1\right)^2\frac{k'^2}{k_e^2} + \left(\frac{k}{k'}\frac{k'^2}{k_e^2} - 1\right)Q_e^2$$

(8/58)

$$= Q_e^2(1-2f)x + \left(k_e^2 - Q_e^2(3f^2 - 3f + \tfrac{1}{2})\right)x^2 + \cdots$$

(8/59)

where we have used (8/43) and (8/44). Substituting into (8/15) gives

$$S_T(Q,\omega) = S_T(Q_e,\omega) + Q_e^2(1-2f){S_T}'x$$
$$+ \left(\left(k_e^2 - Q_e^2(3f^2 - 3f + \tfrac{1}{2})\right)S_T' + \tfrac{1}{2}Q_e^4(4f^2 - 4f + 1){S_T}''\right)x^2 + \cdots$$

(8/60)

We are now in a position to evaluate the integral in (8/26) by substitution of (8/49), (8/52), (8/42), (8/60), (8/41) and (8/46). The zeroth order term in x is simply

$$\int d\omega\, S_T(Q_e,\omega) = \sum_\alpha\sum_\beta \bar{b}_\alpha\bar{b}_\beta S_{\alpha\beta}(Q) + \sum_\alpha\left(\overline{b^2}_\alpha - \bar{b}_\alpha^2\right)c_\alpha$$

(8/61)

which is exactly what we wish to determine. The higher order terms are the corrections that must be made to the experimentally determined

cross-section to obtain this. For these we require the moments of $S_T(Q,\omega)$ which, as stated in chapter 3, are

$$S_1(Q) = \int d\omega\ \omega\ S_T(Q,\omega) = \sum_\alpha \frac{\overline{b^2}_\alpha c_\alpha \hbar Q^2}{2M_\alpha}$$

(8/62)

$$S_2(Q) = \int d\omega\ \omega^2\ S_T(Q,\omega) = \sum_\alpha \overline{b^2}_\alpha c_\alpha \left(\frac{k_B T Q^2}{M_\alpha} + \frac{\hbar^2 Q^4}{4M_\alpha^2} + \cdots\right)$$

(8/63)

The first order term to the correction is thus

$$P_1 = \int d\omega \left((\phi_1(f-1) - f\varepsilon_1 + 3f - 4)S_T(Q_e,\omega) + Q_e^2(1-2f)\frac{\partial S_T}{\partial(Q^2)}\right)x$$

(8/64)

$$= \frac{m}{\hbar k_e^2}\left(((f-1)\phi_1 - f\varepsilon_1 + 3f - 4)S_1(Q_e,\omega) + Q_e^2(1-2f)\frac{\partial}{\partial(Q^2)}S_1(Q_e,\omega)\right)$$

(8/65)

$$= \frac{m}{\hbar k_e^2}\ ((f-1)\phi_1 - f\varepsilon_1 + f - 3)\frac{\hbar Q_e^2}{2}\sum_\alpha \frac{\overline{b^2}_\alpha c_\alpha}{M_\alpha}$$

(8/66)

$$= 2\ ((f-1)\phi_1 - f\varepsilon_1 + f - 3)\ sin^2\ \theta/2 \sum_\alpha \overline{b^2}_\alpha c_\alpha \frac{m}{M_\alpha}$$

(8/67)

which agrees with the result of Powles [8/2]; the second order term is

$$P_2 = \left(\frac{k_B T}{2E} + \frac{k_B T}{E} sin^2\ \theta/2\ \left((8f-9)(f-1)\phi_1 - 3f(2f-3)\varepsilon_1 + 2f(1-f)\phi_1\varepsilon_1\right.\right.$$

$$\left.\left.+(1-f)^2\phi_2 + f^2\varepsilon_2 + 3(4f-5)(f-1)\right)\right)\sum_\alpha \overline{b^2}_\alpha c_\alpha \frac{m}{M_\alpha}$$

$$+2\ sin^2\ \theta/2\ \left(1 + sin^2\ \theta/2\ \left((4f-7)(f-1)\phi_1 + f(7-2f)\epsilon_1 + 2f(1-f)\phi_1\varepsilon_1\right.\right.$$
$$\left.\left.+\ (1-f)^2\phi_2 + f^2\varepsilon_2 + (2f^2 - 7f + 8)\right)\right)\sum_\alpha \overline{b^2}_\alpha c_\alpha \frac{m^2}{M_\alpha^2}$$

(8/68)

The correction, to second order, is the sum of (8/67) and (8/68) which should be subtracted from the result obtained by experiment.

8.2 The steady state case

For a steady state monochromatic incident beam the counts at a given angle are

$$C(\theta) = \overline{b^2} \int d\omega \, \varepsilon(k') \frac{k'}{k} S_T(Q,\omega)$$

(8/69)

$$= \varepsilon(k) \, \overline{b^2} \int d\omega \frac{\varepsilon(k')}{\varepsilon(k)} \frac{k'}{k} S_T(Q,\omega)$$

(8/70)

(8/7), (8/8), and (8/11) to (8/13), which define the integration path, are also applicable in this case. As the incident beam is monochromatic $\lambda_e = \lambda$; (8/6) and (8/14) express this constraint if we put $d_2 = 0$ (and so $f = 1$). Looking at (8/23) we see that this makes $A = 1$ and so reduces the integral in (8/26) to that in (8/70). We see, then, that putting $f = 1$ reduces the time of flight case to the steady state case and so the inelasticity correction for the latter is

$$P = \left(\frac{k_B T}{2E} + \left((3\varepsilon_1 + \varepsilon_2) \frac{k_B T}{E} - 2(\varepsilon_1 + 2) \right) sin^2 \, \theta/2 \right) \sum_\alpha \overline{b^2}_\alpha c_\alpha \frac{m}{M_\alpha}$$

$$+2 \, sin^2 \, \theta/2 \, \left(1 + sin^2 \, \theta/2 \, (5\varepsilon_1 + \varepsilon_2 + 3) \right) \sum_\alpha \overline{b^2}_\alpha c_\alpha \left(\frac{m}{M_\alpha} \right)^2$$

(8/71)

as has been calculated by Yarnell *et al* [8/3].

8.3 Validity of the inelasticity corrections

We have calculated the inelasticity corrections by expanding the integrand in (8/9) as a power series in ω. This is only exact if we take every term but we have kept only terms up to ω^2. It is not possible to do better than this because the higher moments of $S(Q,\omega)$ involve terms in the interaction potential and which are, therefore, related to the structure we are trying to determine. We need to know, then, whether the series has converged sufficiently by the ω^2 term to satisfactorily describe the deviation from the static approximation.

Physically what we are doing in including only the terms independent of structure is to consider free particle effects but to neglect any collective effects. The inelasticity corrections, that are calculated above, do not take any account of contributions to $S(Q,\omega)$ from collective dynamics.

A reasonable criterion for the inelasticity corrections to be good is that the experimental integration path differs only slightly from the constant Q path that gives the result of the static approximation. The correction terms would then be small and the series convergence good. Because the effects of collective modes are not sharp this slightly different path would be passing through essentially the same features as the constant Q path and so the collective dynamics should make little difference. If, though, the experimental integration path is quite different from the constant Q path it will pass through different dynamic features so the inelasticity correction terms calculated would be inadequate. An example of this is that if the integration path at a low elastic momentum transfer were to run, not at constant Q, but

approximately along the line representing the velocity of sound in the melt then the scattering observed would be greater than that obtained in the static approximation because there would be a significant contribution from inelastic scattering from the acoustic mode. This could not be corrected for without using a model of the dynamics.

To consider whether the corrections calculated are likely to be good for our experiments we must look at the integration paths appropriate to the instruments used. Figure 8.1 shows these for D4B using neutrons of wavelength 0.7Å (used for the experiments in this thesis) and 0.5Å. They are quite close to constant Q, getting less so as Q increases. This explains why the inelasticity corrections get larger at higher angles (and why experimental results, particularly for samples containing hydrogen, show a droop at high angles). Nonetheless it would appear that they would pass through much the same dynamic features as constant Q paths so the inelasticity corrections should be fairly good. The curves for 0.5Å are more nearly vertical showing that problems with deviations from the static approximation are reduced by using lower wavelength neutrons.

Figure 8.2 shows the curves for the different detectors of LAD. At high Q, particularly for the low angle detectors, the curves are nearly vertical so we conclude the inelasticity corrections are small and quite adequate. At low Q values, however, this is not the case and the paths deviate very much from the ideal; we cannot expect the inelasticity corrections to be valid here as dynamic effects will be quite important.

This is confirmed by experiment (chapter ten) when it is found that the low Q parts of the spectra for different detectors do not agree.

Because of this we must ignore data in this low Q range where we cannot perform adequate corrections. From the curves in figure 8.2 it has been decided, slightly arbitrarily, to do this for Q <0.3Å^{-1} for the 5° detectors, Q <1.5Å^{-1} for 10°, Q <2.5Å^{-1} for 20°, Q < 3Å^{-1} for 35°, Q <4Å^{-1} for 58°, and Q <5Å^{-1} for 90°.

Because of this LAD is not very useful in determining structure factors in the low Q range. As this is important for transforming data to give radial distribution functions this is a serious short coming. Better results would be obtained from an instrument that was able to measure scattering at much smaller angles such as SANDALS at ISIS or GLAD at IPNS, Argonne.

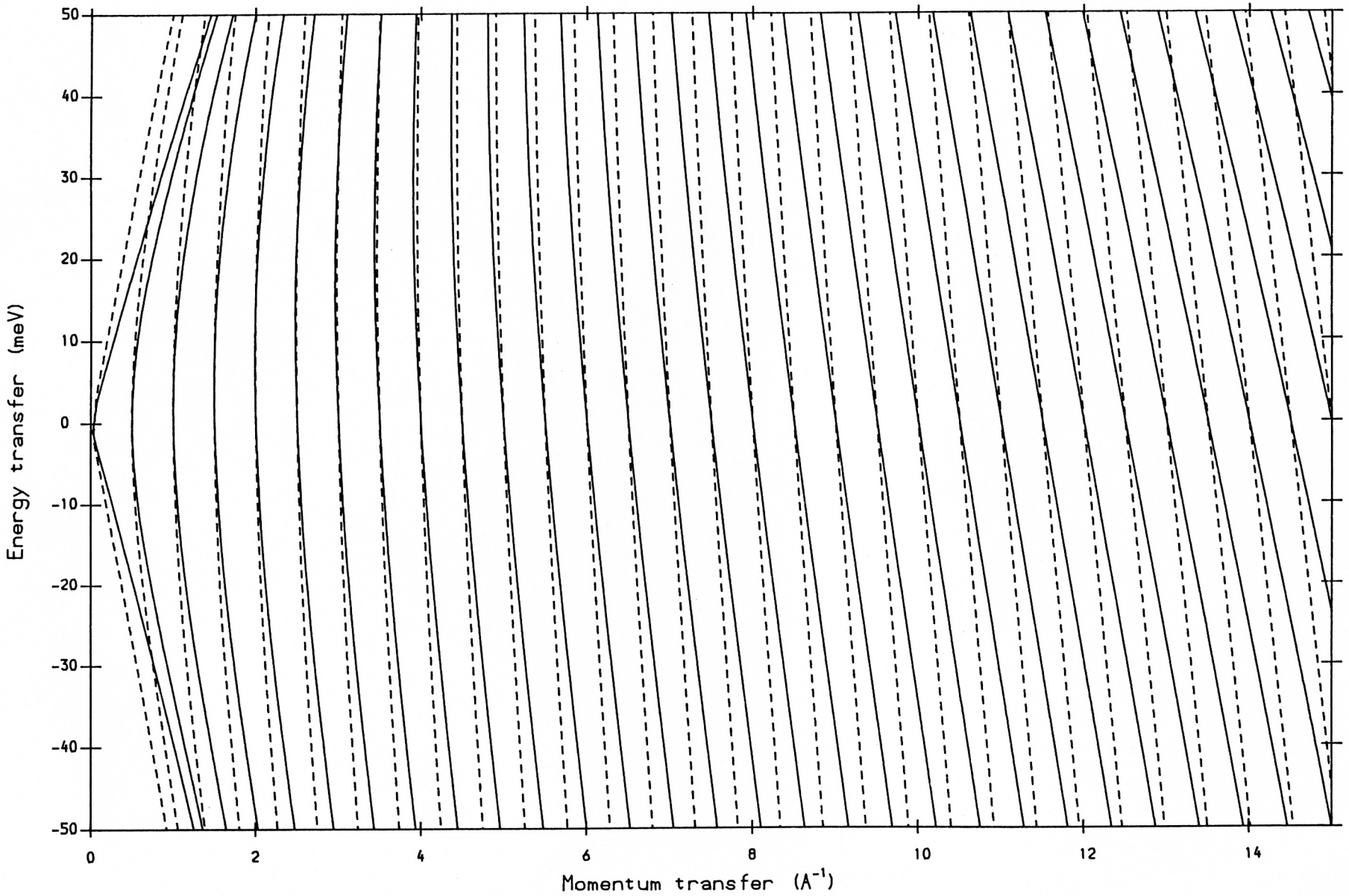


Figure 8.1 Integration paths for D4B with incident wavelengths of 0.7A (solid curves) and 0.5A (dashed curves).

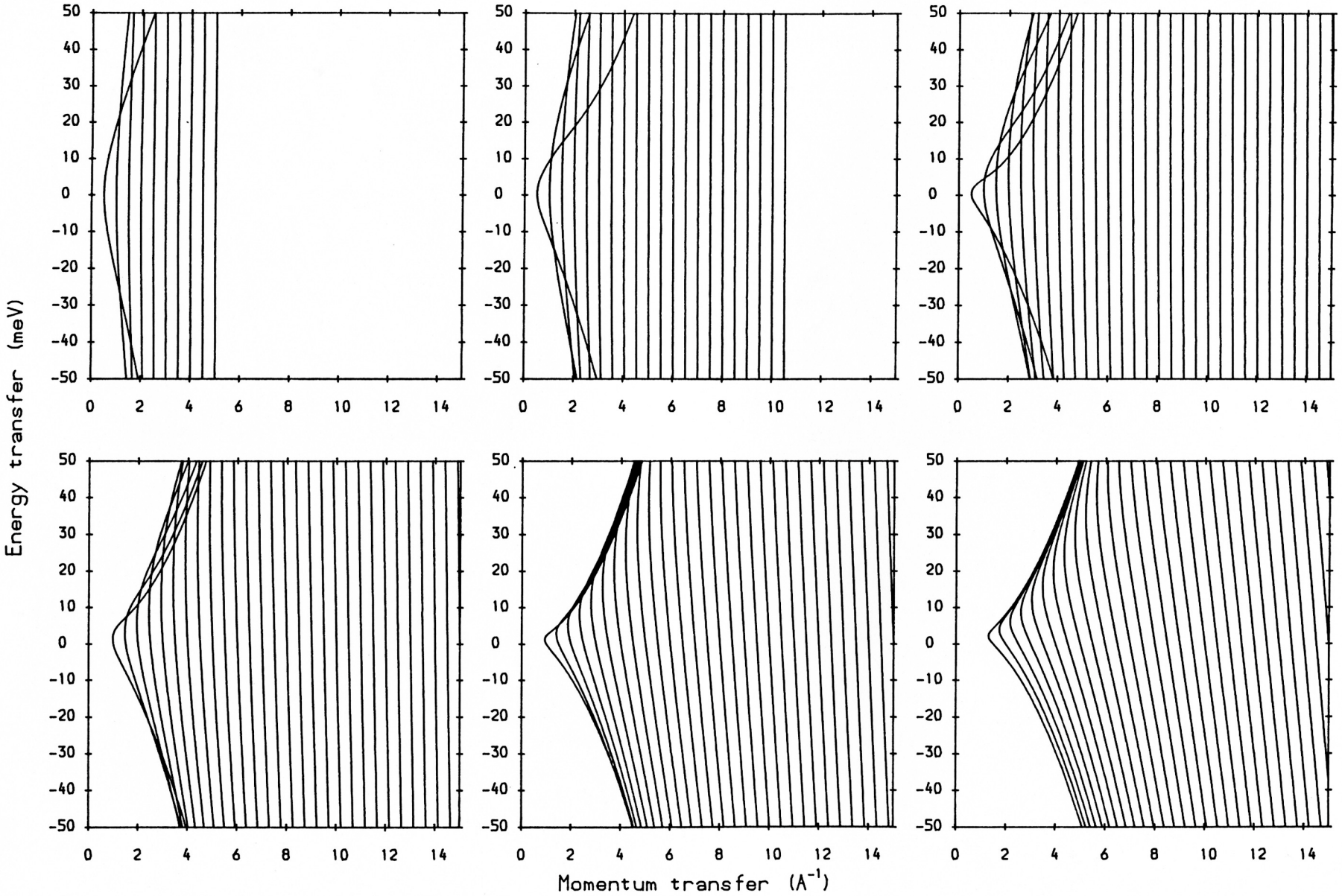


Figure 8.2 Integration paths for LAD detectors at angles of (from left to right, top to bottom) 5°, 10°, 20°, 35°, 58°, and 90°.

Chapter nine

The structure of lithium chloride and its admixture with potassium chloride

9.1 The structure of alkali chlorides

The partial structure factors and partial radial distribution functions have been determined for the molten alkali chlorides NaCl [9/1], RbCl [9/2] and CsCl [9/3]. These have very similar structures with the following characteristic features:

(i) There is a well defined first peak in $g_{+-}(r)$ with a coordination number (obtained by integration of $r^2 g_{+-}(r)$ up to the first minimum in $g_{+-}(r)$) of a little less than six for caesium chloride, decreasing to a little less than five in sodium chloride.

(ii) The functions $g_{++}(r)$ and $g_{--}(r)$ are approximately equal with the first peak in these functions occurring at roughly $\sqrt{2}$ times the distance of the first peak in $g_{+-}(r)$.

(iii) There is charge ordering as shown by the fact that the oscillations in $g_{++}(r)$ and $g_{_}(r)$ are approximately in antiphase with those in $g_{+-}(r)$

(iv) There is short range ordering radially out to a distance of approximately 15Å.

The pair distribution functions for the chlorides of sodium, rubidium, and caesium are shown in figure 9.1 on a distance scale that is normalised to the sum of the ionic radii, r_{+-}, and the details of these are summarised in table 5. The largest difference is a tendency for the first peak in $g_{++}(r)$ (and $g_{--}(r)$) to decrease in size as the cations increase in size from Na^+ to Cs^+.

The coordination number of an ion in a melt is not a clearly defined quantity. Calculated by the integration of $r^2 g_{\alpha\beta}(r)$ up to some point it is dependent on what that point is chosen to be. The coordination numbers quoted here are obtained by integration up to the first minimum in $g_{\alpha\beta}(r)$. Although this is rather critical on the exact position of the minimum it does, nonetheless, provide some information on the type of packing in the structure. We see that the coordination number increases as the cation size increases supporting the hypothesis that the coordination changes from approximately tetrahedral to octahedral.

The main features of the structure of the alkali chlorides can be understood in quite simple terms and can be easily reproduced by a simulation using a potential of the Born-Mayer-Huggins [9/4] form

$$V_{\alpha\beta}(r) = \frac{Z_\alpha Z_\beta e^2}{r} + a_{\alpha\beta} e^{-r/\sigma_{\alpha\beta}} - \frac{C_{\alpha\beta}}{r^6} - \frac{D_{\alpha\beta}}{r^8} \qquad (9/1)$$

where the first term represents Coulomb interaction, the second repulsive interaction due to ionic overlap, and the third and fourth terms van der Waal's interaction. The adjustable parameters are chosen to fit various crystal properties.

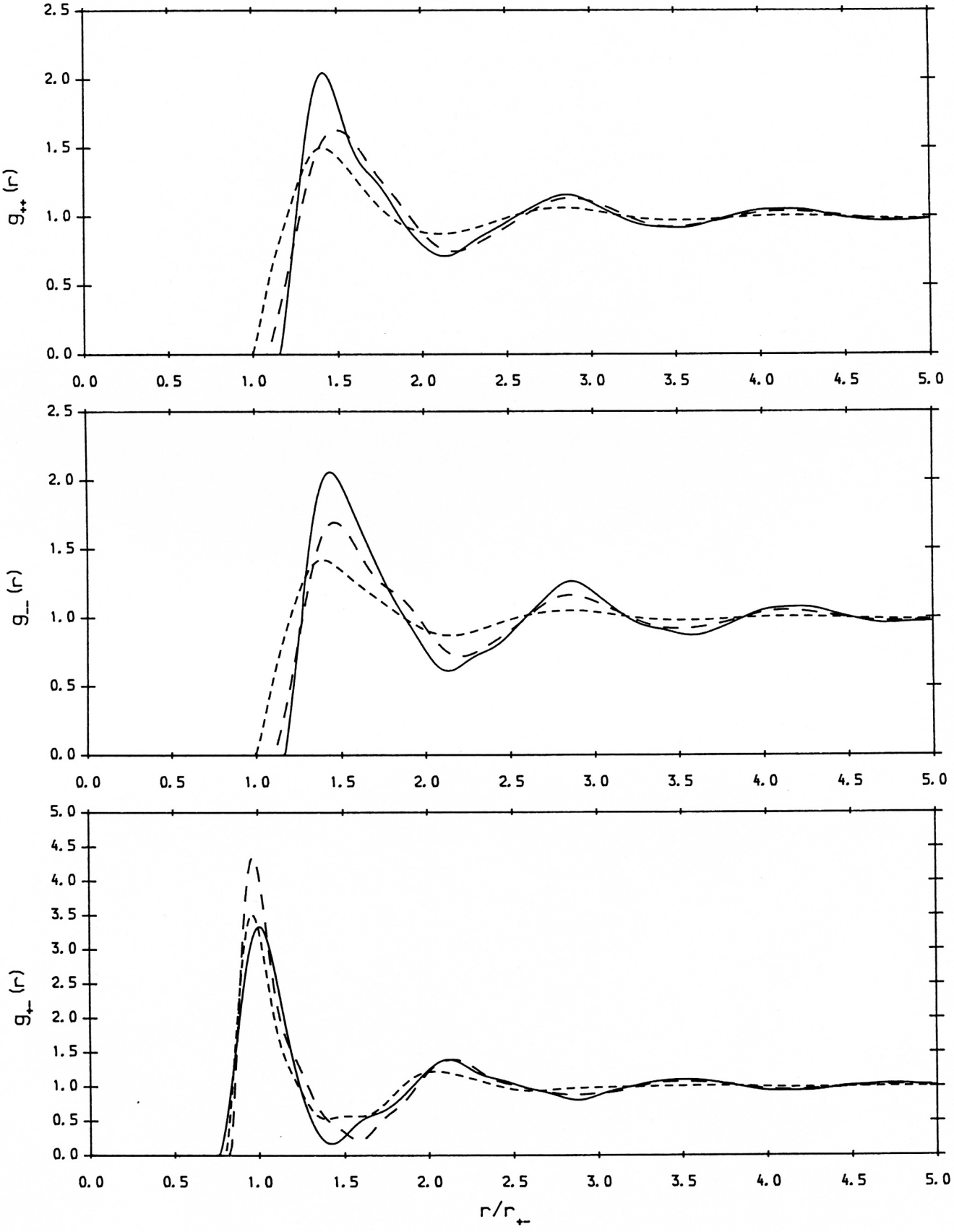


Figure 9.1 Partial radial distribution functions for NaCl (solid curve), RbCl (long dashes) and CsCl (short dashes).

Table 5. Main features of the partial pair distribution functions for some molten alkali chlorides

	Cation	Temperature (K)	Sum of ionic radii	Distance of closest approach	Position of first peak	Height of first peak	Coordination number
$g_{++}(r)$	Li	685	1.2	2.95	3.7	2.2	12.6
	Na	1148	1.9	3.19	3.9	2.05	13.0
	Rb	988	2.96	3.55	4.9	1.63	16.7
	Cs	973	3.38	3.45	4.95	1.50	15.4
$g_{--}(r)$	Li	685	1.2	2.95	3.7	2.2	12.6
	Na	1148	3.62	3.19	3.96	2.06	13.3
	Rb	988	3.62	3.6	4.8	1.69	17.1
	Cs	973	3.62	3.45	4.85	1.42	16.3
$g_{+-}(r)$	Li	685	2.41	1.95	2.3	4.3	3.6
	Na	1148	1.76	2.09	2.76	3.33	4.83
	Rb	988	3.29	2.7	3.2	4.36	7.4
	Cs	973	3.5	2.8	3.4	3.51	5.8

Many simulations have been done using such 'rigid ion' potentials. (A summary is given by Baranyai *et al* [9/5].) They produce results that are generally in good agreement with experiment (although there are differences, notably for caesium chloride; in particular simulation tends to overestimate the degree of structural ordering: it has been suggested that this difference is due to the screening effect of the polarisable cation). A molecular dynamics study of lithium chloride [9/6] has predicted an approximately tetrahedral coordination. This change from the octahedral coordination of caesium chloride is understood as a size effect. A simulation using point cations [9/7] has produced a polymeric chain in the limit of zero cation size.

Light scattering experiments [9/8] on molten alkali and alkaline earth halides have found that the depolarisation ratio (the ratio of the total depolarised intensity to the total polarised intensity) has a minimum for $r_+/r_- \approx \sqrt{2}-1$. This occurs in chlorides, bromides, and iodides (no work has been done on fluorides). This ratio reflects the distortion in symmetry of the surrounding anions. The interpretation of this is that there is a change in local ordering at radius ratios around that at which the size of the unit cell in the face-centred cubic structure is no longer determined by $r_+ + r_-$ but by $2r_-$. Under these conditions the liquid can no longer support octahedral coordination and tends towards either a tetrahedral or planar configuration.

9.2 Lithium chloride

We did an isotopic substitution experiment to test these predictions and find out whether the coordination of lithium chloride, if it is approximately four fold, is tetrahedral or planar. Three samples were

used, one containing ^{35}Cl, one ^{37}Cl, and one the natural mixture. ^{7}Li was used as the cation because ^{6}Li has a very high absorbtion cross-section making the natural mixture fairly absorbent to neutrons too. Scattering intensities were measured for these at 685°C using 0.7Å neutrons at D4B; and also for an empty container and the furnace. They are shown in figure 9.2. At first sight they seem to be somewhat different to those of other alkali halides, the first peak being very sharp and tall, but this is simply a result of the negative scattering length of the lithium which means that $S_{+-}(Q)$ contributes to the total scattering with the opposite sign to that which is usual.

The usual correction procedures were followed to produce the total structure factors shown in figure 9.3. It can be seen that they are nearly flat below $Q \approx 1\text{Å}^{-1}$ and can easily be extrapolated back to a $Q = 0$ value. What this value should be is known as it is related to the isothermal compressibility. Usually, because there are always some systematic errors (for instance, one can never be quite sure exactly how much sample one has in the beam), the extrapolated value does not quite agree with this compressibility limit. The difference in this case is small for all the samples (a few per cent) so the cross-sections are renormalised so that this limit is satisfied. If this is not done then the partial structure factors cannot have the right low Q behaviour.

As was mentioned in the introduction, the essence of an isotopic substitution experiment is that, by varying the isotopic composition and so scattering lengths of the constituent elements three different combinations of the three partial structure factors may be obtained. In chapter three we defined the coherent scattering function $F(Q)$ given by

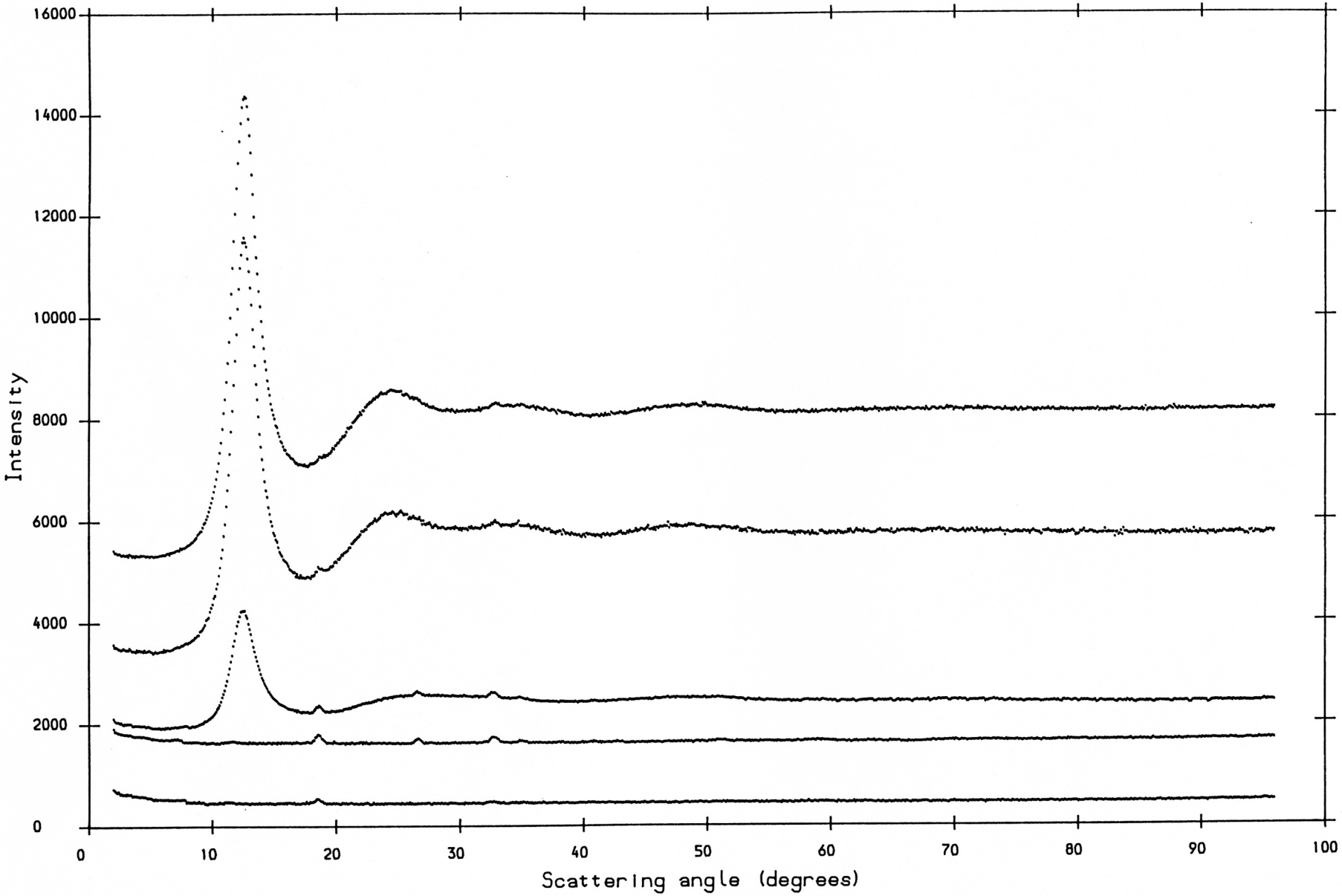


Figure 9.2 Scattering intensities for (from top to bottom) $^{7}Li^{35}Cl$ (which has been displaced upwards by 2000), $^{7}Li^{N}Cl$, $^{7}Li^{37}Cl$, an empty container, and the furnace, all at 685°C.

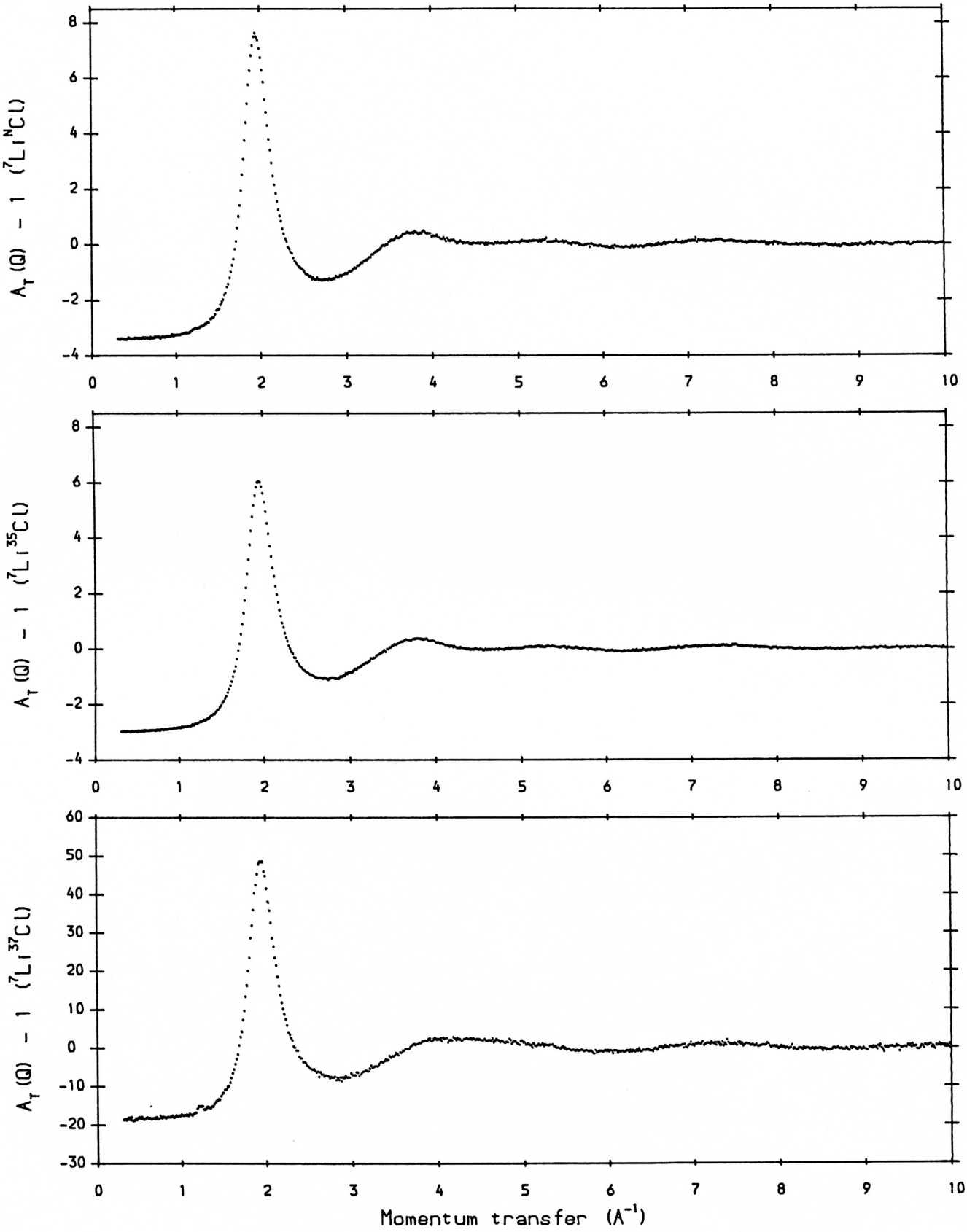


Figure 9.3 Total structure factors for the three samples of lithium chloride.

$$F(Q) = \frac{d\sigma}{d\Omega} - \sum_{\alpha} \overline{b^2}_{\alpha}$$

(9/2)

and related to the partial structure factors by (3/118). For the three samples used in this experiment we get

$$\begin{aligned} F(Q)\ (^{7}\mathrm{Li}^{35}\mathrm{Cl}) &= 0.0121\,(A_{++}-1) - 0.129\,(A_{+-}-1) + 0.342\,(A_{--}-1) \\ F(Q)\ (^{7}\mathrm{Li}^{\mathrm{N}}\mathrm{Cl}) &= 0.0121\,(A_{++}-1) - 0.105(A_{+-}-1) + 0.229\,(A_{--}-1) \\ F(Q)\ (^{7}\mathrm{Li}^{37}\mathrm{Cl}) &= 0.0121\,(A_{++}-1) - 0.034\,(A_{+-}-1) + 0.024\,(A_{--}-1) \end{aligned}$$

(9/3)

This set of simultaneous equations can be solved to give the three partial structure factors as a function of momentum transfer. Because it is fairly ill conditioned (see appendix D for a discussion of the conditioning of sets of simultaneous equations) the statistical scatter of the points defining the partial structure factors is rather larger than that of the original data. Smooth curves can be fitted to these partial structure factors subject to the constraint that they must combine to fit the total structure factors within an acceptable limit. Procedures for doing this have been discussed by McGreevy and Mitchell [9/9].

Such a separation into partial structure factors is shown in figure 9.4. $A_{--}(Q)$ is of the familiar form for alkali halides as is $A_{+-}(Q)$ although it seems rather large. $A_{++}(Q)$, though, looks more like $A_{+-}(Q)$ than $A_{--}(Q)$, to which one would expect it to be similar. The transformations of these to partial pair distribution functions are shown in figure 9.5; it is clear that these cannot be right: we have not successfully separated the partial structure factors. Various things have been tried to remedy this - renormalising to a slightly different compressibility; not renormalising at all; varying the scattering

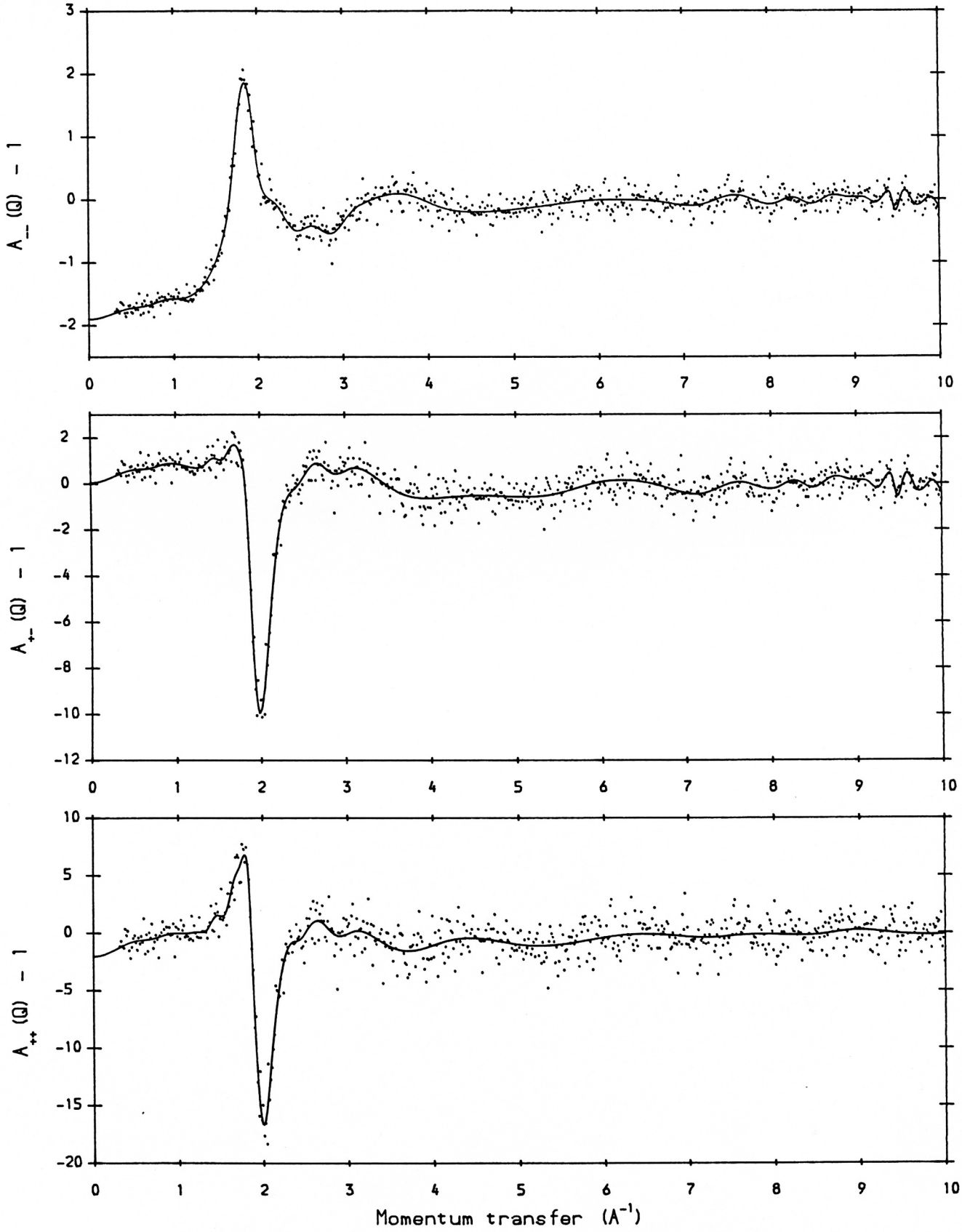


Figure 9.4 The partial structure factors $A_{--}(Q)$, $A_{+-}(Q)$ and $A_{++}(Q)$ for lithium chloride obtained from the three total structure factors.

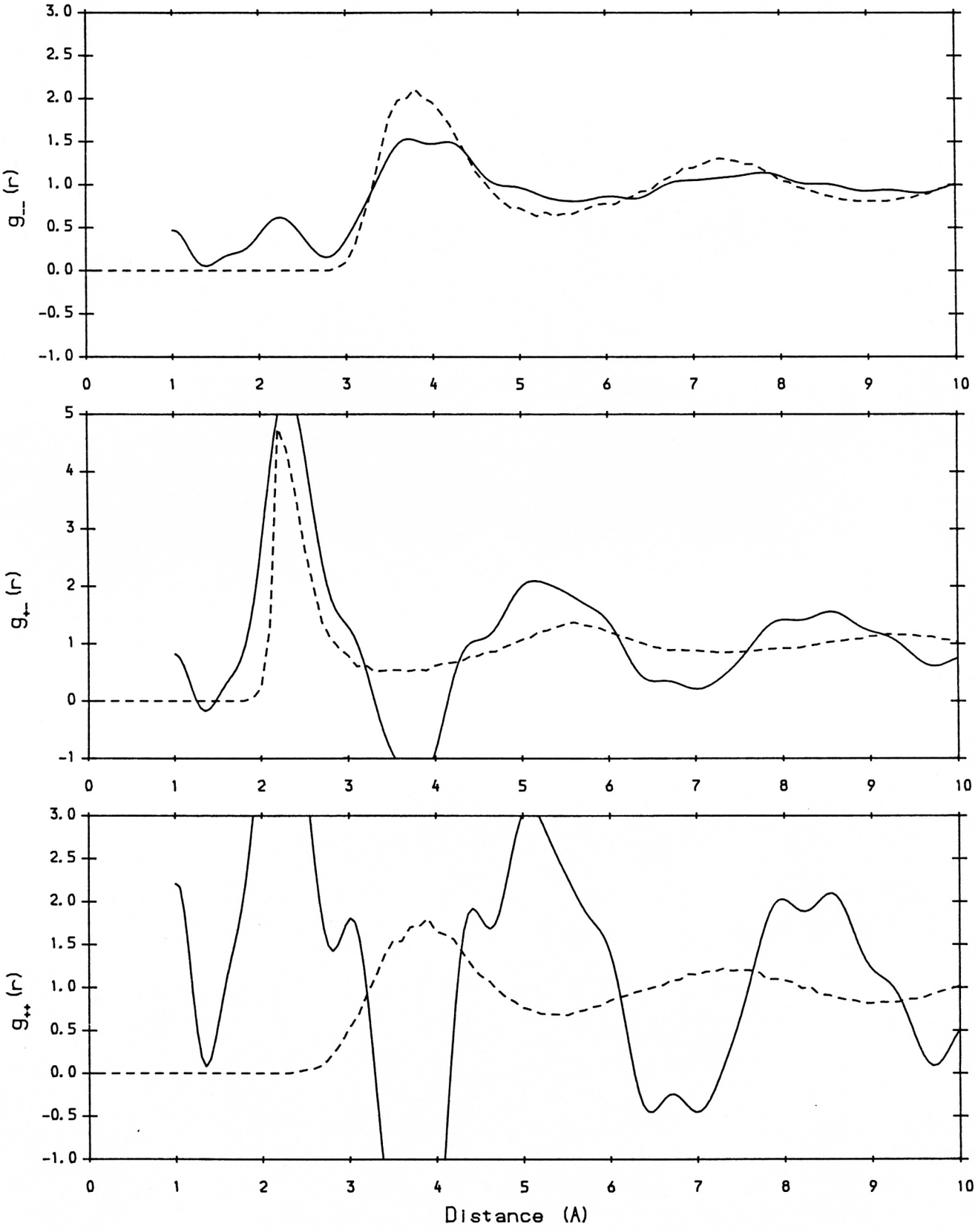


Figure 9.5 The partial pair distribution functions obtained from the partial structure factors (solid lines) compared with simulation (dashed lines).

lengths slightly (as the ^{7}Li value, in particular, may have been measured inaccurately); and adjusting the isotopic composition of the samples slightly. None of these made any qualitative difference to the partial functions obtained.

A different approach was called for. As $A_{++}(Q) \approx A_{--}(Q)$ for all the other alkali halides it is likely the same is true for lithium chloride (although this is the case for which the difference might be expected to be greatest due to the difference in ion sizes). If it assumed this equality does hold for lithium chloride then there are only two independent partial structure factors $A_{\text{like}}(Q)$ $(= A_{++}(Q) = A_{--}(Q))$ and $A_{\text{unlike}}(Q)$ $(= A_{+-}(Q))$ which can be determined using just two samples. The assumption can be then be examined by comparison with the third sample.

Using ^{7}Li^{35}Cl and ^{7}Li^{37}Cl these two partial structure factors were obtained; they are shown in figure 9.6. They are then summed in the proportions appropriate to ^{7}Li^{N}Cl and compared with the experimental data for this sample (figure 9.7). The comparison is really very good indeed, the only significant difference being around the top of the major peak. We conclude that these two partial structure factors together with the assumption $A_{++}(Q) = A_{--}(Q)$ are consistent with our experimental data, allowing for a small systematic error (for the results as they are presented here that error is all on one sample; by a little fiddling with peak heights of the partial structure factors we could spread it between the three samples which would make it look smaller).

Rather than separate into $A_{++}(Q)$, $A_{+-}(Q)$, and $A_{-}(Q)$ we could separate into a different set of partial structure factors, for example those

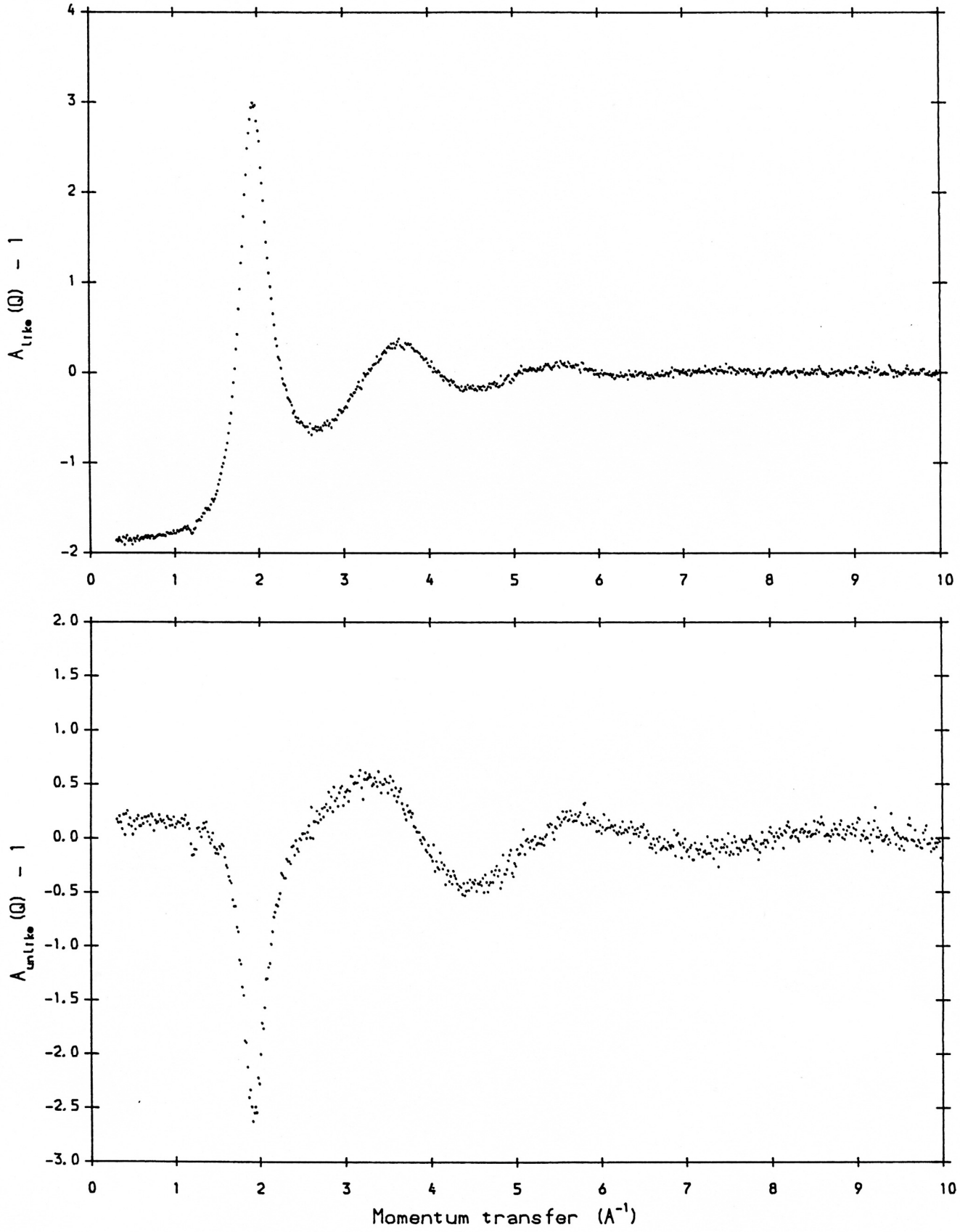


Figure 9.6 The partial structure factors $A_{like}(Q)$ and $A_{unlike}(Q)$ obtained from the total structure factors for $^{7}Li^{35}Cl$ and $^{7}Li^{37}Cl$.

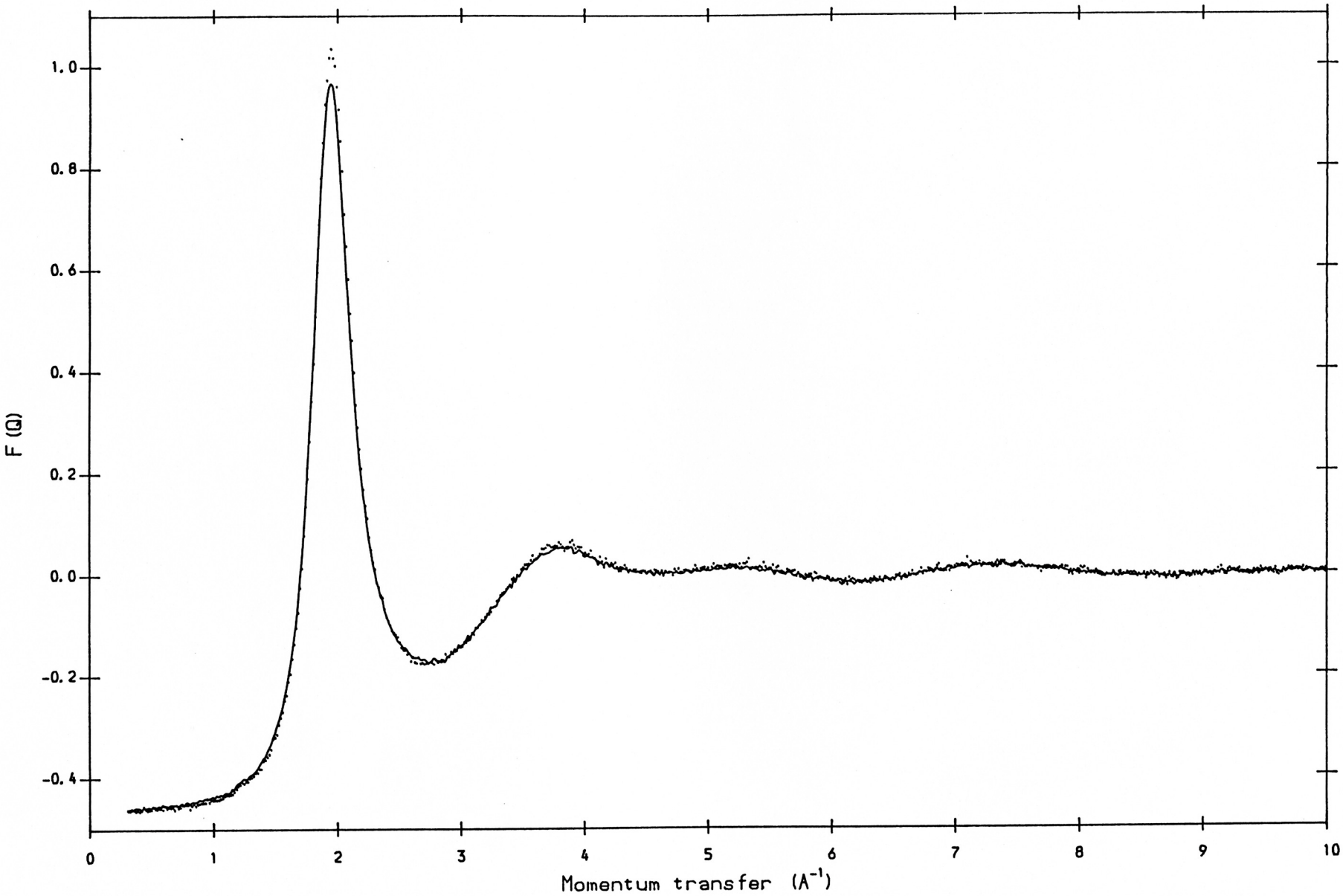


Figure 9.7 The scattering from $^{7}Li^{N}Cl$ (points) compared with that expected from combination of $A_{like}(Q)$ and $A_{unlike}(Q)$ (line).

based on mass and charge, or on number and charge. For the latter the coherent scattering function is given by

$$F(Q) = a_N^2(S_{NN}(Q) - ¼) + 2a_N a_q S_{Nq}(Q) + a_q^2\,(S_{qq}(Q) - ¼)$$

(9/4)

where their large Q limiting values are subtracted from the partial structure factors. The coefficients are

$$a_N = \bar{b}_+ + \bar{b}_-$$

$$a_q = \bar{b}_+ - \bar{b}_-$$

(9/5)

Looking at the definition of these partial structure factors in (3/128) we see that if $A_{++}(Q) = A_{--}(Q)$ we get $S_{Nq}(Q) = 0$ while $S_{qq}(Q)$, being essentially the sum of $A_{++}(Q)$ and $A_{--}(Q)$ is highly structured. The assumption we made above is, then, that $S_{Nq}(Q) = 0$ for all Q.

The partial structure factors $S_{NN}(Q)$, $S_{Nq}(Q)$, and $S_{qq}(Q)$ determined using all three samples are shown in figure 9.8, while $S_{NN}(Q)$ and $S_{qq}(Q)$ obtained from the $^7Li^{35}Cl$ and $^7Li^{37}Cl$ samples on the assumption that $S_{Nq}(Q) \equiv 0$ are shown in figure 9.9. We see that $S_{qq}(Q)$ does not vary much between the two. Most of the scattering from all three samples is due to this partial structure factor so it is the best determined. The errors in the experimental data exhibit themselves in the less well determined structure factors $S_{Nq}(Q)$, and $S_{NN}(Q)$,

It behoves us to consider the root of these errors. It is clearly not poor statistics; the statistics are far better than for most of the previous experiments. The table in appendix D compares the conditioning of the system of the separation matrix appropriate to this experiment

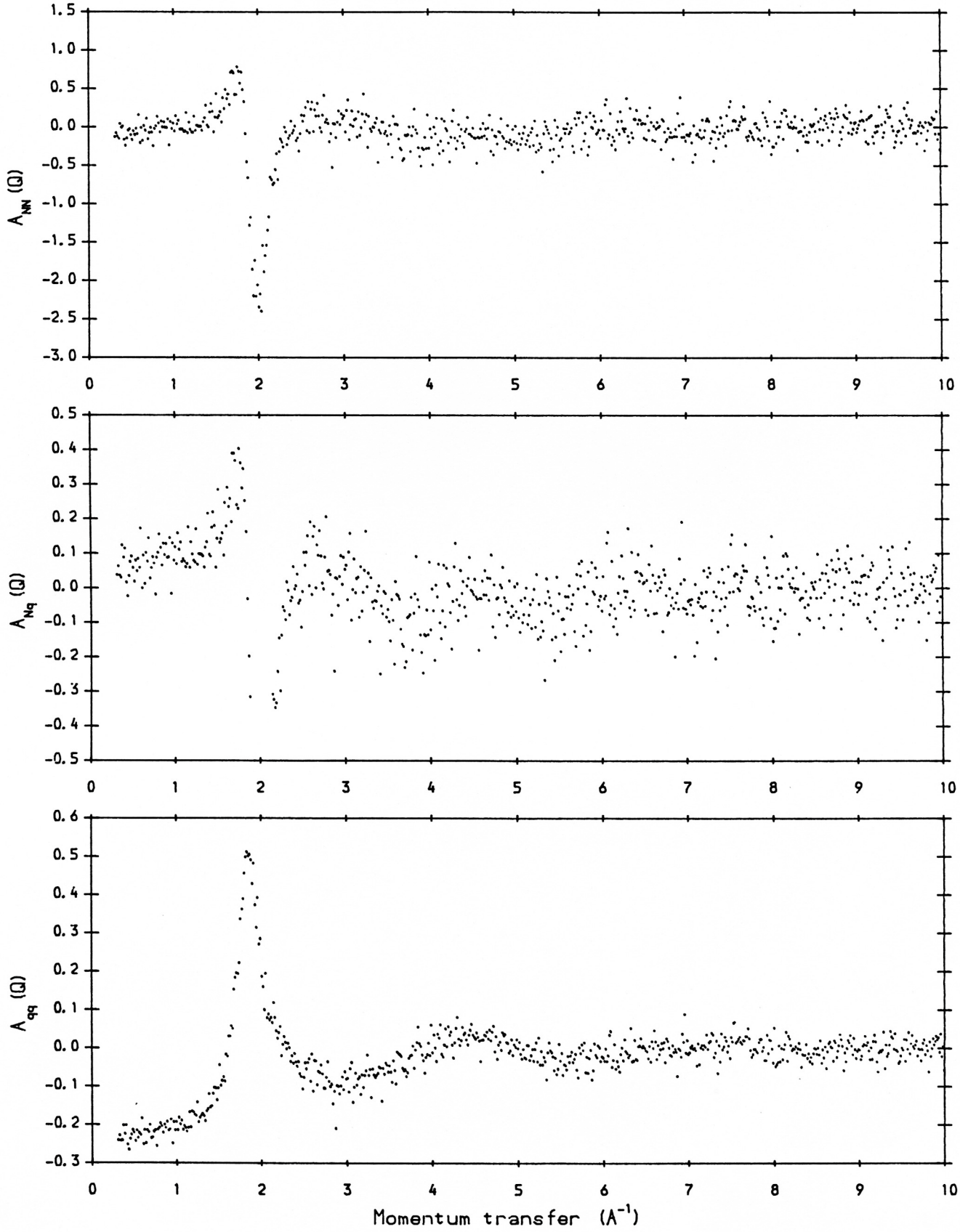


Figure 9.8 The partial structure factors $A_{NN}(Q)$, $A_{Nq}(Q)$ and $A_{qq}(Q)$ for lithium chloride obtained from the three total structure factors.

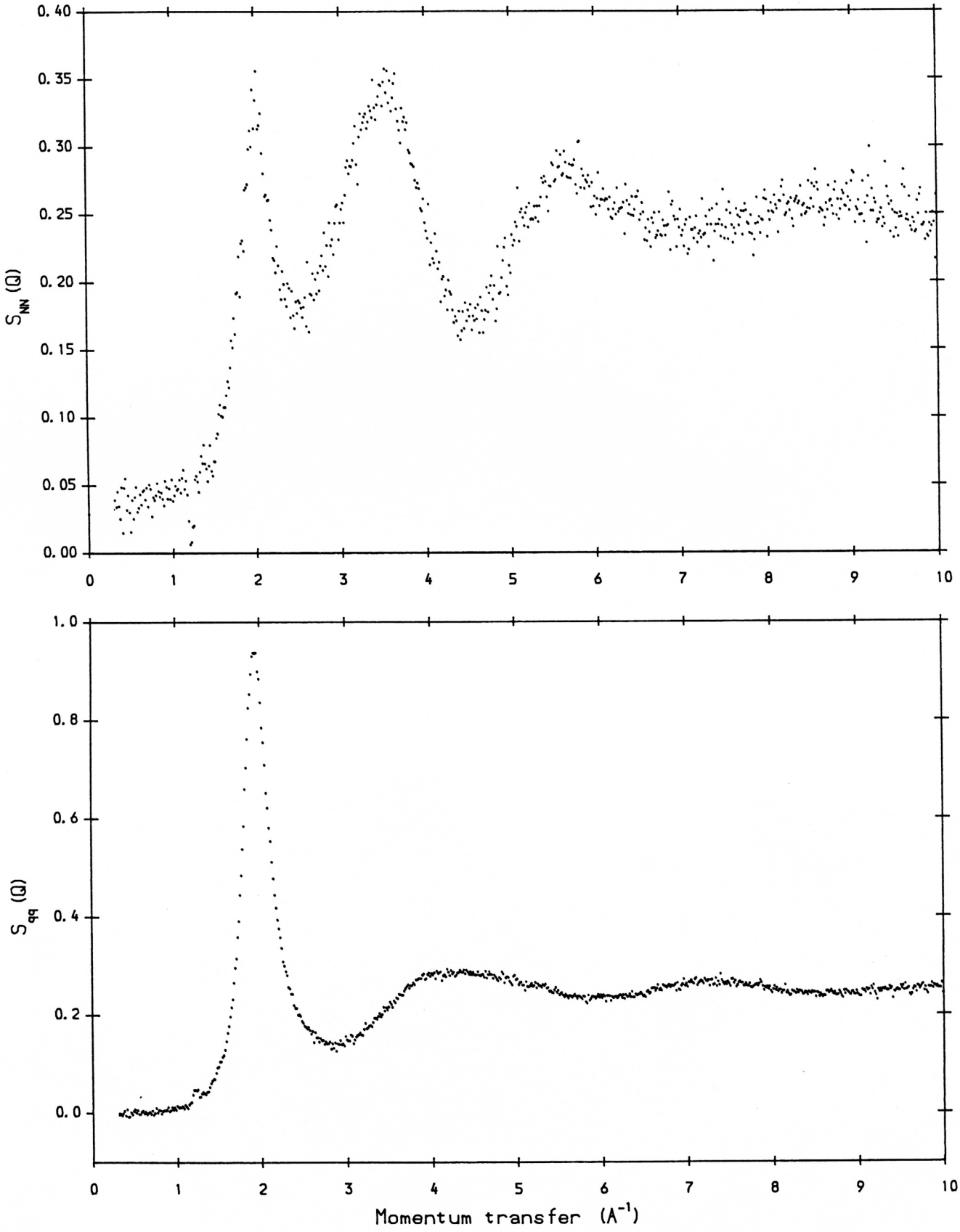


Figure 9.9 The partial structure factors $S_{NN}(Q)$ and $S_{qq}(Q)$ for lithium chloride obtained assuming $S_{Nq}(Q)=0$.

with those of others. Although it is the worst of the cases listed, it is not so by much. The conditioning, then, is not the cause of the problem although it may accentuate it. The conclusion is that some sort of systematic error is causing a problem. (This is worthy of note as it is sometimes said that all that is needed to do more complicated and more difficult isotopic substitution experiments is greater statistical accuracy of the results. This does not mean though, and this experiment is demonstration of this, that systematic errors will not be important; indeed to some extent they are more important as poor statistics will often mask the systematic errors.) This problem is greatest around the peak in the total structure factors. This is where the combination of $A_{\text{unlike}}(Q)$ and $A_{\text{like}}(Q)$ is at variance with the total structure factor for $^{7}\text{Li}^{\text{N}}\text{Cl}$ and it is at this point, too, that the partial structure factors of figure 9.4 differ from what we would expect. This cannot be caused by some slowly varying function of Q such as would be the result of, for example, a miscalculation of absorption coefficients or a slight variation with angle of the multiple scattering.

A possible cause is that the deviation from the static approximation may not be entirely compensated for by the inelasticity corrections which are, as discussed in chapter eight, based on single particle dynamics and ignore any collective effects. The peak in the total structure factors is very sharp and is likely to be associated with a quite sudden narrowing of the quasi-elastic peak in $S_T(Q,\omega)$ which may lead to a not insignificant difference between the integral of $S_T(Q,\omega)$ at constant Q and at constant angle which is partly due to effects of collective dynamics; this can not be corrected for, at least not without some model of the dynamics of the system. It is possible that the

situation is worse for lithium halides than for other alkali halides because of the negative scattering length of the lithium isotope used. (Because of the lightness of the lithium ion the recoil effects are also especially large.) If this supposition is correct the situation could only be improved by using shorter wavelength neutrons and measuring the scattering at lower angles as this is the way to reduce deviation from the static approximation. This might be possible using SANDALS, the small angle diffraction instrument at ISIS.

As far as lithium chloride is concerned, we can be fairly confident that the results in figure 9.6 at least approximately represent the situation, as they are of the form we expect and are consistent with our experimental data. Indeed, they are probably as reliable as the previous results for alkali halides for which the statistical errors are large enough to cover up the problem we have here. That is, if our statistical errors here were comparable we could probably obtain the results we have here within statistical errors without worrying about systematic errors.

The pair distribution functions obtained by transformation of our partial structure factors are shown in figures 9.10 and 9.11 where they are compared with simulation results [9/5]. The small ripples on $g_{\text{unlike}}(r)$ are due to truncation errors (the oscillations in $A_{\text{unlike}}(Q)$ have not died out by the end of the experimental range even though no oscillations are observable in the total structure factors at this point). As a further comparison the total pair distribution functions are compared with those calculated from the simulation results (figure 9.12). This confirms that the simulation overestimates the height of the first peak in $g_{+-}(r)$. Otherwise the agreement is good. The coordination number, obtained from $g_{\text{unlike}}(r)$, is 3.8. The first peaks in $g_{\text{unlike}}(r)$ and $g_{\text{like}}(r)$ are at

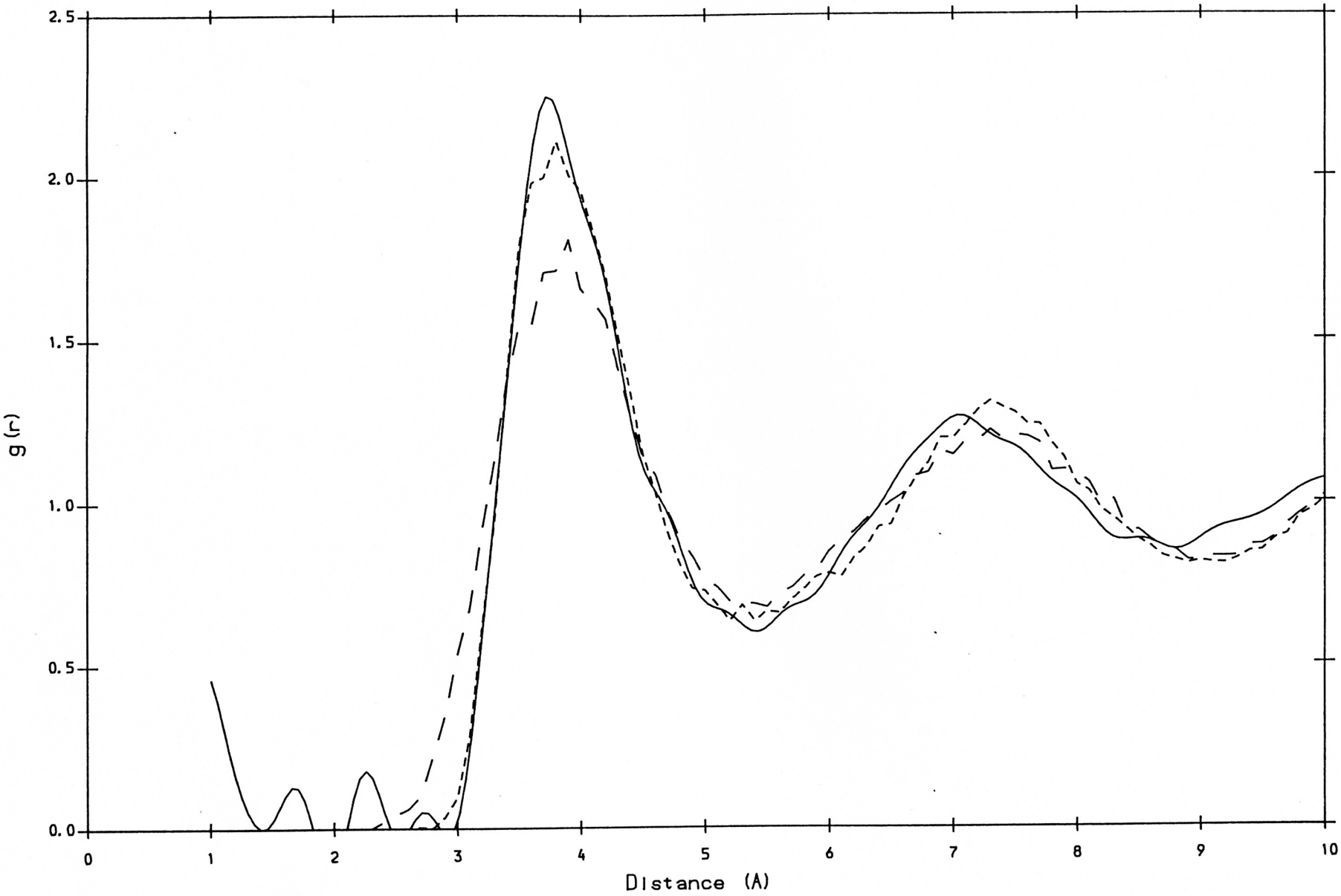


Figure 9.10 The function $g_{like}(r)$ (solid line) for lithium chloride compared with simulated $g_{++}(r)$ (long dashes) and $g_{--}(r)$ (short dashes).

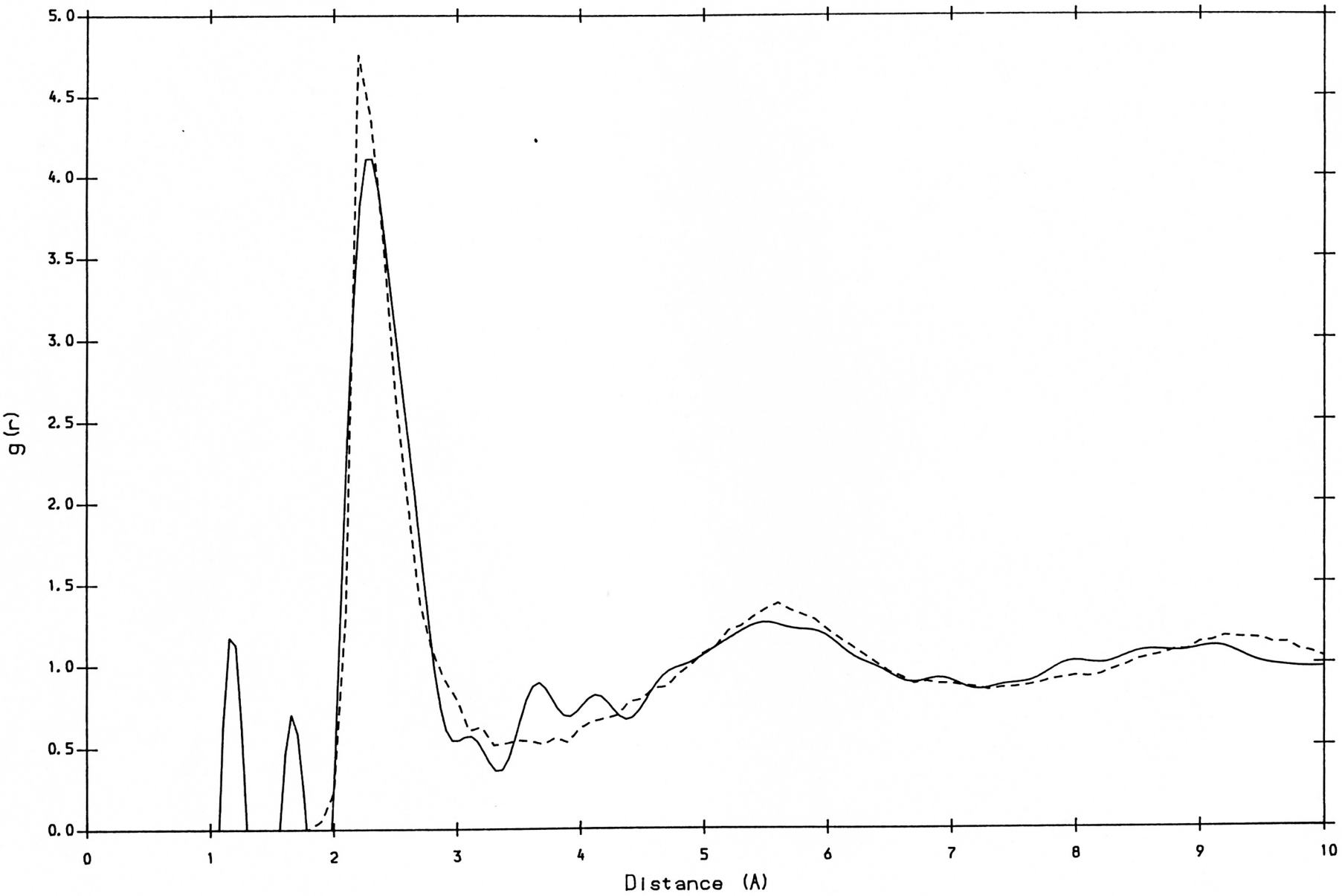


Figure 9.11 The function $g_{unlike}(r)$ (solid line) for lithium chloride compared with simulated $g_{+-}(r)$ (dashes).

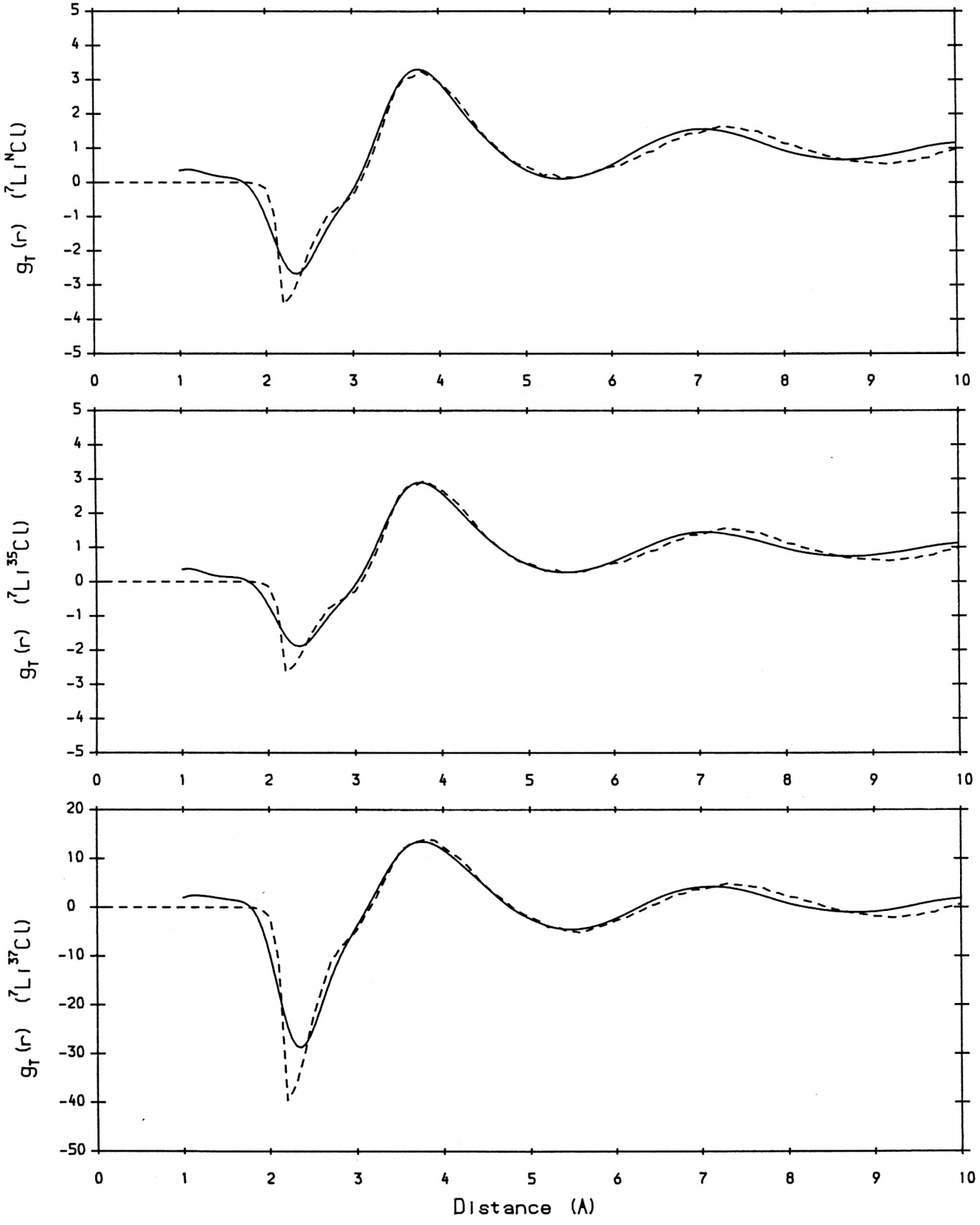


Figure 9.12 Total pair distribution functions (solid lines) compared with simulation (dashed lines) for the three lithium chloride samples.

approximately 2.3Å and 3.7Å respectively. The ratio of these two distances is $1.61 \approx \sqrt{8/3}$, the value expected for tetrahedral coordination. This, together with the good agreement with the simulation for which the coordination is the same leads us to the conclusion that lithium chloride is approximately tetrahedrally coordinated.

This means that there is a significant change in local order at or near the melting point. In the solid phase lithium chloride has the same octahedrally coordinated rock-salt structure as the other alkali chlorides. It would be interesting to make measurements very close to the melting point to see whether this the coordination changes abruptly on melting or gradually over some small temperature range.

9.3 Lithium chloride/potassium chloride mixture

When lithium chloride is mixed in small concentrations with potassium chloride the mobility of the lithium is less than that of the potassium although it is the smaller of the two cations and in the pure salts lithium has the higher mobility. The results of the previous section show that lithium chloride is tetrahedrally coordinated whereas potassium chloride is more nearly octahedrally coordinated. We expect, therefore, that the coordination of Li^+ in a mixture containing only a small proportion of lithium chloride is significantly different to that in the pure salt in such a way that it is difficult for the Li^+ ions to move through the surrounding ions. There may be some kind of excitable mode associated with this trapping: molecular dynamics studies [9/10] show that for a 10% lithium chloride concentration the lithium velocity autocorrelation function shows very definite oscillations which indicate some such mode.

To investigate this we have performed an isotopic substitution diffraction experiment on the system. Using two samples of this 10% lithium chloride, 90% potassium chloride mixture, one containing pure ^{7}Li (for its low absorption) and one zero lithium, a mixture of approximately 54% ^{6}Li, 46% ^{7}Ll that has zero coherent scattering length, it is possible to obtain from the latter the K-K, K-Cl, and Cl-Cl correlations (there being no coherent scattering from the lithium); the difference between that and the former gives the lithium correlations, Li-Li, Li-Cl, and Li-K.

Putting in the scattering lengths we get

$$F(Q)\ (^{0}\mathrm{Li/KCl}) = 0.02727\,(A_{K-K}-1) + 0.1582\,(A_{K-Cl}-1) + 0.2294\,(A_{Cl-Cl}-1) \tag{9/6}$$

$$F(Q)\ (^{7}\mathrm{Li/KCl}) = F(Q)\ (^{0}\mathrm{Li/KCl}) + 0.000121\,(A_{Li-Li}-1) - 0.01054(A_{Li-Cl}-1) - 0.003633\,(A_{Li-K}-1) \tag{9/7}$$

$$= F(Q)\ (^{0}\mathrm{Li/KCl}) + 0.01054\left((A_{Li-Ci}-1) + 0.345\,(A_{Li-K}-1) - 0.0115(A_{Li-Li}-1)\right) \tag{9/8}$$

so, to obtain the term in brackets, the lithium correlations, the relevant separation matrix is

$$\begin{pmatrix} 1 & 0 \\ 1 & 0.01054 \end{pmatrix} \tag{9/9}$$

which has conditioning numbers of the same order of magnitude as, although a little larger than, those for separation of alkali halide structures into three partial structure factors (see appendix D) so, although we are only using two samples here, we need comparable statistics.

Spectra were obtained for both these samples, and also for pure potassium chloride (as a comparison), at 1100K, an empty vanadium container and the furnace. It is the usual practice during such an experiment not to obtain all the data for a spectrum in one scan but to do several and then combine them only when it has been checked that they are consistent with each other. In this experiment there was a problem as can be seen by looking at figure 9.13; there is a change, mainly at low scattering angles, of the ($^{(0)}$Li/K)Cl spectrum with time. It was eventually found, though not until the second of the three days allocated for the experiment, that this was due to a leak allowing air into the beam collimators so that we were observing air scattering. Because of the tight scheduling of instruments at a central research facility such as the high flux reactor it is not possible in these circumstances to repeat what has gone wrong; the best has to be made of the data already obtained.

In figure 9.14 are shown: the spectrum for ($^{(0)}$Li/K)Cl which has been constructed by combining the low angle part of the first scan, for which air scattering appears to be negligible, with the high angle parts of all the others; the spectrum for potassium chloride including air scattering; the spectra for (^{7}Li/K)Cl and the container measured after the collimators had been evacuated; and the spectrum for the furnace before and after the correction of the problem.

It is not possible to properly correct for the air scattering; the experiment should really be repeated. An attempt, though, has been made to do as much as possible. The simplest assumption one can make about the air scattering is that it is constant, independent of sample. It can then be determined by taking the difference of the two furnace spectra.

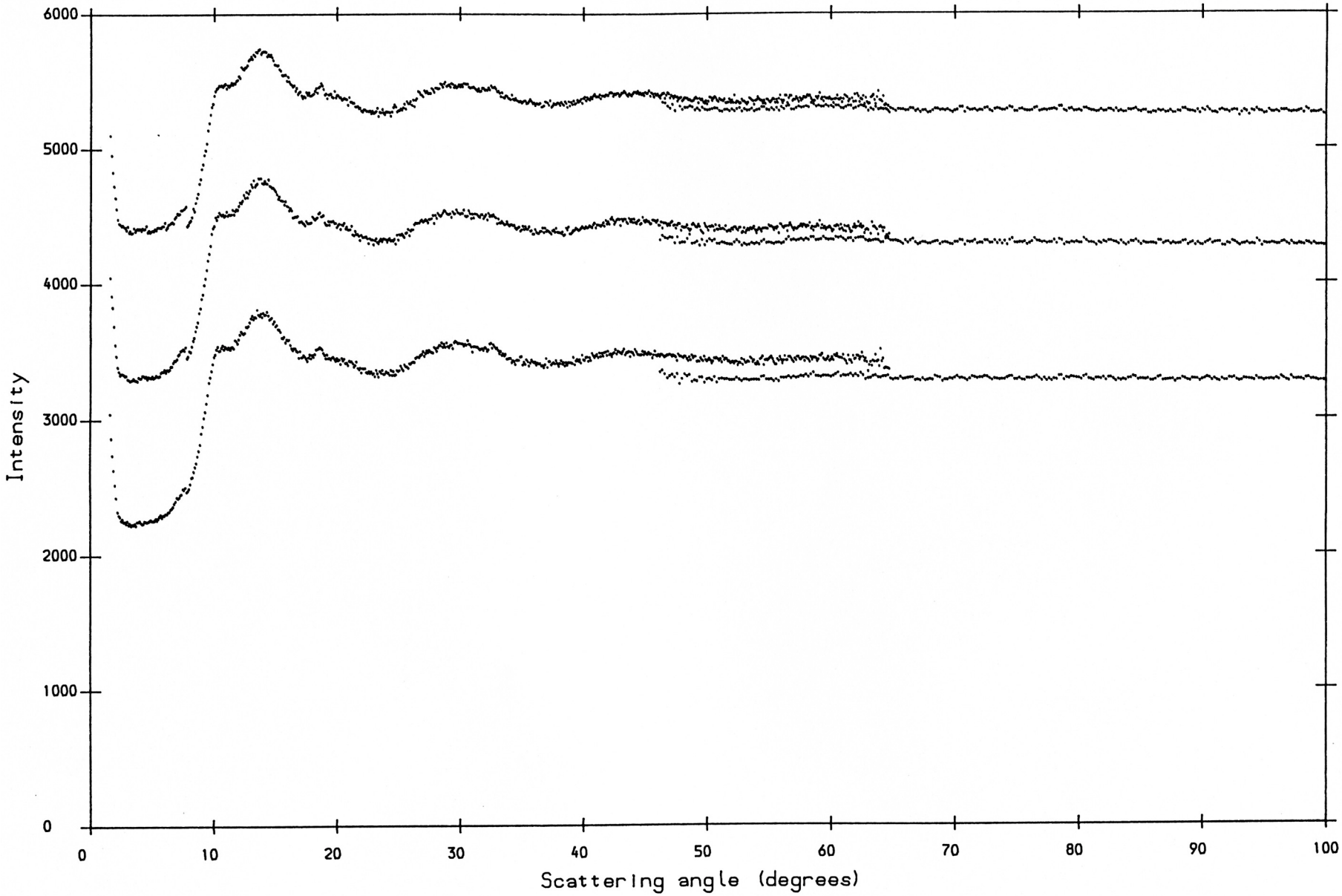


Figure 9.13 Scattering intensities for ($^{(0)}$Li/K)Cl as a function of time. Succesive spectra are displaced upwards by 1000.

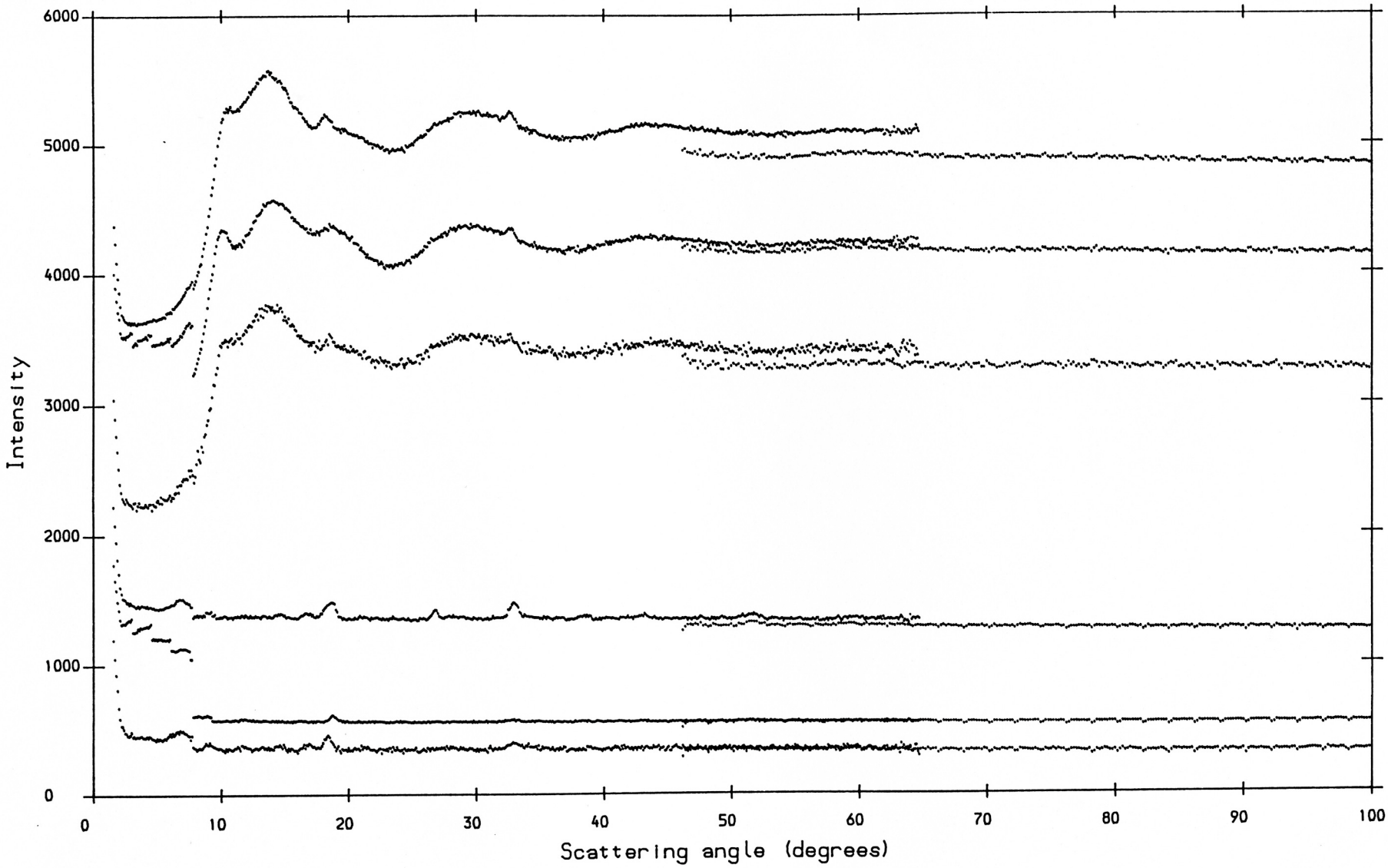


Figure 9.14 Scattering intensities for (from top to bottom) (^{7}Li/K)Cl at 1100K (displaced upwards by 1000), KCl (with air scattering) at 1100K (displaced by 500), ($^{(0)}$Li/K)Cl at 1100K, the empty container at room temperature and the furnace with and without air scattering (the former displaced by 250) at room temperature.

When this was done, and the air scattering subtracted from the spectra of the container and KCl, the usual correction procedures were followed. It was clear that the air scattering was still causing problems as there was a slight downward slope on all the spectra. This was removed by subtracting a straight line of the appropriate slope to give the results shown in figure 9.15.

Not surprisingly, they are very similar, the main difference being the size of the first (small) peak which is larger for KCl than for either of the (Li/K)Cl samples. As the ($^{(0)}$Li/K)Cl contains only K-K, K-Cl, and Cl-Cl correlations (though not in quite the same proportion as the KCl) we can conclude from this that the KCl structure has been disrupted by the presence of LiCl. This peak is mainly due to charge ordering so it would seem that this has been decreased slightly by the addition of the lithium chloride.

$g_T(r)$ for potassium chloride is compared in figure 9.16 with a computer simulation result [9/5]. It appears that the simulation overestimates the degree of ordering beyond the first coordination shell. As mentioned above the same is observed for caesium chloride (it contrasts with the rather good agreement we have seen for lithium chloride) and is possibly due to the screening effect of the larger, more polarisable, cations. This is supported by some recent simulation results for caesium chloride using polarisable dipole potentials that are in better agreement with experiment [9/11].

The total pair distribution functions for the two samples of (Li/K)Cl are compared in figure 9.18. The differences are too small for any reliable conclusions to be drawn.

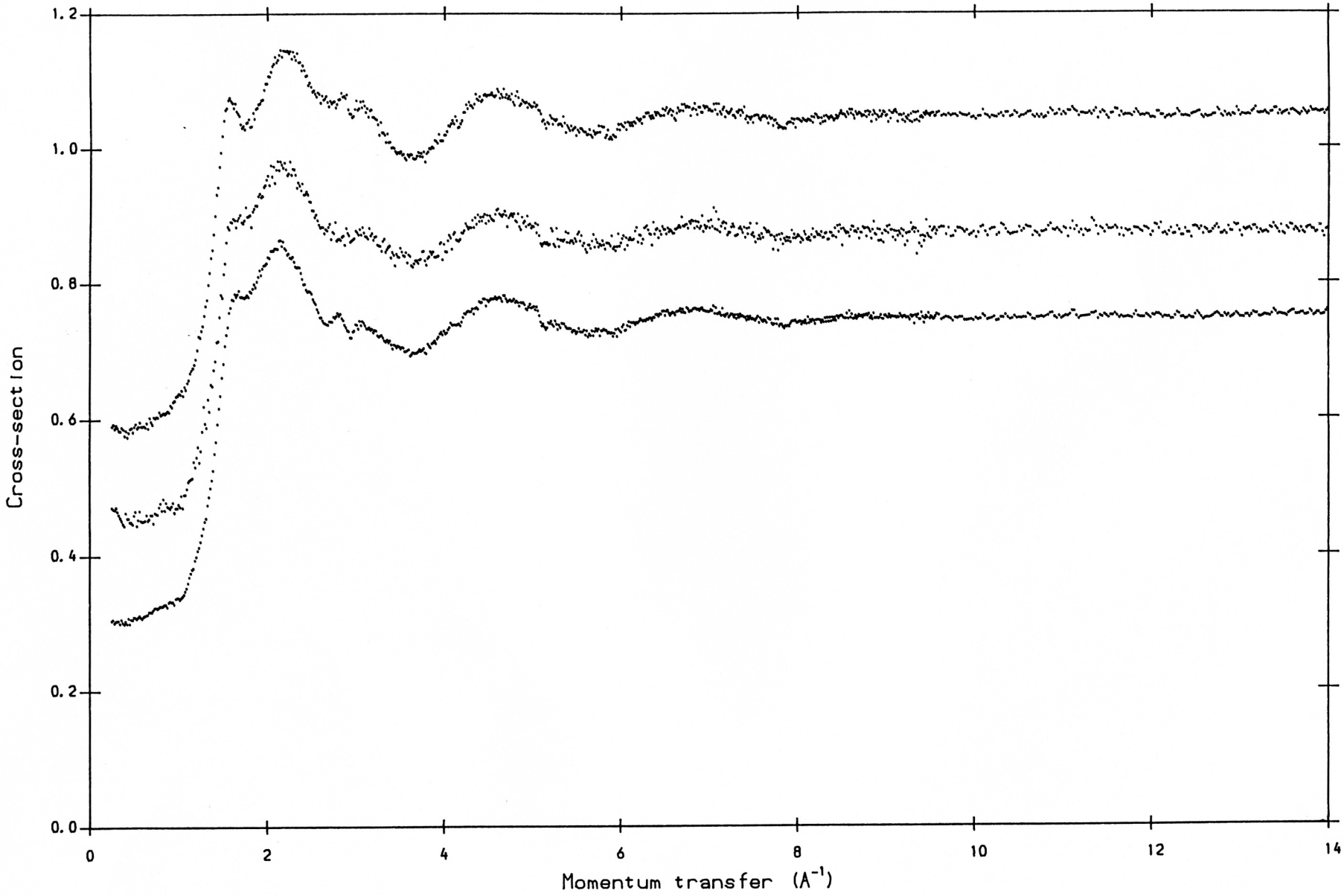


Figure 9.15 Cross-sections for (from top to bottom) KCl (displaced upwards by 0.3), ($^{(0)}$Li/K)Cl (displaced by 0.15), and (^{7}Li/K)Cl at 1100K.

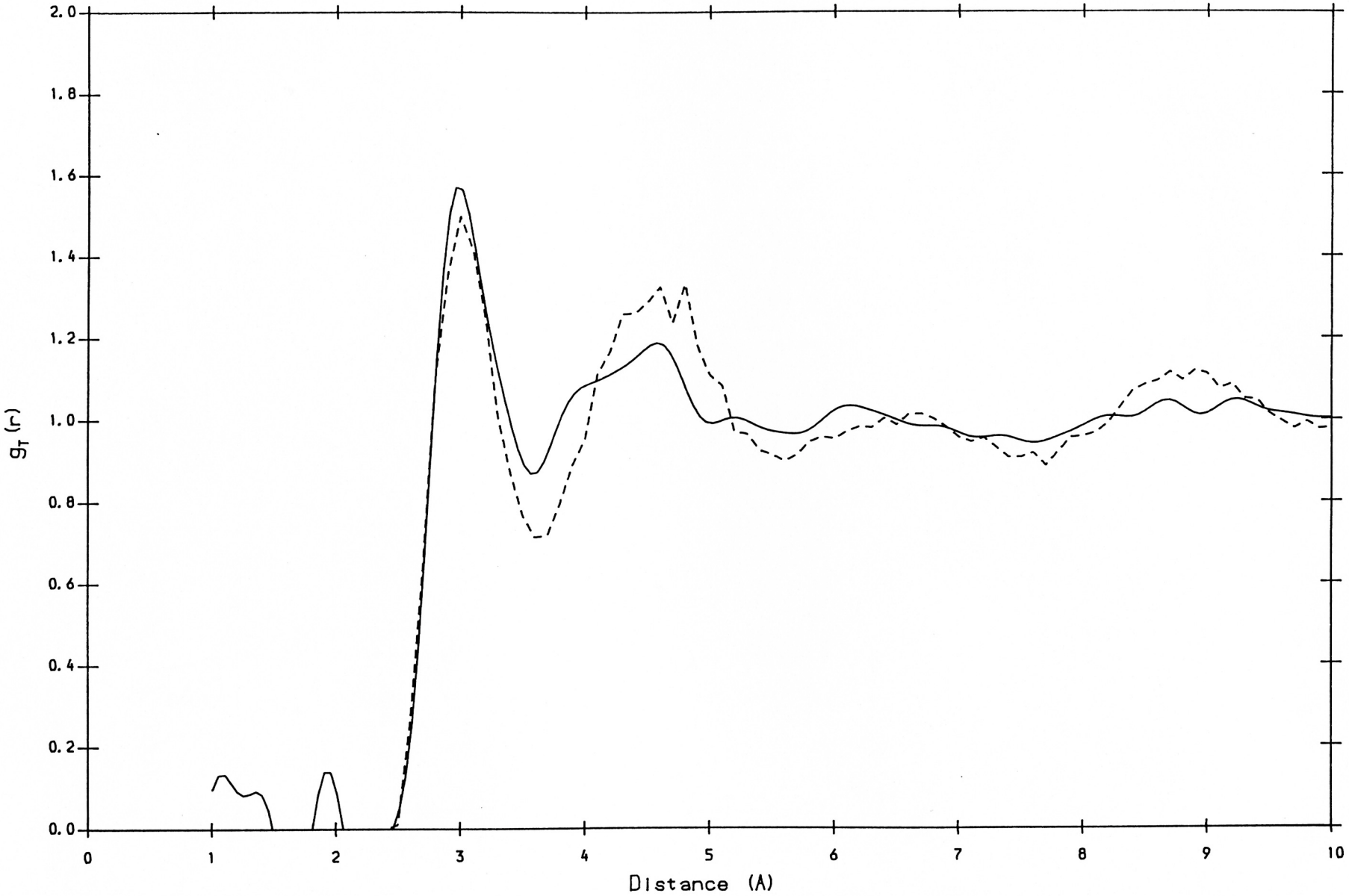


Figure 9.16 $g_T(r)$ for KCl at 1100K (solid line) compared with that obtained by simulation at 1073K (broken line).

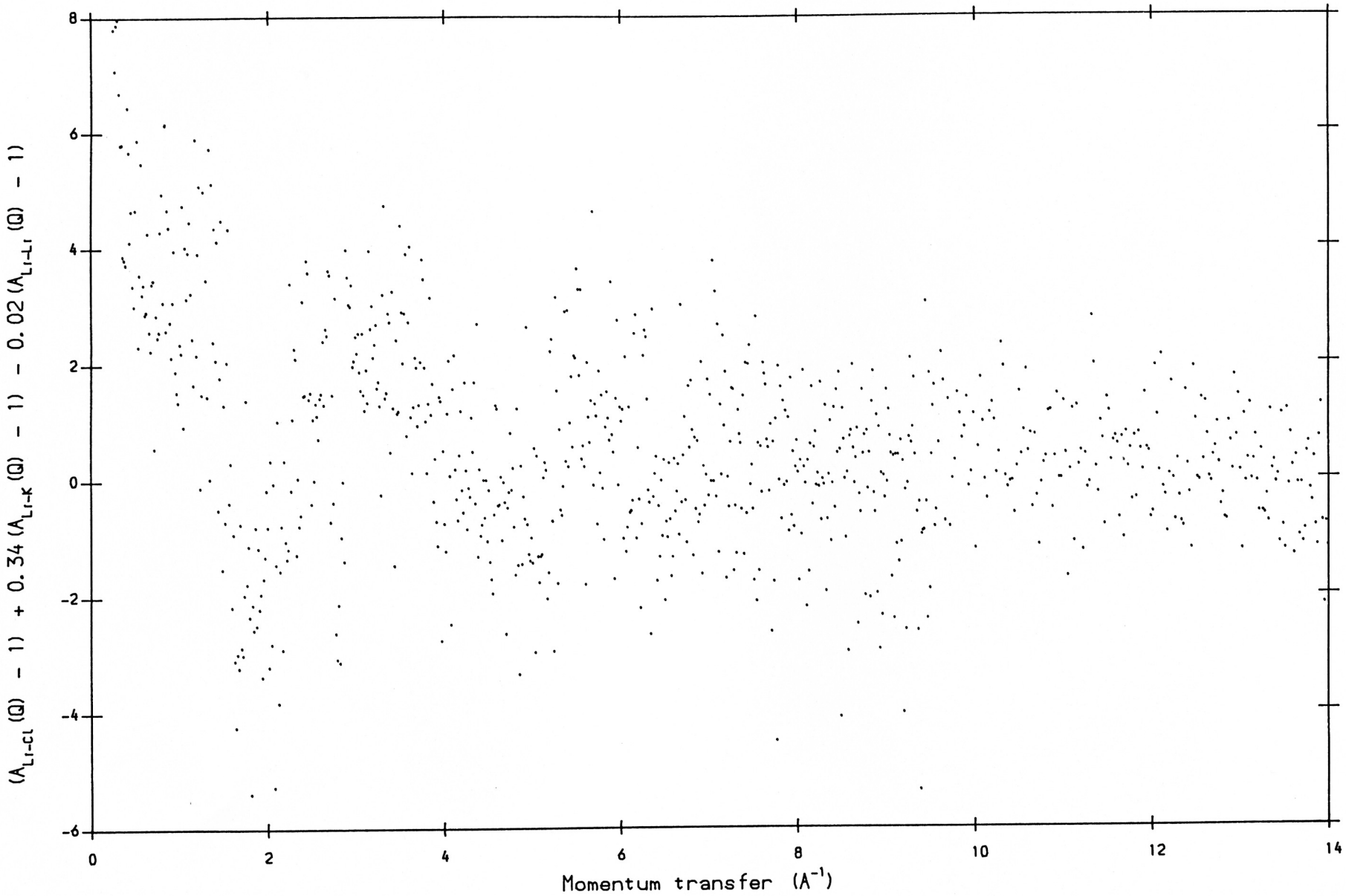


Figure 9.17 The combination of lithium partial structure factors obtained from the total structure factors of the two (Li/K)Cl samples.

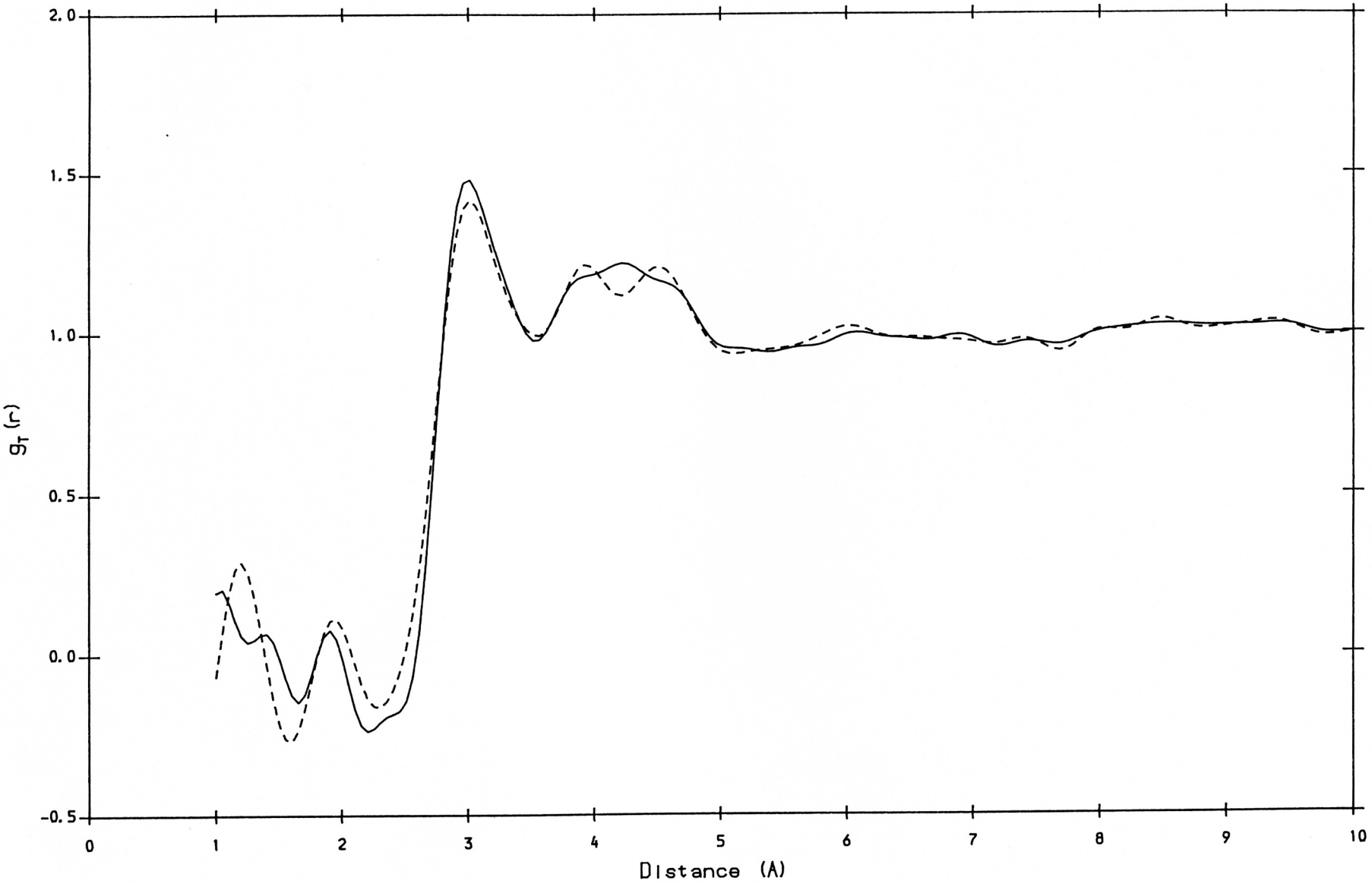


Figure 9.18 $g_T(r)$ for (^{7}Li/K)Cl (solid line) and ($^{(0)}$Li/K)Cl (broken line). $g_T(r)-1$ for the latter has been multiplied by 1.035 so that any differences between the two should be due to lithium correlations.

The statistical accuracy of these results is not very good compared to that for LiCl and that is reflected in the poor statistical quality of the combination of lithium partial structure factors shown in figure 9.17. This does not look unlike the Li-Cl partial structure factor (figure 9.6) in pure LiCl which is not suprising as the major contribution to it is from $A_{\mathrm{Li-Cl}}(Q)$. To obtain more detailed structural information this should be transformed to give a pair distribution function.

Unfortunately, as has been said, the results of this experiment cannot be considered reliable and it should be repeated. From our results we see that we really want better statistics but it is easy enough to achieve those as good as for the experiment on lithium chloride. The lithium structure factors could then be transformed to give a pair distribution function from which deductions about lithium coordination in this system can be drawn.

Chapter ten

The temperature dependence of the structure of molten caesium chloride by time-of-flight diffractometry

The experiment reported here was done in October 1986 in the early days of ISIS operation. The source was not running at anything close to full operating flux so the statistical accuracy of these results is not as good as would be expected now and it would not have been worthwhile to attempt an isotopic substitution experiment. Instead we decided to look at the temperature dependence of the structure of CsCl as this was useful for two reasons. Firstly, the total structure factor near the melting point could be compared with that previously obtained using D4B [10/1] providing a consistency check between the two and a check of the correction procedures for the LAD data. Secondly, until now all structural determinations had been done close to the melting point so nothing was known of temperature dependence (except in the case of $CaCl_2$ [10/2] for which a close Ca-Ca grouping seems to break up as the temperature is raised).

The scattering intensities for CsCl, the empty container, the empty furnace and a vanadium rod at two different scattering angles are shown in figures 10.1 and 10.2. These show the shape of the incident flux spectrum and little else. The sharp dip in the CsCl spectrum at a time of flight of $30msm^{-1}$ is due to a caesium resonance at approximately 6eV.

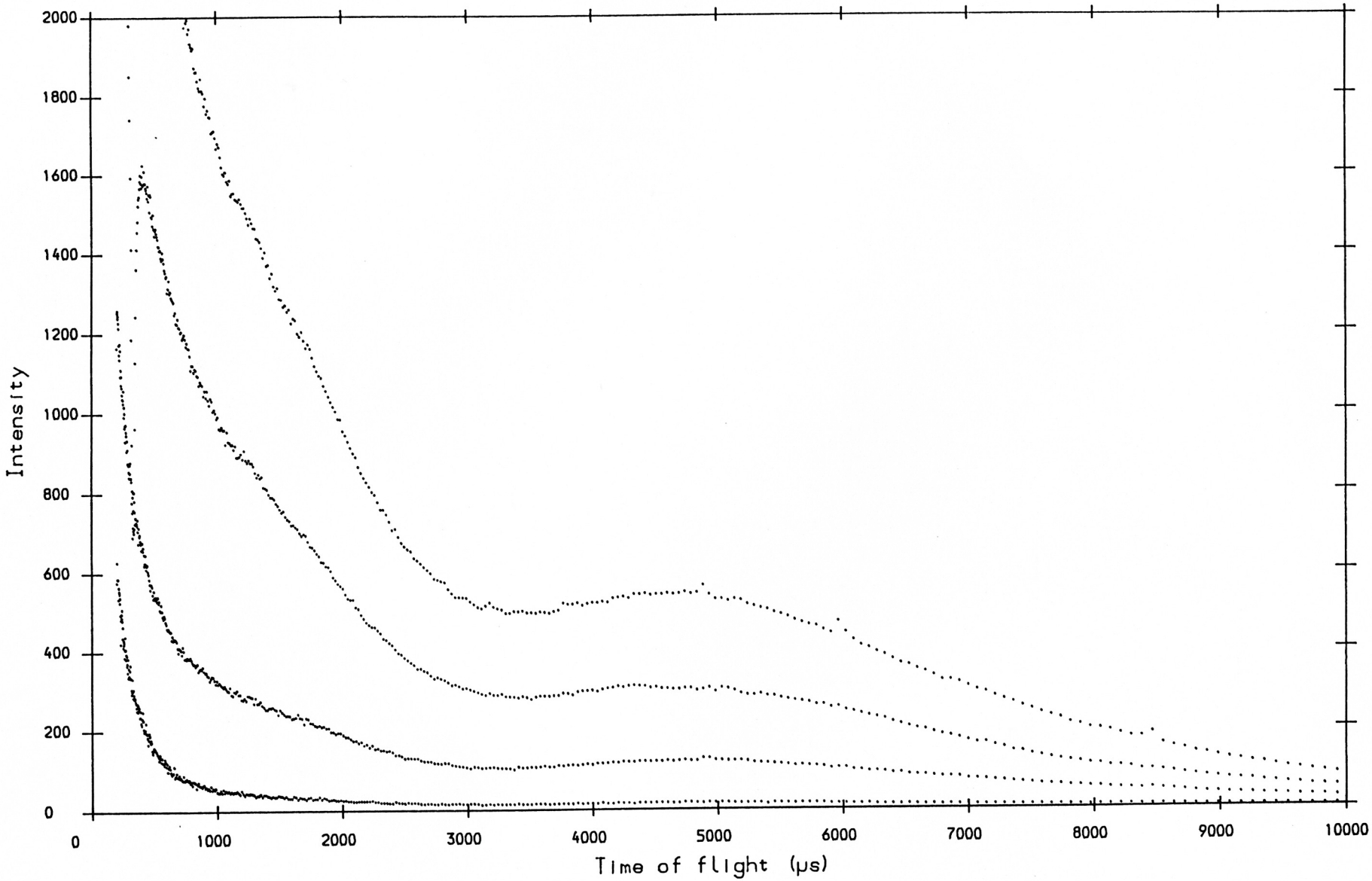


Figure 10.1 Scattering intensities at an angle of 90° for (from top to bottom) a vanadium rod at room temperature, caesium chloride at 970°C, the empty container at 670°C, and the empty furnace at room temperature.

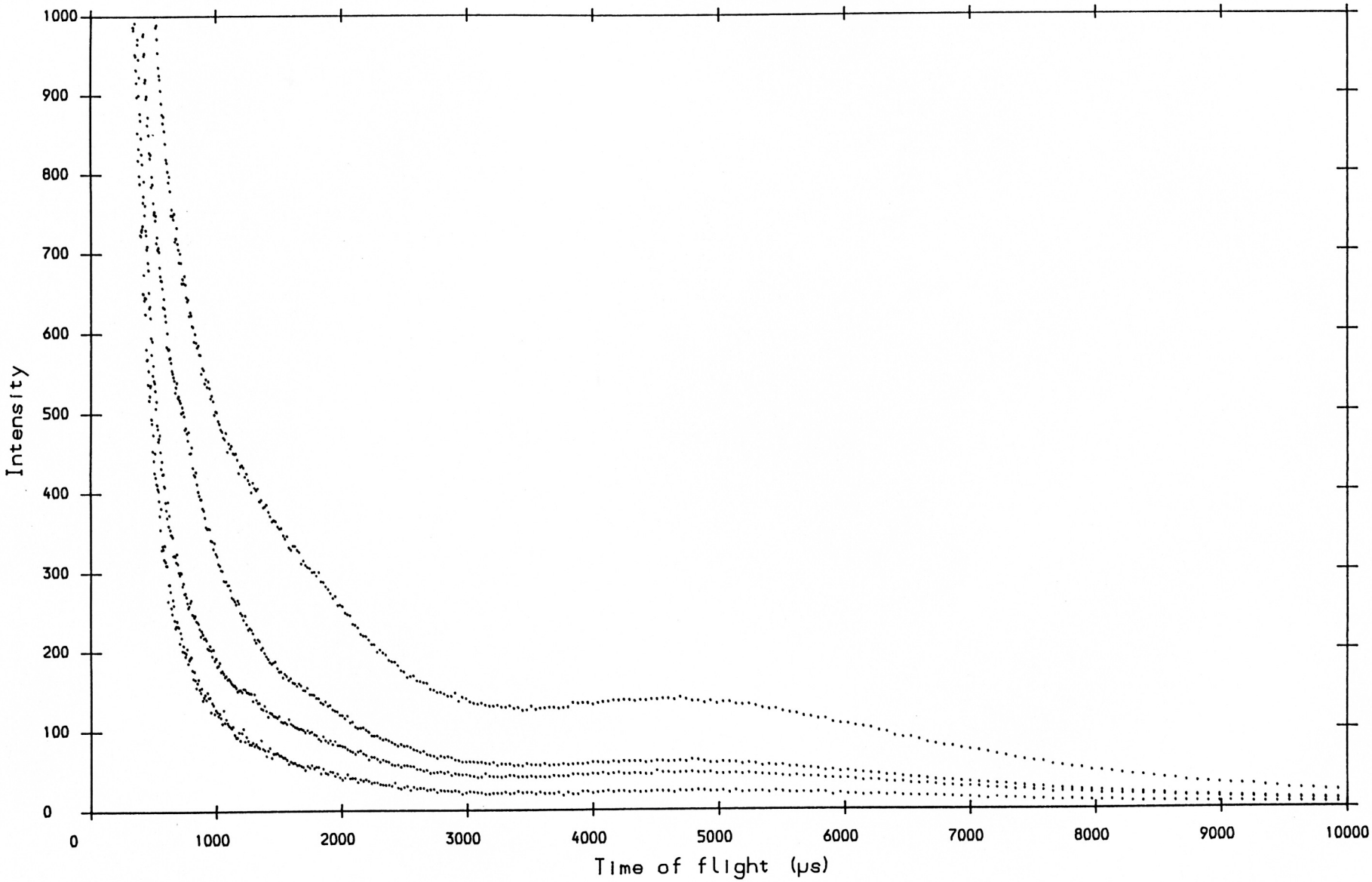


Figure 10.2 Scattering intensities at an angle of 5° for (from top to bottom) a vanadium rod at room temperature, caesium chloride at 970°C, the empty container at 670°C, and the empty furnace at room temperature.

The data is corrected in the manner previously discussed and the results are shown in figures 10.3 and 10.4. Because the experimental data consists of a large number of points, roughly 5000, per spectrum, which provides rather better resolution than is required, it has been regrouped to give fewer points, and as a consequence, better statistics. At the same time the spectra from the different detectors at the same scattering angle have been combined. The original points are at constant time of flight spacing whereas the data has been regrouped into constant Q intervals so the improvement in statistics is better at the low Q end of the spectra than at the high.

The data from the 150° detectors have been ignored as it does not start until a Q value of 2.2Å^{-1} (and, as shall be discussed shortly, this value should later be increased) and is of poor statistical quality in the region we are interested in (the statistics are good at high Q, up to about 100Å^{-1} but there is no structure in $S_T(Q)$ at these values). The caesium resonance is clearly observable in the spectra at 5° and 10°; the edge of it is visible as a slope at high Q in the spectrum at 20°. It is not possible to correct for this so the data for scattered neutron energies above 2eV has been dropped.

Comparing the spectra we note two things: they tend to slightly different values at high Q; and, less these limiting values, they agree with each other well except that the low Q end of each spectrum does not agree too well with that part of the lower angle spectra. The first of these is probably due to some sample dependent background. In calculating corrections for absorption and background scattering we have used the expressions of (6/1), in which it is assumed that the background scattering is independent of sample, that is, it is not

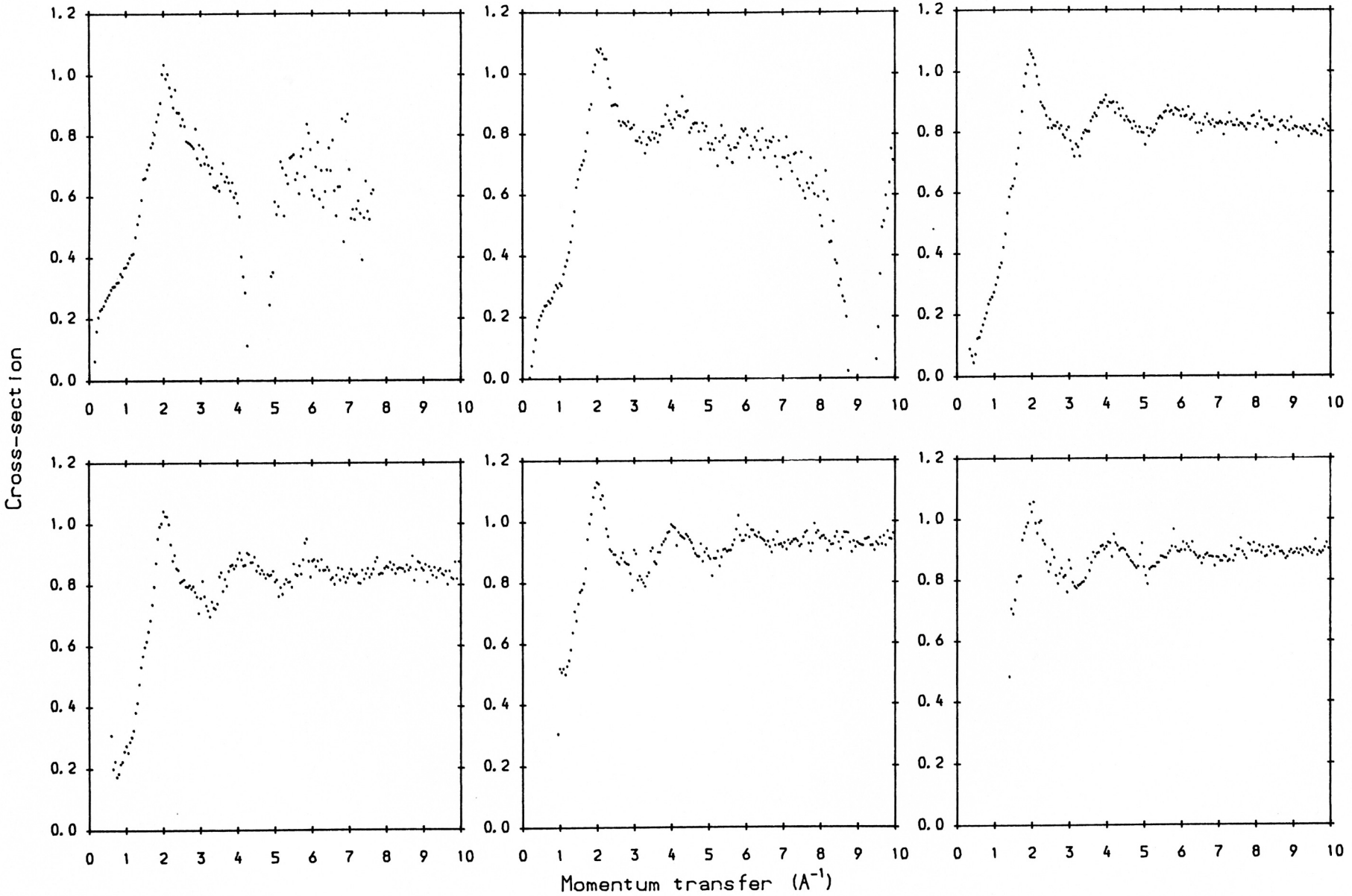


Figure 10.3 The cross-section for caesium chloride at 670°C as measured by detectors at 5°, 10°, 20°, 35°, 58°, and 90°.

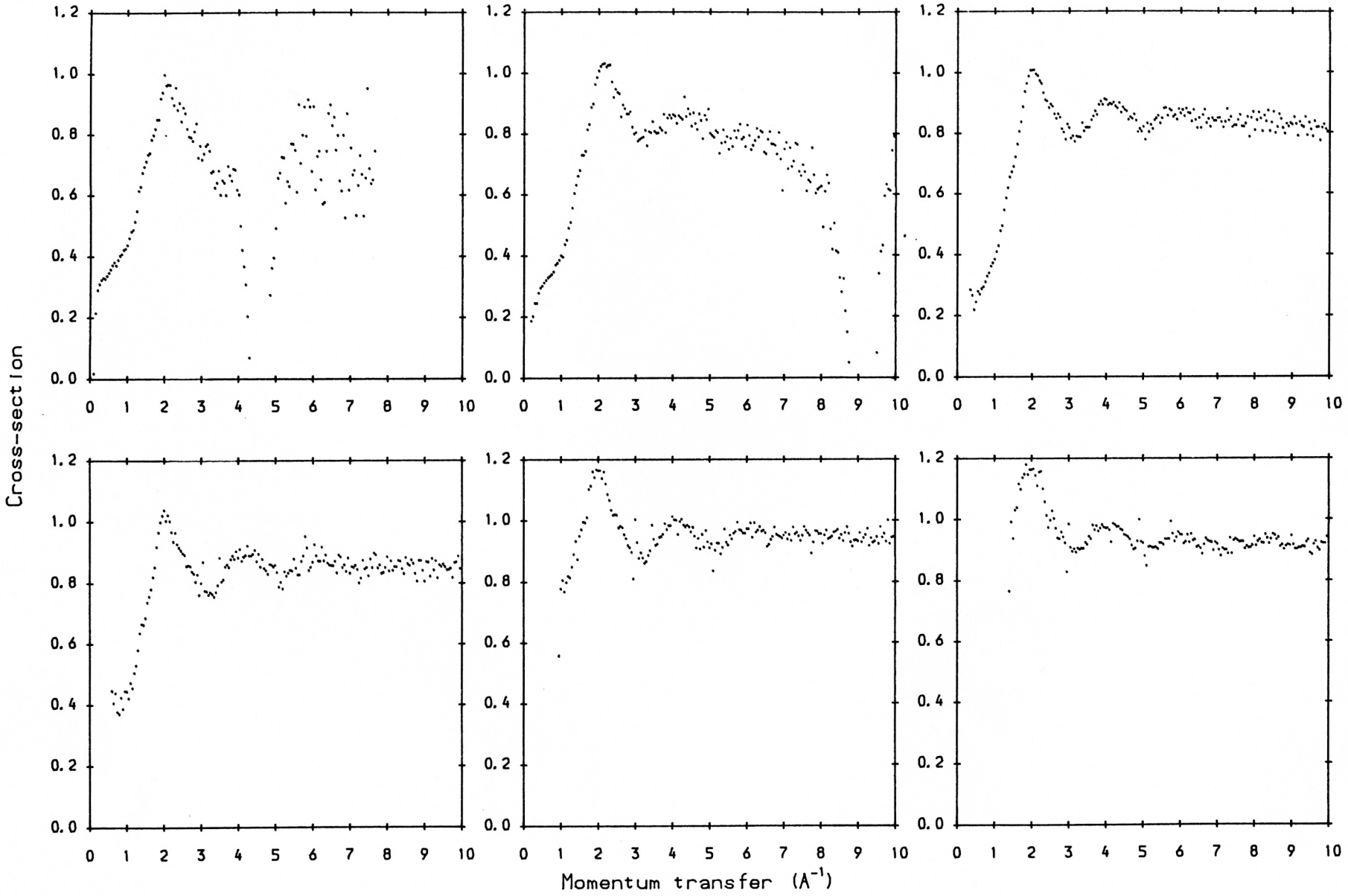


Figure 10.4 The cross-section for caesium chloride at 970°C as measured by detectors at 5°, 10°, 20°, 35°, 58°, and 90°.

absorbed. If the background scattering were attenuated by the sample then we would obtain the result observed here - the incorrect subtraction of the incoherent background (being from vanadium) would give different overall levels for the spectra at different angles. The observation that, at both temperatures, these levels follow the same pattern, decreasing with angle from 10° to 90°, supports this suggestion. The second problem is probably due to the inability to do satisfactory inelasticity corrections for the high wavelength parts of the spectra (although the high absorption and low incident flux at these wavelengths is also less than ideal) and so those regions where the correction seems unreliable (see chapter eight) have also been excluded. We are now left with the data that is shown in figures 10.7 and 10.8.

In order to combine the different spectra to give an $S(Q)$ it is necessary to subtract the high Q limit for each. Although fairly easy for the high angle detectors it is not clear what this limit is for the low angles. The solution adopted is to use a least squares method to fit the six spectra, less their high Q limits, to each other and to zero at high Q: this fit provides the six required values.

The simplest way to combine the spectra now is simply to add them together, though this really should be done taking into account their relative statistical weights. There is, though, a more sophisticated method which also allows the effects of resolution to be included: this is the maximum entropy method.

10.1 The maximum entropy method

This is based on the idea of Shannon [10/3] that there is a unique function

$$H = -\sum_{i=1}^{N} p_i \ln p_i \qquad (10/1)$$

that quantifies our lack of knowledge of an N state system for which only the probabilities p_i for the occurrence of each of the N states are given. This function is called the information entropy. In many situations we have some information about a system and wish to find an underlying distribution of the p_i's. The least biased estimate of this distribution is the one that maximises the information entropy subject to the constraints given by the information available.

We wish to find the distribution function $g(r)$, the information entropy of which may be written as [10/4]

$$H = -4\pi \int_0^R dr\, r^2 g(r)\big(ln\big(g(r)\big) - 1\big) \qquad (10/2)$$

R is a finite limit of integration necessary so that $g(r)$ may be normalisable to be a probability distribution. (In fact $g(r)$ is, strictly, not a probability distribution; and so (10/2) not quite the analogue of (10/1). It can be argued, therefore, that the technique of maximising entropy is not applicable to this problem. As, however, its effect is simply to produce a solution that agrees within statistical error with the experimental data the $g(r)$ it produces can be no less consistent with this data than one produced by any other method.) 1 is

subtracted from $\ln(g(r))$ so that, in the absence of any constraint, maximising H produces $g(r) = 1$ for all r, the result for an ideal gas of point particles.

Suppose that we have some experimental structure factor data $E(Q)$ defined at a set of equally spaced Q values Q_i from ΔQ to $Q_{\max}$. We define $S(Q)$ as the discrete Fourier transform [10/5] of $g(r)$

$$S_j = 1 + \frac{4\pi\rho}{Q_j} \sum_{i=1}^{N} \Delta r \; r_i \; sin \, Q_j r_i \; (g_i - 1)$$

where $r_i = i\Delta r$ $\quad Q_j = j\Delta Q$ $\quad S_j = S(Q_j)$

$\Delta r = \pi / Q_{max}$ $\quad \Delta Q = Q_{max}/N$ $\quad g_i = g(r_i)$

(10/3)

H is also made discrete

$$H = -4\pi \sum_{i=1}^{N} \Delta r \; r_i^2 g_i (ln \; g_i - 1)$$

(10/4)

The constraint we have is that our $S(Q)$ should fall within the error bars of $E(Q)$. This gives a chi squared constraint.

$$\frac{1}{N-1} \sum_{i=1}^{N-1} \frac{(E_k - S_k)^2}{\sigma_k^2} = 1$$

(10/5)

where $2\sigma_k$ is the length of the error bar on the measurement of E_k. We maximise H by using the method of undetermined Lagrange multipliers - so we require that

$$\frac{\partial}{\partial g_j} \left(-4\pi \sum_{i=1}^{N} \Delta r \; r_i^2 g_i (ln \; g_i - 1) - \frac{\lambda}{N-1} \sum_{k=1}^{N-1} \frac{(E_k - S_k)^2}{\sigma_k^2} \right) = 0$$

(10/6)

Or

$$-4\pi\,\Delta r\,r_j^2\,ln\,g_j + \frac{2\lambda}{N-1}\sum_{k=1}^{N-1}\frac{E_k - S_k}{\sigma_k^2}\frac{\partial S_k}{\partial g_j} = 0$$

(10/7)

Using (10/3) this gives

$$r_j\,ln\,g_j - \frac{2\lambda\rho}{N-1}\sum_{k=1}^{N-1}\frac{E_k - S_k}{\sigma_k^2}\frac{1}{Q_k}\;sin\,Q_k r_j = 0$$

(10/8)

So that

$$g_j = exp\left(\frac{2\rho\lambda}{N-1}\sum_{k=1}^{N-1}\frac{E_k - S_k}{\sigma_k^2}\;\frac{sin\,Q_k r_j}{Q_k r_j}\right)$$

(10/9)

Substituting (10/3) into this gives a set of coupled equations in the g_j which, for a given value of λ, may be solved by, for example, the Newton-Raphson method. The procedure, then, is to choose a value of the Lagrangian multiplier λ; solve (10/9) for the g_j by repeated iteration, calculate the value of the constraint function in (10/5); if this is not sufficiently close to 1 then adjust the value of the Lagrange multiplier and repeat the process until either the constraint is satisfied or no progress is being made in approaching it. This differs from the method of Root *et al* [10/4] in solving for the g_j rather than the S_i; this is because the method described here is readily extendable to include resolution as is described in the next section, whereas theirs is not.

This treatment does not allow $g(r)$ to be negative at any point. Although this is a physically reasonable requirement it ignores the fact that our experimental data will have errors in it which might be best expressed by $g(r)$ being less than zero for some parts of the low r range (where we imagine it to be zero). In some cases the structure factor corresponding to a $g(r)$ that is constrained in this way might be in far

worse agreement with the experimental data than one that could be produced if $g(r)$ were allowed to be negative. Because of this the effect of constraining $g(r)$ to be non-negative, which is of direct consequence in the low r region, might also cause significant differences elsewhere. Perhaps, then, we should allow $g(r)$ to be negative.

This can be done by changing the number density used in the calculation. If, for ρ, we put $\rho' = 2\rho$, say, then we will obtain a function $g'(r)$ that is not less than zero. This is related to $g(r)$ by

$$g'(r) - 1 = ½(g(r) - 1)$$

(10/10)

so that $g(r) \geq -1$. In this way we can obtain a $g(r)$ that is allowed to have a little error around $g(r) = 0$. By multiplying by a larger factor we can allow the oscillations about $g(r) = 0$ to be as large as we want. (Although if they need to be large there would seem to be something wrong with the experimental data.)

10.2 The inclusion of resolution effects

When the instrumental resolution is taken into account the observed scattering is no longer expected to be given by $S(Q)$ but by some function, which we will call $F(Q)$, which is related to the structure factor by some resolution function. In its most general form this is written

$$F(Q) = \int R(Q, Q')S(Q')dQ'$$

(10/11)

The structure factor is related to $g(r)$ so

$$F(Q) = \int dQ' R(Q,Q') \frac{4\pi\rho}{Q'} \int_0^\infty dr\, r\, (g(r) - 1) \sin Q'r$$

(10/12)

$$= 4\pi\rho \int_0^\infty dr\, r\, (g(r) - 1) \int_0^\infty dQ' R(Q,Q') \frac{\sin Q'r}{Q'}$$

(10/13)

$$= 4\pi\rho \int_0^\infty dr\, r^2\, (g(r) - 1)\; R(Q,r)$$

(10/14)

where

$$R(Q,r) = \int_0^\infty dQ' R(Q,Q') \frac{\sin Q'r}{Q'r}$$

(10/15)

For perfect resolution $R(Q,Q') = \delta(Q - Q')$ and $R(Q,r) = \sin Qr\,/(Qr)$. Otherwise the function $R(Q,r)$ can be calculated analytically, if possible, or numerically. To include this resolution in the maximum entropy process we have to consider data from each of the scattering angles separately as they have different resolutions.

The constraint is now

$$\frac{1}{N-1} \sum_n \sum_i \frac{(E_{ni} - F_{ni})^2}{\sigma_{ni}^2} = 1$$

(10/16)

where n labels the spectrum and N is the total number of data points for all spectra. F_{ni} is given by

$$F_{ni} = 4\pi\rho \sum_k \Delta r\, r_k^2\, (g_k - 1) R_{nik}$$

(10/17)

from which

$$\frac{\partial F_{ni}}{\partial g_j} = 4\pi\rho\,\Delta r\, r_j^2\, R_{nij}$$

(10/18)

which leads to

$$g_j = exp\left(\frac{2\rho\lambda}{N-1}\sum_n\sum_i \frac{E_{ni}-F_{ni}}{\sigma_{ni}^2}\; R_{nij}\right)$$

(10/19)

10.3 LAD resolution functions

For LAD the resolution function is approximated by a Gaussian in time of flight with a width proportional to the time of flight [10/6]

$$R(\tau,\tau') = \frac{b}{\tau\sqrt{\pi}}\, e^{-b^2(1-\tau'/\tau)^2}$$

(10/20)

where b is related to the full width at half maximum (FWHM) of the Gaussian by

$$b^2 = \frac{4\,ln\,2}{(FWHM/\tau)^2}$$

(10/21)

and the widths are given by $\Delta\tau/\tau =$ 0.11 (5°), 0.06 (10°), 0.028 (20°), 0.017 (35°) and 0.012 (58° and 90°). So, as $Q \propto 1/\tau$,

$$R(Q,Q') \propto Q\, e^{-b^2(1-\tau'/\tau)^2}$$

(10/22)

The constant of proportionality comes from the normalisation:

$$\int_0^\infty \frac{b}{\tau\sqrt{\pi}}\, e^{-b^2(1-\tau'/\tau)^2}\, d\tau' = 1$$

(10/23)

which implies that

$$\int_0^\infty \frac{bQ}{\sqrt{\pi}}\, e^{-b^2(1-Q/Q')^2} \frac{dQ'}{Q'^2} = 1$$

(10/24)

so that

$$R(Q,Q') = \frac{bQ}{Q'^2\sqrt{\pi}} e^{-b^2(1-Q/Q')^2}$$

(10/25)

And

$$R(Q,r) = \frac{bQ}{\sqrt{\pi}} \int \frac{1}{Q'^2} \frac{\sin Q'r}{Q'r} e^{-b^2(1-Q/Q')^2} dQ'$$

(10/26)

10.4 The results

The resolution effects are fairly unimportant in this case, where all the structure is fairly broad, so, given the poor statistical nature of the data, it was felt unnecessary to include them.

The different spectra have simply been added together for each temperature; the results are shown in figures 10.5 and 10.6 together with three curves: two obtained using the maximum entropy process, one allowing $g(r)$ to be negative (labelled 2), the other not (1); and one obtained by fitting cubic splines to the data points. It has been necessary to add some points below the Q range of the experiment including one at $Q = 0$. This can be done by extrapolation of the experimental data. If this is not done the maximum entropy solution gives an $S(Q)$ which diverges at low Q. In the absence of any experimental

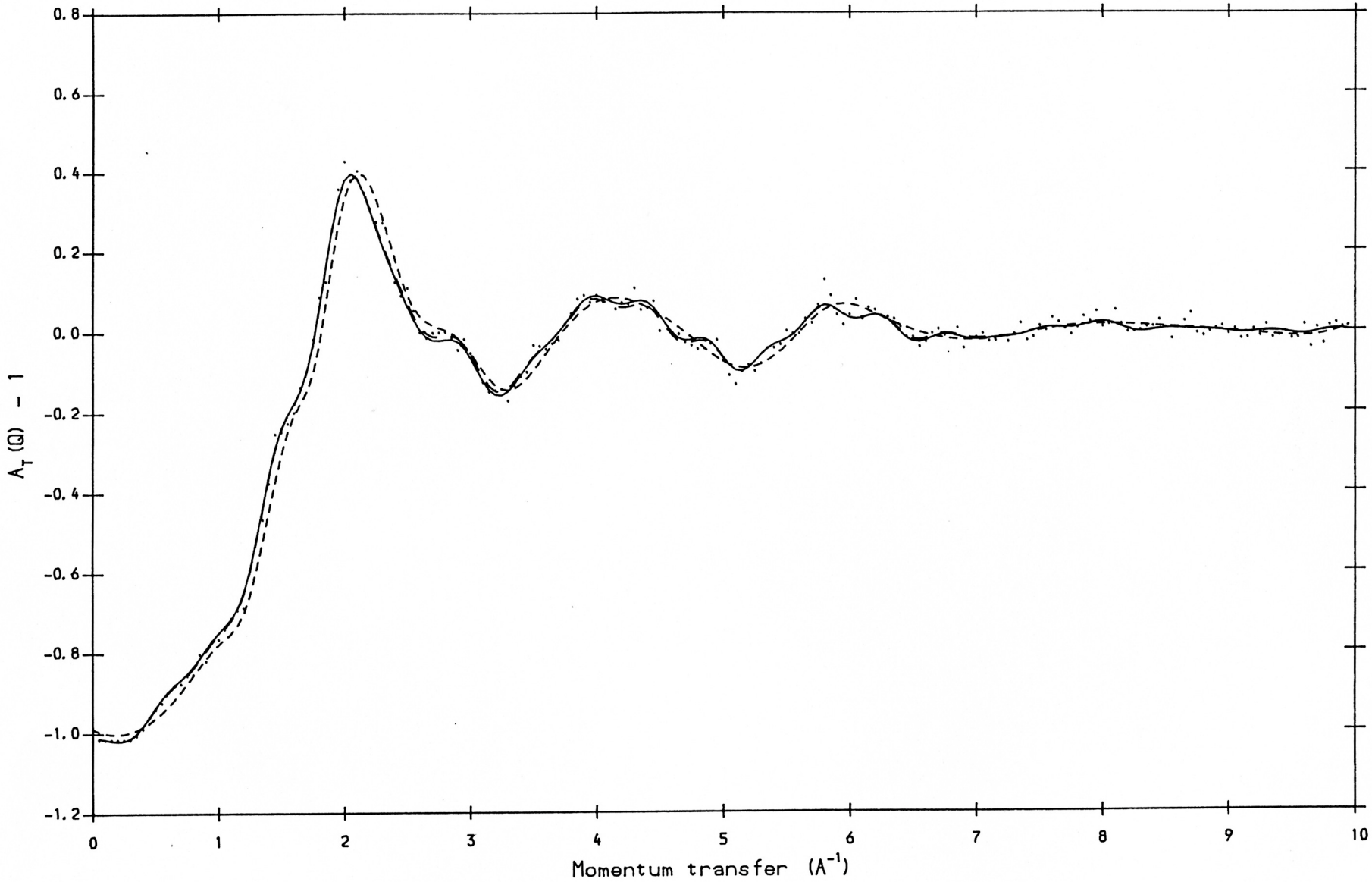


Figure 10.5 The total structure factor for caesium chloride at 670°C. The points are experimental data, the solid line is maximum entropy (1), the long dashes maximum entropy (2), the short dashes A cubic spline smoothing curve.

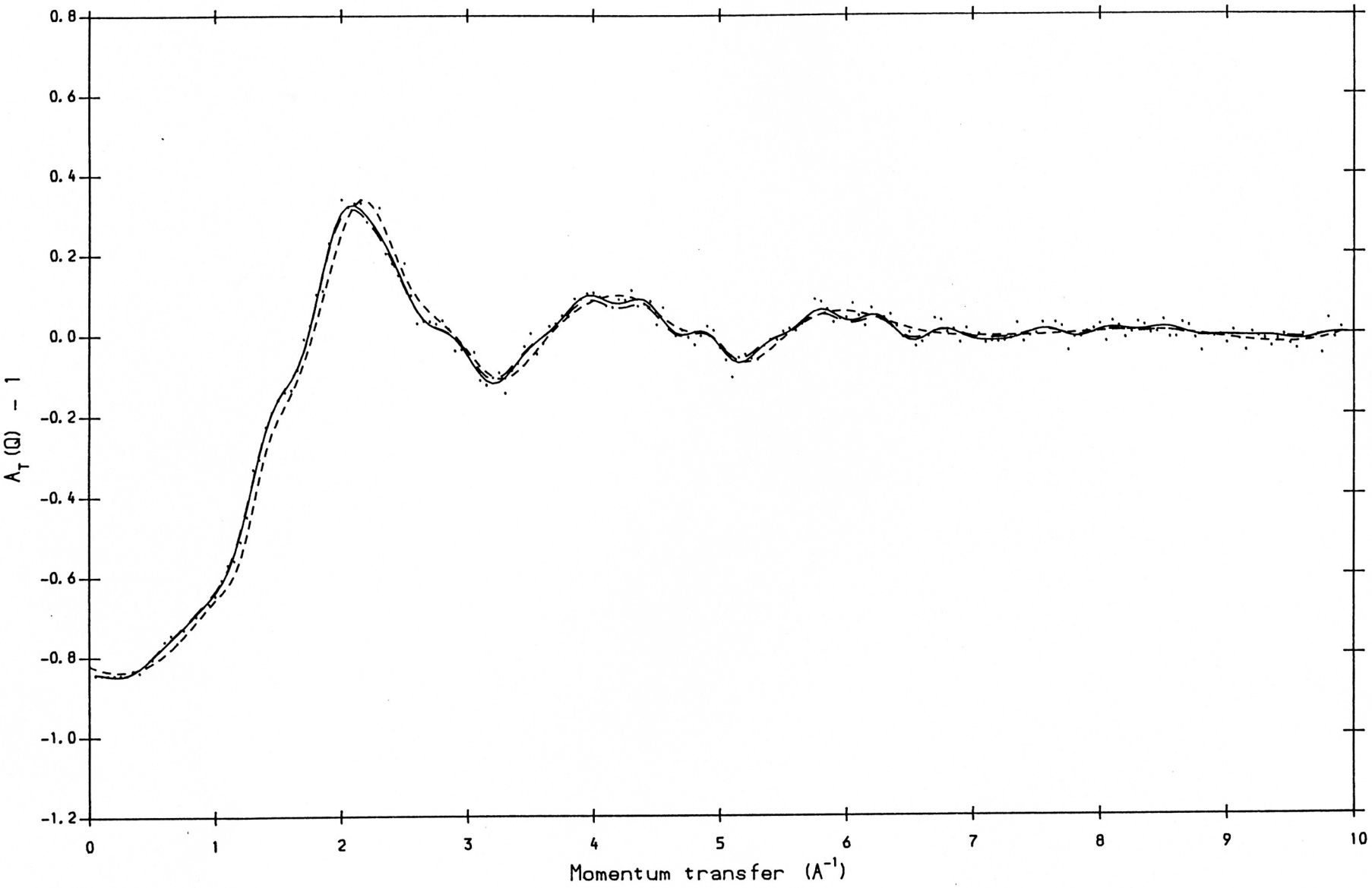


Figure 10.6 The total structure factor for caesium chloride at 970°C. The points are experimental data, the solid line is maximum entropy (1), the long dashes maximum entropy (2), the short dashes a cubic spline smmothing curve.

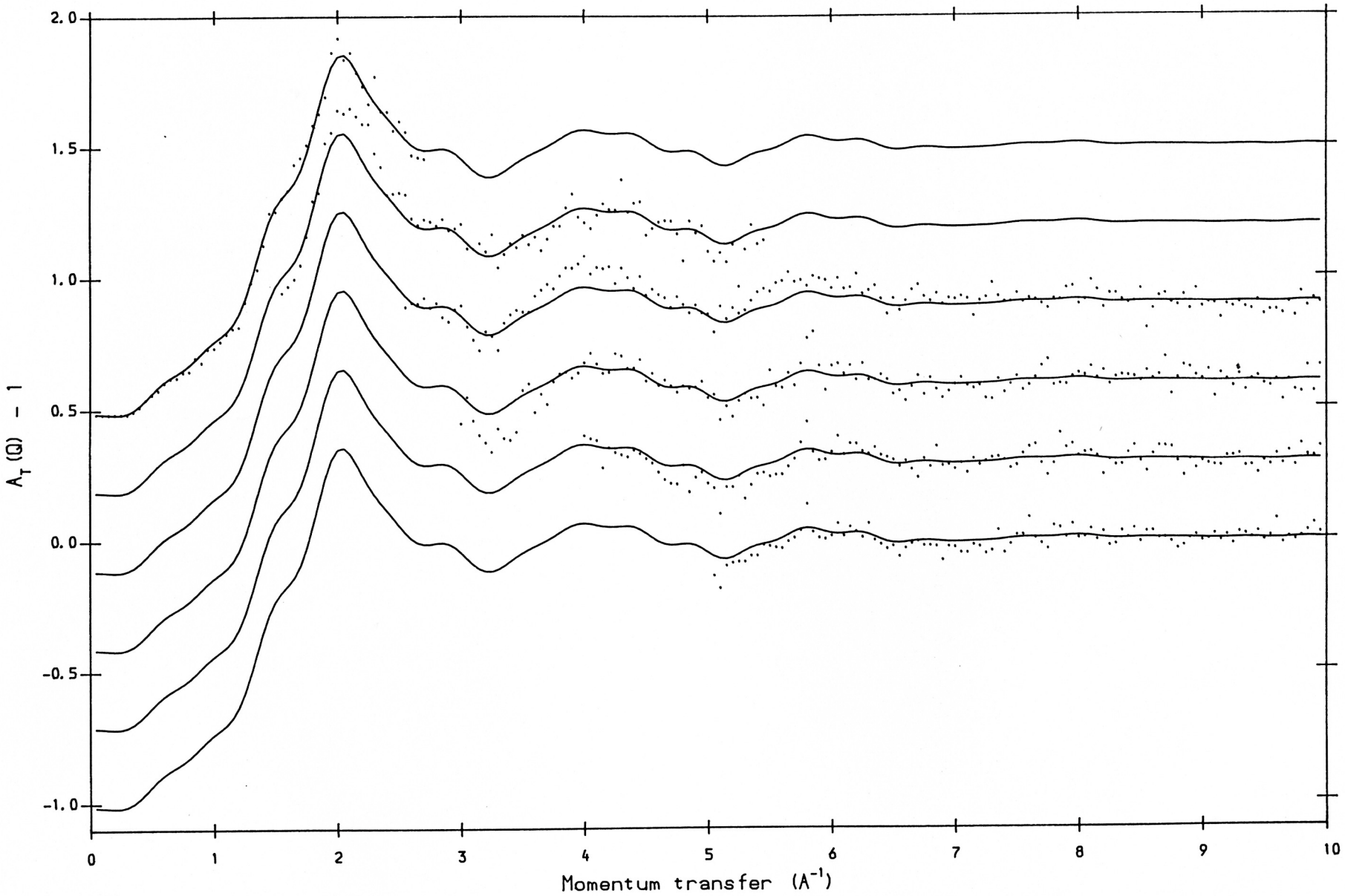


Figure 10.7 The total structure factor for CsCl at 670°C obtained by the maximum entropy method (line) compared with the experimental points for different scattering angles (top 5°, bottom 90°).

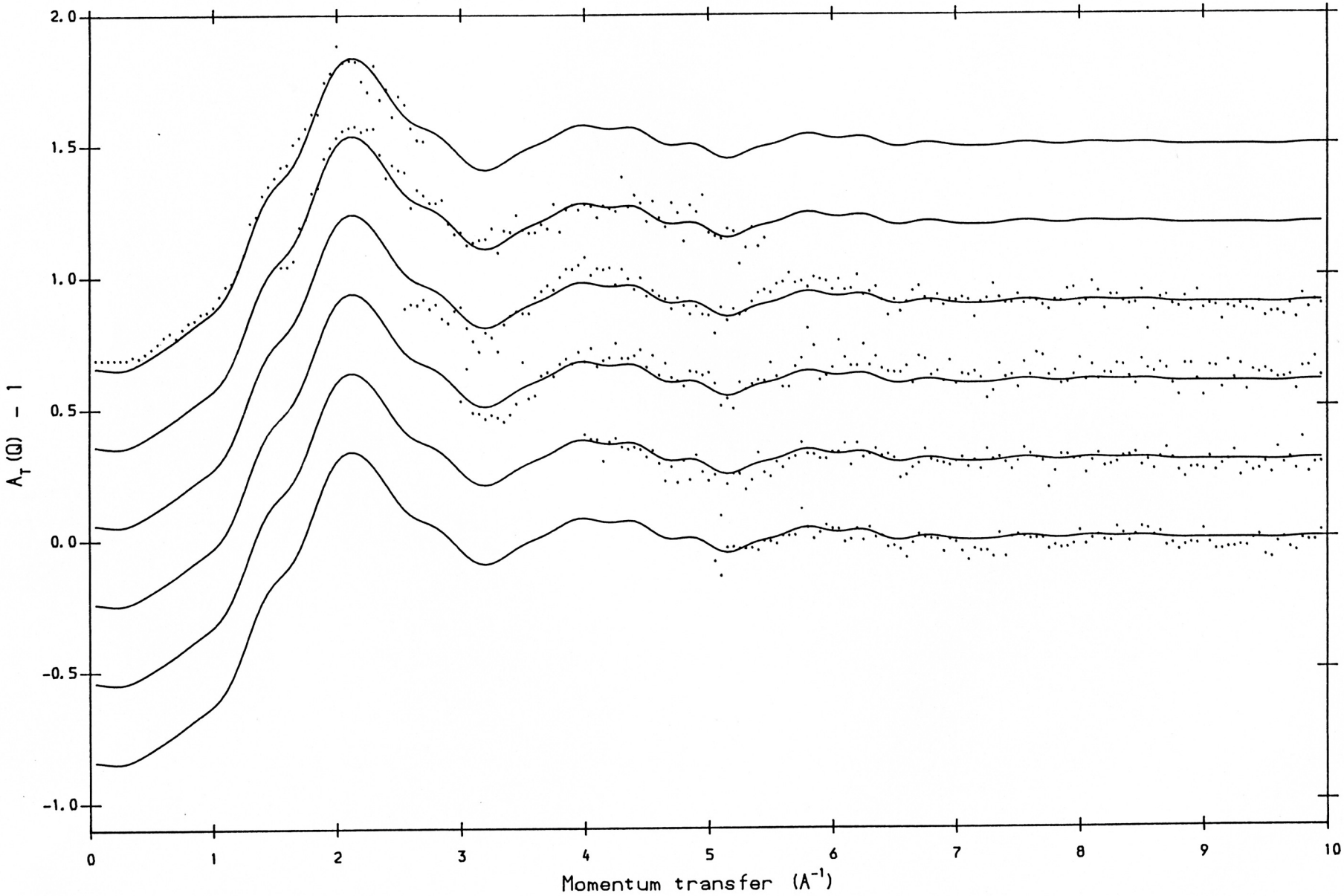


Figure 10.8 The total structure factor for CsCl at 970°C obtained by the maximum entropy method (line) compared with the experimental points for different scattering angles (top 5°, bottom 90°).

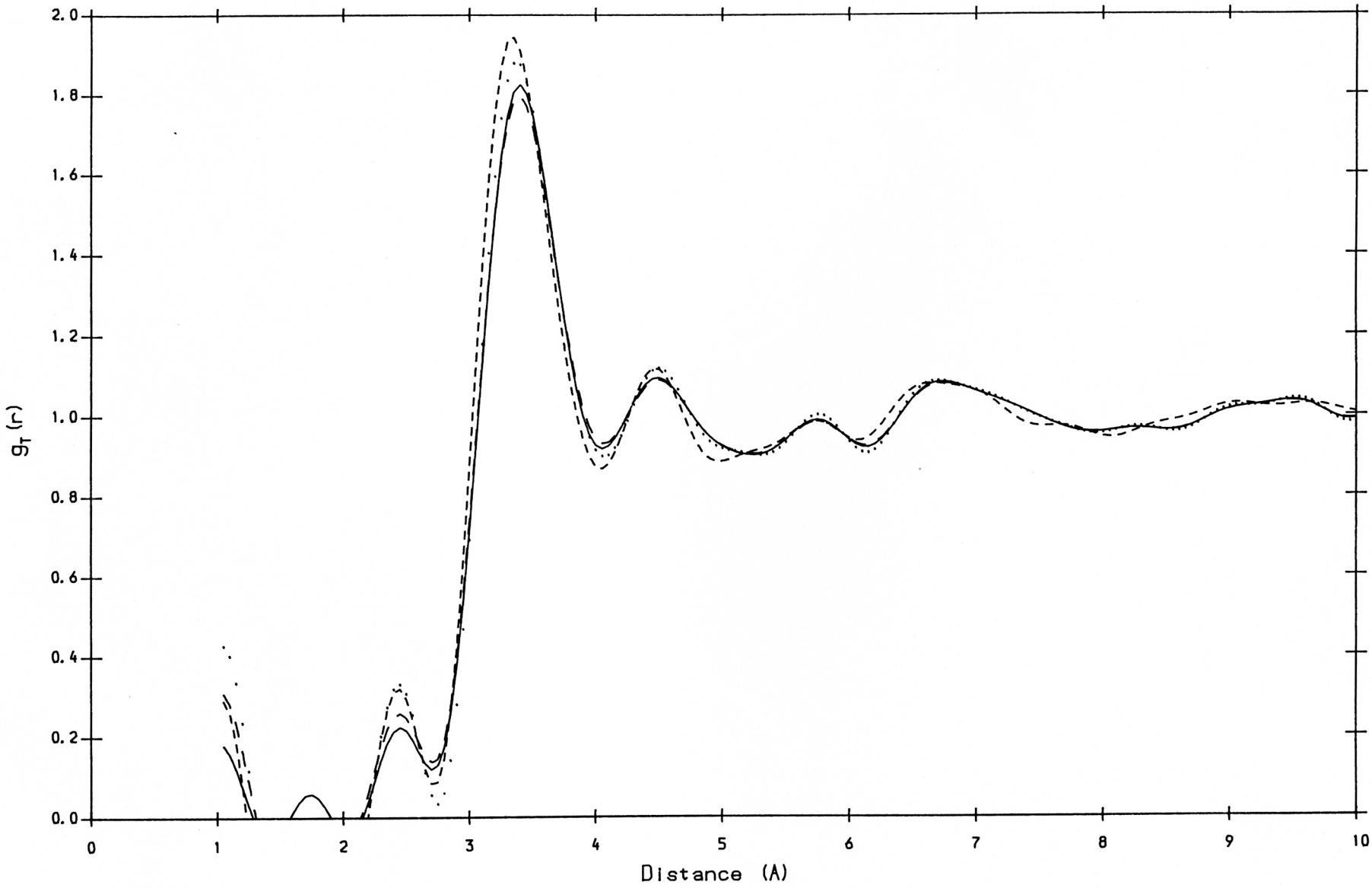


Figure 10.9 $g_T(r)$ for caesium chloride at 670°C. The points are from the experimental data, the solid line is maximum entropy (1), long dashes maximum entropy (2), short dashes from the cubic spline.

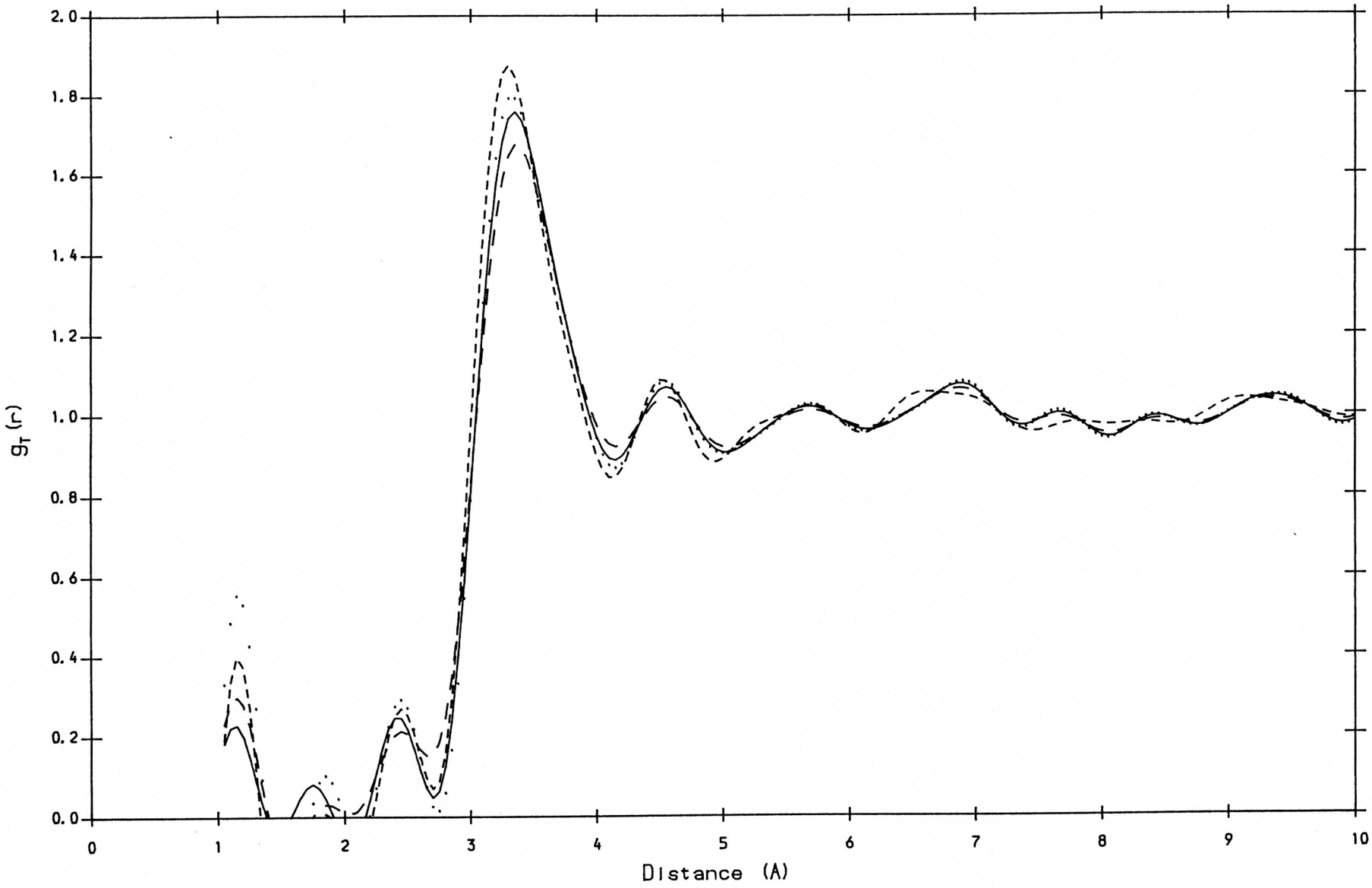


Figure 10.10 $g_T(r)$ for caesium chloride at 970°C. The points are from the experimental data, the solid line is maximum entropy (1), long dashes maximum entropy (2), short dashes from the cubic spline.

data it is more reasonable to require it to behave like the extrapolant than it is to allow it to have this behaviour. The extrapolation to $Q = 0$ is also necessary for a transformation of the experimental data points to a pair distribution function. In figures 10.7 and 10.8 the maximum entropy solution (1) is compared with the data from the separate scattering angles. These three curves transformed to $g(r)$, together with such a transformation of the unsmoothed data points, are shown in figures 10.9 and 10.10.

The two maximum entropy results give structure factors that are very similar. They show small scale oscillations for reasons that are not entirely clear. These oscillations are certainly partly due to the poor statistical quality of the result as they fall within the chi squared constraint relating the maximum entropy $S(Q)$ results to the experimental data. The cubic spline curve differs from these by a small amount over the whole Q range. As far as $g(r)$ is concerned, all four curves are quite similar. The two maximum entropy results have slightly lower peaks. This is to be expected as this method finds the $g(r)$ that is closest to unity consistent with the constraint imposed by the experimental data. The position of the main peak varies slightly between the four transforms, being slightly higher for the maximum entropy results than for the direct transforms. However, the resolution in $g(r)$, $\pi/Q_{\max}$, is only 0.3 which makes this difference insignificant. The differences between the four $g(r)$ curves for each temperature can be thought of as providing an estimate of the likely error in the result.

In figure 10.11 the result at 670°C is compared with that for the same sample measured at 695°C using D4B. The agreement is fairly good.

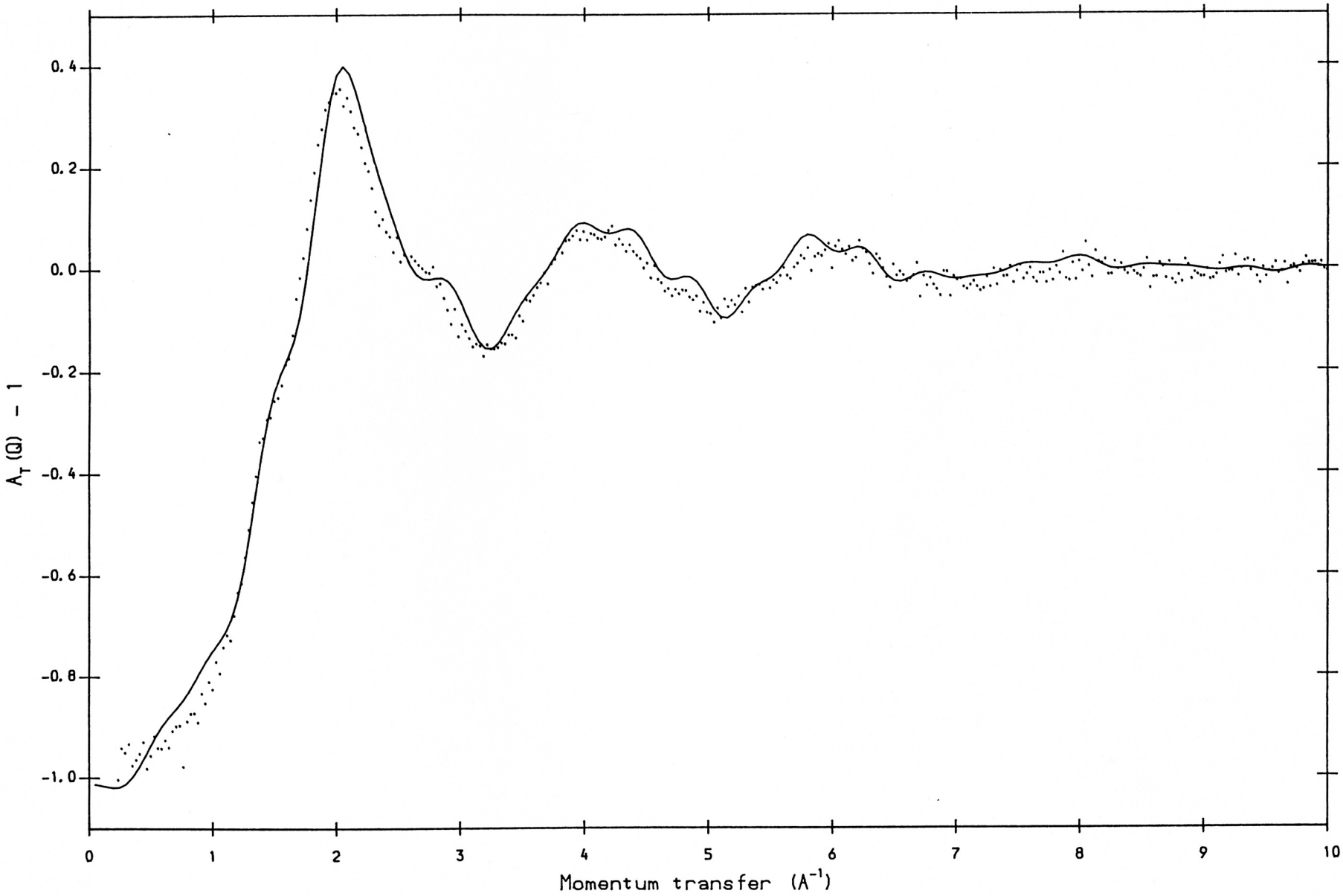


Figure 10.11 The total structure factor for caesium chloride at 670°C measured on LAD (line) compared with that at 695°C measured on D4 (points).

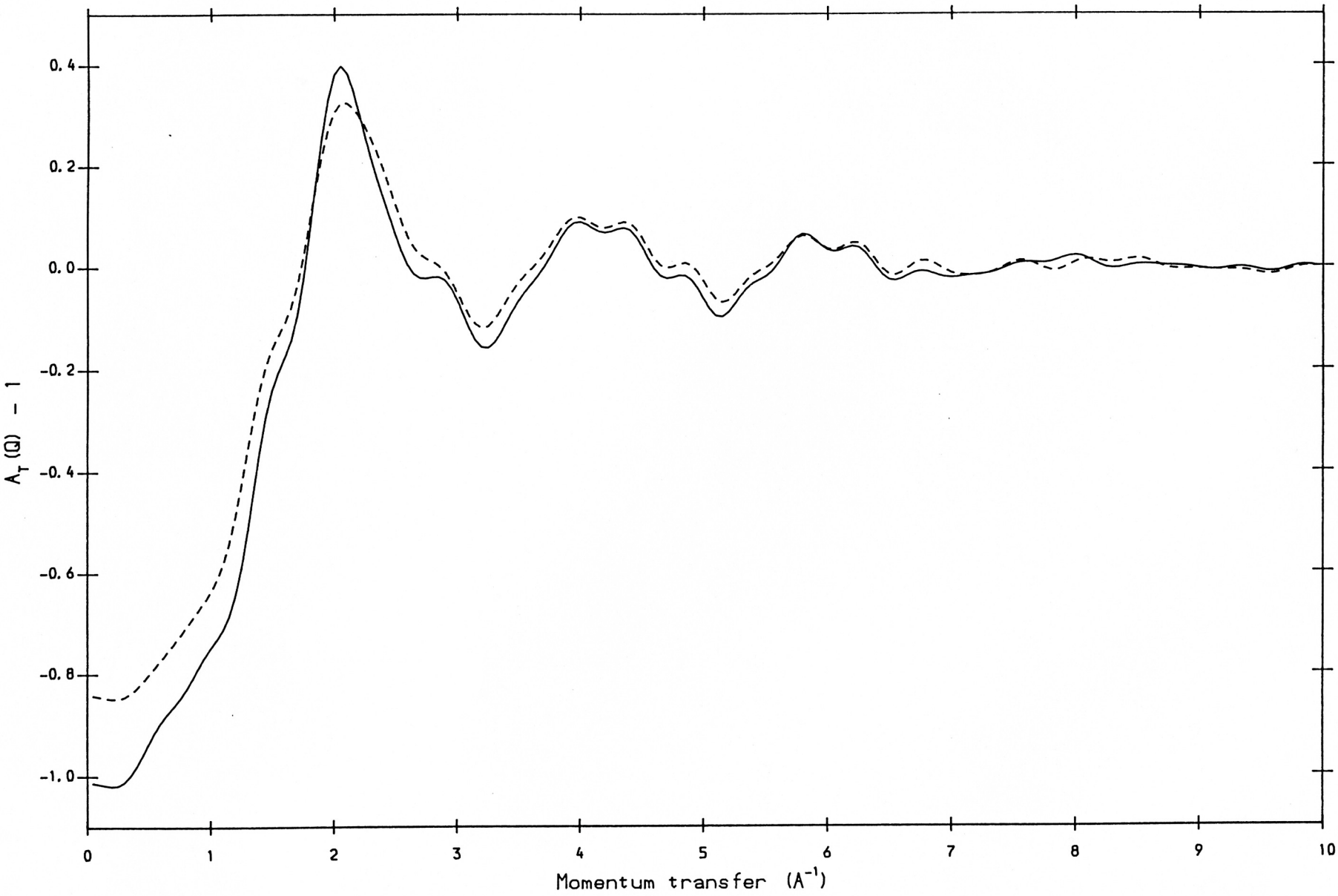


Figure 10.12 The total structure factor for caesium chloride at 670°C (solid line) and at 970°C (broken line).

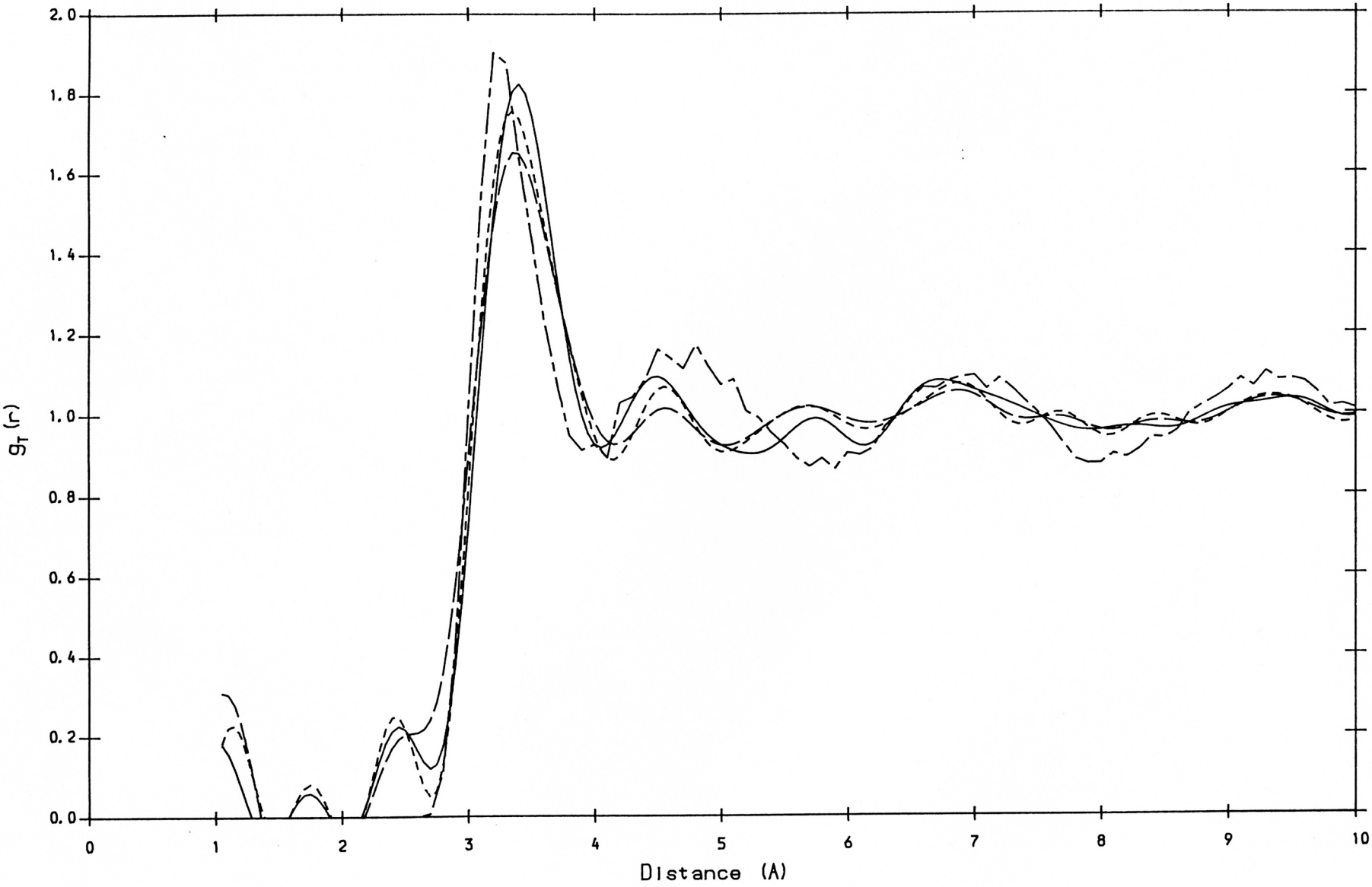


Figure 10.13 The radial distribution functions for caesium chloride at 670°C (solid line), 695°C (D4B data - short dashes) and 970°C (long dashes) compared with that obtained by Monte Carlo simulation at 700°C (long and short dashes).

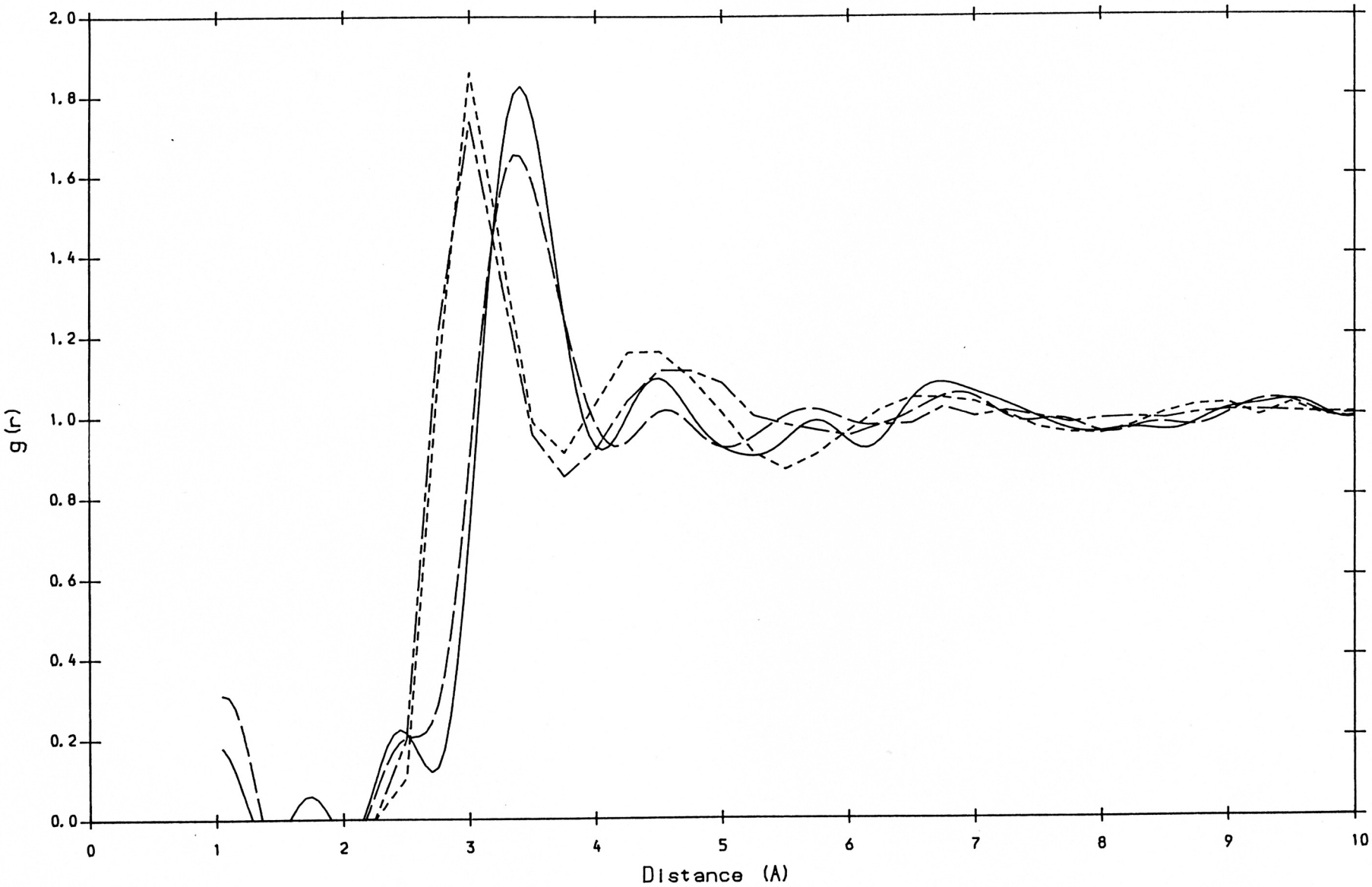


Figure 10.14 The radial distribution functions for CsCl at 670°C (solid line), and 970°C (long dashes) compared with those from a molecular dynamics simulation at 670°C (short dashes) and 970°C (long and short dashes).

The total structure factors at the two temperatures are compared in figure 10.12. The major differences are that the low Q part increases with temperature and the first peak broadens. The first of these is required to conform to the compressibility limit (see chapter three) which gives a value for $A_T(0)$ of -0.97 at 670°C and -0.86 at 970°C.

The difference observed between the pair distribution functions is quite small as can be seen from figure 10.13 where they are compared together with the result for the same sample on D4B and with simulation data. The first peak appears to have decreased slightly in height and broadened very slightly as the temperature has increased from 670°C to 970°C. There is no observable change in its position (the increase in density of 13% might suggest that it should move by about 4%).

Simulation had produced better agreement with the experimental data (obtained at 695°C) when done at a higher temperature. It had been suggested, then, that the differences between simulation and experiment for caesium chloride were a result of the temperature scaling of the potential. The change with temperature now observed experimentally is not of the kind required to support this suggestion.

Chapter eleven

The dynamics of molten caesium chloride

11.1 Principles of data interpretation

We are looking for evidence of collective modes. These correlated motions present themselves as peaked contributions, centred at non-zero energy, to the dynamic structure factor $S(Q,\omega)$ (as observed at constant Q) although they are not necessarily observable as peaks. At very low Q values sound wave modes are well defined and produce two sharp Lorentzian peaks (one at positive energy transfer, one at negative), known as the Brillouin doublet, observable, and clearly distinguishable from the central quasi-elastic peak (also Lorentzian), by light scattering. The optic modes are not so clearly defined in the Raman spectra, though in many salts (but not in caesium chloride) they produce a shoulder (or, in the case of magnesium chloride, a peak) at energies of l0meV to 20meV in the polarised light scattering. Because there are contributions to the Raman scattering from all Q values this cannot be associated with any particular momentum transfer. Results of simulation on sodium iodide [11/1] suggest that peaks are observable in $S_{MM}(Q,\omega)$, corresponding to acoustic modes, up to $Q \approx 0.25 Å^{-1}$ and in $S_{qq}(Q,\omega)$, corresponding to optic modes, up to $Q \approx 0.5 Å^{-1}$. As the momentum transfer increases so does the width of these peaks causing them to overlap the central quasi-elastic peak and, when their width is greater than their

energy, each other: this means that they no longer exhibit themselves as peaks in the dynamic structure factor.

There is a certain amount of disagreement over whether collective excitations can be said to exist if they do not cause peaks in $S(Q,\omega)$. However, one can follow such modes, as Q increases, from a peak to a shoulder in the structure factor and it seems somewhat arbitrary to say that they disappear as soon as the peak turns into a shoulder. Certainly, though, these are not long range collective excitations, as are phonons found in a crystal; they probably extend no further than the next coordination shell.

We can calculate $S(\theta,\omega)$ from our experimental data; it is then convenient to transform this to a function, $S(Q,\omega)$ defined on a grid of points in $(Q-\omega)$ space. This is done either by interpolation or by grouping of the experimental points depending on the resolution required. As we are usually in the region of 'over-damped' modes, that is where there are no peaks observable in $S(Q,\omega)$, we calculate the power spectrum $C_T^L(Q,\omega)$ and use the positions of the peaks in this as an indication of the position of the underlying modes. This tends to slightly overestimate the energy of these modes; further, a little care must be taken in the interpretation as $C(Q,\omega)$ must have a maximum somewhere. As we are looking at quite broad modes care must also be taken in assigning significance to a peak in a function observed along some line in (Q,ω) space, a line of constant Q for example, as such a peak is not necessarily a maximum of the function (that is, a maximum of a constrained function is not necessarily a maximum of the unconstrained function). We must consider the true two dimensional nature of the

functions $S(Q,\omega)$ and $C(Q,\omega)$ to make sure that these peaks do, in fact, represent such maxima.

Rather than calculate $S(Q,\omega)$ or $C(Q,\omega)$ we can also look at the scattering cross-section as this is (from (6/9)) proportional to $S(Q,\omega)$ at low energy transfers and to $C(Q,\omega)$ at high.

11.2 Charge-charge and mass-mass correlations

Because of the binary nature of molten salts we expect there to be two collective modes; in a crystal these are the acoustic and optic modes. Ideally, we would describe these using the correlation functions of two variables (A and B) , $S_{AA}(Q,\omega)$ and $S_{BB}(Q,\omega)$ chosen so that the cross-correlation $S_{AB}(Q,\omega)$ is zero for all Q and ω. For an ionic crystal the appropriate variables are atomic mass and charge, the mass-mass current correlations being the acoustic mode and the charge-charge the optic. At $Q=0$ these are also appropriate to a molten salt. Computer simulation studies suggest that they are good variables for Q values up to the position of the main peak in $S(Q)$; that is, $C^L_{Mq}(Q,\omega)$ is small and the low and high energy modes appear in $C^L_{MM}(Q,\omega)$ and $C^L_{qq}(Q,\omega)$ respectively with frequencies close to those of the corresponding acoustic and optic modes in the crystal. I shall use the terms acoustic and optic to refer to these modes at all Q values with no intention of implying that they are strictly mass-mass or charge-charge in nature at all points. At high Q (greater than roughly 10Å^{-1}) these modes should tend to the single particle, gas-like, limit so the appropriate description is in terms of particle type. In between these two limits the choice of mass and charge as variables may be approximately valid over certain ranges but where $S_{Mq}(Q)$ is large there is a significant amount of coupling of mass-mass

and charge-charge currents (that is, they are not independent) and the two modes come closer together in energy. Isotopic methods allow $C^L_{MM}(Q,\omega)$ and $C^L_{qq}(Q,\omega)$ to be separated and so it is possible to examine the extent of this coupling.

11.3 Charge and mass correlations in caesium chloride

As the IN4 experiment presented in this chapter was intended to supplement a previous experiment using IN6 [11/2] I shall briefly describe this earlier experiment in which isotopes were used in order to separate the charge-charge and mass-mass currents. The cross-section for inelastic scattering can be written as

$$\frac{1}{N}\frac{d^2\sigma}{d\Omega d\omega} = \frac{k}{k_0}\Big(\big(\overline{b^2}_+ - \bar{b}^2_+\big)S_+(Q,\omega) + \big(\overline{b^2}_- - \bar{b}^2_-\big)S_-(Q,\omega) + \bar{b}^2_+ S_{++}(Q,\omega) + 2\bar{b}_+\bar{b}_- S_{+-}(Q,\omega) + \bar{b}^2_- S_{--}(Q,\omega)\Big) \tag{11/1}$$

We may also write this in terms of the set of partial structure factors based on charge and mass, giving

$$\frac{1}{N}\frac{d^2\sigma}{d\Omega d\omega} = \frac{k}{k_0}\frac{1}{\omega^2}\Big(\omega^2\big(\overline{b^2}_+ - \bar{b}^2_+\big)S_+(Q,\omega) + \omega^2\big(\overline{b^2}_- - \bar{b}^2_-\big)S_-(Q,\omega) + a_M^2 C^L_{MM}(Q,\omega) + 2a_M a_q C^L_{Mq}(Q,\omega) + a_q^2 C^L_{qq}(Q,\omega)\Big) \tag{11/2}$$

$$= \frac{k}{k_0}\frac{1}{\omega^2}\ \overline{a^2} C^L_T(Q,\omega) \tag{11/3}$$

where, for an alkali halide, the coefficients are given by

$$a_M = \bar{b}_+ + \bar{b}_- = \begin{cases} 1.715 \text{ for } Cs^{35}Cl \\ 1.509 \text{ for } Cs^{N}Cl \\ 0.874 \text{ for } Cs^{37}Cl \end{cases}$$

(11/4)

$$a_q = \frac{2(\bar{b}_+ M_- - \bar{b}_- M_+)}{M_+ + M_-} = \begin{cases} -1.584 \text{ for } Cs^{35}Cl \\ -1.268 \text{ for } Cs^{N}Cl \\ -0.268 \text{ for } Cs^{37}Cl \end{cases}$$

(11/5)

It is then possible to calculate

$$\frac{C_T^L(Cs^{37}Cl)}{2.586} - \frac{C_T^L(Cs^{N}Cl)}{18.682} = C_{MM}^L - 0.449C_{Mq}^L + \omega^2(0.26S_+ + 0.006S_-)$$

$$\approx C_{MM}^L(Q,\omega)$$

(11/6)

and

$$\frac{C_T^L(Cs^{N}Cl)}{2.76} - \frac{C_T^L(Cs^{37}Cl)}{1.826} = C_{qq}^L - 1.743C_{Mq}^L + \omega^2(0.162S_+ + 0.125S_-)$$

$$\approx C_{qq}^L(Q,\omega)$$

(11/7)

where we can write the approximate equalities because it is assumed that the cross-correlation term, $C_{Mq}^L(Q,\omega)$ is small (the statistical accuracy of the results does not allow us to actually determine it). Assuming this we expect the peaks in $C_{MM}^L(Q,\omega)$ and $C_{qq}^L(Q,\omega)$ to be well separated. As it is shown, this is the case; it then follows that the assumption is good.

In this way functions approximating to $C_{MM}^L(Q,\omega)$ and $C_{qq}^L(Q,\omega)$ were calculated and from the positions of the peaks in these dispersion curves for the charge-charge (optic) and mass-mass (acoustic) modes were plotted. These are shown in figure 11.1. It can be seen that the acoustic and optic modes are, in general, well separated although they

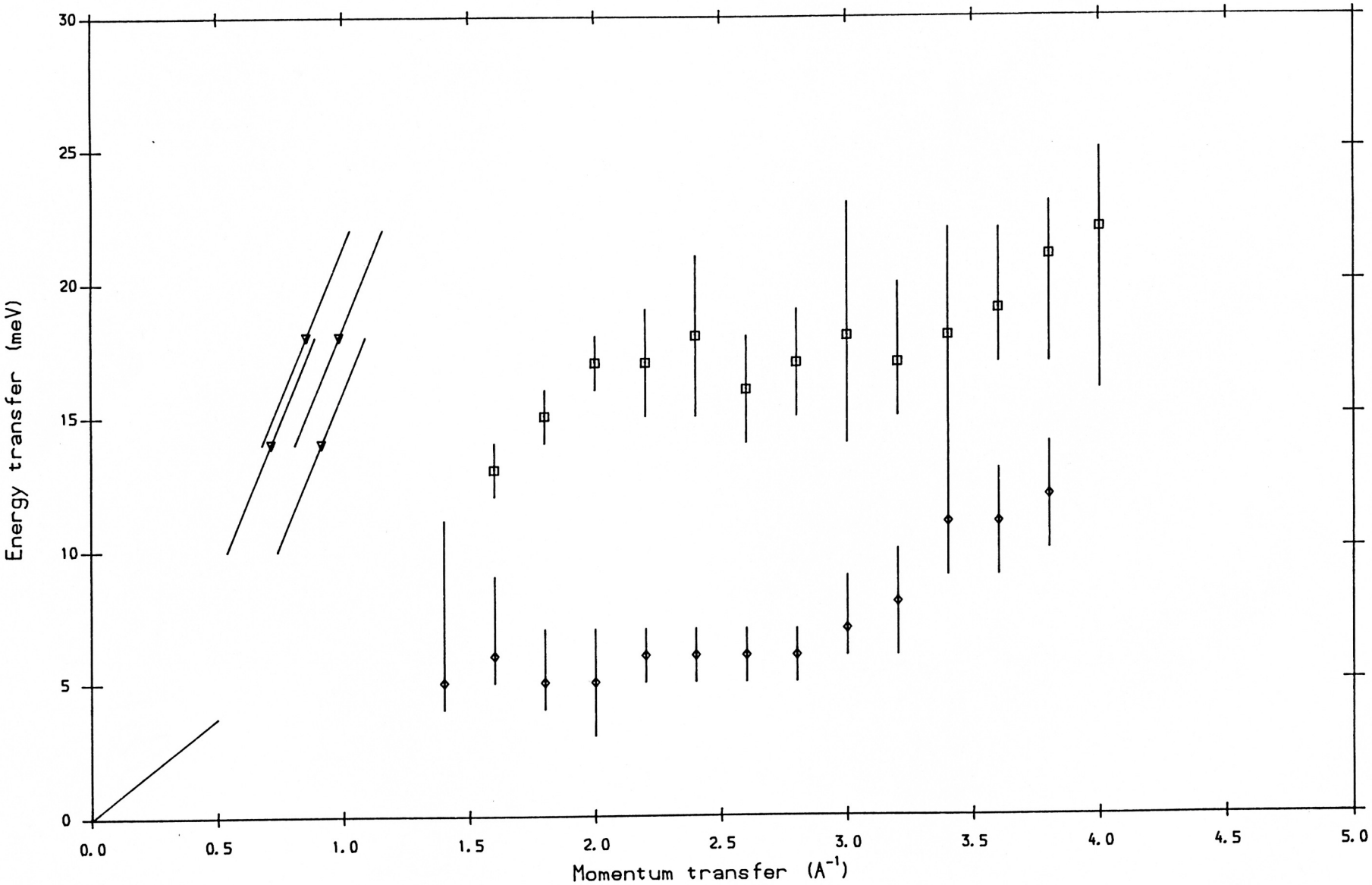


Figure 11.1 Quasi-dispersion curves for molten caesium chloride. Peak positions of $C^{L}_{MM}(Q,\omega)$ (◇) and $C^{L}_{qq}(Q,\omega)$ (□) from IN6 data and of $C^{L}_{T}(Q,\omega)$ (▽) from IN4 data are shown. The solid line represents the velocity of sound.

seem to approach each other in energy at $Q \approx 1.4 Å^{-1}$ which is where S_{Mq} has a pronounced maximum [11/3]. The acoustic mode can easily be extrapolated to the sound velocity [11/4] (note that the line representing the sound velocity in figure 11.1 differs from that of [11/2] which is in error); nothing can be inferred from the IN6 data about the behaviour of the optic mode for momentum transfers of less than $1.5 Å^{-1}$.

11.4 An experiment using IN4

The IN4 experiment was intended to obtain some information in this low Q region inaccessible with IN6. The cross-section here is low, and the incident flux on IN4 is lower than that on IN6, so an experiment using isotopes was not feasible. In any case the charge-charge and mass-mass correlations are expected to be well separated in energy at these Q values. With an incident neutron wavelength of 1.04Å spectra were obtained for molten CsCl at 700°C, an empty vanadium container and the empty furnace. The spectra for negative angles were added to those of the corresponding positive and then the 1024 time channels of each spectrum were paired to give 512 of width 8μs ($\Delta\tau = 2 \mu s m^{-1}$ as the flight path is 4m). The usual correction procedures were then followed.

The corrected scattering cross-section for six of the detectors are shown in figure 11.2; this is converted to $S(Q,\omega)$ in figure 11.3. Figure 11.4 shows $S(Q,\omega)$ interpolated onto a set of lines of constant Q. The energy of the incident neutrons was 79.8meV so that for the most part $\hbar\omega_0 \gg \hbar\omega$ and so, from (6/9) the cross-section is approximately proportional to $S(Q,\omega)$; this is why the results in 11.2 and 11.3 look little different. We see that the central quasi-elastic peak is very

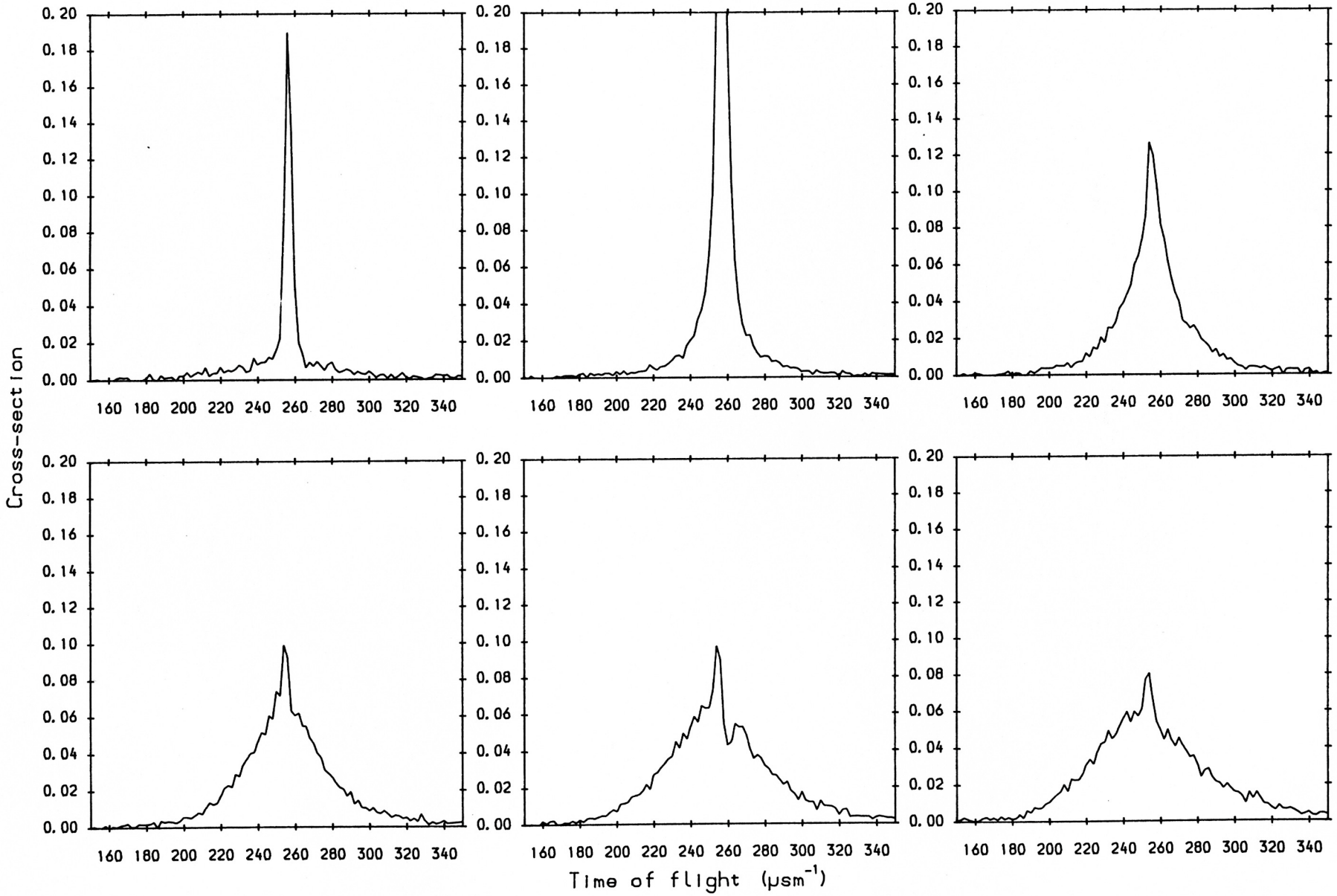


Figure 11.2 Corrected scattering cross-sections for caesium chloride at angles of 4.5°, 18°, 31.5°, 45°, 58.5°, and 69.75° on IN4.

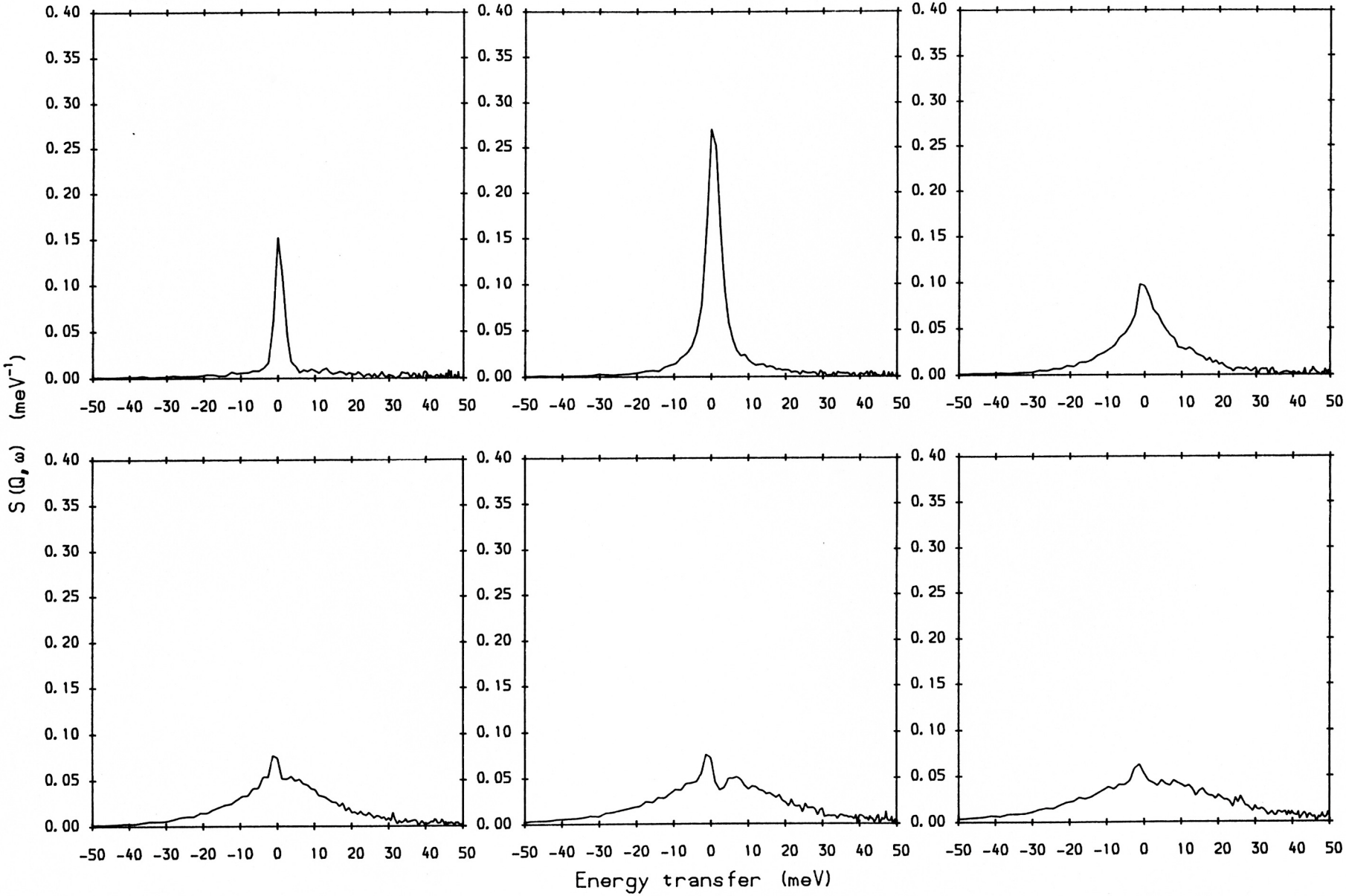


Figure 11.3 S(Q,ω) for caesium chloride calculated at constant angle for angles of 4.5°, 18°, 31.5°, 45°, 58.5°, and 69.75°.

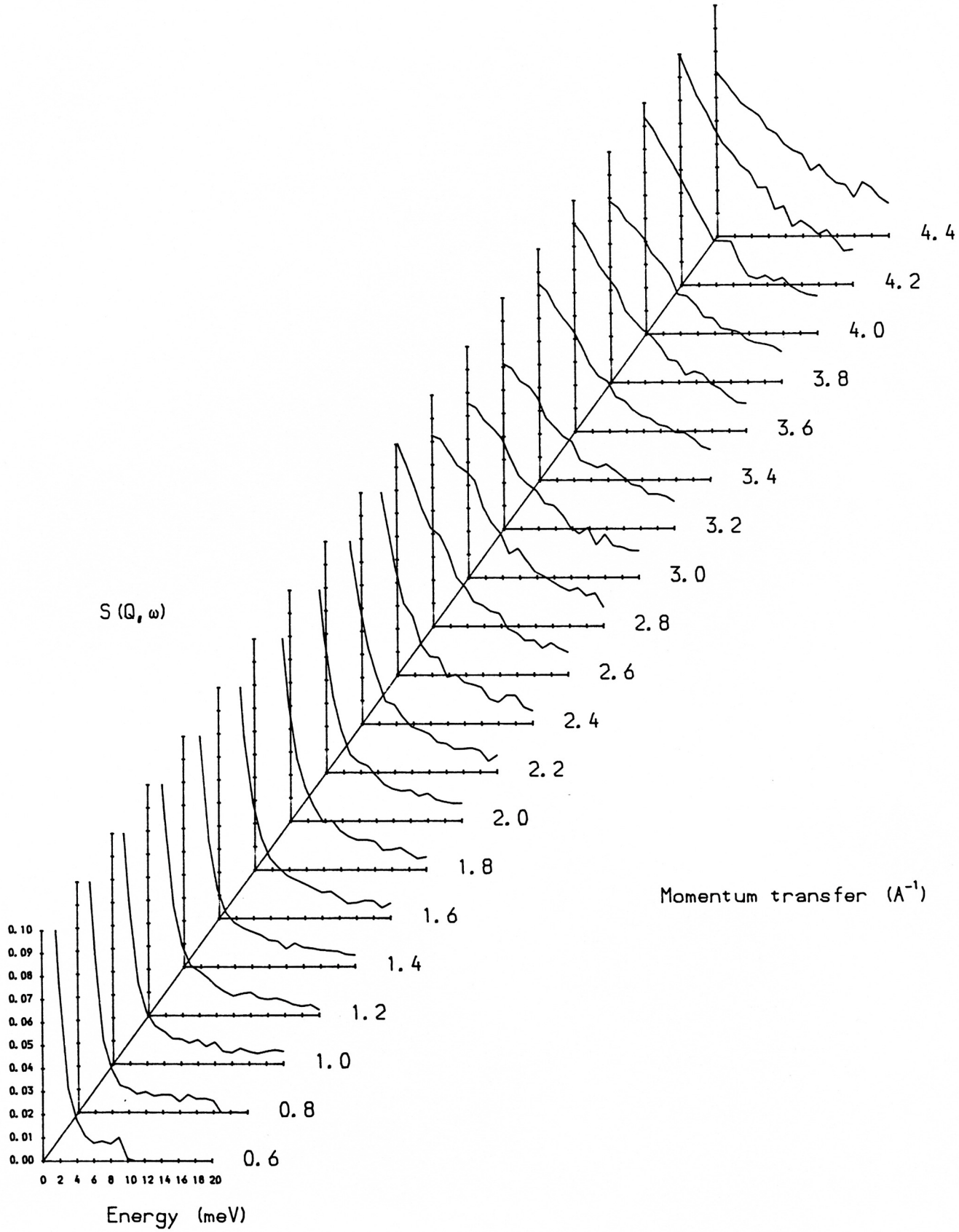


Figure 11.4 S(Q, ω) for caesium chloride at 700°C as a function of energy and momentum transfer.

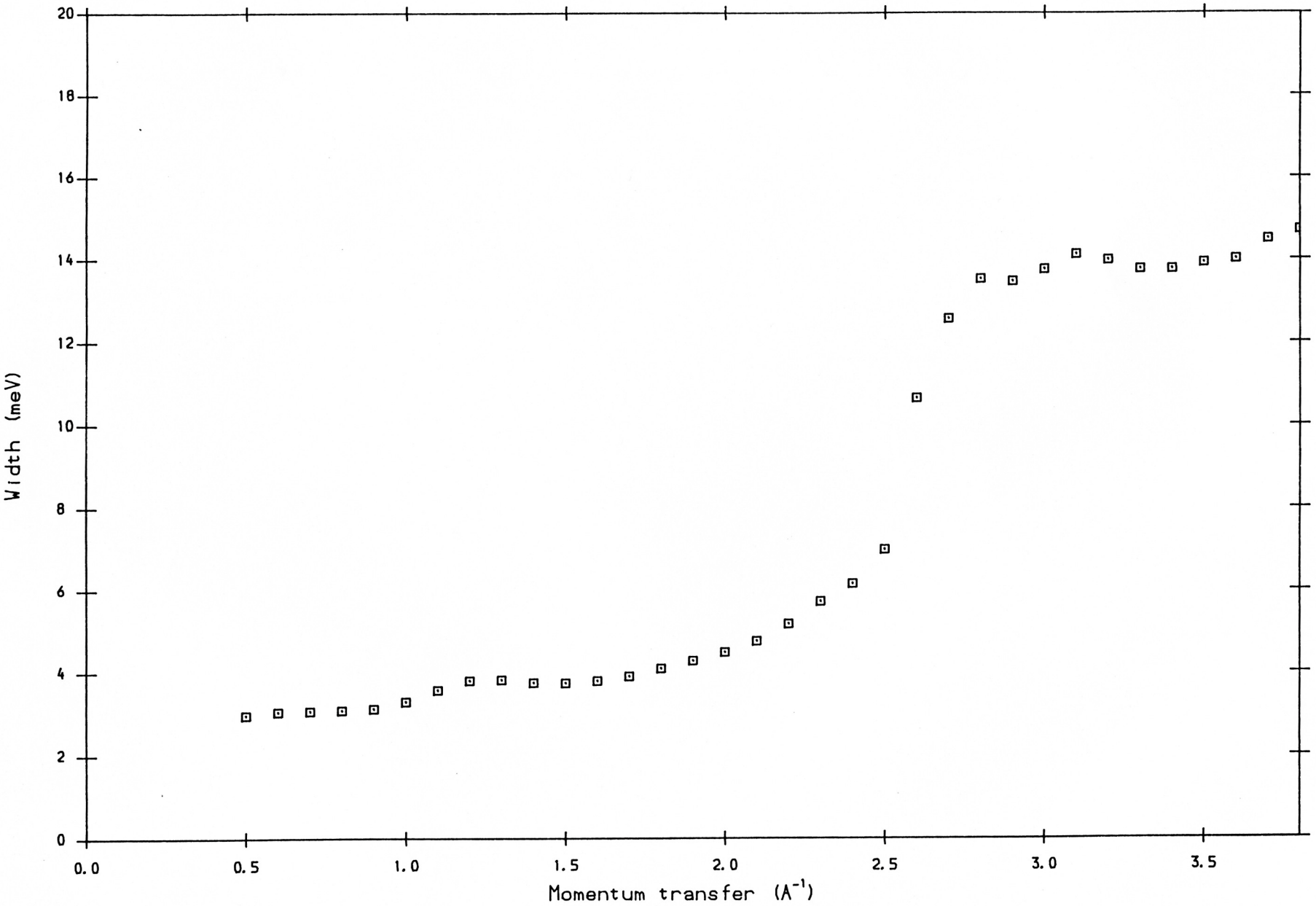


Figure 11.5 Width of the quasi-elastic peak of $S(Q,\omega)$ for CsCl at 700°C.

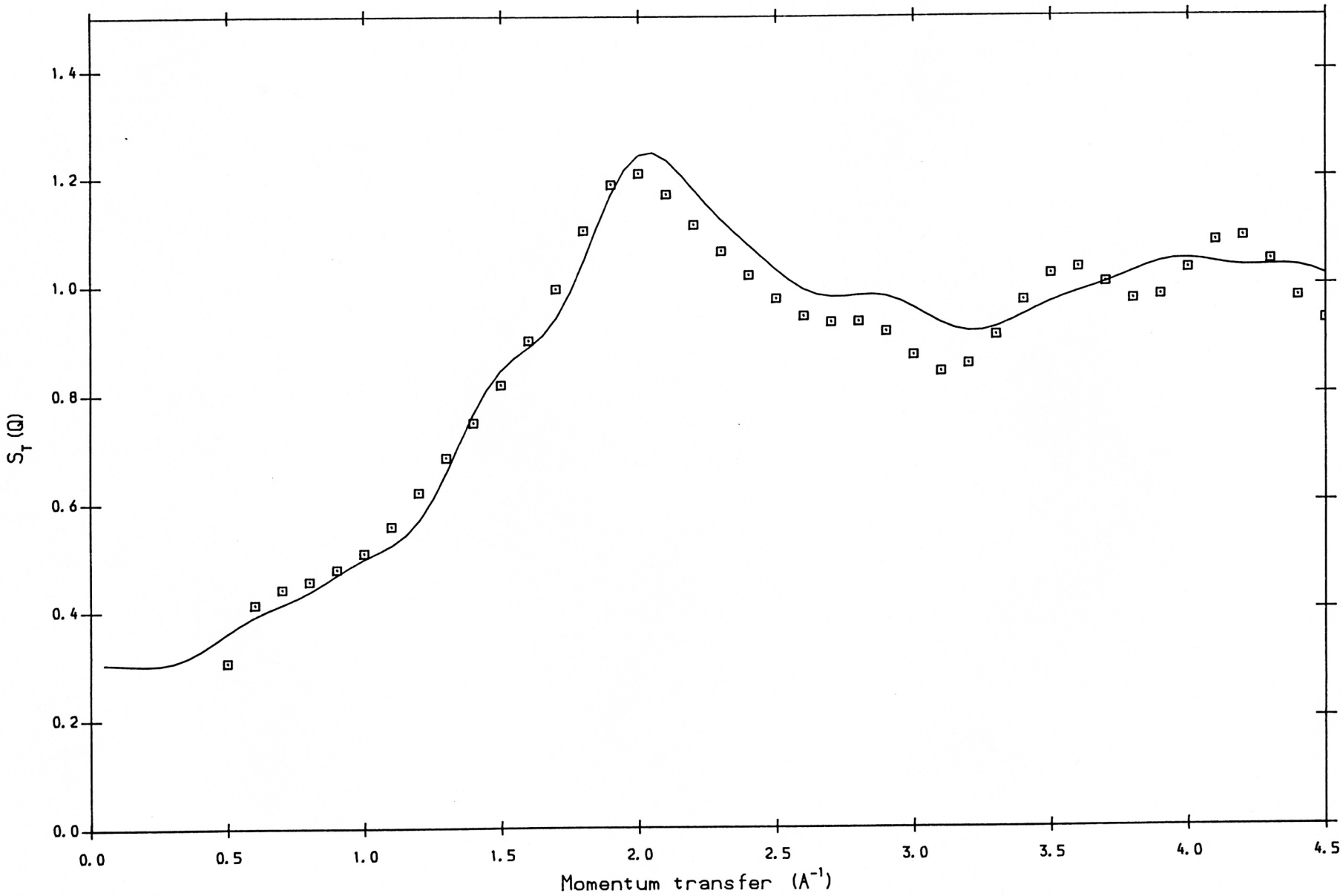


Figure 11.6 Total structure factor for caesium chloride at 700°C calculated by integration of $S(Q,\omega)$ (⊡) compared with that at 670°C obtained using LAD (solid line).

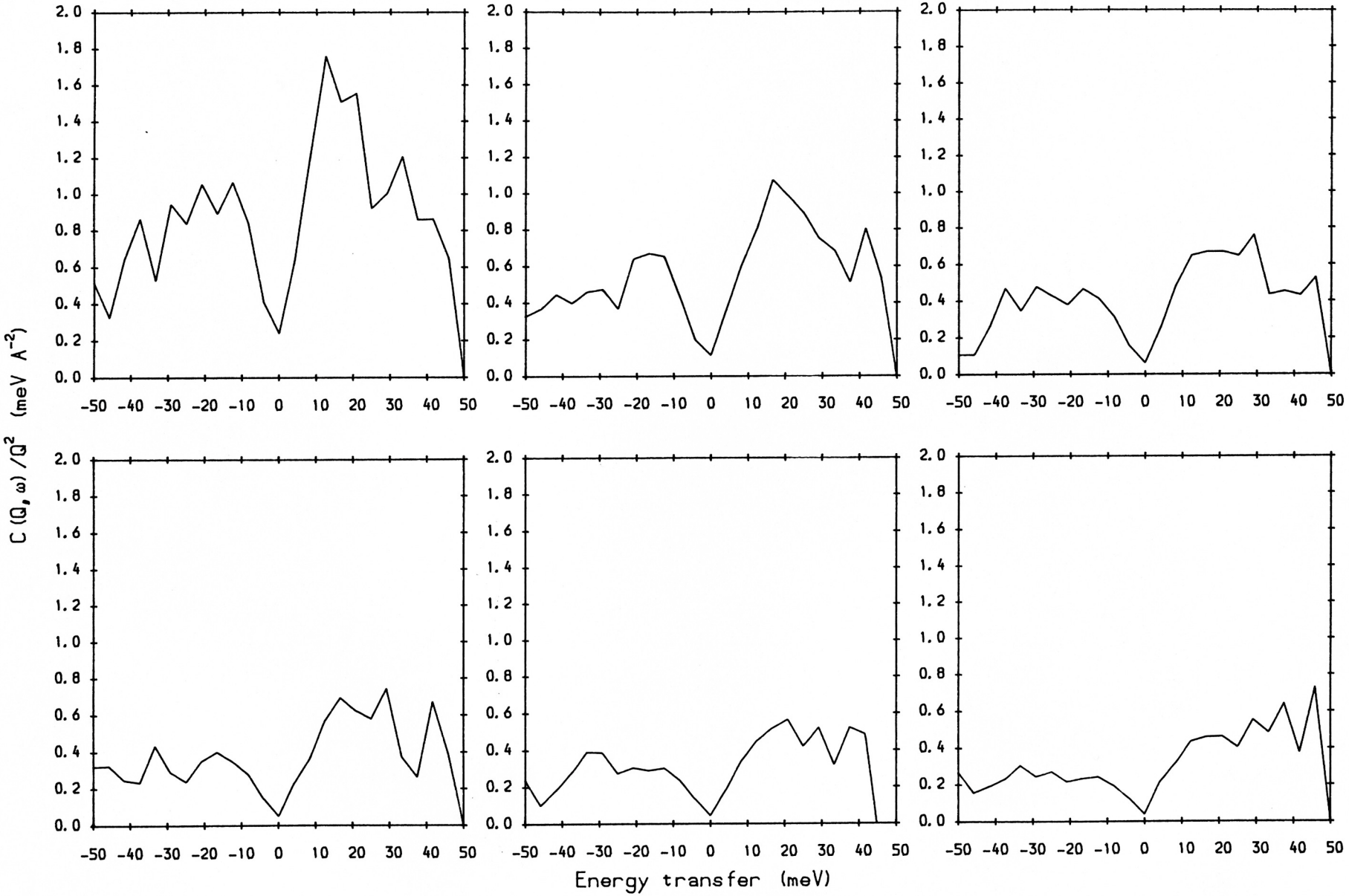


Figure 11.7 C(Q,ω) for caesium chloride calculated at constant scattering angle for angles of 4.5°, 6.75°, 9°, 11.25°, 13.5°, and 15.75°.

narrow at low angles, and so low Q, and broadens as the angle increases. Its width as a function of Q is shown in figure 11.5. This is in agreement with the results of the previous studies and shows that the switch from diffusive behaviour at low Q to free particle behaviour at high Q is quite sudden and occurs approximately at the position of the first peak in the structure factor. This is similar to the behaviour observed for molten sodium [11/5].

$S(Q)$ has been calculated by integration of $S(Q,\omega)$ with respect to energy at constant Q; in figure 11.6 it is compared with the diffraction data obtained in the previous chapter. It can be seen that it is in good agreement.

Only the lowest angle detectors provide information in the region that cannot be explored with IN6. Here the central sharp peak of $S(Q,\omega)$, the width of which (approximately 3meV) is determined by instrumental resolution, is associated with $S_{MM}(Q,\omega)$ as well as the diffusive motions. We see there is also a much broader contribution (width approximately 18meV) of low intensity; this is associated with $S_{qq}(Q,\omega)$.

$C_T^L(Q,\omega)$ is calculated for the six lowest angle detectors and is shown in figure 11.7. Given the statistical accuracy of the results there is no point in trying to calculate this function along lines of constant Q as was done for the IN6 data. The statistical errors are quite large but it is possible to estimate the positions of the underlying peaks, for the lowest angles at least, and these provide the points of the dispersion curve shown in figure 11.1. They are consistent with the optic mode rising from its minimum value at $Q \approx 1.4 Å^{-1}$ towards the crystal

Brillouin zone centre ($Q = 0$) longitudinal optic phonon energy of 18meV [11/6].

The new high energy transfer (HET) instrument at ISIS should allow this to be confirmed at slightly lower Q values. The better resolution of this instrument will give a better estimate of the energy of this optic mode. It is expected that this experiment will take place soon.

Simulation of caesium chloride [11/7] predicts that the optic mode is less damped than we have found here. One should be careful of drawing conclusions from this though as simulation results are unreliable at low Q, as the wavelength of the modes approaches the size of the simulation box. This is particularly true for the charge-charge mode.

Chapter twelve

The structure and dynamics of molten and fast ion conducting silver iodide.

12.1 The structure of α-phase silver iodide

Silver iodide undergoes a structural phase change at 147°C to form its α-phase which is well known for its fast ion conducting properties. Its electrical conductivity increases rapidly by a factor of 10^4 at the phase transition: this conductivity has been found to be due to conduction by vagile cations [12/1]. The structure of this phase has been extensively studied using neutron and x-ray diffraction although interest has been primarily in the Bragg scattering, attempting to assign the silver ions to sets of lattice sites [12/2-12/6]. There is, however, also an appreciable amount of diffuse scattering but this has been considered to be due to disordered cations only [12/7] or to silver-silver and silver-iodine, but not to iodine-iodine, correlations [12/8]. A neutron scattering experiment has been performed with this in mind [12/9] but isotopic substitution was not used and no conclusion concerning disorder in the iodide lattice could be drawn. The Debye-Waller factors obtained in the Bragg scattering studies are large and of the same order of magnitude (≈9Å^2 at 500°C [12/6]) for both silver and iodide ions which indicates considerable displacements from lattice sites for both cations and anions. This would indicate that the iodine-

iodine contribution to the diffuse scattering may be as important as the silver-silver contribution.

I present here the results of a neutron diffraction experiment using two samples of AgI: one containing predominantly the silver-109 isotope and the other the natural mixture of silver isotopes. The reason that three have not been used was that on this occasion we had planned to look at molten silver iodide but had not realised that the vanadium which formed the containers we were using would displace the silver ions from the melt. As a consequence we ruined one of the samples by melting it; this left two which we used to study the α-phase (for which this displacement is not a problem).

The samples were powdered and sealed into our standard vanadium containers under vacuum. Using 0.7Å neutrons and the D4B diffractometer spectra were obtained for the two samples, an empty vanadium container, the furnace, and a vanadium bar, all at 300°C; they are shown, normalised using a monitor count, in figure 12.1. Two things are immediately obvious about the Bragg peaks: firstly, that they differ significantly between samples confirming that they are not due solely to the iodide lattice; secondly, that the intensity of the Bragg peaks is remarkably small compared to the diffuse scattering which implies a large degree of disorder in the structure.

There is though, clearly, a problem with this data. The spectrum for ^{109}AgI slopes down at high angles and is, in general, of greater intensity than that of the ^{N}AgI sample although it has a smaller coherent scattering length than the latter. It was assumed that during the preparation of this sample it became contaminated with a small

proportion of hydrogen (perhaps in the form of water). As this would be distributed randomly throughout the sample the scattering from it (which is mainly incoherent - hydrogen has a very large incoherent scattering cross-section) would be completely structureless. Because of the lightness of hydrogen, though, there would be a significant Placzek effect.

This problem did not recur when the same sample, this time in a silica container, was used for the experiment on molten silver iodide. This suggests that the hydrogen contamination was actually in the vanadium, though it is not known how it might have got there. This does not make any difference to the correction procedure.

The data has been corrected following the usual procedures but with the inclusion of a hydrogen correction term for the ^{109}AgI. This takes the form of a Placzek correction for hydrogen which was calculated using the theoretical free particle dynamic structure factor (3/151) for hydrogen (the incoherent scattering is relatively unimportant as the high Q limiting level is subtracted from the cross-section later so removing any incoherent scattering). The proportion of hydrogen in the sample was estimated from the Placzek correction at high Q to be about 4% (by number). Departures at low Q from this free particle dynamic structure factor were corrected for using the deviations of $g(r)$ from zero at low r.

The Bragg peaks have been separated from the diffuse scattering by fitting Gaussians to the peaks and subtracting these from the experimental data to leave diffuse scattering. The errors involved in doing this are no larger than the statistical errors that are present in

the data; however it is only the major peaks that are clearly defined that can be subtracted in this way. The diffuse scattering is shown in figure 12.2; that for the ^{N}AgI sample agrees well with that found by Fuess *et al* [12/9].

The areas under the Bragg peaks can be integrated and compared with those predicted by the model in which the silver ions are distributed randomly over the twelve tetrahedral (¼,0,½) sites [12/6]. The measurements of the Bragg peaks were not very accurate (D4B is not the right sort of instrument for this sort of work) but they did agree reasonably well with this model, not only for the natural sample but for the ^{109}AgI too. This provides additional support for this model which was based on an experiment on natural silver iodide only.

Because we have only two samples it is not possible to determine the three partial structure factors $A_{++}(Q)$, $A_{+-}(Q)$, and $A_{--}(Q)$; it is only possible to find two linear combinations of these. The scattering lengths involved happen to be such that it is possible to choose two combinations that are very close to

$$g_{+}(r) = g_{++}(r) + g_{+-}(r)$$
$$g_{-}(r) = g_{--}(r) + g_{+-}(r) \qquad (12/1)$$

which describe the distribution of ions (of either species) around cations and anions respectively. This means that the two partial distribution functions we obtain do actually have a physical significance.

These two partial structure factors are obtained. They are shown in figure 12.3. There is a lot of small scale structure which is probably

due to remnants of Bragg peaks; it should not be interpreted as genuine structure in the diffuse scattering. These are transformed to give the partial pair distribution functions shown in figure 12.4. The ripples continuing to large r in these are presumably due to the Bragg peak remnants. They are not of the size generally considered significant.

The first peak in the two combinations of partial pair distribution functions is similar and is due to the contribution of $g_{+-}(r)$: we would expect the nearest correlation to be Ag-I due to electrostatic forces and this is the characteristic anion-cation nearest neighbour peak as found in molten salts. It occurs at a distance of 2.8Å which is the sum of the atomic radii of silver and iodine, being significantly smaller than the sum of the ionic radii. This suggests that this peak corresponds to a largely covalent bonding between silver and iodine atoms. Integrating under this peak for $g_{-}(r)$ gives a coordination number of approximately five. This is an overestimate of the number of silver ions in the first coordination shell as it includes a contribution from the iodide ions in the next shell. It is, therefore, consistent with the tetrahedral coordination model describing the Bragg scattering.

For $g_{-}(r)$ there is a broad peak centred around 4.6Å which does not occur in $g_{+}(r)$. This would seem, therefore, to occur in the I-I pair distribution function but not in that of Ag-Ag; it is at a distance just larger than the iodine ionic diameter and corresponds to the mean separation of neighbouring iodide ions. There are no major peaks in $g_{+}(r)$ after the first Ag-I peak indicating almost uniform distribution of ions around the cations and so very little structure in $g_{++}(r)$.

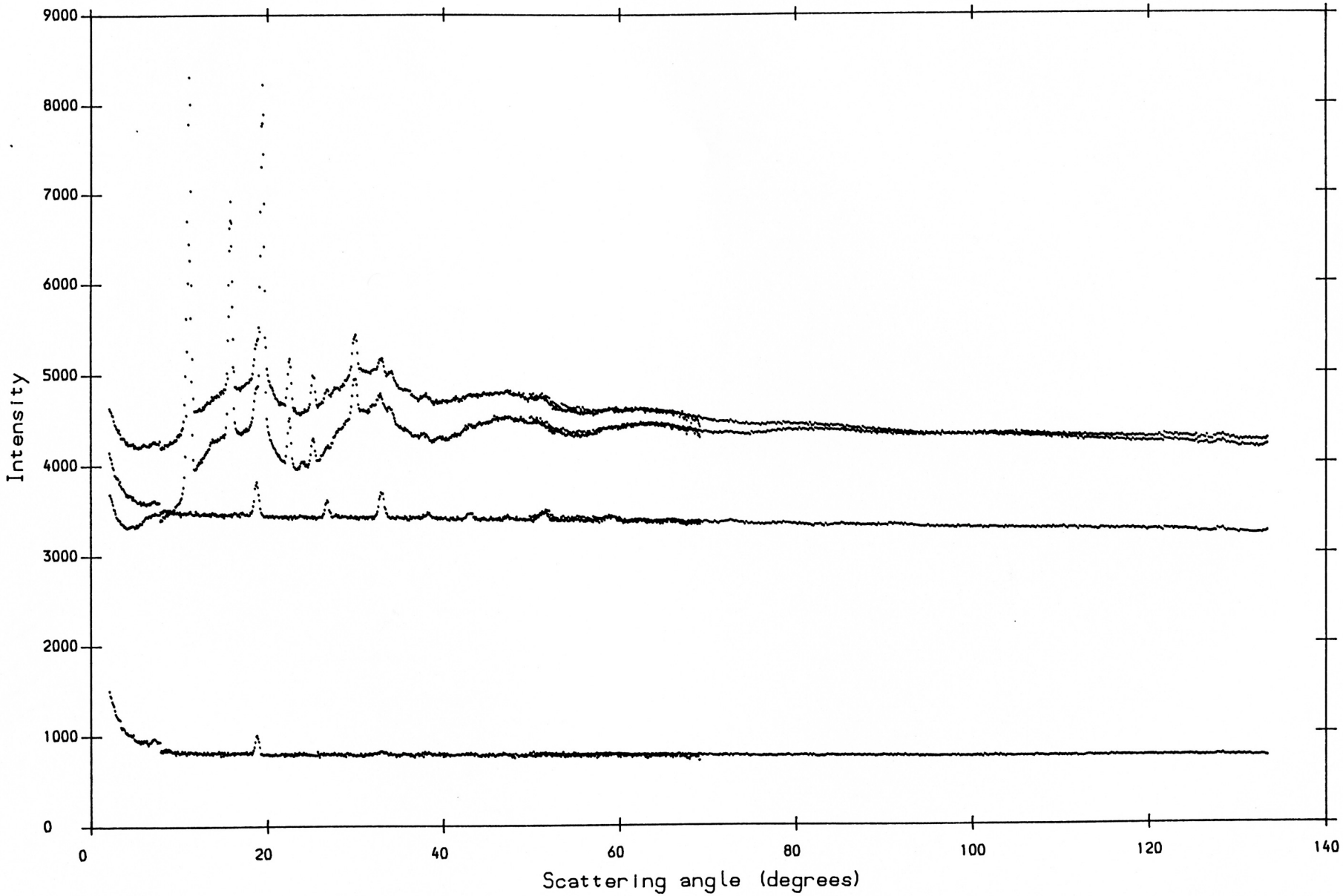


Figure 12.1 Scattering intensities for (from top to bottom) α-^{109}AgI, α-^{N}AgI, an empty container and the furnace, all at 300°C.

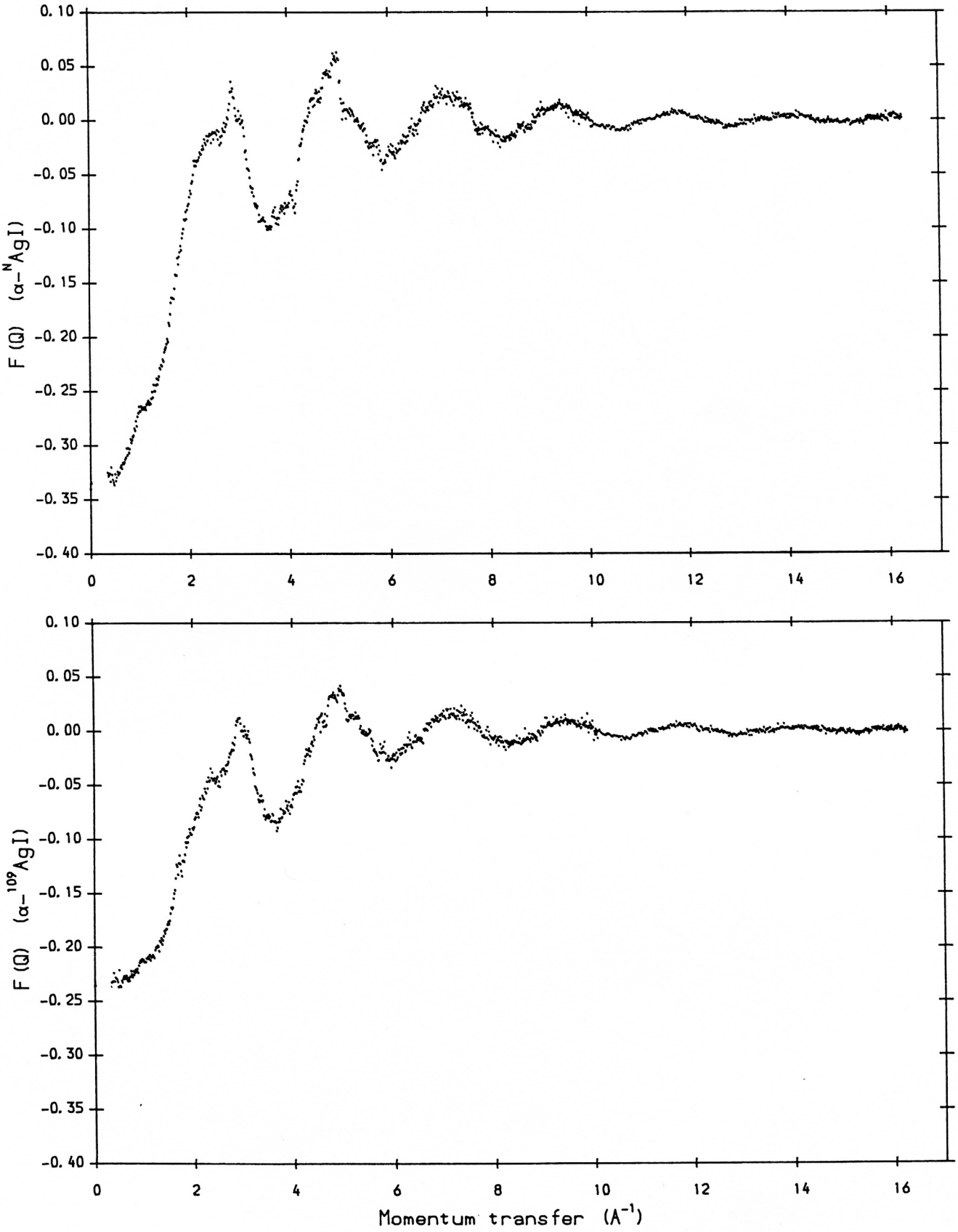


Figure 12.2 The corrected diffuse scattering functions for α-^{N}AgI and α-^{109}AgI.

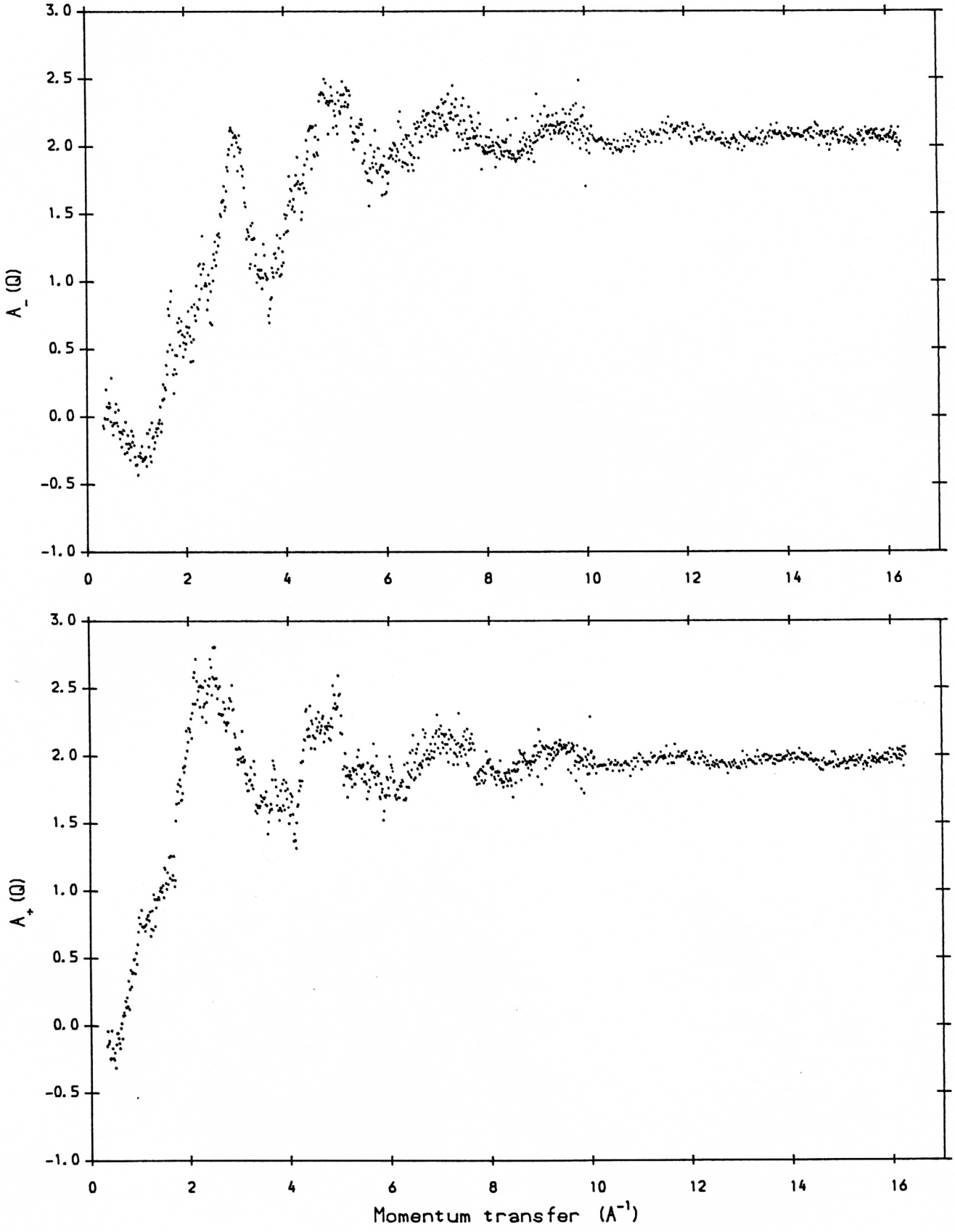


Figure 12.3 The partial diffuse structure factors $A_{-}(Q)$ and $A_{+}(Q)$ for α-AgI.

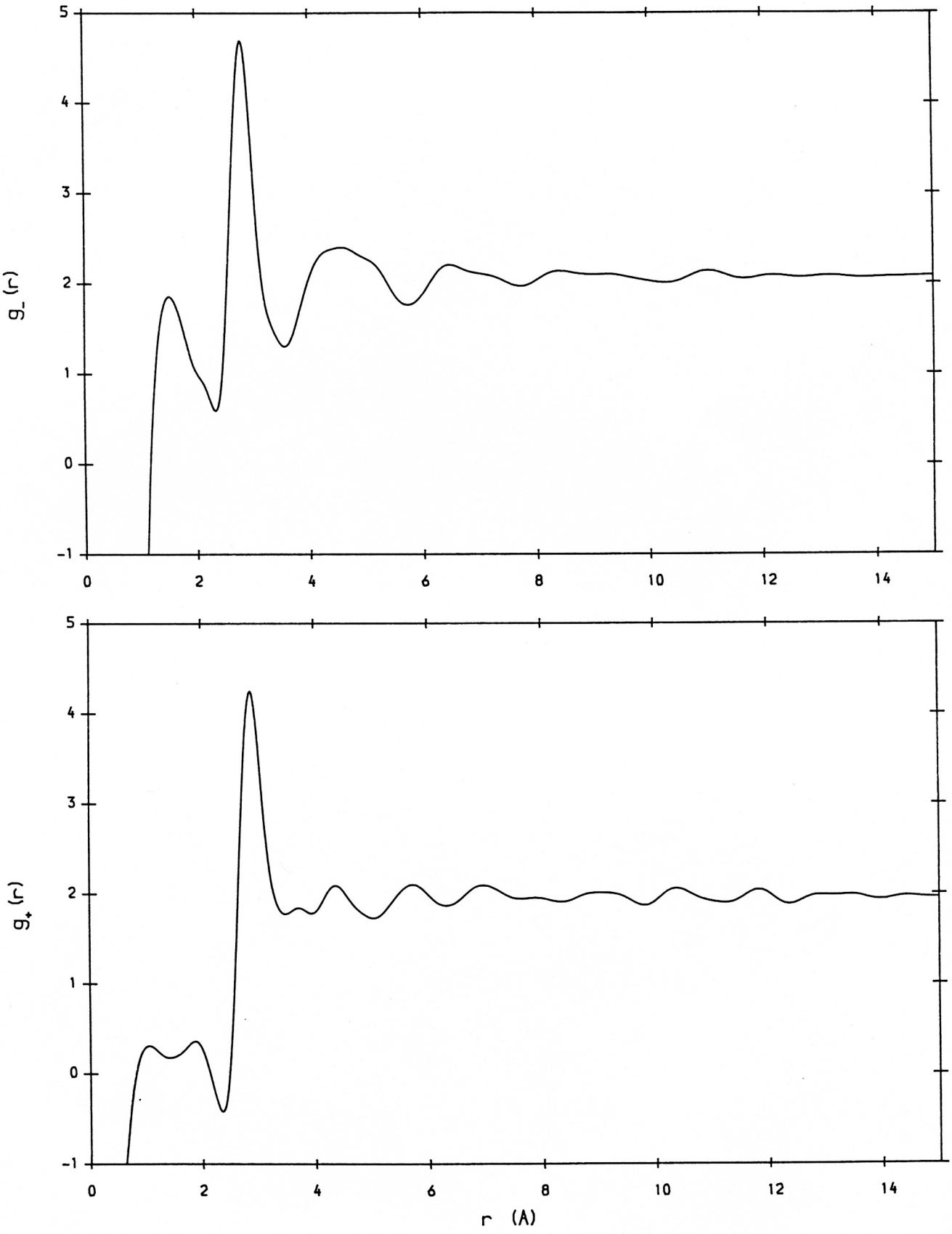


Figure 12.4 The partial radial distribution functions $g_-(r)$ and $g_+(r)$ for α-AgI.

It is interesting to compare these results with those for molten cuprous chloride [12/10,12/11]. Cuprous chloride, like silver iodide, is only weakly ionic. Unlike silver iodide, and also cuprous bromide and iodide, it does not have an α-phase in the solid state though its electrical conductivity as it approaches the melting point is comparable to that of these salts [12/12]. This conductivity is predominantly cationic in all four of these substances [12/1] although it is only for silver iodide that the structural phase change accompanies a rapid increase in electrical conductivity.

Comparing our combinations of both partial structure factors and pair distribution functions with those that would be obtained from the CuCl partial functions we find a remarkable similarity. It seems, therefore, that our results are consistent with the disordered structure in α-AgI being very much like that of molten CuCl. Of particular interest is the lack of structure in the cation-cation pair distribution function, the main feature that distinguishes the structure of molten CuCl from those of the alkali halides. This lack of structure is associated with the ease of movement of the cations which makes the electrical conductivity so high.

12.2 The structure of molten silver iodide

The next step was to determine the structure of molten AgI and compare it with the α-phase. The sample of ^{107}AgI that had been contaminated was purified and it and the two samples we had previously used were packed into silica containers. These were made quite long and thin to reduce problems with absorption (both silver isotopes have

fairly large cross-sections for neutron capture). We measured spectra for all three of these, again using 0.7Å neutrons with the D4B diffractometer, at 600°C and for the ^{107}AgI at 300°C to use with our previous results. The scattering was also measured for an empty container at 600°C and 300°C, for the furnace, and for a vanadium rod to be used as calibration. These are shown in figure 12.5; they show little more than the characteristic silica scattering pattern.

The usual correction procedures yield the results shown in figures 12.6 and 12.7. From the first of these we see that the scattering from the melt and from the fast ion conductor are, despite the large temperature difference, really very similar especially for scattering angles greater than about 25° ($Q \approx 4$Å^{-1}) where the two are, apart from one Bragg peak, indistinguishable within the statistical accuracy of the experiment. At lower angles there is Bragg scattering from the solid which means the diffuse scattering must be lower than it is in the melt (the total scattering must be the same in both cases); this occurs mainly by a reduction in the scattering in the first main peak in the structure factor.

These have both been transformed (taking into account the differing densities) to give the pair distribution functions shown in figure 12.8. The small ripples are due to truncation errors in the Fourier transformation. It is noticeable that they are very similar; indeed it is doubtful if any of the differences are larger than the uncertainty we can ascribe to the function. We can conclude from this that the structures of the solid and melt are very similar; the former being moderated with a long range ordering that does not appreciably alter the short range ordering found in the melt. This similarity is consistent

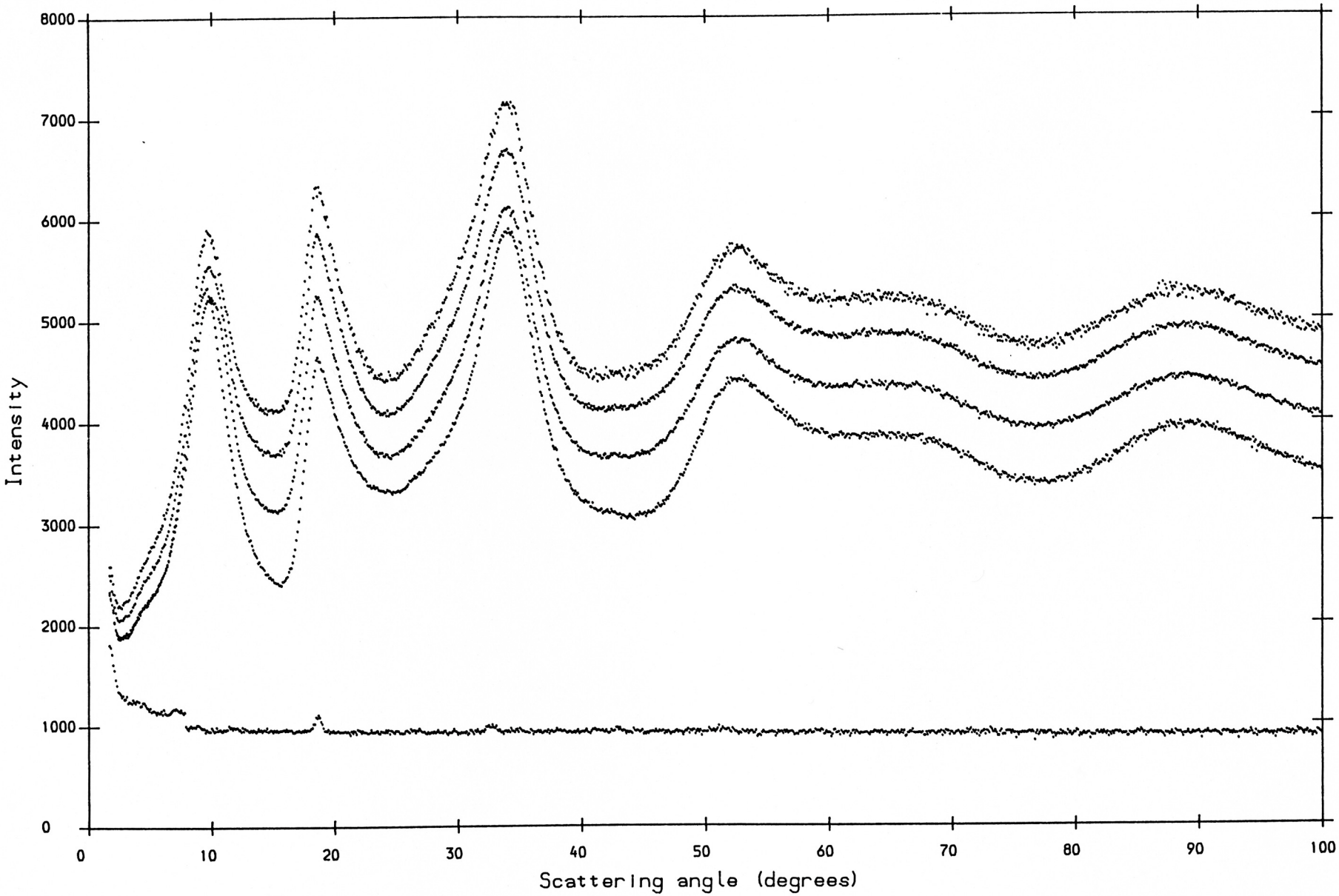


Figure 12.5 Scattering intensities for (from top to bottom) ^{107}AgI, ^{N}AgI, ^{109}AgI, and an empty cell, all at 600°C, and the furnace at room temperature.

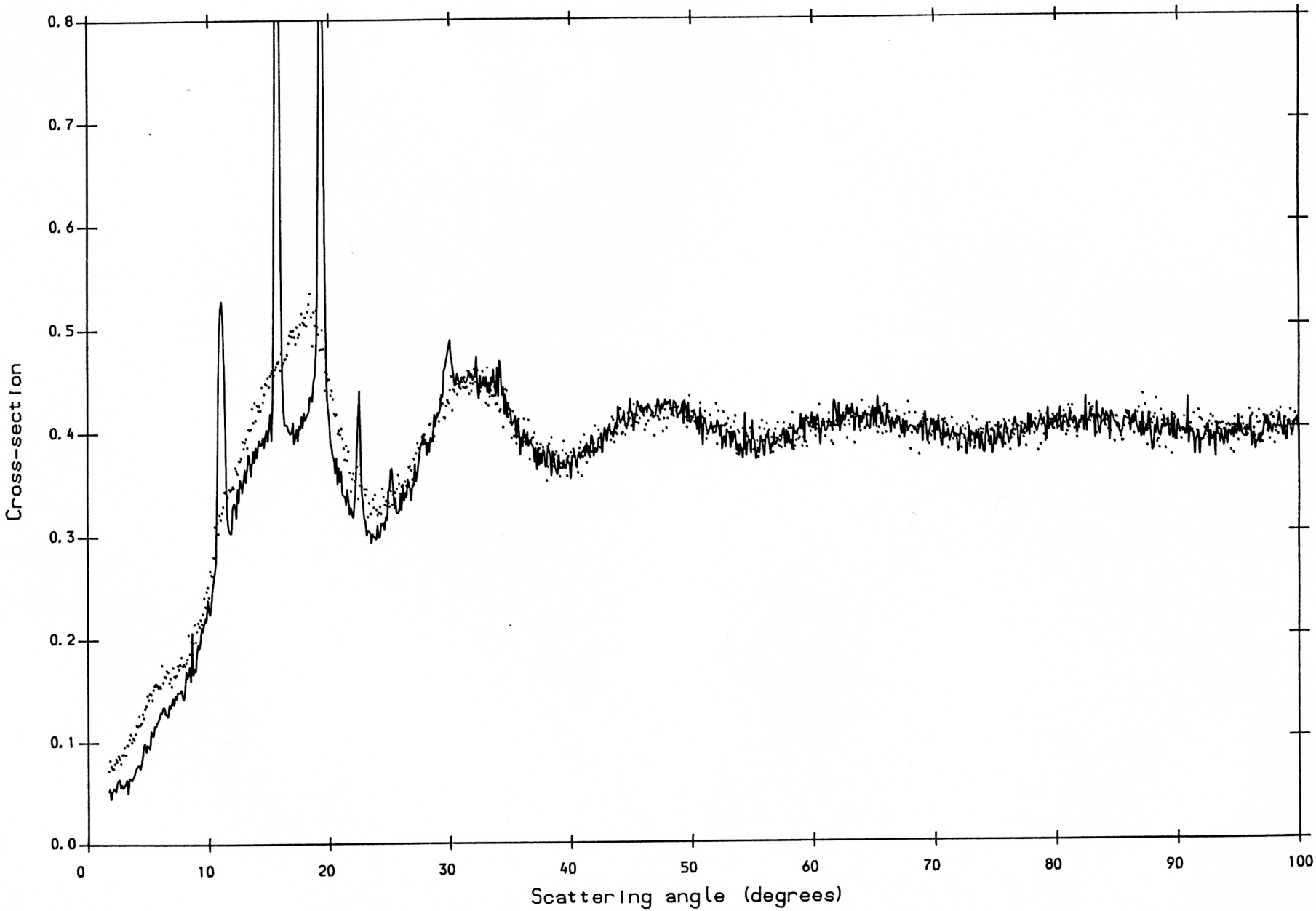


Figure 12.6 Corrected scattering cross-sections for ^{107}AgI at 600°C (points) and 300°C (line).

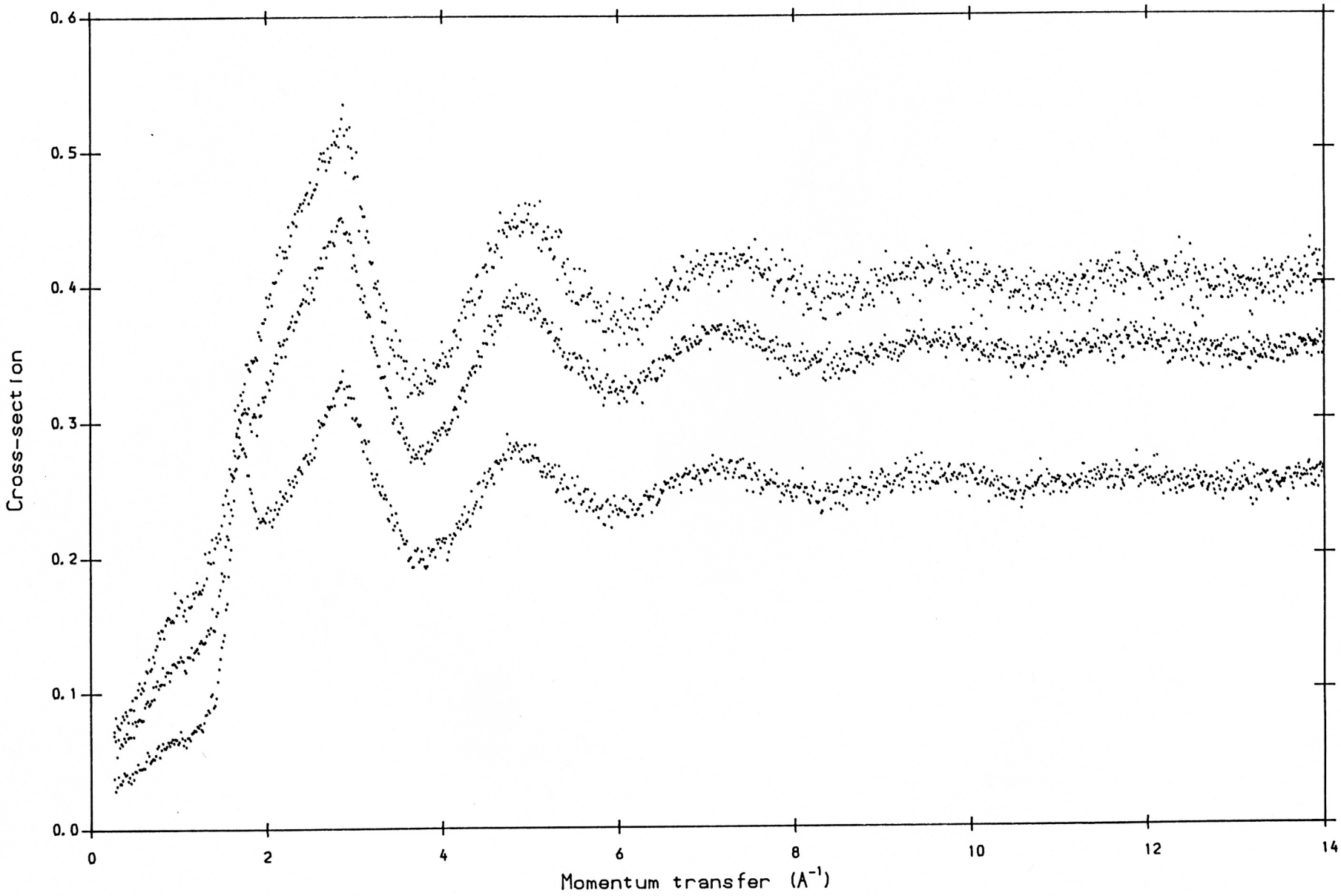


Figure 12.7 Corrected scattering cross-sections for ^{107}AgI (top), ^{N}AgI, and ^{109}AgI (bottom) at 600°C.

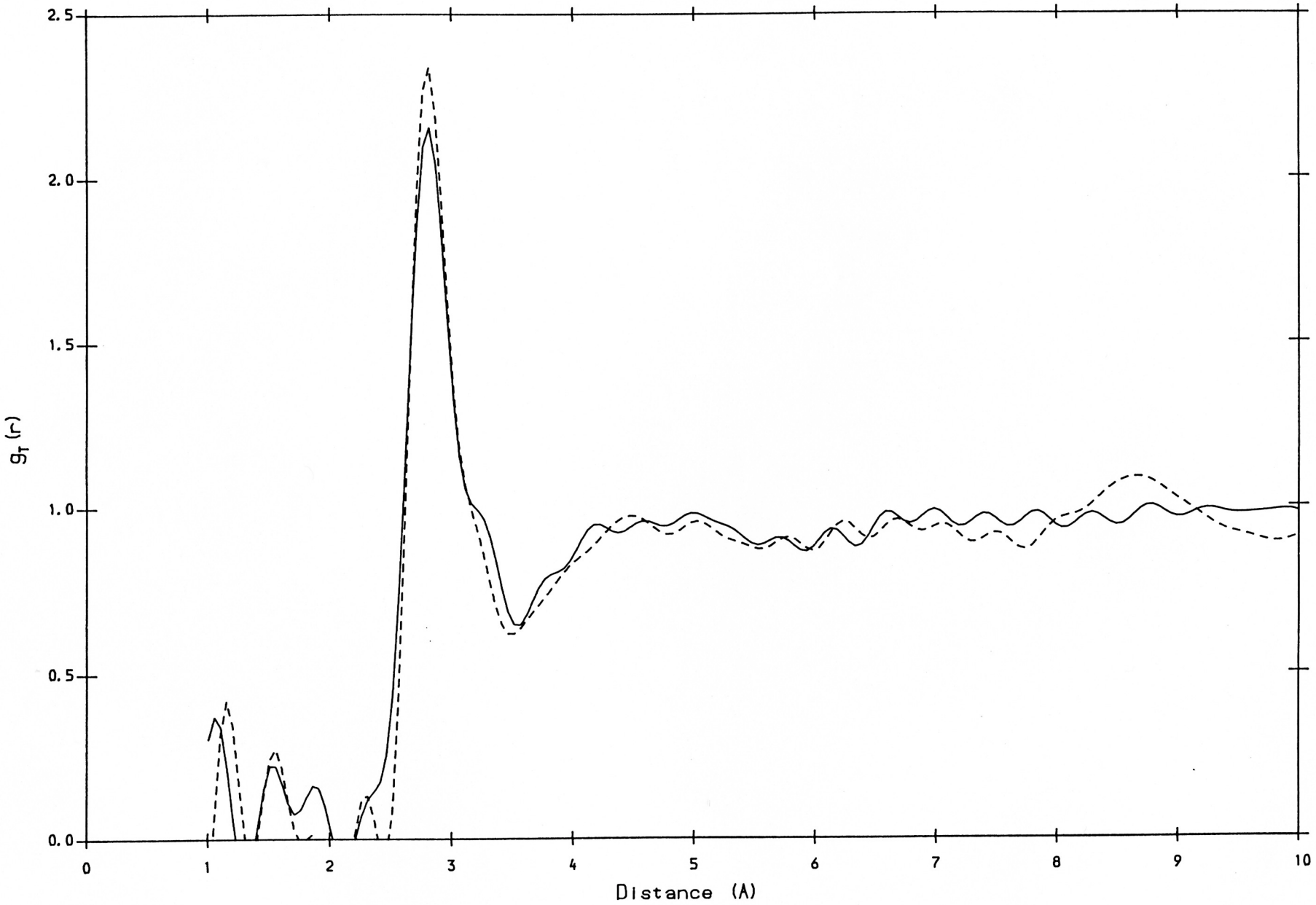


Figure 12.8 Radial distribution functions for ^{107}AgI at 600°C (solid line) and 300°C (broken line).

with there being large amplitude vibrations of the iodide ions in the α-phase making it more liquid like in local order even though the iodide ions are clearly tied to lattice sites.

The cross-sections for the three different samples molten are shown in figure 12.7. These show the typical gross features of the structures of molten salts: a large, broad first peak followed by decaying oscillations of about the same period. There is also a narrow peak at a scattering angle of about 11° in the ^{109}AgI that is small in the ^{N}AgI and visible as a shoulder in the ^{107}AgI. It is at the same position as the (1,1,0) Bragg peak in the solid. As the ^{109}AgI is the salt with the smallest silver scattering length this peak must have something to do with iodine correlations. This does not mean that it is only due to iodine; merely that it cannot be entirely due to silver-silver correlations. More likely, it is related to charge ordering.

There also seems to be a shoulder at an angle of approximately 6° ($Q \approx 1\text{Å}^{-1}$). Inelastic neutron scattering experiments confirm this. It is a feature that has not been observed in alkali chlorides for which the structure factors usually seem to tend quite smoothly to their $Q = 0$ limit, although it is similar to features observed in zinc chloride [12/13] and magnesium chloride [12/14] at approximately the same momentum transfer (which are sometimes known as 'pre-peaks'). In these two salts it occurs in $A_{++}(Q)$ and so is associated with cation-cation correlations beyond the cation-anion coordination. Zinc chloride has a strongly tetrahedral coordination of chloride ions about the cation; this peak is due to correlations between the tetrahedra. Magnesium chloride has a planar coordination of four anions about the Mg^{2+} ion. The 1Å^{-1} peak is here due to a layer type structure of these planar

arrangements. Given our knowledge of silver iodide it would seem more likely that this low Q peak is related to anions in this salt, there being fairly strong iodine-iodine correlations between which fit the smaller silver ions.

None of these three cross-sections tend to the limit at high angles that would be expected from the scattering cross-sections of silver and iodine. This was expected in the case of ^{107}AgI - when this was removed from the furnace after the experiment it was found that some of the salt had not run down the tube when it molt; this means there was not as much sample in the beam as expected. The ^{N}AgI sample appeared to only just fill the beam but there should have been plenty of ^{109}AgI.

It is common practice to renormalise scattering cross-sections to give the right value at $Q = 0$ (as was discussed in chapter nine concerning lithium chloride) and thus this problem might be overcome. However, due to the behaviour of these structure factors at low Q, which we have seen is not like that of alkali halides, it is not possible to extrapolate them to a $Q = 0$ value with any reliability, and this must be done to perform the renormalisation. In any case the isothermal compressibility of silver iodide is not known (though it could be estimated from the values for the bromide and chloride of silver which are [12/15]).

Instead the cross-sections have been multiplied by the appropriate factor to get the right value at high angles (having ascertained that a sensible separation into partial structure factors could not be obtained as they are). The partial structure factors then obtained are shown in figure 12.9. These are of the form that might be expected. There is a

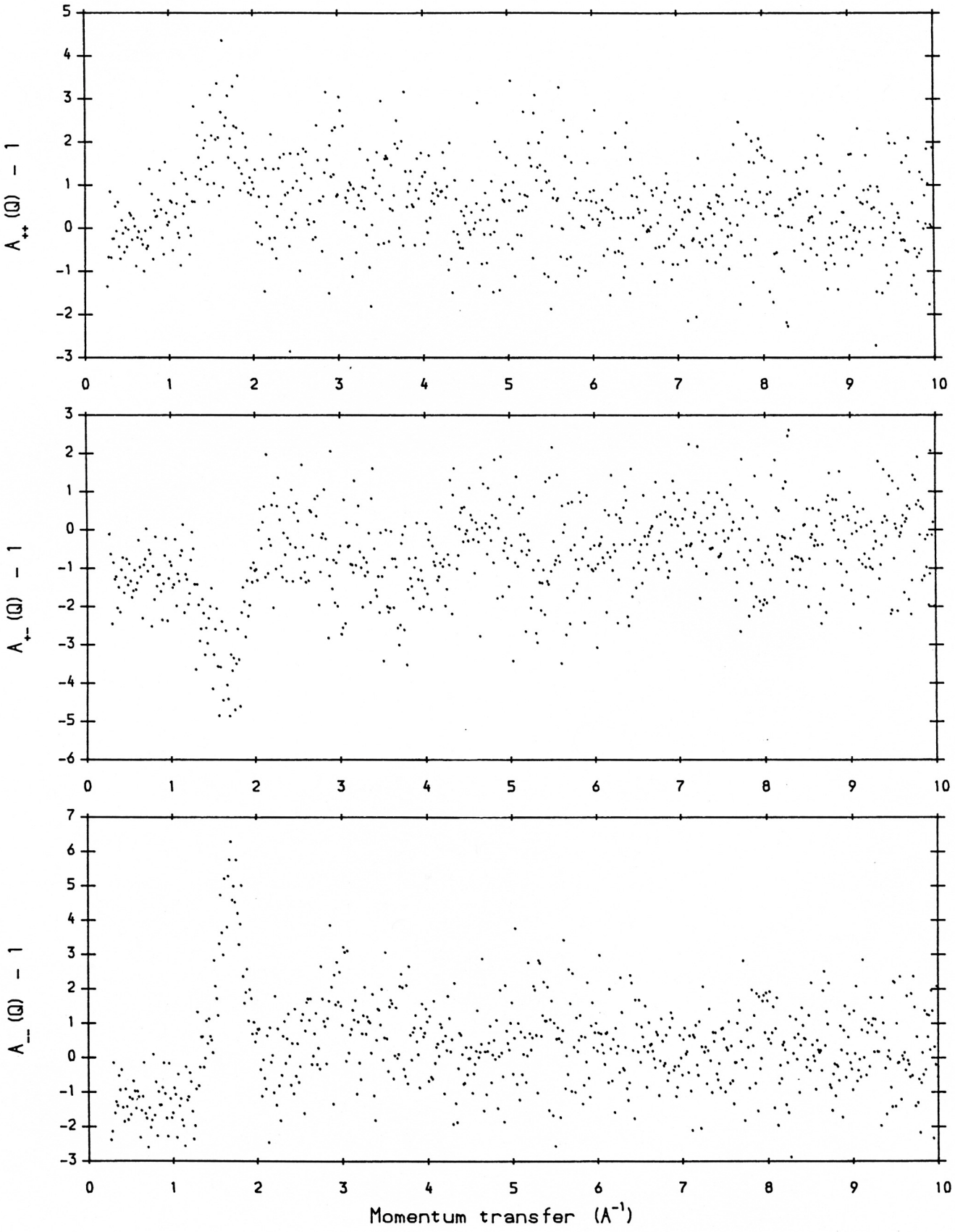


Figure 12.9 Partial structure factors for molten silver iodide obtained from the three total structure factors.

peak at $Q \approx 1.8 Å^{-1}$ (this is the sharp peak in the ^{109}AgI spectrum) in the Ag-Ag and I-I correlations, which is much sharper in the former than the latter, which corresponds to a dip in the Ag-I partial structure factor. Comparison of these with the results of Eisenberg *et al* shows that they are very similar to the CuCl partial structure factors. However, the low Q limits are not sensible and they cannot be transformed into pair distribution functions that are remotely sensible. We conclude that though these structure factors are probably qualitatively correct and support the hypothesis that the structure of molten AgI is similar to that of molten CuCl, they cannot be considered quantitively correct.

Some theoretical work has been done on systems such as cuprous chloride and silver iodide trying to reproduce such structure. An example is an HNC calculation by Silbert [12/16] who used the interaction potentials of Parinello *et al* [12/17]

$$V_{Ag-Ag} = \alpha_k \frac{0.014804}{r^{11}} + \text{Coulomb term} \tag{12/2}$$

$$V_{Ag-I} = \alpha_k \left(\frac{446.64}{r^7} - \frac{2.3472}{r^4} - \frac{6.9331}{r^6} \right) + \text{Coulomb term} \tag{12/3}$$

$$V_{I-I} = \alpha_k \left(\frac{114.48}{r^9} - \frac{1.1736}{r^4} \right) + \text{Coulomb term} \tag{12/4}$$

where the distances are measured in Angstroms, the constant α_k has the value

$$\alpha_k = 14.399 \text{ meV} \tag{12/5}$$

and the Coulomb terms are calculated assuming the effective charges on

the ions are +0.6 and -0.6 times the electron charge. The partial pair distribution functions produced by this calculation are shown in figure 12.10. Although we have no experimental partial pair distribution functions with which to compare them we can do an experimental comparison by combining them in the appropriate proportions to give total $g(r)$ functions and comparing with the those obtained by transforming the experimental total structure factors. This is done in figure 12.11. From this it is clear that the theoretical results, although producing partial pair distribution functions that are roughly of the form that was wanted, need improving. The first peak in $g_T(r)$ is too low and occurs too early. This might be caused by using a density that is too large (the density must be supplied as a parameter to an HNC calculation), though experimental data has been used.

It is interesting to note that Ruff *et al* [12/18] have produced a structure of this sort using a fairly simple model in which the disorder in the cation structure is represented by including 'phantom' cations.

12.3 The dynamics of silver iodide

The only other molten fast ion conductor which has been the subject of this sort of dynamics investigation is $SrCl_2$ [12/19]. For this it was shown that there are, in addition to the broad acoustic and optic modes (being nearly mass-mass and charge-charge current correlations) observed in other molten salts, two relatively well defined modes having parallel dispersions with slopes roughly equal to the velocity of sound which are neither mass-mass nor charge-charge in nature. Such modes do not occur in the alkaline earth chlorides, $MgCl_2$ and $CaCl_2$, which do not have fast ion conducting properties.

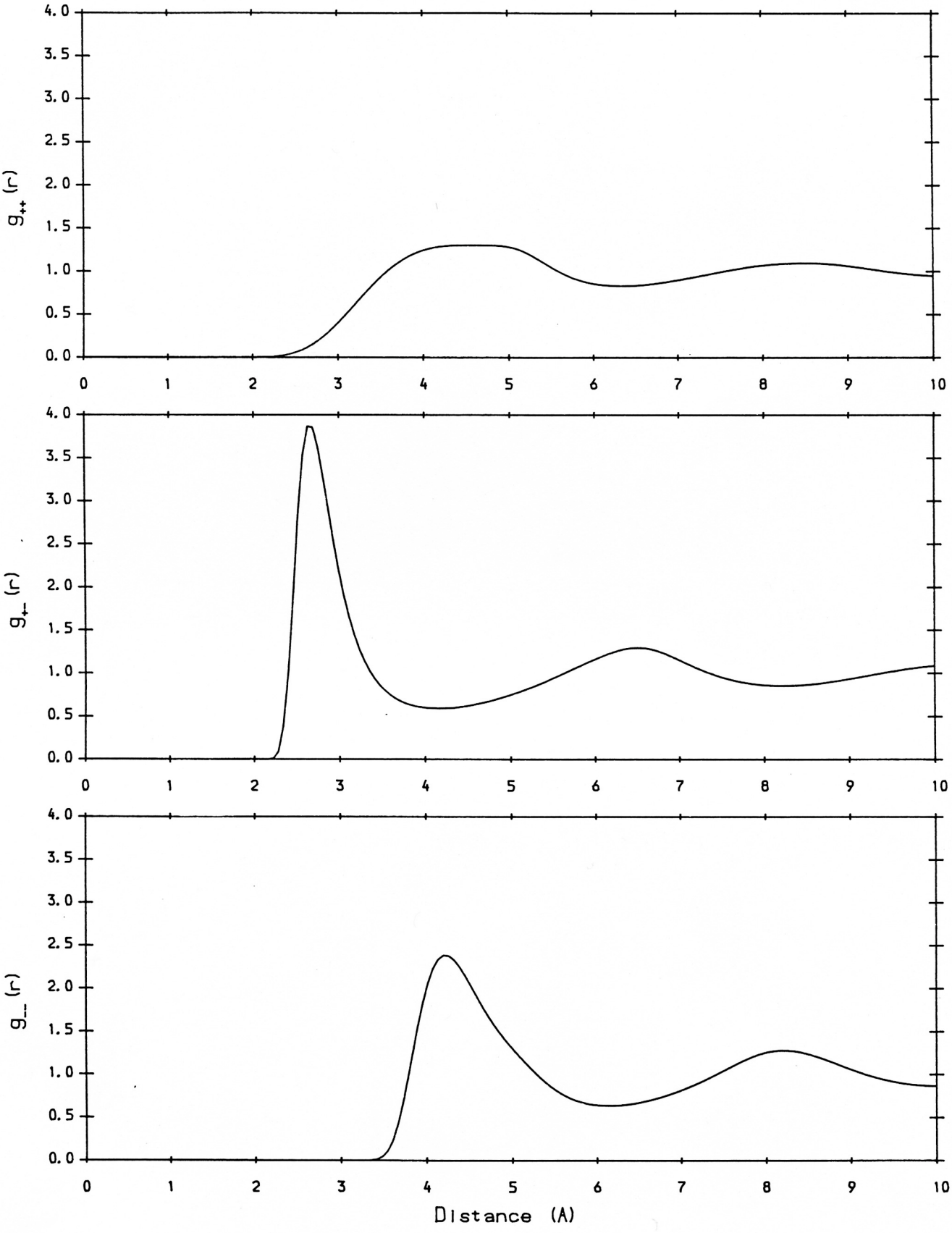


Figure 12.10 Partial pair distribution functions for molten silver iodide from an HNC calculation.

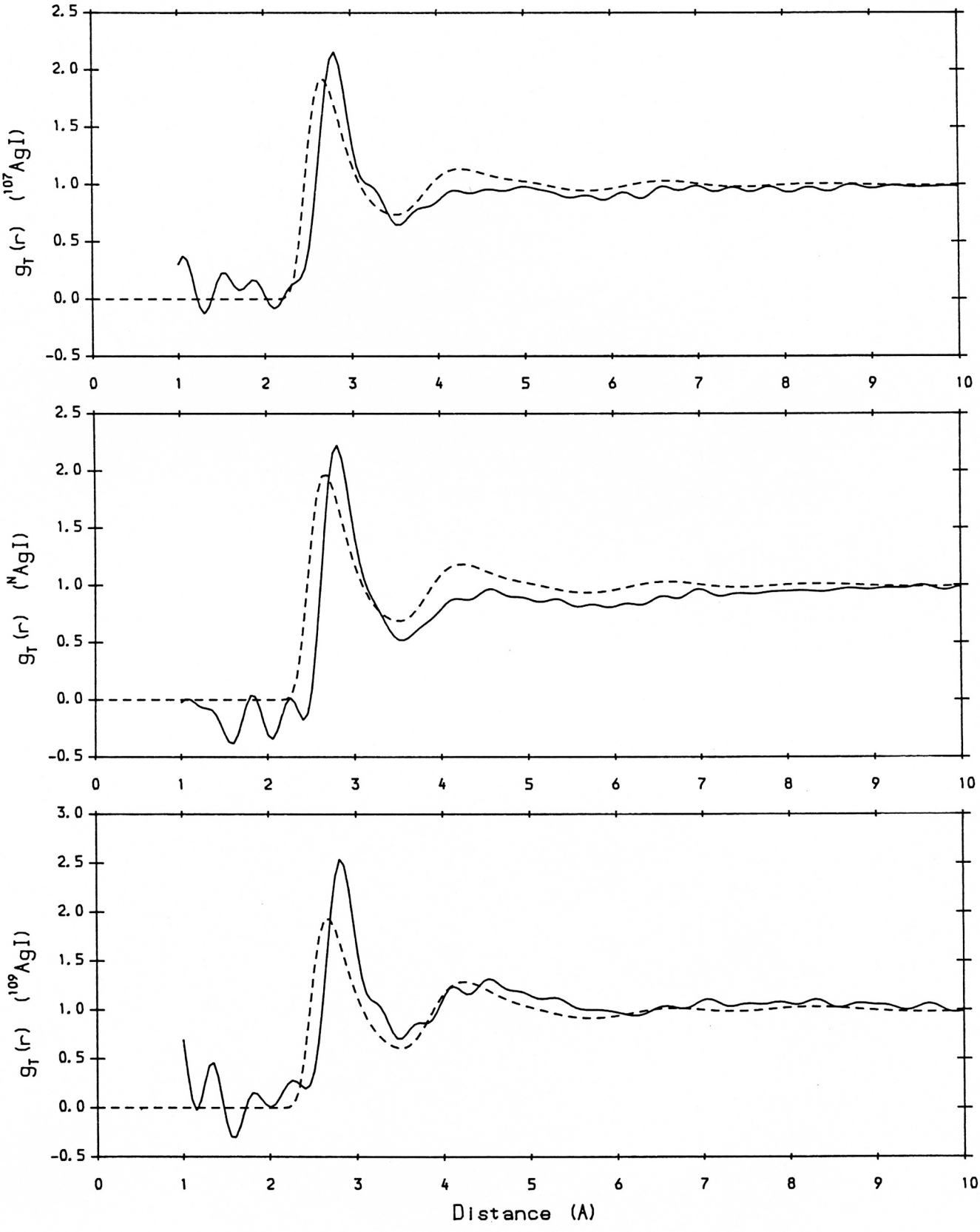


Figure 12.11 Total pair distribution functions (solid lines) compared with HNC (dashed lines) for the three samples of molten silver iodide.

Of course there are significant differences between AgI and $SrCl_2$. The different stochiometric ratio suggests that AgI might have acoustic and optic modes more similar to those of alkali halides than to those of alkaline earth halides although the significant covalent character of AgI might effect this. The fast ion conduction of $SrCl_2$ is due to relatively few anions whereas in α-AgI the conduction is by the cations which have a rather more highly disordered and liquid like structure. Nevertheless it was thought that there might be found dynamic features in the melt that also existed in the α-phase.

As sufficient neutron beam time was not available we were not able to measure, as we had hoped we would, cross-sections for three samples of different silver isotopic composition and so determine the nature of any modes we might find. Instead we concentrated on the ^{N}AgI measuring the cross-section at 600°C and at 300°C. Then we did the same for ^{109}AgI but for rather less time to allow us to make a qualitative comparison. The experiment was done on IN6 using 5.1Å neutrons. The scattering from an empty silica container at 300°C and at 527°C (this experiment was done at the same time as another one using the same containers at a different temperature; an intermediate temperature was selected for the silica) and from the empty furnace was also measured.

The scattering intensities measured by the lowest and highest angle detectors are shown in figures 12.12 and 12.13. The usual correction procedures were followed giving the results shown in figure 12.14 for a scattering angle of 97.3°. We see immediately that there is a large difference between the results for the melt and for the fast ion conductor, more so than is the case for $SrCl_2$. Apart from the wider quasi-elastic peak in the melt which is to be expected because, firstly,

the iodide ions are free to diffuse in the melt and, secondly, because the temperature is much higher, all the high energy structure in the melt is absent in the fast ion conductor. It is not so easy to see differences between the two samples though there is perhaps a more pronounced peak at around 1000μsm^{-1} in the α-^{109}AgI than in the α-^{N}AgI.

The coefficients a_M and a_q take the values

$$a_M = \begin{cases} 1.125 \text{ for } {}^{N}\text{AgI} \\ 0.947 \text{ for } {}^{109}\text{AgI} \end{cases}$$

$$a_q = \begin{cases} 0.160 \text{ for } {}^{N}\text{AgI} \\ -0.037 \text{ for } {}^{109}\text{AgI} \end{cases}$$

(12/6)

We can write the total structure factor in terms of the mass and charge partials or in terms of the particle partials:

$$S_T(Q,\omega)\ ({}^{N}\text{AgI}) = 1.266\, S_{MM}(Q,\omega) + 0.0256\, S_{qq}(Q,\omega) + 0.36\, S_{Mq}(Q,\omega) + 0.049\, S_{+}(Q,\omega) + 0.081\, S_{-}(Q,\omega)$$

(12/7)

$$= 0.356\, S_{++}(Q,\omega) + 0.279\, S_{--}(Q,\omega) + 0.630\, S_{+-}(Q,\omega) + 0.049\, S_{+}(Q,\omega) + 0.081\, S_{-}(Q,\omega)$$

(12/8)

$$S_T(Q,\omega)\ ({}^{109}\text{AgI}) = 0.879\, S_{MM}(Q,\omega) + 0.0014\, S_{qq}(Q,\omega) + 0.07\, S_{Mq}(Q,\omega) + 0.027\, S_{+}(Q,\omega) + 0.081\, S_{-}(Q,\omega)$$

(12/9)

$$= 0.176\, S_{++}(Q,\omega) + 0.279\, S_{--}(Q,\omega) + 0.442\, S_{+-}(Q,\omega) + 0.027\, S_{+}(Q,\omega) + 0.081\, S_{-}(Q,\omega)$$

(12/10)

From these we see that the charge-charge contribution to both is very small. Thus, if mass and charge are the appropriate variables to

describe the dynamic modes of AgI, scattering will be almost entirely due to the mass-mass mode for both samples and so the spectra from each will be very similar.

The scattering intensities for each angle are plotted as a function of energy in figure 12.15. A number of peaks can be observed in these; their positions are plotted to give the quasi-dispersion curves in figure 12.16. There is one low energy acoustic type mode and another mode at approximately constant Q. These can also be seen in the surface plots of figures 12.17 and 12.18 from which it can be seen that the constant Q mode is far more clearly defined than the acoustic mode. The latter can almost certainly be considered to exist at higher momentum transfer; it is not observed simply because it runs into the constant Q mode which hides it. The plots of $C(Q,\omega)$ (figure 12.19) show this - at high angles there is only one low energy peak. As the scattering decreases and the constant Q mode moves to higher energy the peak splits allowing the acoustic mode to be seen. This can be followed down to the lowest angle detector at approximately the same energy. We conclude that the acoustic mode exists over the entire momentum range measured by this experiment with an energy of about 6meV. This may increase a little at the low Q end but this is uncertain as it is here derived from the position of the peak in $C(Q,\omega)$ which tends to overestimate the energy of the underlying mode.

The results for molten ^{109}AgI are very similar (figure 12.20). Although there may be small differences they are very difficult to interpret especially as the statistics are rather poor for the sample of ^{109}AgI. The results seem to be consistent with the acoustic mode being a

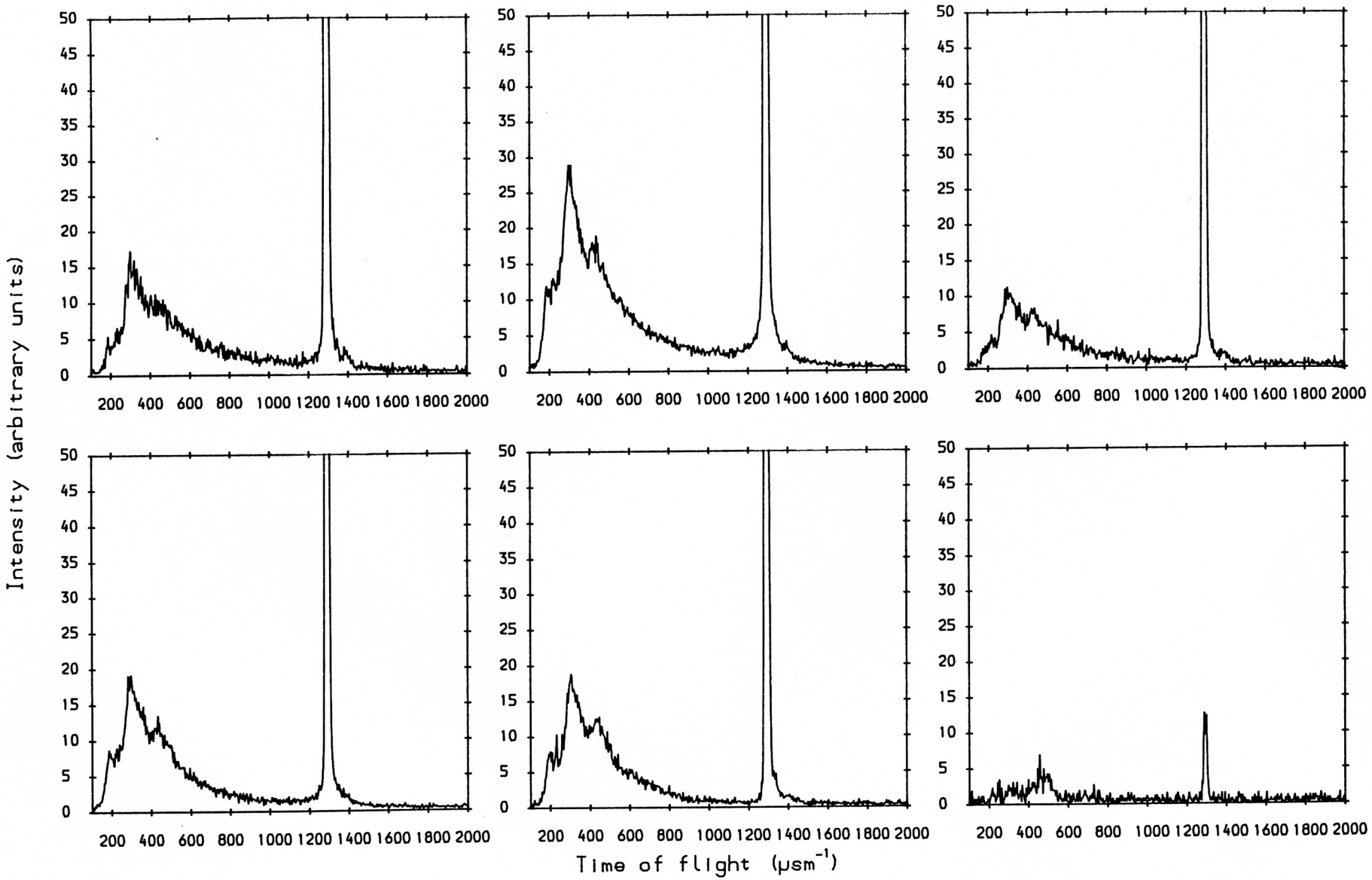


Figure 12.12 Scattering intensities (normalised to monitor count) for α-^{N}AgI at 300°C, molten ^{N}AgI at 600°C, α-^{109}AgI at 300°C, molten ^{109}AgI at 600°C, an empty silica container at 527°C, and the empty furnace at 527°C, all at a scattering angle of 11.9°.

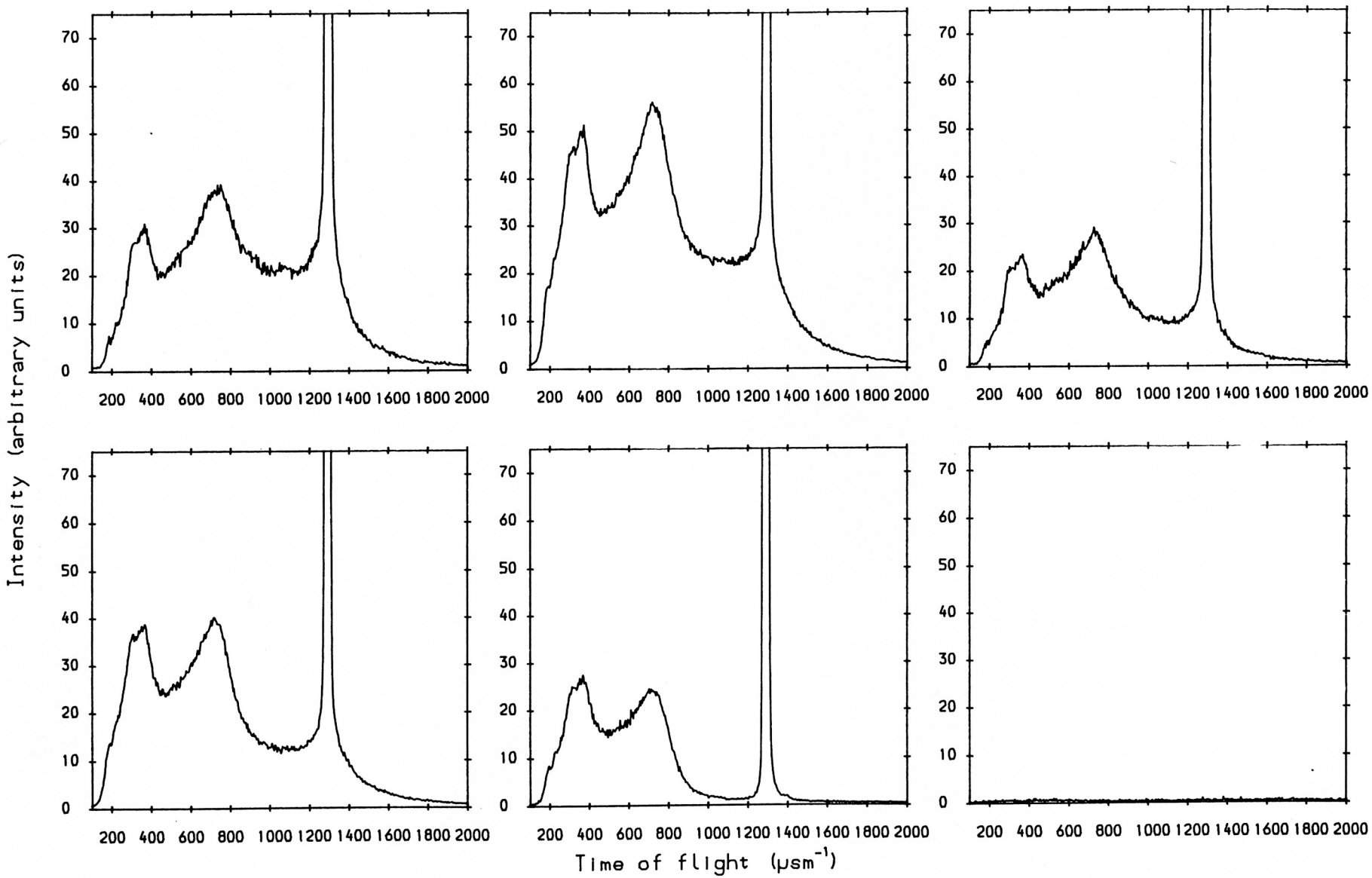


Figure 12.13 Scattering intensities (normalised to monitor count) for α-^{N}AgI at 300°C, molten ^{N}AgI at 600°C, α-^{109}AgI at 300°C, molten ^{109}AgI at 600°C, an empty silica container at 527°C, and the empty furnace at 527°C, all at a scattering angle of 111.6°.

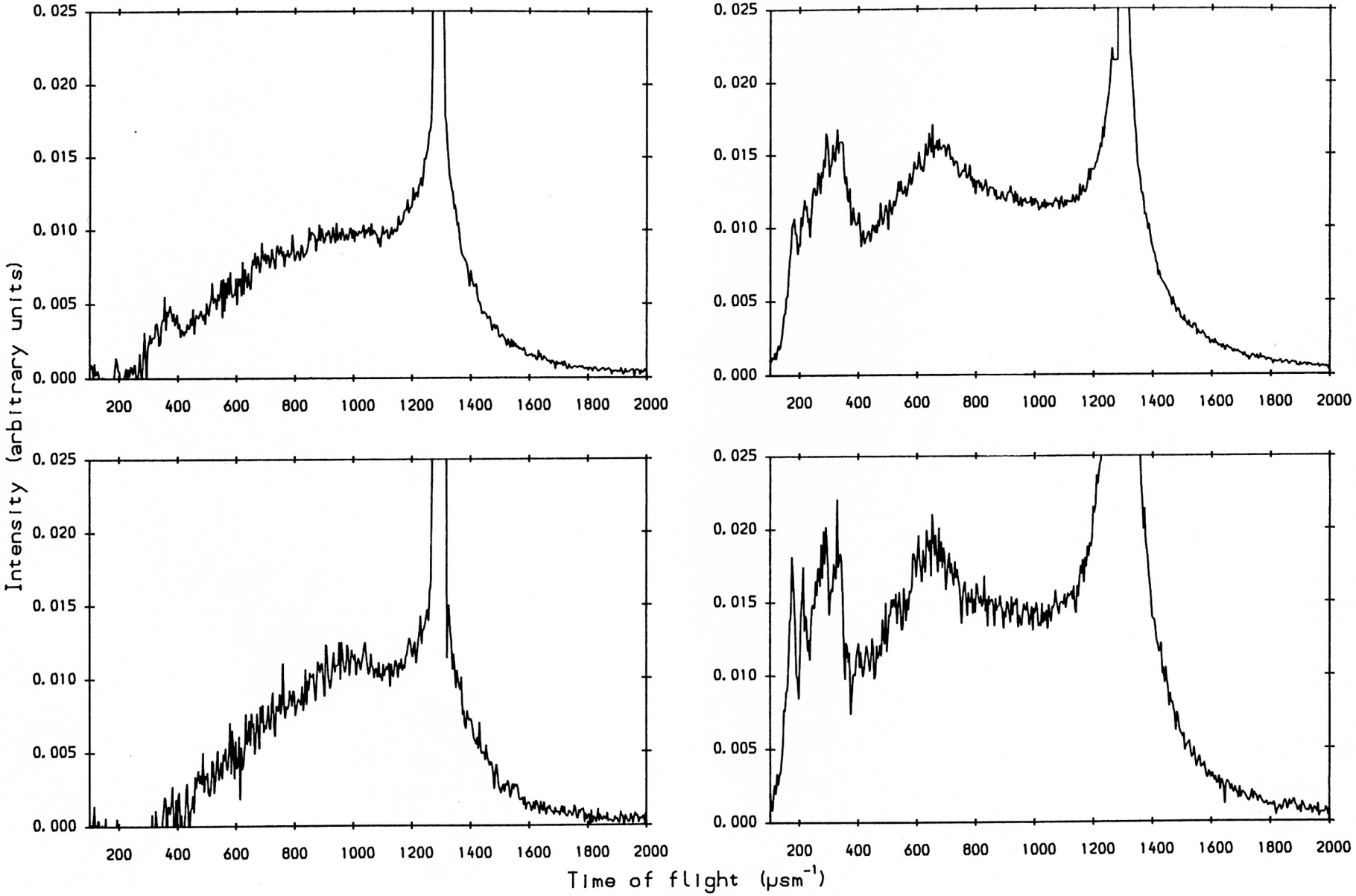


Figure 12.14 Corrected spectra for α-^{N}AgI at 300°C, molten ^{N}AgI at 600°C, α-^{109}AgI at 300°C, and molten ^{109}AgI at 600°C, all at a scattering angle of 97.3°.

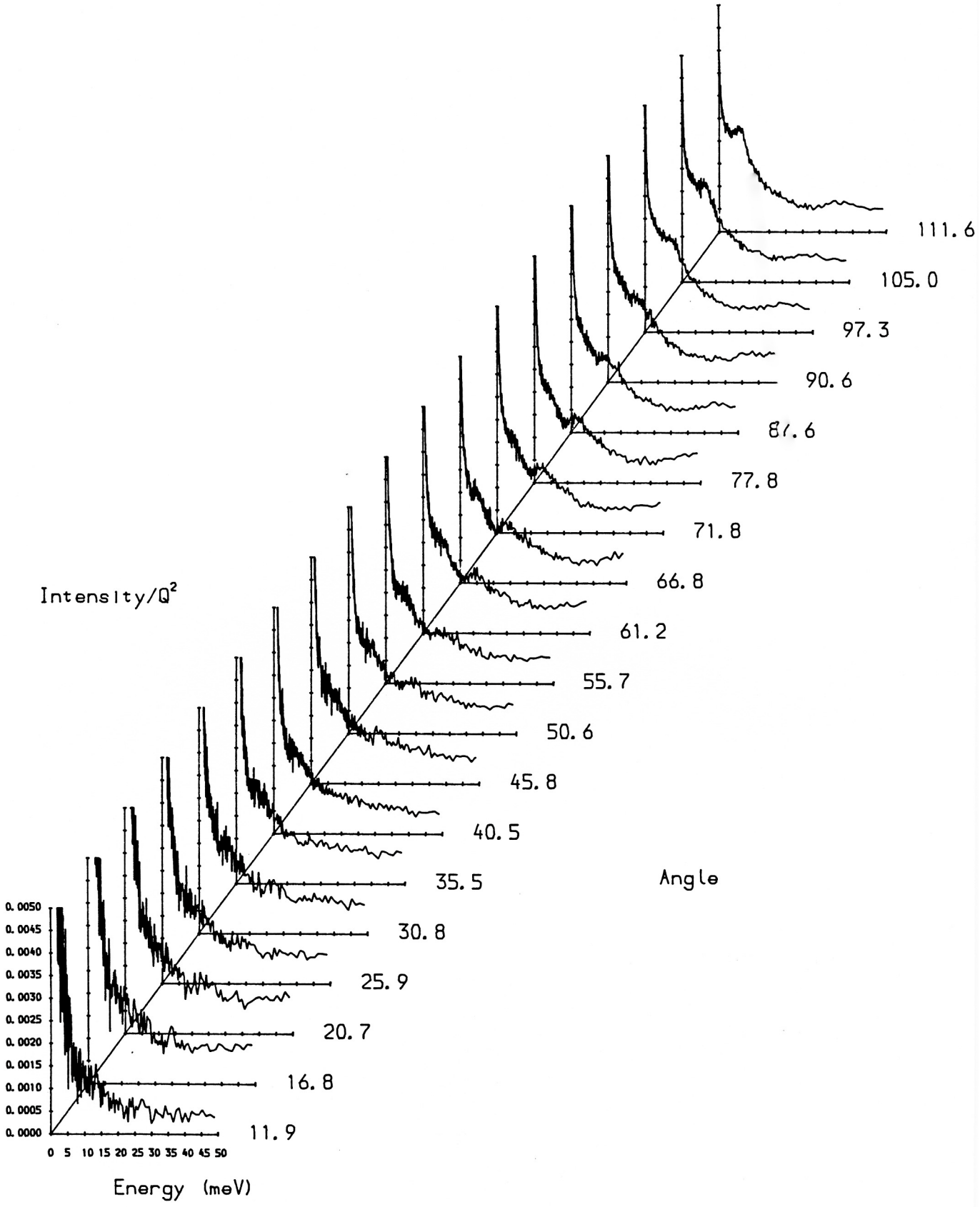


Figure 12.15 The scattering intensities divided by Q^2 for molten ^{N}AgI at 600°C as determined by the different detectors.

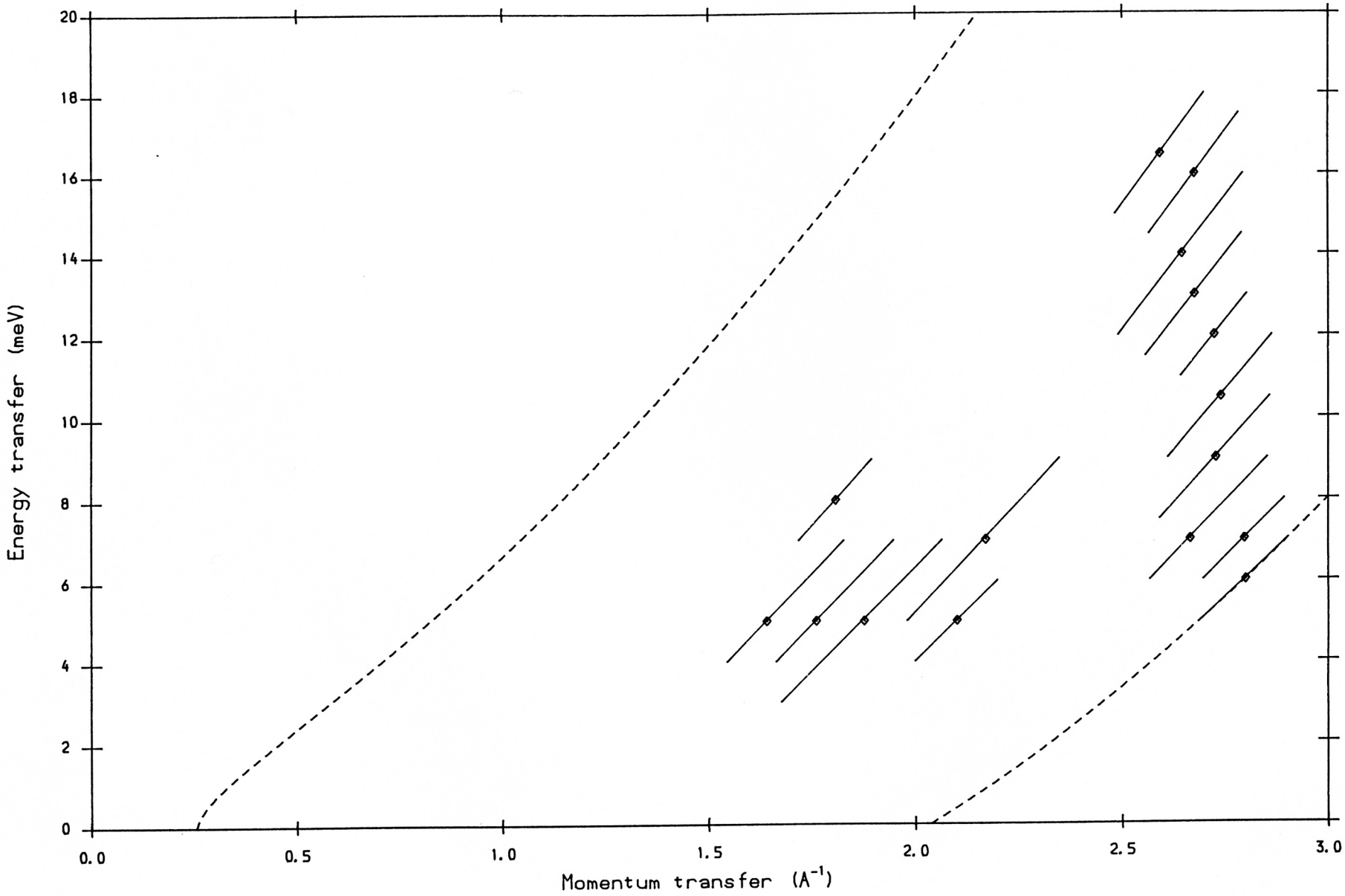


Figure 12.16 Quasi-dispersion curves for molten AgI. The dashed lines indicate the region accesible by the experiment.

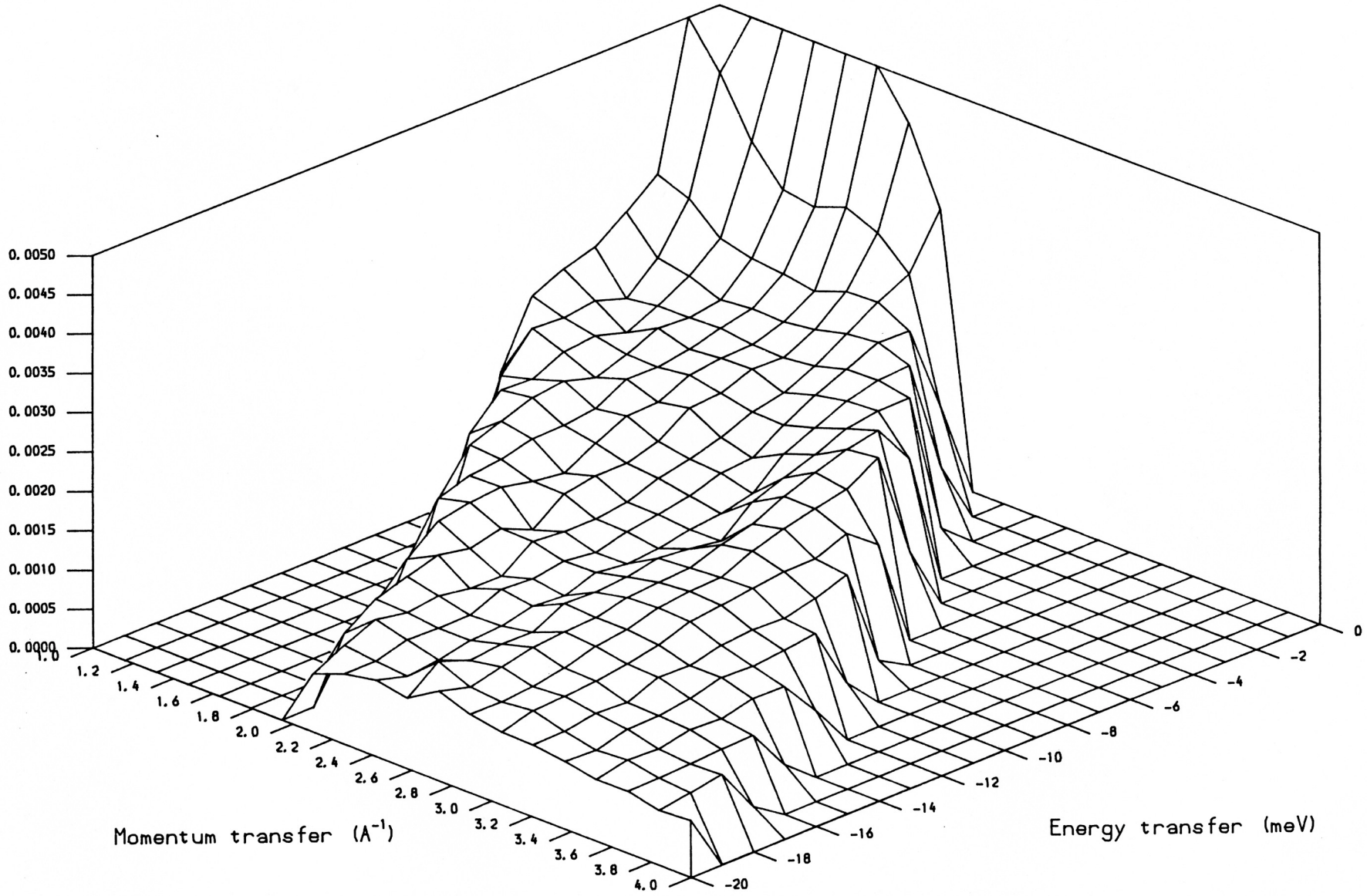


Figure 12.17 The scattering intensity divided by Q^2 for molten ^{N}AgI at 600°C.

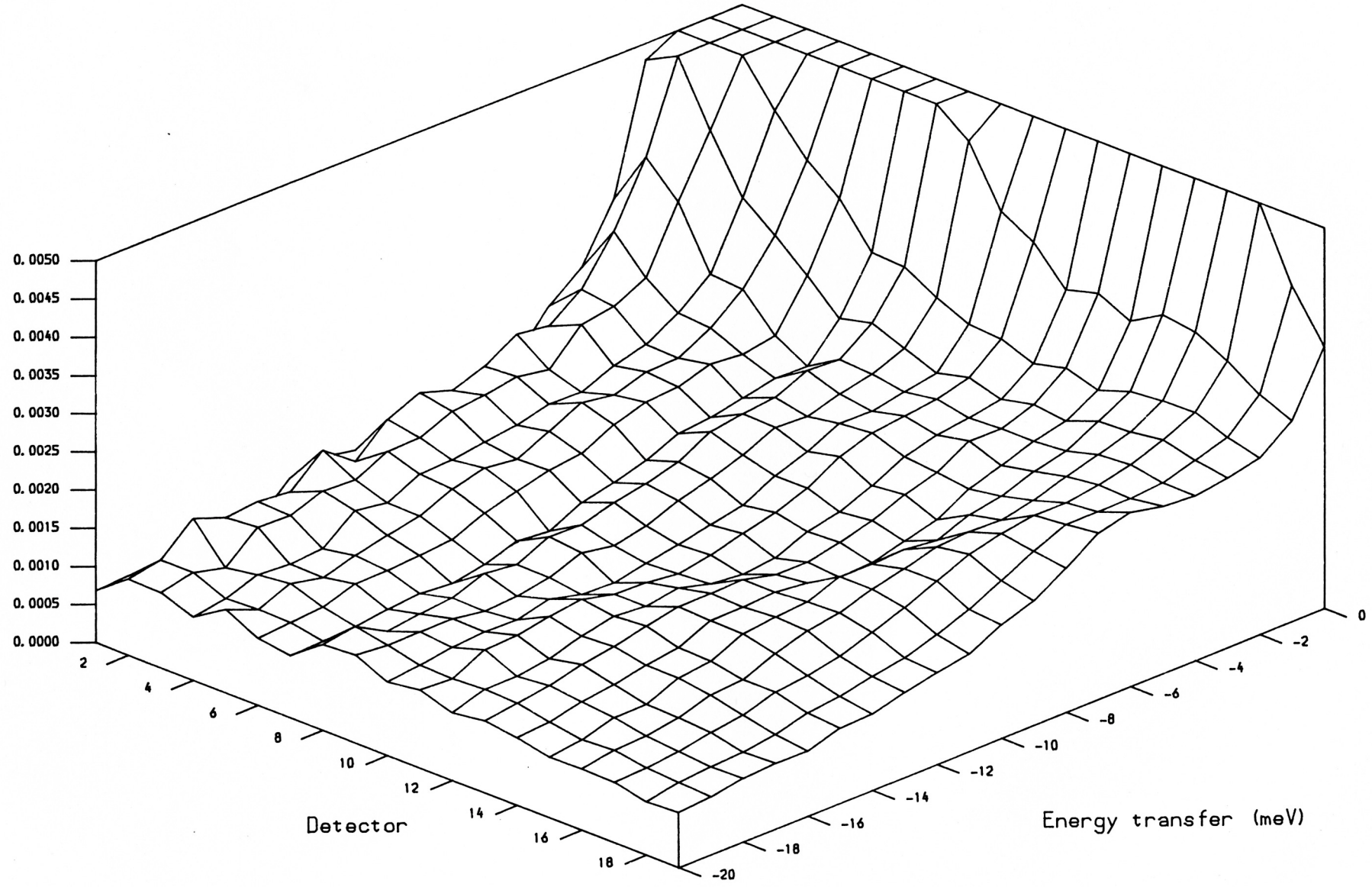


Figure 12.18 The scattering intensity divided by Q^2 for molten ^{N}AgI at 600°C.

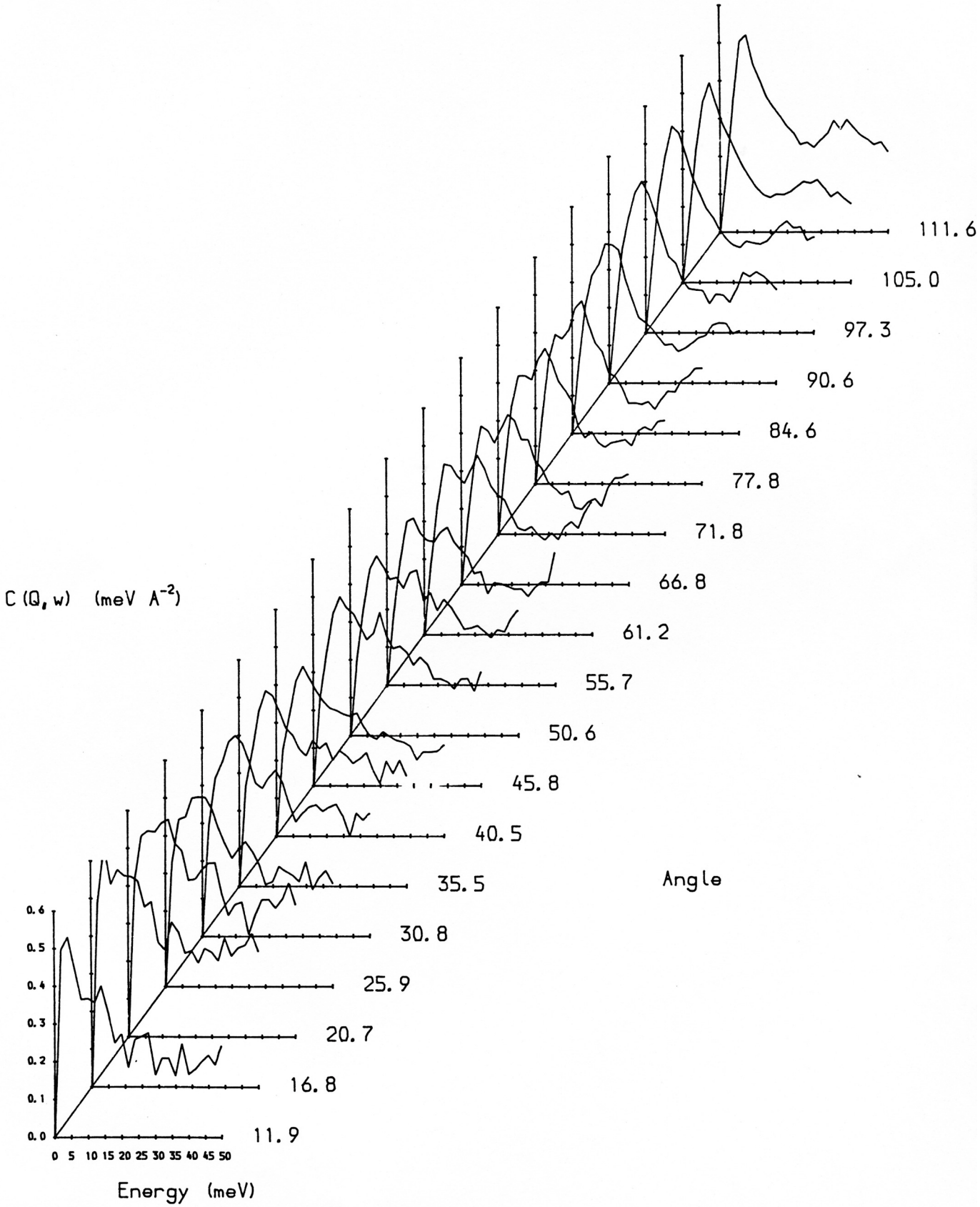


Figure 12.19 C(Q, w) for molten ^{N}AgI at 600°C as determined by the different detectors.

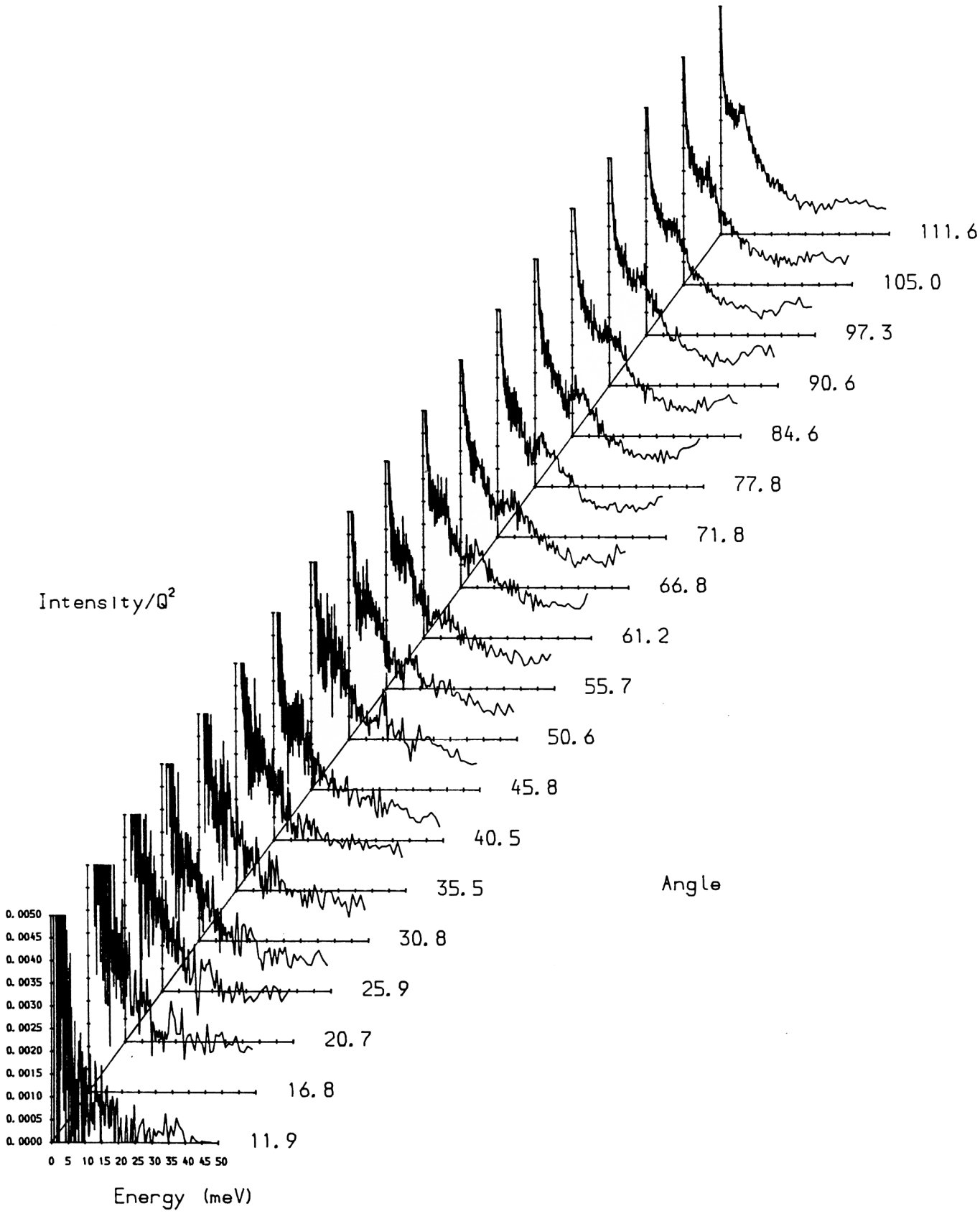


Figure 12.20 The scattering intensities divided by Q^2 for molten ^{109}AgI at 600°C as determined by the different detectors.

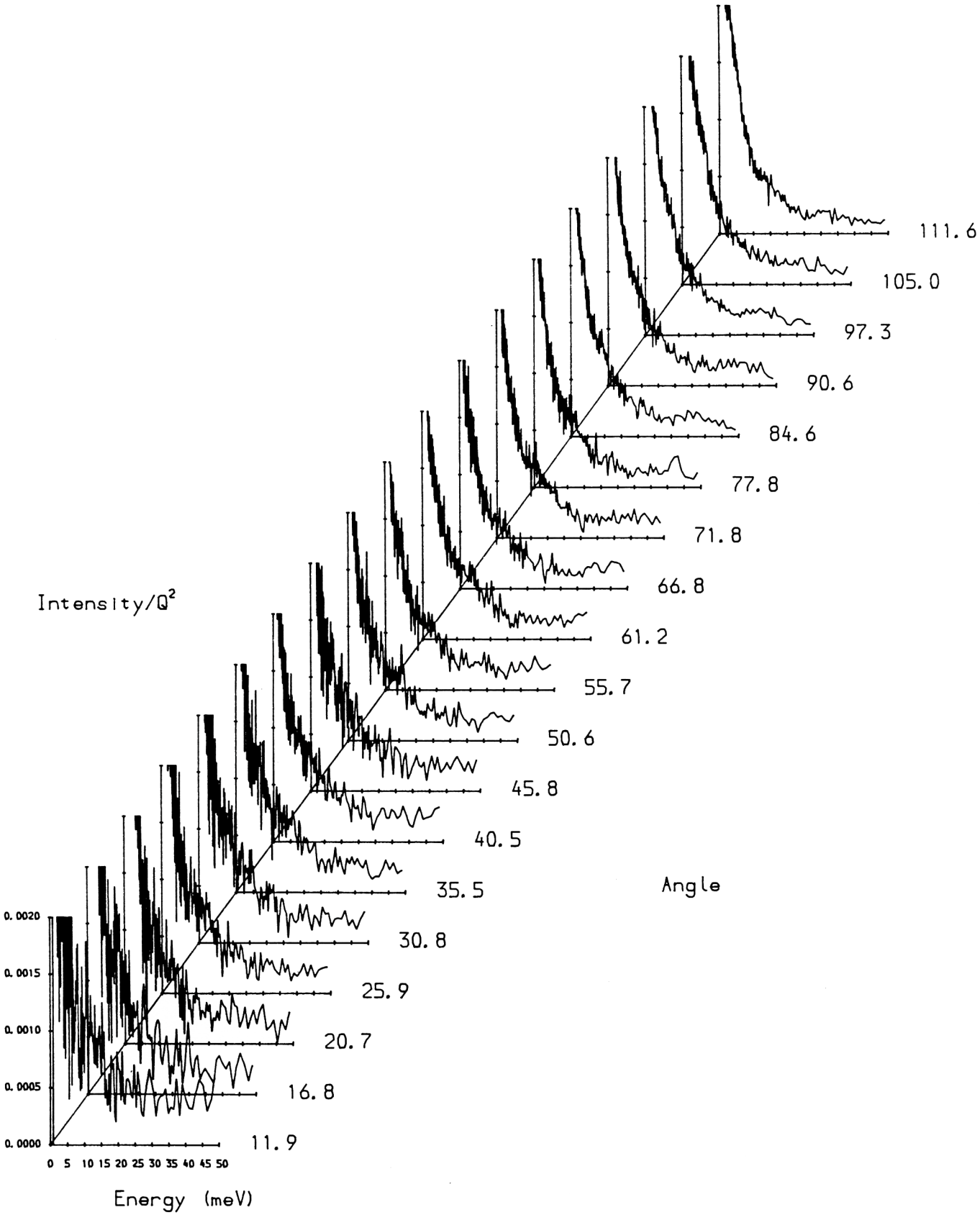


Figure 12.21 The scattering intensities divided by Q^2 for α-^{N}AgI at 300°C as determined by the different detectors.

mass-mass correlation; they are not inconsistent with the same being true of the constant Q mode.

Although the inelastic scattering is of lower intensity for the α-phase which makes the statistics rather poorer it is quite clear that there is no evidence for the constant Q mode in this phase - this accounts for the absence of high energy scattering in figure 12.14. The acoustic mode may just be observable but the evidence is not conclusive. There is, though, a peak in the scattering intensity as a function of time of flight, which can be observed as a shoulder in the intensity on an energy scale (figure 12.21, observable at high angles at approximately 15meV, as one would expect an optic mode to be. This is clearer in the ^{109}AgI. As the ^{109}Ag scattering length is smaller than that of the natural mixture this should, I think, be interpreted as the surrounding scattering from the quasi-elastic peak being smaller so making this peak clearer rather than the peak being larger. This does however suggest that this mode is not mass-mass in nature (as it should then be smaller in the ^{109}AgI). More than that it is not sensible to conclude given the poor statistical nature of the data. It is not impossible that this same mode exists in the melt; there it would be hidden by the constant Q mode.

We have, then, determined that molten silver iodide has an acoustic mode apparently similar to those of alkali halides. An optic mode is not observed but this is not surprising because a charge-charge mode, if present, would present only a small contribution to the entire scattering and, further, it would be hidden by the third mode at high angles. This third mode occurs at a constant Q, or nearly constant Q, value of approximately 2.8Å^{-1} and so appears to occur at the first major

peak of the static structure factor $S(Q)$. Thus, the peak in the static structure factor which represents structural correlations, seems to exhibit itself as a peak in $S(Q,\omega)$ (at constant ω) over quite a wide energy range whereas in alkali halides $S(Q,\omega)$ is only significantly affected around zero energy transfer. There is also some evidence to suggest that the same thing happens at the next peak in the structure factor with the effects extending out to, at least, 50meV. The only case where anything similar has been observed is that of strontium chloride where the extra modes mentioned above come out of structure factor peaks though they then slope approximately according to the velocity of sound whereas here the slope is much steeper and, if anything, negative. Although we have not observed this mode in the fast ion conductor we cannot rule out the possibility that it might exist at higher temperatures, nearer the melting point. Indeed, it has been suggested that the α-phase exists in two forms, the higher temperature form having a more highly disordered cation structure than the lower [12,20,12/21]: this extra mode might be present in the higher temperature form. Against this is the observation that the structure appears to change little between the two temperatures, despite the melting transition.

The height and width of the quasi-elastic peak are shown in figure 12.22 and in figure 12.23 $S(Q)$ calculated by integration under the quasi-elastic peak is compared with the diffraction data obtained using D4B. We see that the $S(Q)$ so calculated confirms the results of the D4B experiment which found two small peaks or shoulders at approximately 1.1Å^{-1} and 1.8Å^{-1} (the latter being much larger for the ^{109}AgI sample), below the principle peak. The second of these is associated with a much larger maximum in the height of the quasi-elastic peak and a minimum in

its width. This may be an example of de Gennes narrowing [12/22] which is when the various sum rules (see chapter 3, section 4) can only be satisfied when the height of the quasi-elastic peak increases if it also narrows. There is no such minimum in the width at the position of the 1.1$Å^{-1}$ peak; indeed it appears to be nearly a maximum. This is the sort of behaviour we might expect of the peak in the structure factor at 2.8$Å^{-1}$ which must be very broad as it extends out to form the constant Q mode. We cannot determine this, though, as it is outside the range of this experiment. It is interesting to note that the width here, which must be of the order of 10meV, is similar to that observed in polaronic materials such as Nd(Pb)$Mn0_3$ [12/23].

We have seen that molten silver iodide has some interesting features in its dynamics distinguishing it from the alkali halides and alkaline earth halides that have been studied. It would be interesting to see whether they are also found in the other silver halides or in the cuprous halides. In particular silver chloride would be worth studying because of the possibility of isotopic substitution of both silver and chlorine.

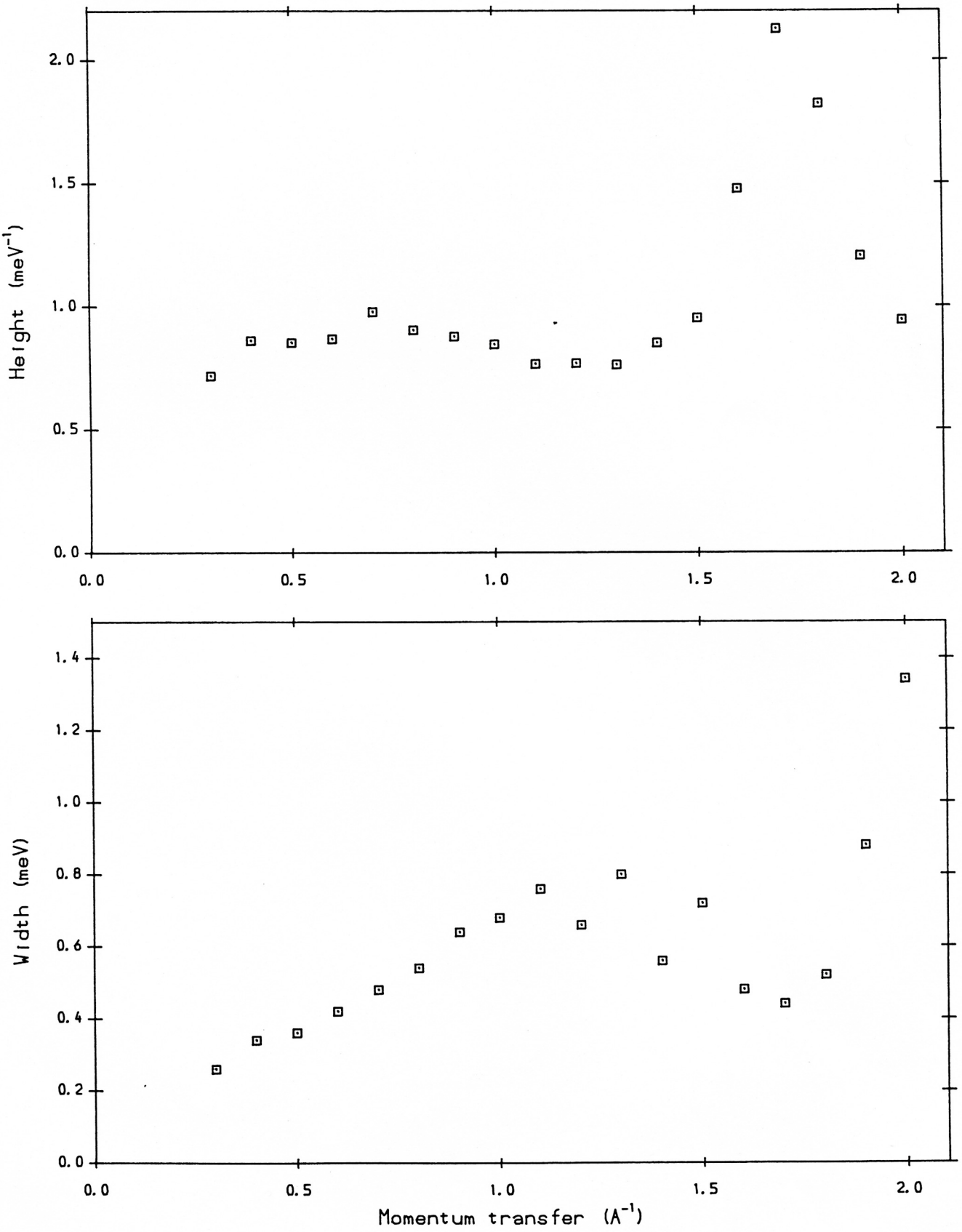


Figure 12.22 The height and width of the quasi-elastic peak in $S(Q,\omega)$ for molten AgI.

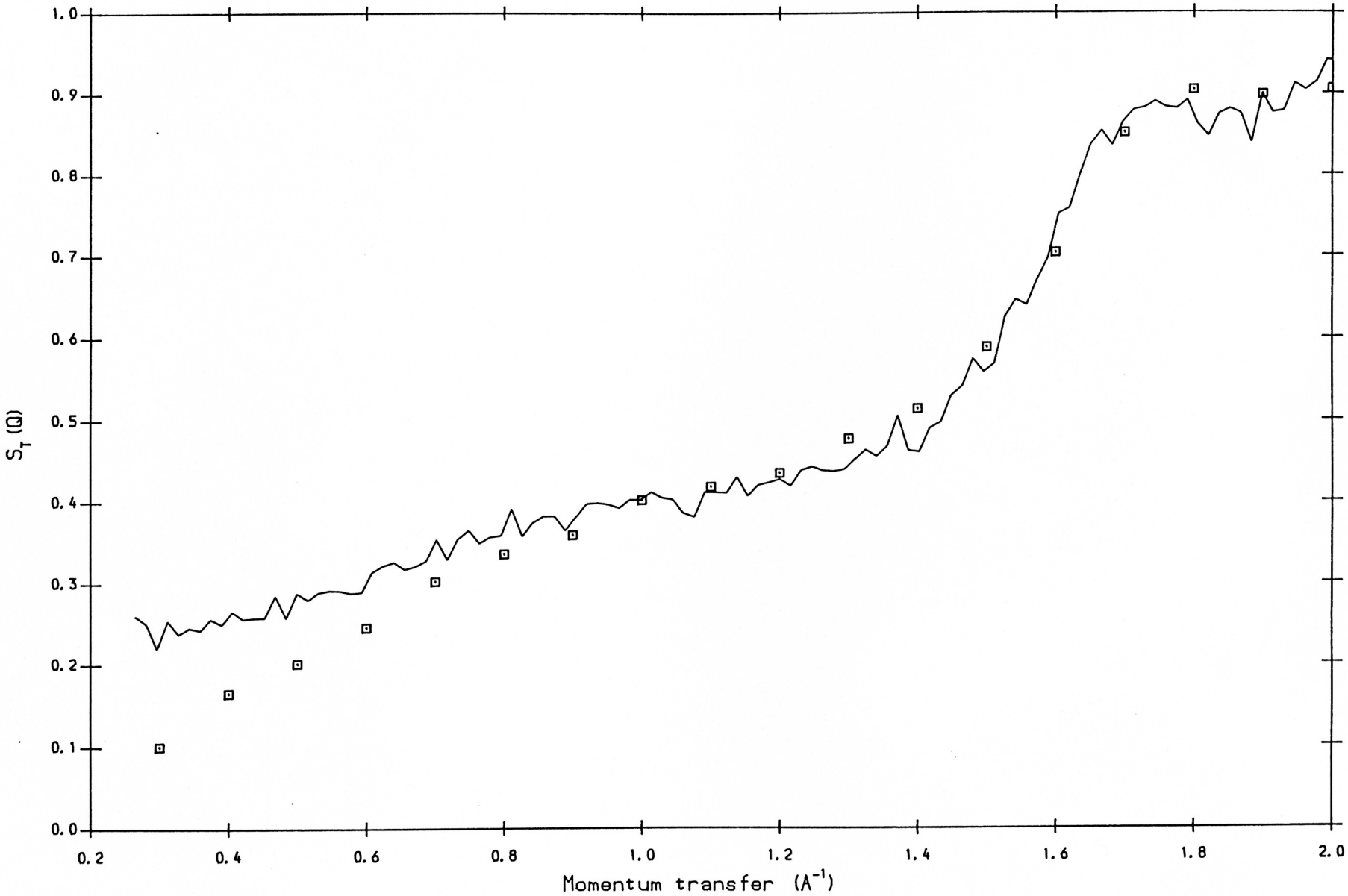


Figure 12.23 The total structure factor for AgI at 600°C calculated by integration of $S(Q,\omega)$ (□) compared with that at obtained using D4B (solid line).

Appendix A

Neutron scattering parameters and properties of molten salts

A.1 Atomic and ionic radii [A/1]

Ion	Atomic radius (Å)	Ionic radius (Å)
Li^+	1.52	0.60
Na^+	1.86	0.95
K^+	2.31	1.33
Rb^+	2.44	1.48
Cs^+	2.62	1.69
Ag^+	1.44	1.26
Cl^-	0.99	1.81
I^-	1.33	2.16

A.2 Scattering properties of nuclei [A/2]

Nucleus	$\bar{b}$	σ	$\overline{b^2}$	σ_a	% abundance
^{6}Li	$0.187-0.026i$	0.98	0.078	940.	7.5
^{7}Li	-0.220	1.44	0.115	0.0454	92.5
^{N}Li	-0.203	1.40	0.111	70.5	
^{35}Cl	1.17	21.62	1.720	44.1	75.77
^{37}Cl	0.308	1.2	0.095	0.433	24.23
^{N}Cl	0.9579	16.63	1.323	33.5	
^{133}Cs	0.542	3.96	0.315	29.	100.
^{N}K	0.367	2.10	0.167	2.1	
^{107}Ag	0.764	7.44	0.592	38.	51.83
^{109}Ag	0.419	2.55	0.203	91.	48.17
^{N}Ag	0.597	5.09	0.405	63.3	
^{127}I	0.528	4.52	0.360	6.2	100.

A. 3 Composition of enriched isotopes used

Isotope	Composition
^{35}Cl	99.64% ^{35}Cl 0.36% ^{37}Cl
^{37}Cl	5% ^{35}Cl 95% ^{37}Cl
^{6}Li	95.30% ^{6}Li 4.70% ^{7}Li
^{7}Li	1% ^{6}Li 99% ^{7}Li

A. 4 Mean scattering lengths of the samples

Salt	$\overline{b^2}$	$\bar{b}_+$	$\bar{b}_-$	$\bar{b}$
CsCl	0.819	0.542	0.9579	0.750
^{107}AgI	0.476	0.764	0.528	0.646
^{109}AgI	0.282	0.419	0.528	0.474
^{N}AgI	0.383	0.597	0.528	0.563
$^{7}Li^{35}Cl$	0.914	-0.216	1.167	0.476
$^{7}Li^{37}Cl$	0.146	-0.216	0.351	0.068
$^{7}Li^{N}Cl$	0.719	-0.216	0.9579	0.371
KCl	0.745	0.367	0.9579	0.662
$^{7}Li_{0.1}K_{0.9}Cl$	0.743		0.9579	0.633
$^{(0)}Li_{0.1}K_{0.9}Cl$	0.742		0.9579	0.644

A.5 Physical properties of molten salts [A/1]

Salt	m.pt (°C)	Number density (10^{22} cm^{-3})	K_T (10^{-6} cm^3J^{-1})	Velocity of sound (ms^{-1})
CsCl	645	1.978 at 670°C 1.749 at 970°C	429 at 700°C	1145 at 670°C 942 at 970°C
AgI	552	2.839 at 600°C		
LiCl	610	4.206 at 660°C	217 at 700°C	1996 at 660°C
KCl	772	2.213 at 827°C	384 at 800°C 457 at 900°C	1549 at 827°C

Appendix B

Properties of Heisenberg operators

Quantum mechanics may be formulated in two ways, known as the Schrödinger picture and the Heisenberg picture. In the former the operators representing physical variables are constant in time (and so, therefore, are their eigenfunctions). The state vector $\psi(t)$ representing the state of the system at any given time varies according to Schrödinger's equation

$$\frac{\partial\psi(t)}{\partial t} = \frac{1}{i\hbar} H\,\psi(t) \qquad \text{(B/1)}$$

where H is the Hamiltonian operator for the system. In the Heisenberg picture the time dependence is carried in the operators while the state vector remains constant. The Heisenberg operator $A(t)$ corresponding to the Schrödinger operator A is

$$A(t) = T^{\dagger}AT \qquad \text{(B/2)}$$

where

$$T = e^{-iHt/\hbar} \qquad \text{(B/3)}$$

where the exponentiation of the Hamiltonian can be understood in terms of the series expansion

$$T = e^{-iHt/\hbar} = 1 - \frac{it}{\hbar} H - \frac{1}{2}\frac{t^2}{\hbar^2} H^2 + \frac{1}{3!}\frac{it^3}{\hbar^3} H^3 + \ldots$$

(B/4)

The expectation value of the physical quantity represented by A is

$\langle\psi(t)|A|\psi(t)\rangle$ in the Schrödinger picture

$\langle\psi|A(t)|\psi\rangle$ in the Heisenberg picture

(B/5)

It can be shown using (B/1) and (B/2) that these two expressions are equal, as they must be, representing as they do the same observable. The Schrödinger equation is not appropriate to the Heisenberg picture; instead we have an equation describing the time dependence of the operator. From (B/2) and (B/3) we obtain

$$\frac{d}{dt} A(t) = \frac{i}{\hbar} HA(t) - \frac{i}{\hbar} A(t)H + T^{\dagger}\frac{\partial A}{\partial t}T$$

(B/6)

If A does not vary explicitly with time then this reduces to the commutator

$$\frac{d}{dt} A(t) = \frac{i}{\hbar} [H, A(t)]$$

(B/7)

B.1 Properties of Heisenberg operators

A few useful properties of Heisenberg operators are:

i) If A commutes with the Hamiltonian H the Heisenberg and Schrödinger operators are the same at all times. (B/7) shows that under this condition the Heisenberg operator is constant and thus always equal to its value at $t = 0$, the Schrödinger operator. Alternatively

$$A(t) = T^{\dagger}AT = AT^{\dagger}T = A$$

(B/8)

ii) The Hermitian conjugate, $A^{\dagger}(t)$, of the Heisenberg operator, $A(t)$, corresponding to the Schrödinger operator A is the Heisenberg operator corresponding to $A^{\dagger}$:

$$\big(A(t)\big)^{\dagger} = (T^{\dagger}AT)^{\dagger} = T^{\dagger}A^{\dagger}T = A^{\dagger}(t)$$

(B/9)

It follows that if A is Hermitian then so is $A(t)$

iii) A function of $A(t)$ is, in general, the Heisenberg operator corresponding to the same function of A:

$$\big(A(t)\big)^{2} = T^{\dagger}ATT^{\dagger}AT = T^{\dagger}AAT = A^{2}(t)$$

(B/10)

So in general

$$\big(A(t)\big)^{n} = A^{n}(t)$$

(B/11)

From which it follows that

$$e^{\alpha A(t)} = T^{\dagger}e^{\alpha A}T$$

(B/12)

(iv) If $A(t_1)$ and $B(t_2)$ are two Heisenberg operators the value of $\langle\psi|A(t_1)B(t_2)|\psi\rangle$ depends not on t_1 and t_2 individually but only on their difference. To see this we note that for any operator $C(t)$

$$\langle\psi|e^{iHt/\hbar}C|\psi\rangle = e^{-iE_{\psi}t/\hbar}\langle\psi|C|\psi\rangle$$

(B/13)

where E_{ψ} is the eigenvalue of the Hamiltonian for the state ψ. So

$$\langle\psi|A(t_1)B(t_2)|\psi\rangle = \langle\psi|e^{iHt_1/\hbar}Ae^{-iHt_1/\hbar}e^{iHt_2/\hbar}Be^{-iHt_2/\hbar}|\psi\rangle \tag{B/14}$$

$$= e^{iE_\psi t_1/\hbar}\langle\psi|Ae^{iH(t_2-t_1)/\hbar}Be^{-iHt_2/\hbar}|\psi\rangle \tag{B/15}$$

$$= \langle\psi|Ae^{iH(t_2-t_1)/\hbar}Be^{-iH(t_2-t_1)/\hbar}|\psi\rangle \tag{B/16}$$

$$= \langle\psi|A(0)B(t_2-t_1)|\psi\rangle \tag{B/17}$$

v) Where $\langle\ \rangle$ denotes the thermal average at temperature T,

$$\langle A(0)B(t)\rangle = \langle B(t)A(i\hbar\beta)\rangle \tag{B/18}$$

where $\beta = 1/k_BT$. To prove this we observe that

$$\langle A(0)B(t)\rangle = \frac{1}{Z}\sum_\lambda e^{E_\lambda\beta}\,\langle\lambda|A(0)B(t)|\lambda\rangle \tag{B/19}$$

where Z is the partition function

$$= \frac{1}{Z}\sum_\lambda \langle\lambda|AT^\dagger BTe^{-H\beta})|\lambda\rangle \tag{B/20}$$

Because we are summing over all states this can be written as

$$= \frac{1}{Z}\sum_\lambda \langle\lambda|T^\dagger BTe^{-H\beta}A)|\lambda\rangle \tag{B/21}$$

$$= \frac{1}{Z}\sum_\lambda e^{-E_\lambda\beta}\,\langle\lambda|e^{H\beta}T^\dagger BTe^{-H\beta}A)|\lambda\rangle \tag{B/22}$$

$$= \langle B(t-i\hbar\beta)A(0)\rangle = \langle B(t)A(i\hbar\beta)\rangle \tag{B/23}$$

Appendix C

Delta functions and Fourier transforms

C.1 The Kronecker delta

The Kronecker delta symbol is defined as

$$\delta_{ij} = \begin{cases} 1, & i = j \\ 0, & i \neq j \end{cases} \qquad \text{(C/1)}$$

It can be considered to be an element of the identity matrix.

C.2 The Dirac delta function

This is defined such that

$$\delta(x - x_0) = 0 \text{ if } x \neq x_0 \qquad \text{(C/2)}$$

$$\int_a^b \delta(x - x_0)\, dx = 1 \text{ if } a \leq x_0 \leq b \qquad \text{(C/3)}$$

$$\int_a^b f(x)\, \delta(x - x_0)\, dx = f(x_0) \text{ if } a \leq x_0 \leq b \qquad \text{(C/4)}$$

If x has dimensions of length $\delta(x - x_0)$ has dimensions of (length)$^{-1}$. It can also be written as the limit of an integral. Consider

$$f(x) = \int_{-k_0}^{k_0} e^{ikx} dk$$

(C/5)

$$= 2k_0 \frac{\sin k_0 x}{k_0 x}$$

(C/6)

The total area under the curve defined by this function is

$$2\int_{-\infty}^{\infty} \frac{\sin k_0 x}{k_0 x}\, d(k_0 x) = 2\pi$$

(C/7)

As k_0 gets larger the central peak of $f(x)$ gets higher and narrower so that $f(x)$ becomes more like $2\pi\delta(x)$. This means we can write the delta function as the limiting form of this integral.

$$\delta(x) = \frac{1}{2\pi}\int_{-\infty}^{\infty} e^{ikx}\, dk$$

(C/8)

The three dimensional delta function is defined as

$$\delta(\boldsymbol{r} - \boldsymbol{r}_0) = \delta(x - x_0)\delta(y - y_0)\delta(z - z_0)$$

(C/9)

and has the following properties

$$\delta(\boldsymbol{r} - \boldsymbol{r}_0) = 0 \ \textit{if} \ \ \boldsymbol{r} \neq \boldsymbol{r}_0$$

(C/10)

$$\int_V \delta(\boldsymbol{r} - \boldsymbol{r}_0)\, d^3\boldsymbol{r} = 1 \text{ if } \boldsymbol{r}_0 \text{ is within the integration volume } V$$

(C/11)

$$\int_V f(\boldsymbol{r})\, \delta(\boldsymbol{r} - \boldsymbol{r}_0)\, d^3\boldsymbol{r} = f(\boldsymbol{r}_0) \text{ if } \boldsymbol{r}_0 \text{ is within the integration volume } V$$

(C/12)

The integral form of the three dimensional delta function is

$$\delta(\boldsymbol{r}) = \frac{1}{(2\pi)^3} \int e^{i\boldsymbol{k}.\boldsymbol{r}}\, d^3\boldsymbol{k}$$

(C/13)

where the integral is over all space.

C.3 Fourier transforms

The Fourier transform $F(s)$ of a function $f(t)$ is defined to be

$$F(s) = \int_{-\infty}^{\infty} f(t) e^{ist}\, dt$$

(C/14)

$f(t)$ can then be written as the inverse Fourier transform of $F(s)$

$$f(t) = \frac{1}{2\pi} \int_{-\infty}^{\infty} F(s) e^{-ist}\, ds$$

(C/15)

which is proved as follows

$$\frac{1}{2\pi} \int_{-\infty}^{\infty} F(s) e^{-ist}\, ds = \frac{1}{2\pi} \int_{-\infty}^{\infty} \int_{-\infty}^{\infty} f(t') e^{ist'}\, e^{-ist}\, dt' ds$$

(C/16)

$$= \int_{-\infty}^{\infty} f(t') \delta(t - t')\, dt' = f(t)$$

(C/17)

The Fourier transform can also be written as

$$F(s) = \int_{-\infty}^{\infty} f(t) \cos st\ dt + i \int_{-\infty}^{\infty} f(t) \sin st\ dt$$

(C/18)

where the first integral is the cosine Fourier transform and the second is the sine Fourier transform. For an even function ($F(s) = F(-s)$) the sine Fourier transform is zero, while for an odd function ($F(s) = -F(-s)$)

the cosine Fourier transform vanishes.

In three dimensions the Fourier transform is defined as

$$F(\boldsymbol{s}) = \int f(\boldsymbol{t}) e^{i\boldsymbol{s}.\boldsymbol{t}}\, d^3\boldsymbol{t}$$

(C/19)

and the inverse Fourier transform is

$$f(\boldsymbol{t}) = \frac{1}{(2\pi)^3} \int F(\boldsymbol{s}) e^{-i\boldsymbol{s}.\boldsymbol{t}}\, d^3\boldsymbol{s}$$

(C/20)

where the integrals are taken over all space. If $\boldsymbol{f(t)}$ depends only on the magnitude of $\boldsymbol{t}$, not on its direction then (C/19) can be integrated over two dimensions

$$F(s) = \int_0^{2\pi} d\phi \int_{-1}^{1} d(\cos\theta) \int_0^{\infty} dt\, f(t)\, t^2\, e^{ist\cos\theta}$$

(C/21)

$$F(s) = \frac{4\pi}{s} \int_0^{\infty} f(t)\, t \sin st\, dt$$

(C/22)

and inversely

$$f(t) = \frac{1}{2\pi^2 t} \int_0^{\infty} F(s)\, s \sin st\, ds$$

(C/23)

Appendix D

The conditioning of sets of linear equations

To determine the n partial structure factors of a system by neutron scattering we measure n total structure factors, each being a different combination of the partials. We then solve the simultaneous equations. This can be written in vector form as

$$\boldsymbol{F} = \boldsymbol{M}\,\boldsymbol{A}_p \qquad \text{(D/1)}$$

where $\boldsymbol{F}$ and $\boldsymbol{A}_p$ are vectors of the coherent scattering functions and partial structure factors; the elements of the separation matrix $\boldsymbol{M}$ are determined by the scattering lengths of the isotopes used. The solution is given by

$$\boldsymbol{A}_p = \boldsymbol{M}^{-1}\,\boldsymbol{F} \qquad \text{(D/2)}$$

We wish to have some idea of the reliability of this solution. Errors can arise in two ways. There may be errors in the total structure factors; an error $\Delta\boldsymbol{F}$ gives an error $\boldsymbol{M}^{-1}\Delta\boldsymbol{F}$ in the calculated partial structure factors which may be large if some elements of $\boldsymbol{M}^{-1}$ are large (here we assume that the matrix $\boldsymbol{M}$ is scaled so that its matrix elements are approximately unity: then by large we mean much greater than unity). There are also errors in the matrix elements as these are based on scattering lengths which are not known exactly. This again causes large errors in $\boldsymbol{A}_p$ if there are large elements in $\boldsymbol{M}^{-1}$. To see this consider one such element

$$M_{ji}^{-1} = m_{ij}/|\boldsymbol{M}|$$

(D/3)

where $|\boldsymbol{M}|$ denotes the determinant of $\boldsymbol{M}$ and m_{ij} is the cofactor of M_{ij} (and therefore unaffected by a change in M_{ij}). The assumption that M_{ij}^{-1} is large means that m_{ij} must be large compared with $|\boldsymbol{M}|$. Since one of the terms in the expansion of $|\boldsymbol{M}|$ along the i^{th} row or down the j^{th} column is $M_{ij}m_{ij}$ a small error in M_{ij} (relative to $|\boldsymbol{M}|$) may cause a large relative error in $|\boldsymbol{M}|$ and therefore a large relative error in M_{ij}^{-1}

It is useful to be able to assign some number to a matrix that is a measure of the magnitude of that matrix. Such a number is called the norm, denoted by $\|\boldsymbol{M}\|$. It is reasonable to require of it that

i) $\|\boldsymbol{M}\| \geq 0,\ \|\boldsymbol{M}\| = 0$ if, and only if, $\boldsymbol{M} = 0$

ii) $\|c\boldsymbol{M}\| = |c|\,\|\boldsymbol{M}\|$ where c is a real number

iii) $\|\boldsymbol{M} + \boldsymbol{N}\| \leq \|\boldsymbol{M}\| + \|\boldsymbol{N}\|$ (the triangle inequality)

iv) $\|\boldsymbol{M}\boldsymbol{N}\| \leq \|\boldsymbol{M}\|\,\|\boldsymbol{N}\|$ (the Schwarz inequality)

There are many possible ways of defining $\|\boldsymbol{M}\|$ such that it satisfies these conditions. Three such are: the Euclidean norm

$$\|\boldsymbol{M}\|_E = \sqrt{\sum_i \sum_j M_{ij}^2}$$

(D/4)

the spectral norm

$$\|\boldsymbol{M}\|_S = \max_i \sqrt{\lambda_i \boldsymbol{M}\boldsymbol{M}^T}$$

(D/5)

that is, the square root of the largest eigenvalue of $\boldsymbol{M}\boldsymbol{M}^T$, and

$$\|\boldsymbol{M}\|_M = \max_i \sum_j |M_{ij}|$$

(D/6)

where the sum is taken over the row for which it is greatest.

The condition that some of the elements of $\boldsymbol{M}^{-1}$ be large for ill conditioning can now be expressed as: the norm of $\boldsymbol{M}^{-1}$ be large. But we have said that $\boldsymbol{M}$ should be scaled so that its elements are approximately unity. We can remove this condition if we use as our measure of ill conditioning the product of the norms of $\boldsymbol{M}$ and $\boldsymbol{M}^{-1}$ (as multiplying $\boldsymbol{M}$ by c causes $\|\boldsymbol{M}\|$ to be multiplied by c and $\|\boldsymbol{M}^{-1}\|$ by $1/c$). This makes our conditioning numbers independent of the units in which the elements of the matrix are expressed. We can define, using our three definitions for the norm, three such numbers known as Turing's M conditioning number

$$T_M = \|\boldsymbol{M}\|_M \, \|\boldsymbol{M}^{-1}\|_M = \max_i \sum_j \left|M_{ij}^{-1}\right| \; \max_i \sum_j \left|M_{ij}\right| \tag{D/7}$$

Turing's N conditioning number

$$T_N = \|\boldsymbol{M}\|_E \, \|\boldsymbol{M}^{-1}\|_E = \sqrt{\sum_i \sum_j M_{ij}^2} \sqrt{\sum_i \sum_j \left(M_{ij}^{-1}\right)^2} \tag{D/8}$$

and the spectral conditioning number

$$T_S = \|\boldsymbol{M}\|_S \, \|\boldsymbol{M}^{-1}\|_S = \sqrt{\lambda_{max}(\boldsymbol{M}\boldsymbol{M}^T)/\lambda_{min}(\boldsymbol{M}\boldsymbol{M}^T)} \tag{D/9}$$

(see, for example [D/l]). The larger the conditioning number the poorer the conditioning of the matrix. The smallest possible values for these numbers are unity for T_M and T_S and n (the dimension of the matrix) for T_N which occur for the identity matrix.

It is important to note that the matrix connects the partial structure factors with the coherent scattering functions which are essentially cross-sections; and not the total structure factors $A_T(Q)$

obtained by dividing the cross-sections by the square of the mean coherent scattering length. When negative scattering lengths are involved, as in the case of lithium chloride, the latter, for some of the samples, can become quite large, as is the case for $^{7}Li^{37}Cl$. The very much larger conditioning number of the separation matrix from these to the partial structure factors reflects the fact that the total structure factors are on quite different scales so that the errors are not of a comparable size. If we wish to compare the conditioning for different experiments we must use the matrix connecting the scattering cross-sections, for which the errors are all of approximately the same size, to calculate the conditioning numbers.

I have calculated the conditioning numbers defined here for a number of different experiments that have been performed on molten salts to allow a comparison. They are shown in table 6.

Table 6. Conditioning numbers for different molten salt structural determinations

System	Samples	Matrix	Partials	T_M	T_N	T_S
LiCl	$^{7}Li^{35}Cl$	0.0117 -0.126 0.340	A_{++}			
	$^{7}Li^{N}Cl$	0.0117 -0.103 0.229	A_{+-}	141	188	187
	$^{7}Li^{37}Cl$	0.0117 -0.038 0.031	A_{--}			
	$^{7}Li^{35}Cl$	0.904 -2.630 1.912	S_{NN}			
	$^{7}Li^{N}Cl$	0.540 -1.742 1.378	S_{Nq}	108	200	199
	$^{7}Li^{37}Cl$	0.0184 -0.153 0.321	S_{qq}			
	$^{7}Li^{35}Cl$	0.352 -0.126	A_{like}	8	18	18
	$^{7}Li^{37}Cl$	0.0425 -0.038	A_{unlike}			
NaCl	$Na^{35}Cl$	0.0329 0.211 0.337	A_{++}			
	$Na^{N}Cl$	0.0329 0.148 0.166	A_{+-}	85	73	72
	$Na^{37}Cl$	0.0329 0.071 0.038	A_{--}			
KCl	$K^{35}Cl$	0.0337 0.215 0.342	A_{++}			
	$K^{N}Cl$	0.0337 0.176 0.229	A_{+-}	52	68	66
	$K^{37}Cl$	0.0337 0.057 0.024	A_{--}			
RbCl	$Rb^{35}Cl$	0.1253 0.414 0.342	A_{++}			
	$Rb^{N}Cl$	0.1253 0.339 0.229	A_{+-}	34	43	42
	$Rb^{37}Cl$	0.1253 0.109 0.024	A_{--}			
CsCl	$Cs^{35}Cl$	0.0734 0.317 0.342	A_{++}			
	$Cs^{N}Cl$	0.0734 0.260 0.229	A_{+-}	37	47	46
	$Cs^{37}Cl$	0.0734 0.084 0.024	A_{--}			
(Li/K)Cl	(^{7}Li/K)Cl	1. 0.	with Li	192	190	190
	($^{(0)}$Li/K)Cl	1. 0.01054	without Li			
AgI	^{107}AgI	0.1459 0.202 0.0697	A_{++}			
	^{N}AgI	0.0891 0.158 0.0697	A_{+-}	82	111	110
	^{109}AgI	0.0439 0.111 0.0697	A_{--}			
$MgCl_2$	$Mg^{35}Cl_2$	0.0321 0.280 0.608	A_{++}			
	$Mg^{N}Cl_2$	0.0321 0.229 0.408	A_{+-}	86	106	105
	$Mg^{37}Cl_2$	0.0321 0.074 0.042	A_{--}			
$CaCl_2$	$Ca^{35}Cl_2$	0.0267 0.255 0.608	A_{++}			
	$Ca^{N}Cl_2$	0.0267 0.209 0.408	A_{+-}	100	123	122
	$Ca^{37}Cl_2$	0.0267 0.067 0.042	A_{--}			
$SrCl_2$	$Sr^{35}Cl_2$	0.0548 0.365 0.608	A_{++}			
	$Sr^{N}Cl_2$	0.0548 0.299 0.408	A_{+-}	56	72	71
	$Sr^{37}Cl_2$	0.0548 0.096 0.042	A_{--}			

References

Chapter one

1/1 De Rerum Natura
Titus Lucretius Carus (translated by W H D Rouse)
Heinemann (London) 1943 (3rd edition)

1/2 W Friedrich, P Knipping and M Laue
Sitzb. Math.-Phys. Klasse Bayer. Akad. Wiss. Munchen 303 (1912)

1/3 P Debye and P Scherrer
Gottingen Nachrichten 16 (1916)

1/4 X-ray diffraction in liquids
F Zernicke and J A Prins
Zeitschrift für Physik **41** 184 (1927)

1/5 Debye P and Menke H
Ergeb. d. Tech. Rontgenk. (1931)

1/6 The diffraction of X-rays by liquid elements
Gingrich N S
Reviews of Modern Physics **15** 90-110 (1943)

1/7 The partial structure factors of liquid Cu-Sn
J E Enderby, D M North, and P A Egelstaff
Philosophical Magazine **14** 961-970 (1966)

1/8 Structure factor and radial distribution function of liquid argon
J L Yarnell, M J Katz, R G Wenzel, and S H Koenig
Physical Review A **7** 2130-2144 (1973)

1/9 The structure factor for liquid metals. I. The application of neutron diffraction techniques
D M North, J E Enderby, and P A Egelstaff
Journal of Physics C **1** 784-793 (1968)

1/10 The correlation of molecular orientations in liquid water by neutron and X-ray scattering
D I Page and J G Powles
Molecular Physics **21** 901-926 (1971)

1/11 The structure of an aqueous solution of nickel chloride
G W Neilson and J E Enderby
Proceedings of the Royal Society of London A **390** 353-371 (1983)

1/12 Electrical properties of unusual ionic melts
F Hensel
Advances in Physics **28** 555-594 (1979)

1/13 The structure of molten sodium chloride
F G Edwards, J E Enderby, R A Howe and D I Page
Journal of Physics C **8** 3483-3490 (1975)

1/14 Comments on the structure of molten salts
S Biggin and J E Enderby
Journal of Physics C **15** L305-309 (1982)

1/15 Analyse structurale des liquides ioniques KCl et CsCl par diffraction de neutrons
J-Y Derrien and J Dupuy
Journal de Physique **36** 191-198 (1975)

1/16 The ion pair distribution functions in molten rubidium chloride
E W J Mitchell, P F J Poncet and R J Stewart
Philosophical Magazine **34** 721-732 (1976)

1/17 The structure of molten CsCl
J Locke, R L McGreevy, S Messoloras, E W J Mitchell and R J Stewart
Philosophical Magazine B **51** 301-315 (1985)

1/18 The structures of molten magnesium and manganese (II) chlorides
S Biggin, M Gay and J E Enderby
Journal of Physics C **17** 977-985 (1984)

1/19 The structure of molten calcium chloride
S Biggin and J E Enderby
Journal of Physics C **14** 3577-3583 (1981)

1/20 The determination of the partial pair distribution functions for molten strontium chloride
R L McGreevy and E W J Mitchell
Journal of Physics C **15** 5537-5550 (1982)

1/21 The structure of molten barium chloride
F G Edwards, R A Howe, J E Enderby and D I Page
Journal of Physics C **11** 1053-1057 (1978)

1/22 The partial structure factors of molten cuprous chloride from neutron diffraction measurements
D I Page and K Mika
Journal of Physics C **4** 3034-3044 (1971)

1/23 Neutron diffraction determination of the partial structure factors of molten CuCl
S Eisenberg, J-F Jal, J Dupuy, P Chieux and W Knoll
Philosophical Magazine A **46** 195-209 (1982)

1/24 Structure of molten silver chloride
J-Y Derrien and J Dupuy
Physics and Chemisty of Liquids **5** 71-91 (1976)

1/25 The structure of molten zinc chloride
S Biggin and J E Enderby
Journal of Physics C **14** 3129-3136 (1981)

1/26 The structure of molten nickel chloride
R J Newport, R A Howe and N D Wood
Journal of Physics C **18** 5249-5257 (1985)

1/27 M Chemla
French Patent No 1,216,418 (25th April 1960)

1/28 Neutron scattering studies of the dynamics of molten alkali halides
R L McGreevy, E W J Mitchell and F M A Margaça
Journal of Physics C **17** 775-796 (1984)

1/29 Possible observation of short wavelength charge fluctuation scattering in a molten alkali halide
J R D Copley and G Dolling
Journal of Physics C **11** 1259-1268 (1978)

1/30 The observation of longitudinal optic vibrational modes in molten rubidium chloride
R L McGreevy and E W J Mitchell
Journal of Physics C **15** L1001-1006 (1982)

1/31 Density fluctuations in molten salts. I. Inelastic neutron scattering from liquid RbBr
D L Price and J R D Copley
Physical Review A **11** 2124-2133 (1976)

1/32 Inelastic neutron scattering studies of collective modes in molten CsCl
R L McGreevy, E W J Mitchell, F M A Margaça and M A Howe
Journal of Physics C **18** 5235-5247 (1985)

1/33 Collective modes in molten alkaline earth chlorides: III Inelastic neutron scattering from molten $MgCl_2$ and $CaCl_2$
R L McGreevy and E W J Mitchell
Journal of Physics C **18** 1163-1178 (1985)

1/34 Collective modes in molten alkaline earth bromides II Inelastic neutron scattering from $MgBr_2$, $CaBr_2$ and $SrBr_2$
M C Fairbanks, M A Howe and R L McGreevy In preparation

1/35 Collective modes in molten alkaline earth chlorides: II Inelastic neutron scattering from molten $SrCl_2$
F M A Margaça, R L McGreevy and E W J Mitchell
Journal of Physics C **17** 4725-4739 (1984)

Chapter two

2/1 Theory of neutron scattering from condensed matter
S W Lovesey
Clarendon Press (Oxford) 1984

Chapter three

3/1 Correlations in space and time and Born approximation scattering in systems of interacting particles
L van Hove
Physical Review **95** 249-262 (1954)

3/2 The scattering of neutrons by systems of heavy nuclei
G Placzek
Physical Review **86** 377-388 (1952)

3/3 Theory of slow neutron scattering by liquids.
I A Rahman, K S Singwi and A Sjölander
Physical Review **126** 986-996 (1962)

3/4 Statistical physics
Landau and Lifshitz
Pergammon Press (London) 1958

3/5 Structure of binary liquid mixtures.
I N W Ashcroft and D C Langreth
Physical Review **156** 685-692 (1967)

3/6 A theory of the electrical properties of liquid metals. Ill The resistivity of binary alloys
T E Faber and J M Ziman
Philosophical Magazine **11** 153-173 (1965)

3/7 Structural aspects of the electrical resistivity of binary alloys
A B Bhatia and D E Thornton
Physical Review B **2** 3004-3012 (1970)

3/8 Dynamic structure factors and neutron scattering in molten salts
M C Abramo, M Parinello and M P Tosi
Journal of Physics C **7** 4201-4212 (1974)

3/9 Theory of thermal neutron scattering
W Marshall and S W Lovesey
Clarendon Press (Oxford) 1971

3/10 Scattering of slow neutrons by a liquid
G H Vineyard
Physical Review **110** 999-1010 (1958)

3/11 Atomic dynamics in liquids
N H March and M P Tosi
Macmillan (London) 1976

3/12 Accidental deviations of density and opalescence at the critical point of a single substance
L S Ornstein and F Zernike
Proceedings of the Acadamy of Sciences, Amsterdam **17** 793-806 (1914)

3/13 Exact solution of an integral equation for the structure of a primitive model of electrolytes
A Waisman and J L Lebowitz
Journal of Chemical Physics **52** 4307-4309 (1970)

3/14 On the hyper-netted chain approximation in the theory of classical fluids
G S Rushbrooke
Physica **26** 259-265 (1960)

3/15 Analysis of classical statistical mechanics by means of collective coordinates
J K Percus and G J Yevick
Physical Review **110** 1-13 (1958)

3/16 Equation of state calculation by fast computing machines
N Metropolis, A W Rosenbluth, M M Rosenbluth, A H Teller and E Teller
Journal of Chemical Physics **21** 1087-1092 (1953)

Chapter four

4/1 Slow neutron multiple scattering
V F Sears
Advances in Physics **24** 1-45 (1975)

Chapter five

5/1 Neutron research facilities at the ILL high flux reactor
Institut Max von Laue - Paul Langevin (1983)

5/2 Neutron scattering instruments at the ISIS facility
ISIS user guide, RAL (1987)

5/3 ISIS annual report 1986
RAL report RAL-86-061 (1986)

5/4 The study of the structure and dynamics of molten salts by neutron scattering
R L McGreevy
D. Phil, thesis, Oxford 1981

Chapter six

6/1 Inelastic scattering from a liquid sample confined within a cylindrical container: subtraction and attenuation corrections
P F J Poncet
ILL internal report 77PO139S (1977)

6/2 Subtraction and attenuation corrections for liquid samples confined within two coaxial cylinders
P J F Poncet
ILL internal report 77PO15S (1977)

Chapter seven

7/1 Slow neutron multiple scattering
V F Sears
Advances in Physics **24** 1-45 (1975)

7/2 Multiple scattering of neutrons in vanadium and copper
I A Blech and B L Averbach
Physical Review **137** 1113-1116 (1965)

7/3 Monte Carlo methods
J M Hammersley and D C Handscomb
Methuen (London) 1964

7/4 Monte Carlo evaluation of multiple scattering and resolution effects in double differential neutron scattering cross-section measurements
F G Bischoff, M L Yeater, and W E Moore
Nuclear Science and Engineering **48** 266-280 (1972)

7/5 Monte Carlo calculation of multiple scattering effects in thermal neutron scattering experiments
J R D Copley
Computer Physics Communications **7** 289-317 (1974)

Chapter eight

8/1 The scattering of neutrons by systems of heavy nuclei
G Placzek
Physical Review **86** 377-388 (1952)

8/2 The analysis of a time-of-flight neutron diffractometer for amorphous materials: the structure of a molecule in a liquid
J G Powles
Molecular Physics **26** 1325-1350 (1973)

8/3 Structure factor and radial distribution function of liquid argon
J L Yarnell, M J Katz, R G Wenzel, and S H Koenig
Physical Review A **7** 2130-2144 (1973)

Chapter nine

9/1 The structure of molten sodium chloride
F G Edwards, J E Enderby, R A Howe and D I Page
Journal of Physics C **8** 3483-3490 (1975)

9/2 The ion pair distribution functions in molten rubidium chloride
E W J Mitchell, P F J Poncet and R J Stewart
Philosophical Magazine **34** 721-732 (1976)

9/3 The structure of molten CsCl
J Locke, R L McGreevy, S Messoloras, E W J Mitchell and R J Stewart
Philosophical Magazine B **51** 301-315 (1985)

9/4 Interatomic distances in crystals of the alkali halides
M L Huggins and J E Mayer
Journal of Chemical Physics 643-646 (1933)

9/5 Monte Carlo simulation of the complete set of alkali halides
A Baranyai, I Ruff and R L McGreevy
Journal of Physics C **19** 453-456 (1986)

9/6 Structure of molten alkali chlorides: I a molecular dynamics study
M Dixon and M J Gillan
Philosophical Magazine B **43** 1099-1112 (1981)

9/7 Structure of classical liquid of charged hard spheres and point ions
M Gillan, B Larsen, M P Tosi and N H March
Journal of Physics C **9** 889-907 (1976)

9/8 Depolarisation ratios for Raman scattering from molten alkali and alkaline earth halides
M Fairbanks, R L McGreevy and E W J Mitchell
Journal of Physics C **19** L53-58 (1986)

9/9 The determination of the partial pair distribution functions for molten strontium chloride
R L McGreevy and E W J Mitchell
Journal of Physics C **15** 5537-5550 (1982)

9/10 Ionic dynamics in the LiCl-KCl system at liquid state
F Lantelme and P Turq
Journal of Chemical Physics **77** 3177-3187 (1982)

9/11 R L McGreevy - private communication

Chapter ten

10/1 The structure of molten CsCl
J Locke, R L McGreevy, S Messoloras, E W J Mitchell and R J Stewart
Philosophical Magazine B **51** 301-315 (1985)

10/2 Structure factors at low Q in molten $MgCl_2$ and $CaCl_2$
S E Day and R L McGreevy
Physics and Chemistry of Liquids **15** 129-136 (1985)

10/3 The Mathematical Theory of Communication
C E Shannon and W Weaver
University of Illinois Press (Urbana) 1949

10/4 Maximum entropy analysis of liquid diffraction data
J H Root, P A Egelstaff and B G Nickel
Institute of Physics Conference Series **81** 71-80 (1986)

10/5 Numerical Fourier transforms in one, two, and three dimensions for liquid state calculations
F Lado
Journal of Computational Physics **8** 417-433 (1971)

10/6 W S Howells (RAL) - private communication

Chapter eleven

11/1 Molecular dynamics studies of molten NaI: III longitudinal and transverse currents
M Dixon
Philosophical Magazine B **48** 13-29 (1983)

11/2 Inelastic neutron scattering studies of collective modes in molten CsCl
R L McGreevy, E W J Mitchell, F M A Margaça and M A Howe
Journal of Physics C **18** 5235-5247 (1985)

11/3 The structure of molten CsCl
J Locke, R L McGreevy, S Messoloras, E W J Mitchell and R J Stewart
Philosophical Magazine B **51** 301-315 (1985)

11/4 Molten salts handbook
G J Janz
Academic Press (New York) 1967

11/5 Single particle motion in liquid sodium
C Morkel and W Gläser
Physical Review A **33** 3383-3390 (1986)

11/6 Lattice dynamics of cesium chloride
A A Z Ahmad, H G Smith, N Wakabayashi and M K Wilkinson
Physical Review B **6** 3956-3961 (1972)

11/7 M Dixon - unpublished work

Chapter twelve

12/1 Electrical conductivity measurements on cuprous halides
J B Wagner and C Wagner
Journal of Chemical Physics **26** 1597-1601 (1957)

12/2 Crystal structure of high temperature silver iodide, α-AgI
L W Strock
Zeitschrift für Physikalische Chemie B **25** 441-459 (1934)

12/3 Additions and corrections to "Crystal structure of high temperature silver iodide, α-AgI"
L W Strock
Zeitschrift für Physikalische Chemie B **31** 133-140 (1936)

12/4 Crystal structure and phase transitions of some metallic halides. (IV) On the anomalous structure of α-AgI
S Hoshino
Journal of the Physical Society of Japan **12** 315-326 (1957)

12/5 Distribution and anharmonic thermal vibrations of cations in α-AgI
S Hoshino, T Sakuma and Y Fujii
Solid State Communications **22** 763-765 (1977)

12/6 The structure of superionic compounds by powder neutron diffraction. I. Cation distribution in α-AgI
A F Wright and B E F Fender
Journal of Physics C **10** 2261-2267 (1977)

12/7 The structure of α-AgI
M Suzuki and H Okazaki
Physica Status Solidi a **42** 133-140 (1977)

12/8 Structural study of superionic phase of AgI
Y Tsuchiya, S Tamaki and Y Waseda
Journal of Physics C **12** 5361-5369 (1979)

12/9 Diffuse neutron scattering from β- and α-AgI
H Feuss, K Funke and J Kalus
Physica Status Solidi a **32** 101-107 (1975)

12/10 The partial structure factors of molten cuprous chloride from neutron diffraction measurements
D I Page and K Mika
Journal of Physics C **4** 3034-3044 (1971)

12/11 Neutron diffraction determination of the partial structure factors of molten CuCl
S Eisenberg, J-F Jal, J Dupuy, P Chieux and W Knoll
Philosophical Magazine A **46** 195-209 (1982)

12/12 Extended X-ray absorption fine structure investigation of mobile ion density in superionic AgI, CuI, CuBr, and CuCl
J B Boyce, T M Hayes and J C Mikkelsen Jnr
Physical Review B **23** 2876-2896 (1981)

12/13 The structure of molten zinc chloride
S Biggin and J E Enderby
Journal of Physics C **14** 3129-3136 (1981)

12/14 The structures of molten magnesium and manganese (II) chlorides
S Biggin, M Gay and J E Enderby
Journal of Physics C **17** 977-985 (1984)

12/15 Isothermal compressibilities and thermal pressure coefficients of molten salts
B Cleaver and P N Spencer
High temperatures - high pressures **7** 539-547 (1975)

12/16 HNC calculation of the partial structure factors of molten AgI
A J Stafford and M Silbert
Zeitschrift für Physik B 67 31-33 (1987)

12/17 Structural transitions in superionic conductors
M Parinello, A Rahman and P Vashishta
Physical Review Letters **50** 1073-1076 (1983)

12/18 Modelling a molten superionic conductor in the mean spherical approximation
I Ruff, A Baranyai and O A Pizio
Chemical Physics Letters 150 958 (1988)

12/19 Collective modes in molten alkaline earth chlorides: II Inelastic neutron scattering from molten $SrCl_2$
F M A Margaça, R L McGreevy and E W J Mitchell
Journal of Physics C **17** 4725-4739 (1984)

12/20 Temperature dependence of the Raman depolarisation ratio in α-AgI
G Mariotto, A Fontana, E Cazzanelli, F Rocca, M P Fontana, V Mazzacurati and G Signorelli
Physical Review B **23** 4782-4783 (1981)

12/21 Raman spectroscopic studies of a continuous order-disorder transition in α-AgI
A Fontana, G Mariotto and M P Fontana
Physical Review B **21** 1102-1104 (1980)

12/22 Liquid dynamics and inelastic scattering of neutrons
P G de Gennes
Physica **25** 825-839 (1959)

12/23 R L McGreevy, D A Keen - private communication

Appendix A

A/1 Molten salts handbook
G J Janz
Academic Press (New York) 1967

A/2 Theory of neutron scattering from condensed matter
S W Lovesey
Clarendon Press (Oxford) 1984

Appendix D

D/1 A first course in numerical analysis
A Ralston
McGraw Hill (New York) 1965